



TECHNICAL REPORT

ARL-TR-98-2
2 July 1998

Copy Number

6

Test and Development of High Data Rate Millimeter Wave Data Links over Low Elevation Paths for Physical Security Systems

Technical Report under Contract N00039-91-C-0082
TD No. 08A1011, Non RF/Non Hardwire Data Link

Robert L. Rogers and Matthew A. Koerner

Prepared for: Defense Threat Reduction Agency
45045 Aviation Drive • Dulles, VA 20166-7517

Monitored by: Naval Sea Systems Command
Department of the Navy • Washington, DC 20362-5101

19991004 219

Approved for public release; distribution is unlimited.

Applied Research Laboratories • The University of Texas at Austin • Post Office Box 8029 • Austin, Texas 78713-8029

DTIC QUALITY INSPECTED 4

UNCLASSIFIED

REPORT DOCUMENTATION PAGE			Form Approved OMB No. 0704-0188	
Public reporting burden for this collection of information is estimated to average 1 hour per response, including the time for reviewing instructions, searching existing data sources, gathering and maintaining the data needed, and completing and reviewing the collection of information. Send comments regarding this burden estimate or any other aspect of this collection of information, including suggestions for reducing this burden, to Washington Headquarters Services, Directorate for Information Operations and Reports, 1215 Jefferson Davis Highway, Suite 1204, Arlington, VA 22202-4302, and to the Office of Management and Budget, Paperwork Reduction Project (0704-0188), Washington, DC 20503.				
1. AGENCY USE ONLY (Leave blank)	2. REPORT DATE <div style="text-align: center;">2 Jul 98</div>	3. REPORT TYPE AND DATES COVERED <div style="text-align: center;">technical</div>		
4. TITLE AND SUBTITLE Test and Development of High Data Rate Millimeter Wave Data Links over Low Elevation Paths for Physical Security Systems, Technical Report under Contract N00039-91-C-0082, TD No. 08A1011, Non RF/Non Hardwire Data Link			5. FUNDING NUMBERS N00039-91-C-0082, TD No. 08A1011	
6. AUTHOR(S) Rogers, Robert L. Koerner, Matthew A.			8. PERFORMING ORGANIZATION REPORT NUMBER ARL-TR-98-2	
7. PERFORMING ORGANIZATION NAMES(S) AND ADDRESS(ES) Applied Research Laboratories The University of Texas at Austin P.O. Box 8029 Austin, Texas 78713-8029				
9. SPONSORING/MONITORING AGENCY NAME(S) AND ADDRESS(ES) SPONSOR: Defense Threat Reduction Agency, 45045 Aviation Drive, Dulles, VA 20166-7517 MONITOR: Naval Sea Systems Command, Department of the Navy, Washington, DC 203662-5101			10. SPONSORING/MONITORING AGENCY REPORT NUMBER DSWA-TR-98-50	
11. SUPPLEMENTARY NOTES				
12a. DISTRIBUTION/AVAILABILITY STATEMENT Approved for public release; distribution is unlimited.			12b. DISTRIBUTION CODE	
13. ABSTRACT (Maximum 200 words) This report documents testing of a millimeter wave data link for its applicability to physical security systems. Propagation measurements were made at 27.3 GHz and 60 GHz. The feasibility of using these data links for high speed (1.5 Mbps tested) data transmission over low elevation transmission paths was established. Tests were conducted at Eglin Air Force Base (AFB), Davis Monthan AFB, and Minot AFB. The longest path over land tested was 9.6 km at 27.3 GHz. A 10.8 km path was tested over Choctawhatchee Bay, also at 27.3 GHz. Signal strength, weather conditions, and received test data and error statistics were collected simultaneously during the tests. Monthly and bimonthly averages of received power and weather conditions were computed from the measurements and showed seasonal variability at all three of the test sites. Histograms of received power, also generated from the test data, showed considerable variation on a monthly and bimonthly basis. In all cases, a high degree of reliability was observed with percent error-free times ranging from 99.5% to 99.8%. The longest observation time was over 9000 hr at Davis Monthan AFB. Important observations (cont'd)				
14. SUBJECT TERMS data link high speed data transmission hom antenna low-cost COTS data link low elevation transmission path millimeter wave data link physical security system			15. NUMBER OF PAGES 215	
17. SECURITY CLASSIFICATION OF REPORT UNCLASSIFIED			16. PRICE CODE	
			20. LIMITATION OF ABSTRACT SAR	
18. SECURITY CLASSIFICATION OF THIS PAGE UNCLASSIFIED		19. SECURITY CLASSIFICATION OF ABSTRACT UNCLASSIFIED		

UNCLASSIFIED

SF 298 (cont'd)

ARL-TR-98-2, Test and Development of High Data Rate Millimeter Wave Data Links over Low Elevation Paths for Physical Security Systems, Technical Report under Contract N00039-91-C-0082, TD No. 08A1011, Non RF/Non Hardwire Data Link

12. Abstract (cont'd)

of signal fluctuations caused by boundary effects of the terrain and the objects in or near the propagation path were made. These data should assist users in deployment of the data links, especially when using low elevation transmission paths for long distance signal transmission.

TABLE OF CONTENTS

	<u>Page</u>
LIST OF FIGURES.....	vii
LIST OF TABLES	xv
EXECUTIVE SUMMARY	xvii
1.0 INTRODUCTION.....	1
2.0 SYSTEM DESCRIPTION AND TEST LOCATIONS.....	9
2.1 SYSTEM DESCRIPTION.....	9
2.2 LONG-RANGE (KA-BAND) DATA LINK	12
2.3 SHORT-RANGE (V-BAND) LINK	17
2.4 DESCRIPTION OF TEST SEQUENCE.....	21
2.5 DESCRIPTION OF TEST LOCATIONS.....	23
2.6 EGLIN AFB, C-3 TO C-10.....	25
2.7 EGLIN AFB, KING HANGAR TO A-3	32
2.8 MINOT AFB, NW END OF RUNWAY TO TOP OF BASE HOSPITAL	33
2.9 DAVIS MONTHAN AFB, SKEET RANGE TO LAW BUILDING	34
3.0 LONG-RANGE TEST RESULTS.....	39
3.1 EGLIN, C-3 TO C-10 TEST, 1995	39
3.2 EGLIN, KING HANGAR TEST	48
3.3 MINOT AFB TEST, NOVEMBER 1995 THROUGH MARCH 1996.....	67
3.4 DAVIS MONTHAN TEST.....	82
3.4.1 Seasonal Average Statistics.....	83
3.4.2 Summer Data Set 62271158.....	96
3.4.3 Fall Data Set 62701448.....	99
3.4.4 Winter Data Set 70512036.....	105
3.5 NONPRECIPITATION-INDUCED SIGNAL FLUCTUATIONS.....	110

	<u>Page</u>
4.0 SHORT-RANGE TESTS.....	111
4.1 EGLIN, SHORT-RANGE C-3 TEST	111
4.1.1 Description of Data Set 52010850.....	112
4.1.2 Description of Data Set 52120806.....	116
4.2 DAVIS MONTHAN, SHORT-RANGE LINK TEST	121
4.3 INTERCEPT TESTS.....	125
5.0 BAFFLED PYRAMIDAL HORN ANTENNA	131
5.1 THE PYRAMIDAL HORN	132
5.1.1 Pyramidal Horn Configuration	132
5.1.2 Aperture Field Effects	134
5.2 WIDE-FLARE, PYRAMIDAL X-BAND HORN AND MODELS	135
5.2.1 Construction	135
5.2.2 Two-Dimensional Numerical Models.....	136
5.3 NUMERICAL RESULTS.....	140
5.3.1 E-Plane Numerical Results.....	140
5.3.2 H-Plane Numerical Results.....	144
5.4 EXPERIMENTAL RESULTS	150
5.4.1 Setup	150
5.4.2 Measurements	152
5.4.3 Comparison to an Optimum-Gain Horn	155
5.5 APPLICATION OF BAFFLED PYRAMIDAL HORN	157
6.0 CONCLUSIONS	159
APPENDIX A - LOW-COST DEMONSTRATION LINK	161
APPENDIX B - NUMERICAL ANTENNA ANALYSIS.....	171
B.1 E-PLANE, TWO-DIMENSIONAL PEC MFIE	173
B.2 H-PLANE, TWO-DIMENSIONAL PEC EFIE	174
B.3 MOMENT METHOD	176
B.4 INTEGRATION	178
B.5 INTERIOR-FIELDS AND FAR-FIELDS	179

	<u>Page</u>
B.6 DIRECTIVITY, DIRECTIVE GAIN, AND BEAM PATTERNS.....	179
B.7 INPUT IMPEDANCE AND GAIN.....	180
APPENDIX C - DD FORM 1494.....	183
GLOSSARY.....	201
REFERENCES.....	207

This page intentionally left blank.

LIST OF FIGURES

<u>Figure</u>		<u>Page</u>
2.1	General test setup and data collection system.....	10
2.2	Long-range transmitter block diagram	13
2.3	Long-range receiver block diagram.....	14
2.4	Short-range transmitter block diagram.....	18
2.5	Short-range receiver block diagram	20
2.6	Typical installation in a utility room or tower	24
2.7	Test site 1 at Eglin AFB.....	26
2.8	Test site 2 at Eglin AFB.....	27
2.9	Test site at Minot AFB	28
2.10	Test site at Davis Monthan AFB	29
2.11	Photograph of Eglin tower at C-3, showing short- and long-range receivers	30
2.12	Photograph of long-range transmitter at C-10, showing top of building with large antenna for the tracking radar.....	31
2.13	Setup of the short- and long-range receivers on top of the SPS office building (building 1540) at Davis Monthan.....	35

<u>Figure</u>		<u>Page</u>
2.14	Setup of the short- and long-range transmitter on top of the skeet building at Davis Monthan.....	36
3.1	Vertical polarization time series data from 51630819: bit error rate, temperature at the receiver, wind speed, and measured signal strength.....	42
3.2	Vertical polarization time series data from 51630819: block count, rainfall rate, sweep/lock indicator, and percent error-free seconds of transmission.....	43
3.3	Scatter plot of signal strength versus wind speed for 51630819. Each data point is an average of 12 data points.....	44
3.4	Horizontal polarization time series data from 52211111: bit error rate, temperature at the receiver, wind speed, and measured signal strength.....	45
3.5	Horizontal polarization time series data from 52211111: block count, rainfall rate, sweep/lock indicator, and percent error-free seconds of transmission.....	46
3.6	Scatter plot of signal strength versus wind speed for 52211111. Each data point is an average of 53 data points.....	47
3.7	Seasonal average power.....	51
3.8	Seasonal average temperature.....	52
3.9	Seasonal average wind speed.....	53
3.10	Seasonal cumulative rainfall.....	54

<u>Figure</u>		<u>Page</u>
3.11	Histogram of signal strength data from May 1996 through November 1996	58
3.12	Histogram of signal strength data from July 1996.....	59
3.13	Histogram of signal strength data from August 1996	60
3.14	Histogram of signal strength data from September 1996	61
3.15	Histogram of signal strength data from October 1996.....	62
3.16	Vertical polarization time series data from 62060635: bit error rate, temperature at the receiver, wind speed, and measured signal strength.....	63
3.17	Vertical polarization time series data from 62060635: block count, rainfall rate, sweep/lock indicator, and percent error-free seconds of transmission.....	64
3.18	Vertical polarization time series data from 62831341: bit error rate, temperature at the receiver, wind speed, and measured signal strength.....	65
3.19	Vertical polarization time series data from 62831341: block count, rainfall rate, sweep/lock indicator, and percent error-free seconds of transmission.....	66
3.20	Seasonal average power	68
3.21	Seasonal average temperature.....	69
3.22	Seasonal average wind speed	70

<u>Figure</u>		<u>Page</u>
3.23	Histogram of signal strength data from November through April 1996.....	71
3.24	Histogram of signal strength data for December 1995.....	72
3.25	Histogram of signal strength data for January 1996.....	73
3.26	Histogram of signal strength data for February 1996.....	74
3.27	Histogram of signal strength data for March 1996.....	75
3.28	Vertical polarization time series data from 60341059: bit error rate, temperature at the receiver, wind speed, and measured signal strength.....	78
3.29	Vertical polarization time series data from 60341059: block count, rainfall rate, sweep/lock indicator, and percent error-free seconds of transmission.....	79
3.30	Vertical polarization time series data from 60660520: bit error rate, temperature at the receiver, wind speed, and measured signal strength.....	80
3.31	Vertical polarization time series data from 60660520: block count, rainfall rate, sweep/lock indicator, and percent error-free seconds of transmission.....	81
3.32	Bimonthly average power.....	84
3.33	Bimonthly average temperature and power.....	85
3.34	Bimonthly average wind speed.....	86

<u>Figure</u>		<u>Page</u>
3.35	Bimonthly cumulative rainfall at the transmitter and receiver.....	87
3.36	Representative averages of bit error rate (BER) and percent error-free seconds (% EFS)	90
3.37	Histogram of signal strength data from June 1996 through June 1997	91
3.38	Histogram of signal strength data for July and August 1996	92
3.39	Histogram of signal strength data for November and December 1996	93
3.40	Histogram of signal strength data for March and April 1997	94
3.41	Vertical polarization time series data from 62271158: bit error rate, temperature at the receiver, wind speed, and measured signal strength.....	97
3.42	Vertical polarization time series data from 62271158: block count, rainfall rate, sweep/lock indicator, and percent error-free seconds of transmission.....	98
3.43	Vertical polarization time series data from 62701448: bit error rate, temperature at the receiver, wind speed, and measured signal strength.....	100
3.44	Vertical polarization time series data from 62701448: block count, rainfall rate, sweep/lock indicator, and percent error-free seconds of transmission.....	101
3.45	Scatter plot of signal power standard deviation versus average temperature for data set 62701448	103

<u>Figure</u>		<u>Page</u>
3.46	Scatter plot of signal power standard deviation versus average wind speed for data set 62701448.....	104
3.47	Vertical polarization time series data from 70512036: bit error rate, temperature at the receiver, wind speed, and measured signal strength.....	106
3.48	Vertical polarization time series data from 70512036: block count, rainfall rate, sweep/lock indicator, and percent error-free seconds of transmission.....	107
3.49	Scatter plot of signal power standard deviation versus average wind speed for data set 70512036.....	108
3.50	Scatter plot of signal power standard deviation versus average temperature for data set 70512036.....	109
4.1	Horizontal polarization time series data from 52010850: bit error rate, temperature at the receiver, wind speed, and measured signal strength.....	114
4.2	Horizontal polarization time series data from 52010850: block count, rainfall rate, sweep/lock indicator, and percent error-free seconds of transmission.....	115
4.3	Horizontal polarization time series data from 52120806 (Hurricane Erin data set): bit error rate, temperature at the receiver, wind speed, and measured signal strength.....	118
4.4	Horizontal polarization time series data from 52120806 (Hurricane Erin data set): block count, rainfall rate, sweep/lock indicator, and percent error-free seconds of transmission	119

<u>Figure</u>		<u>Page</u>
4.5	Horizontal polarization time series data from 52120806 (Hurricane Erin data set): wind speed, wind direction, barometric pressure, and rainfall	120
4.6	Vertical polarization time series data from 63100384 (5–12 November, autumn-winter data): bit error rate, temperature at the receiver, wind speed, and measured signal strength.....	124
4.7	Vertical polarization time series data from 63100384 (5–12 November, autumn-winter data): block count, rainfall rate, sweep/lock indicator, and percent error-free seconds of transmission.....	126
4.8	Vertical polarization time series data from 70070845 (7–14 January, autumn-winter data): bit error rate, temperature at the receiver, wind speed, and measured signal strength.....	127
4.9	Vertical polarization time series data from 70070845 (7–14 January, autumn-winter data): block count, rainfall rate, sweep/lock indicator, and percent error-free seconds of transmission.....	128
5.1	Pyramidal horn.....	133
5.2	Two-dimensional models	137
5.3	E-plane, calculated on-axis directivity and gain	141
5.4	Calculated E-plane, interior magnetic fields at 10.5 GHz	143
5.5	Calculated E-plane beam patterns at 10.5 GHz.....	145

<u>Figure</u>		<u>Page</u>
5.6	H-plane, calculated on-axis directivity and gain	146
5.7	Calculated H-plane, interior electric fields at 10.5 GHz.....	148
5.8	Calculated H-plane beam patterns at 10.5 GHz.....	149
5.9	Pyramidal horn loaded with combination baffle.....	151
5.10	Measured on-axis gain versus frequency for E-plane and H-plane baffles.....	153
5.11	Measured gain and aperture efficiency of horn with combination baffle	154
5.12	Measured beam patterns at 10.5 GHz.....	156
A.1	Low-cost transceiver block diagram.....	165
A.2	Low-cost data link functional diagram.....	167

LIST OF TABLES

<u>Table</u>	<u>Page</u>
ES.1 Results summary for long-range link tests	xix
2.1 Characteristics of the long-range data link.....	16
2.2 Characteristics of the short-range data links.....	21
3.1 Long-range data link characteristics.....	40
3.2 Statistics from the two data sets shown, transmitted bit pattern: QRSS, 1024 bits/block.....	41
3.3 Data link characteristics	50
3.4 Summary of Eglin AFB tests (King Hangar to A-3) (high RF traffic environment)	50
3.5 Statistics from two 1-week data sets shown, transmitted bit pattern: QRSS, 1024 bits/block	55
3.6 Calculated rainfall statistics for Eglin King Hangar to A-3 path	56
3.7 Data link characteristics	76
3.8 Summary of Minot AFB long-range link information	77
3.9 Statistics from the two data sets shown, transmitted bit pattern: QRSS, 1023 bits/block.....	82
3.10 Davis Monthan data link characteristics	89

<u>Table</u>		<u>Page</u>
3.11	Summary of Davis Monthan AFB tests.....	89
3.12	Statistics from the three data sets shown, transmitted bit pattern: QRSS, 1024 bits/block	95
4.1	Link characteristics of short-range link at Eglin AFB	113
4.2	Statistics from the two data sets shown, transmitted bit pattern: 2047 bits/ block.....	116
4.3	Link characteristics of short-range link at Davis Monthan AFB	122
4.4	Statistics from the data sets shown, transmitted bit pattern: 1023 bits/block.....	123
4.5	Summary of Davis Monthan AFB short-range link information, November 1996–March 1997	123
5.1	Dimensions of wide-flare X-band pyramidal horn	136
5.2	Dimensions used in two-dimensional models.....	139
5.3	Calculated dimensions of optimum-gain horn.....	157
A.1	Link budget	168
A.2	Specifications of the low-cost demonstration link.....	169
A.3	Low-cost data link features	170

EXECUTIVE SUMMARY

The goal of this project was to determine the reliability of millimeter wave data links for automatic physical security systems. For this purpose, test data links were set up at Eglin Air Force Base (AFB) in Ft. Walton Beach, Florida, Minot AFB near Minot, North Dakota, and Davis Monthan AFB in Tucson, Arizona.

Seven key elements were successfully demonstrated in this test:

- 1) Established the feasibility of low elevation millimeter wave data transmission at Ka-band (27.1 GHz) for highly reliable data transmission at low elevation overland up to 9.6 km and over-water links up to 10.8 km.
- 2) Millimeter wave data transmission reliability was tested at V-band for up to 1.3 km ranges in high RF traffic environments. No identifiable interference was observed on any of the test data.
- 3) Millimeter wave data links are very insensitive to electronic interference even when the electronic interference is near or in band, because of the highly directional nature of the antennas.
- 4) Reliable performance with commercial low-cost components was demonstrated under a wide variety of weather conditions.
- 5) Low power transmission was demonstrated. The long-range transmitter had an output power of 100 mW, the short-range transmitter had an output power of 50 mW, and data rates of 1.5 Mbps were transmitted with low bit error rates.
- 6) A low-cost two-way K-band (24 GHz) link was constructed and demonstrated with very low-cost parts. A similar Ka-band link can be constructed. Low-cost commercially available antennas with gains greater than 37 dB were implemented with this link.

- 7) A low-cost horn antenna was designed and tested at X-band (10 GHz), which can provide moderate gain (20–24 dB) with compact, low-cost, rugged antenna design. This design is scaleable to Ka-band (27 GHz) or V-band (60 GHz).

Because physical security systems must be deployed and removed quickly and easily with a minimum of equipment, the antennas for the link cannot be mounted arbitrarily high. This effort focused on the reliability of low elevation “barely-line-of-sight” paths for 27 GHz and 60 GHz data links. The 27 GHz data link (the long-range link) was used for path links of nominally 7 km, and the 60 GHz data link was used for path lengths of nominally 1 km. The actual path lengths tested for the long-range link and their location are listed in Table ES.1.

The modulation for all of the data links used here is continuous phase frequency-shift keying (CPFSK or FSK). The deviation ratio for the 1.5 Mbps data transmission rate was about 0.1, so the modulation was effectively narrow-band FM modulation. The 19.2 Kbps data rate links used a deviation ratio of about 15 and, therefore, was effectively wideband modulation.

Good performance was observed for the long-range data link in all climactic tests as shown in Table 1.1. Three of the four test sites gathered large quantities of accurate data on which reliable statistical calculations could be made. It was found that the 27.3 GHz transmission path was reliable and was suited for physical security systems. It is important to note that anomalous signal fluctuations occurred under calm conditions, which were most likely due to boundary effects from the “barely-line-of-sight path.” The fluctuations did not unduly interfere with the reliability of the transmission channel in these tests, but should be noted and the circumstances that might cause their occurrence avoided if possible in future system deployments. To the authors' knowledge, this work documents the first time this type of signal fluctuation has been reported.

Table ES.1
Results summary for long-range link tests.

Eglin AFB C-3 to C-10 Test Area	7 km over pine trees 25–35 ft height 19.2 Kbps data rate Statistics from a limited sample of data Average bit error rate (BER) $8.0e-5$ Percent error-free time 99.81
Eglin AFB A-3 to King Hangar	10.8 km over water 19.2 Kbps data rate Total test time: 3985 h Average BER $2.7e-4$ Percent error-free time 99.5%
Minot AFB Building 1062 to Base Hospital	6.7 km over moderate building clutter 1.5 Mbps data rate 2248 h Average BER $6.8e-6$ Percent error-free time 99.92%
Davis Monthan AFB Skeet Range to Building 4413	9.6 km over aircraft storage area 1.5 Mbps data rate Total test time: 9017 h Average BER $5.4e-4$ Percent error-free time 99.7%

Test results of the short-range data link performed at Eglin AFB C-3 and Davis Monthan AFB were reported. The lengths of these two paths were 0.8 km and 1.13 km respectively. The data collected from these tests indicated that the links performed reliably for short ranges and in the environments tested. Tests were also conducted at Minot AFB with a range of 1.3 km. Because of difficulties with the hardware, few accurate test results were available. However, the use of the link at 1.3 km in the North Dakota climate appeared to be feasible.

During all testing, weather was continuously monitored at the receiver. For the long data paths at Eglin (A-3 to King Hangar, 10.8 km — the transmitter was at the beach, the receiver was across the bay) and Davis Monthan (9.6 km), the weather was also recorded at the transmitter. This was found to be helpful for determining the location of intense storm cells, as well as useful for checking the accuracy of weather measurements.

1.0 INTRODUCTION

This report describes the testing of a millimeter wave data link for distributed physical security systems. A series of tests were conducted that provided a proof-of-concept demonstration for the feasibility of these data links for the application for physical security systems. In addition to this testing, a low-cost prototype was constructed to demonstrate that a small battery-powered data link with part costs of approximately \$2000 for a link pair was feasible, and would transmit the desired video (standard 30 frame/s video) and digital data signals. Digital data were sent at a rate of 1.5 Mbps and 19.2 Kbps to assist in the assessment of quality of the transmission path. Transmission path lengths varied from under 1 km to a maximum of 10.8 km.

Tests were conducted at five locations:

- 1) Eglin Air Force Base (AFB) C-3 to C-10, Eglin AFB, Florida:
 - high humidity
 - low elevation over trees
 - high RF traffic
- 2) Eglin AFB A-3 to King Hangar, Eglin AFB, Florida:
 - high humidity
 - high rainfall
 - over water
 - high RF traffic
- 3) Minot AFB, Minot, North Dakota:
 - cold weather testing
 - low elevation path
- 4) Davis Monthan AFB, Tucson, Arizona:
 - desert testing
 - high RF traffic environment
 - low elevation path over metallic clutter (aircraft)
 - seasonal effects

5) Quantico, Virginia:

- proof-of-concept demonstration
- limited testing
- low-cost link
- portable, battery-operated link
- realtime video with two-way data transmission

Reliable wireless data links for physical security systems are desirable for distributed automatic systems. The demands for electromagnetic spectrum and solving the problems of interference are increasing. The requirement for a secure data link that does not interfere with other communications in peacetime or with military operations at any time, has been addressed in this effort with the use of a millimeter wave data link. In the past, millimeter wave data links were expensive and useful only in permanent installations where the high hardware cost was not prohibitive. With the advent of MMICs (monolithic microwave/millimeter wave integrated circuits), the rapid commercialization of direct-broadcast satellite systems, and now the LMDS (Local Multipoint Distribution Service), the cost of components for this frequency band has been reduced significantly. This trend is expected to continue. The effort described in this report was undertaken with the anticipation that these technologies would become available.¹ Low cost and manufacturability are essential for communications in physical security systems. High quality components are now becoming available so that transceiver modules operating at Ka-band could be manufactured for costs of \$500–\$1000 per transceiver. This appears to be feasible, and a low-cost demonstration unit is described in Appendix A of this report.

Because the rapid development of receiver and transmitter components in industry is currently being pursued for commercial applications, this investigation focused on the propagation, reliability, and antenna development aspects of the data link. Assessing the reliability of a transmission channel is a key step in

determining the suitability of a type of data link for use in a system.²⁻⁴ Antennas are a critical component of a data link. Rugged, low-cost antennas with adequate gain are essential to the successful implementation of this technology. The low-cost link developed in this effort utilized a low-cost reflector antenna that is currently being used for satellite TV service and that is described in Appendix A. This antenna provided a gain at K-band (24 GHz) of more than 38 dB. Furthermore, this antenna cost about \$50 per unit, retail. This configuration is especially beneficial for long-range links that are separated by many kilometers.

Some applications require less range, and reflector antennas are relatively more sensitive to physical damage than horn antennas. Moderate and high gain horn antennas are either inconveniently large, or they require expensive lenses. A horn antenna was developed to circumvent these problems and provide a rugged, compact, and inexpensive antenna with adequate gain for moderate ranges. The basic concepts developed for this antenna may also allow higher gain antennas to be produced with this low-cost design.

Many manufacturers of communications systems claim ranges of 7 km or greater for their equipment. However, very often the conditions under which these ranges can be achieved are not stated. Furthermore, in some cases the advertised range assumes optimal propagation conditions and optimum system performance. Hence, the conditions would have to be "mountain top to mountain top" on a clear and calm day, although even these propagation conditions are not always perfect.⁵ This is rarely the situation encountered for a security system.

Millimeter wave data links have the potential to provide a portable low-cost and low power means of transmitting high data rates over distances of 10 km with high reliability, as evidenced by tests conducted at Eglin AFB. Ambient conditions can have a dramatic impact on the link. Although standard models exist for the microwave and millimeter wave propagation calculations, physical security systems often operate under conditions that are not accounted for in these models. In most cases, it is not practical or desirable to make the antenna

elevations much higher than existing structures and/or the treetop canopy. Thus, the link will be transmitting over paths close to the ground and at low grazing angles. The data presented in this report show that, as expected, rainfall had some effect on the transmission path. In some cases, low elevation transmission paths had significant excess path loss even when a clear line-of-sight existed.

These tests focused on Ka-band and V-band measurements. Ka-band was selected because it was relatively less sensitive to rainfall than higher frequencies, and it was also possible to find commercially available hardware that could be manufactured at low cost.⁶ The short-range data link operating frequency of 60 GHz was selected because this is the oxygen absorption line. Signals at this frequency are absorbed in the atmosphere with an attenuation rate of about 16 dB/km at sea level. This high rate of absorption limits the range of transmission. Although this limits the useful range to about 1 km over which this link can be used, it also limits the possibility of unwanted signal intercept and signal interference. The results of the tests showed that the 27-GHz link was highly reliable in most circumstances. However, propagation measurements over a 7-km path close to the tree tops showed fluctuations in the signal levels during calm conditions. Current propagation measurements have not reported these types of fluctuations.⁷ These fluctuations appeared to be polarization-dependent.

Seven key elements were successfully demonstrated in this test:

- 1) Established the feasibility of low elevation millimeter wave data transmission at Ka-band (27.1 GHz) for highly reliable data transmission at low elevation overland up to 9.6 km and over-water links up to 10.8 km.
- 2) Millimeter wave data transmission reliability was tested at V-band for up to 1.3-km ranges in high RF traffic environments. No identifiable interference was observed on any of the test data.

- 3) Millimeter wave data links are very insensitive to electronic interference even when the electronic interference is near or in band, because of the highly directional nature of the antennas.
- 4) Reliable performance with commercial low-cost components was demonstrated under a wide variety of weather conditions.
- 5) Low power transmission was demonstrated. The long-range transmitter had an output power of 100 mW, the short-range transmitter had an output power of 50 mW, and data rates of 1.5 Mbps were transmitted with low bit error rates.
- 6) A low-cost two-way K-band (24 GHz) link was constructed and demonstrated with very low-cost parts. A similar Ka-band link can be constructed. Low-cost commercially available antennas with gains greater than 37 dB were implemented with this link.
- 7) A low-cost horn antenna was designed and tested at X-band (10 GHz), which can provide moderate gain (20–24 dB) with compact, low-cost, rugged antenna design. This design is scaleable to Ka-band (27 GHz) or V-band (60 GHz).

This investigation was intended to provide data regarding the feasibility of low-angle overland millimeter wave data links. Low angle of propagation is strongly dependent on the terrain and the meteorological conditions. Most existing data are for center frequencies of hundreds of megahertz to a few gigahertz, but the frequencies used in the tests described in this report are an order of magnitude higher. Therefore, the data collected for lower frequency links have limited applicability for these higher frequencies. In the case of conventional permanent microwave link installations, tall structures can be used to assure clearance of all obstacles and to reduce diffraction effects on the ground. In physical security applications, this is not practical, and often the minimum height necessary to obtain a clear line-of-sight must be used. Ranges from 1–10.8 km were used for the tests discussed in this report. At the frequencies used in these tests, it was found that ground and interfering objects

were often within the first Fresnel zone of the propagation path between the transmitter and the receiver.⁶ Objects within the first Fresnel zone are close to the center line of the path between the two antennas and can cause significant degradation of the signal transmission. Weather conditions also had a significant impact on the link performance, and to insure that valid statistics were gathered, data collection over extended periods of time were performed.

Because the focus of this test was placed on reliability, most of the measurements were oriented towards collecting long-term reliability statistics. Some tests were conducted to introduce deliberate interference. The tests were successful in demonstrating there was no interference at any time during any of the testing. Typical applications for these systems require extended periods of operation with no monitoring and no adjustments.

To facilitate data collection, an automatic data collection system was used to continuously test the transmission path and record it on a laptop computer. This system was very reliable for most of the tests and allowed long periods of unattended data collection. The longest period of unsupervised operation was 20 weeks. During this time, the long-range link functioned without any problems and the short-range link experienced no RF problems. This data collection system proved to be a powerful tool for evaluating the data link channel quality. This system allowed a continuous test to run in realistic environments at very low cost.

A demonstration link was constructed that consisted of a low-cost link that would in principle meet most of the requirements. The link was also a two-way link that could be used to communicate data in half-duplex mode. With modest improvements in the low frequency circuits, this link could be made to operate with high data rates (for example, realtime video) in full duplex mode. The data rates possible with this link are in excess of several Mbps. This system was built entirely from low-cost commercial components. For example, the reflector antenna used was the standard offset-fed 18 in. reflector that is used for direct

satellite reception for households. This antenna cost about \$50 with all of the mounting hardware. The measured gain from this antenna at 24 GHz is in excess of 37 dB. A previously available alternative antenna cost over \$3500 and did not have as high a gain. Similar improvements have been made on most of the critical components needed for transmitters and receivers. The demonstration link utilizes only these mass-produced components.

This report is organized as follows: Section 2.0 is a description of the testing locations and the data acquisition system that was used; Section 3.0 is a description of the results from the long-range data link tests; Section 4.0 is a description of the results from the short-range data link tests; Section 5.0 is a description of the low-cost data link; and Section 6.0 contains the conclusions.

This page intentionally left blank.

2.0 SYSTEM DESCRIPTION AND TEST LOCATIONS

2.1 SYSTEM DESCRIPTION

Two long-range (Ka-band) and two short-range (V-band) test systems were designed and constructed for this study. One set of long- and short-range systems was used for testing at Eglin AFB and the other set was used at Minot and Davis Monthan AFBs. Differences between the two long-range systems as well as the two short-range systems were minor and will be discussed in the following description and results. The main purpose of the propagation tests was to determine the feasibility of using data links in what is called "barely line-of-sight" paths. In this report, "barely line-of-sight" means that the transmission path is nominally line-of-sight, but the path is very low to the ground. In several cases, there were objects such as aircraft tails and trees that were higher than the path, but a line-of-sight was available to one side of the obstruction(s). The path elevation above terrain features or clutter was usually less than 10 ft. This put the obstructing elements in the first Fresnel zone.

The test systems were installed at fixed locations and configured to transmit and receive continuously over extended periods of time. In a general test setup, the transmitter was fixed to a structure that gave the system a line-of-sight just above the ground clutter. The transmitting carrier was modulated with continuous-phase FSK digital data of a known pattern. The receiver was mounted in a similar manner and aligned with the transmitter. Link performance, data statistics, and environmental conditions were monitored at the receiver and archived through a laptop PC at periodic intervals of time. This general setup is illustrated in Fig. 2.1.

As mentioned previously, digital data were modulated onto the carrier signals by means of continuous-phase FSK. The purpose of the data transmission was two-fold. First, actual bit error rates were measured over the

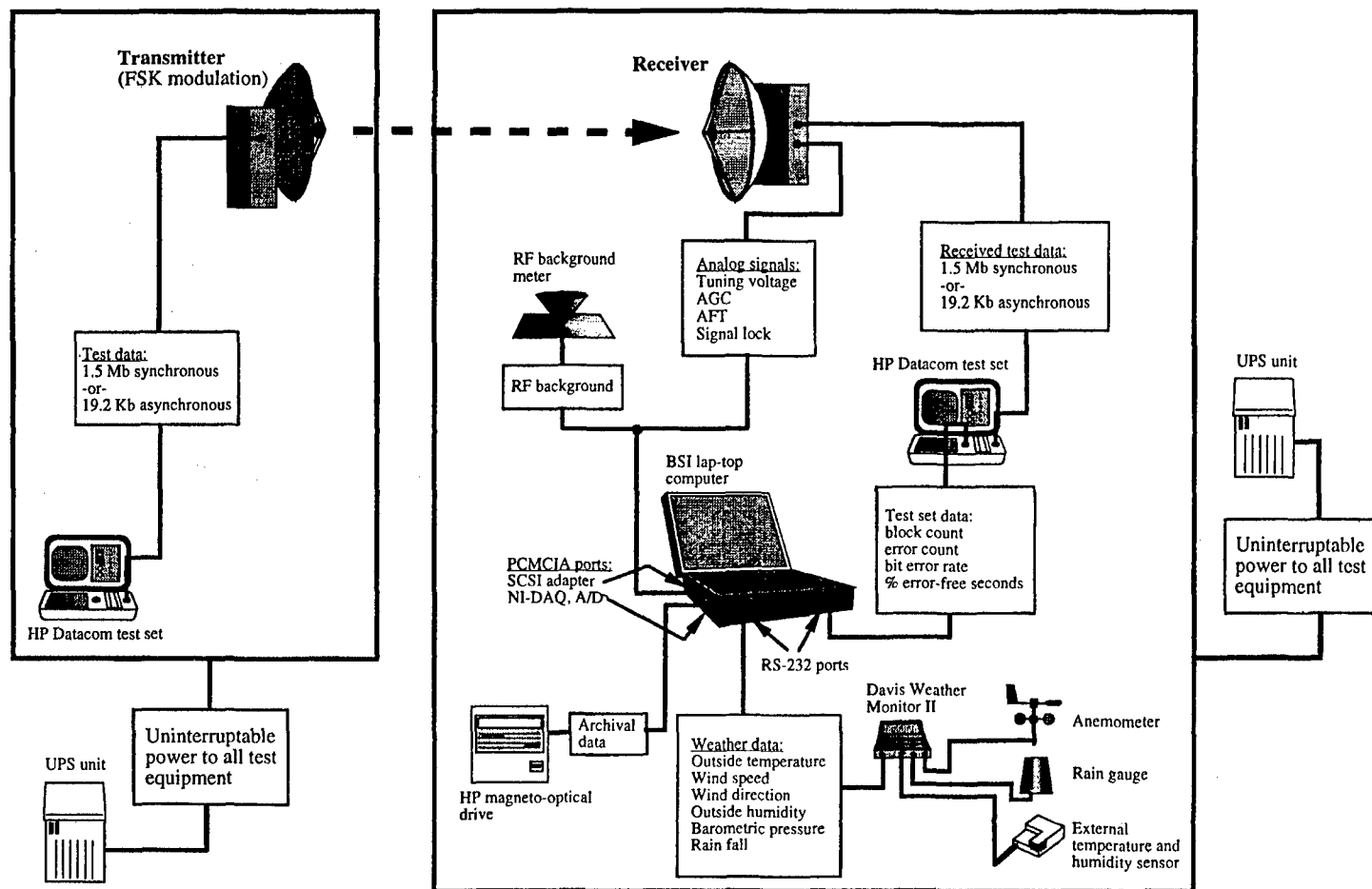


Figure 2.1
General test setup and data collection system.

channel. This provided a measured quantity that could be compared with calculations. Second, one of the purposes of this study was to assess the problems associated with RF interference and possible spurious signal reception; encoding the transmitted test signal with a known data pattern provided a means to distinguish the test signal from interfering signals. Interfering signals appearing as signal strength enhancements would also cause errors in the received data. Thus, periods of interference would not be mistaken for ducting or focusing because of refractive changes in the atmosphere.

A data rate of 19.2 Kbps was used for the long- and short-range links at Eglin AFB. This is a typical RS-232 rate that met the requirements for data sent from many different security devices. The receivers used in all of the test systems had a selectable channel bandwidth of 7 or 17 MHz. The narrow 7-MHz setting was chosen for all of the tests. With 7 MHz of bandwidth, the 19.2-Kbps data were sent with a frequency deviation ratio of approximately 15. A much higher data rate of 1.5 Mbps was used at Minot and Davis Monthan AFBs. This rate was chosen to exploit the bandwidth properties of the system. The short- and long-range carrier frequencies could support much higher data rates than 1.5 Mbps, but this was the highest rate that the telecommunication test sets used to generate the data. At 1.5 Mbps the test sets only produced synchronous data, so the data were Manchester-encoded before transmission. Fitting the Manchester-encoded 1.5 Mbps data into a 7-MHz band required using narrow-band FM modulation with a frequency deviation ratio of approximately 0.1.

In addition to using the encoded data to distinguish the transmitted signal from interfering sources, a background RF power meter was placed at each receiver location to measure the power of possible interfering signals. It is believed that harmonics of high-powered sources such as radar systems on the Air Force bases could cause interference. Therefore, the RF power meters were designed to operate over a frequency range from 2–18 GHz with 40 dB of dynamic range. The power meters' RF front-ends consisted of a low noise amplifier feeding a detector diode. The output of the diode in each power meter

was buffered with a precision low-frequency operational amplifier circuit and a logarithmic amplifier. Conical antennas were used with the power meters for their broadband characteristics. The antennas consisted of a metal cone suspended over a ground plane. The vertex of the cone was placed in the center of the ground plane so that the cone flared up and away from the ground. The cones were 2 1/2 in. high by 4 in. in diameter, and the ground planes were 1 ft². Two power meters were built, one for each set of long- and short-range systems. At each test site except Minot, the long- and short-range receivers were located close enough to one another so that only one power meter was necessary. At Minot, no RF background level data were taken for the short-range system.

2.2 LONG-RANGE (KA-BAND) DATA LINK

Figure 2.2 shows the block diagram of a long-range transmitter. The transmitter utilizes a voltage-tuned dielectric resonator oscillator (VT-DRO) tuned to a center frequency of 13.65 GHz, and a doubling amplifier to provide a 27.3-GHz carrier with 100 mW (20 dBm) of power. The transmitted carrier is modulated through the voltage applied to the tuning pin of the VT-DRO. The incoming baseband digital signal is buffered, added to a dc offset to set the center frequency, and then applied to the tuning pin. The low transmit power level was chosen so that a low-probability-of-intercept could be maintained. This power level proved to be adequate for all of the tests, even when the range was extended past 10.8 km over water.

The long-range transmitters and receivers used Cassegrain reflector antennas (see Figs. 2.2 and 2.3). These antennas were chosen because they are relatively compact high gain antennas. The stated factory gain of these antennas was 37 dB, but repeated measurements under a variety of conditions showed a maximum gain of about 35 dB. Thus, the effective radiated power from the transmitters was approximately 55 dBm.

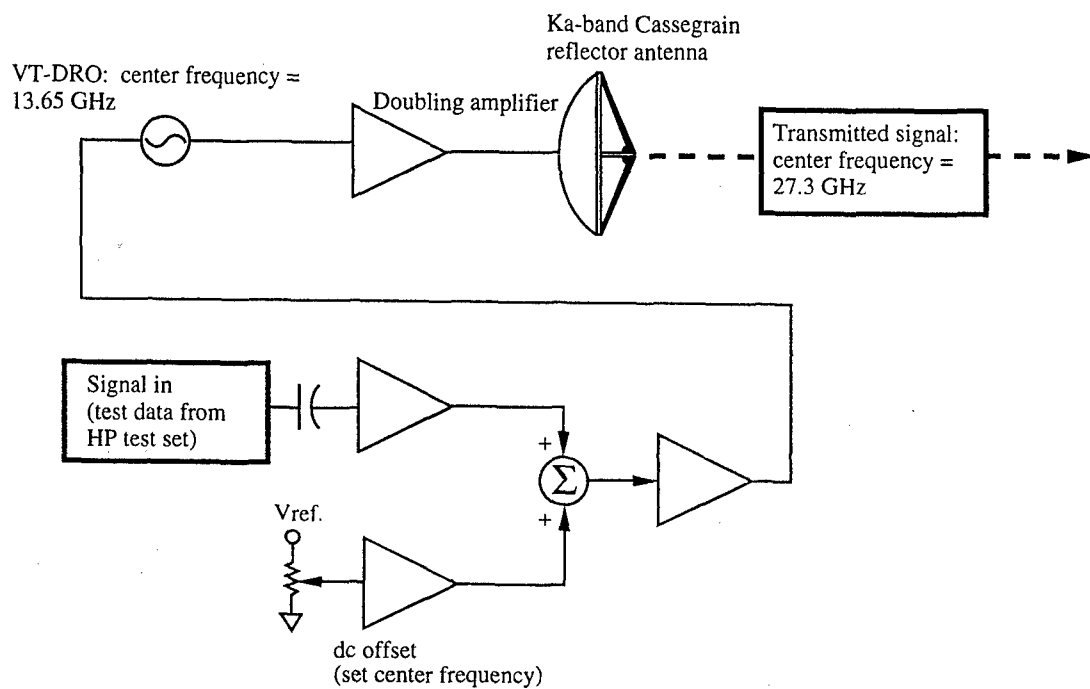


Figure 2.2
Long-range transmitter block diagram.

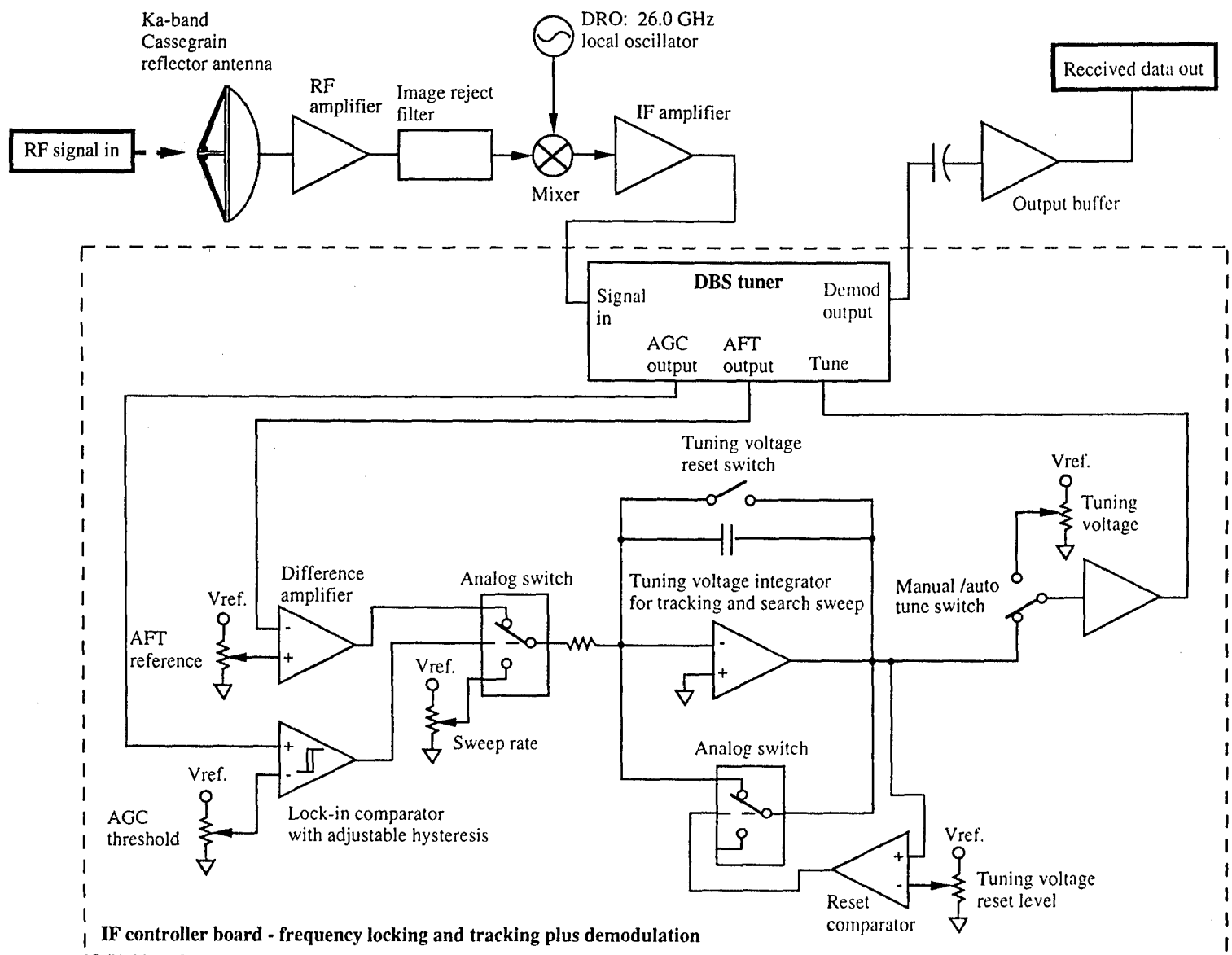


Figure 2.3
Long-range receiver block diagram.

A block diagram of a long-range receiver is shown in Fig. 2.3. A low noise RF amplifier is used to increase the system's link margin and decrease the receiver's noise figure. The RF amplifier output feeds a mixer with a DRO local oscillator (LO) running at 26.0 GHz. The IF output of the mixer is amplified before the IF controller board. The receiver's IF circuitry is designed around a Sharp DBS tuner (a receiver module containing an amplifier, an automatic gain control (AGC), a voltage-controlled oscillator (VCO), several filters, and a phase-locked loop demodulation circuit in a single package that is manufactured by Sharp Electronics) that was intended for use in satellite receivers. The DBS tuner provides automatic gain control, demodulation, and control voltages necessary for tracking the received signal. The DBS tuner has an input bandwidth of approximately 950–1750 MHz that gives the receiver a tuning range of 26.9–27.8 GHz. This wide tuning range allows the receiver to track large drifts in the transmitter and local oscillator. The DBS tuner also has a selectable IF bandwidth of 7 and 17 MHz. The narrow 7-MHz filter setting was chosen in all of the tests, as mentioned previously.

The receiver shown in Fig. 2.3 can operate in either manual-tune mode or automatic-tune mode. In manual-tune mode the user can manually tune the DBS tuner to an IF frequency within the tuner's range. In automatic-tune mode the frequency locking and tracking circuit takes over. During signal fades severe enough to cause the receiver to unlock, the receiver will revert to a "search" mode where the tuning voltage will sweep between two predetermined values until the signal strength returns and allows the receiver to reacquire the signal. The AGC voltage from the tuner is used to determine when a signal is found. If the AGC voltage passes a set threshold, a signal has been found and the tracking circuit goes into "lock" mode. Hysteresis was added to the AGC threshold comparator to allow the signal to drop to a very low value before the receiver loses lock and goes into "search" mode. The AGC hysteresis prevents the receiver from jumping in and out of "lock" mode during fading events where the signal strength is marginal. Once the receiver is in "lock" mode, it follows the slow frequency deviations of the signal using the automatic fine tune (AFT)

voltage of the tuner. The AFT voltage is proportional to the location of the signal within the tuner's IF passband. To implement the slow tracking of the signal, the AFT voltage from the DBS tuner is subtracted from an AFT reference. This difference is fed back through an integrator and amplifier to the tuner's tuning input. Characteristics of the long-range data link are given in Table 2.1.

Table 2.1
Characteristics of the long-range data link.

Transmitter Power	20 dBm
Transmit Antenna Gain	34 dB
Modulation Type	FSK
Receiver Noise Figure	4 dB (max.)
Receiver Bandwidth (IF)	7 MHz / 17 MHz (7 MHz used for testing)
Calculated Link Margin at 7 km	50 dB
Data Rate: Tested / Max	1.5 Mbps / 3.6 Mbps

Although DROs are very stable frequency sources, the frequency locking and tracking circuit was used to eliminate the question of whether or not observed amplitude fluctuations were caused by frequency drift or actual fades. The tracking circuitry was not an expensive feature to add to the receiver, and can be used in other types of RF front-ends that are not as stable as DROs. The same circuit was also used with the free-running Gunn diode oscillators in the short-range data link receivers and the low-cost data links described in Appendix A.

The spectral efficiency of this data link was not optimum because the bandwidth of the filters and the maximum data rates available from the telecommunication test sets were fixed ahead of time. The maximum data rate available from the test set was 1.5 Mbps. The data were Manchester-encoded in order to encode the clock information and remove any baseline wander from the transmitted signal. The bandwidth requirement was doubled over the non-

encoded data. Thus the spectral efficiency of the data link was about 0.2 bps/Hz. This could be improved considerably if a different encoding scheme were used.

The link margin appeared to be high in the long-range data link design, but path losses and weather conditions caused substantial degradation at these frequencies. Because high gains are available from relatively small antennas, the link margins can be relatively high even when the transmitter powers are low (i.e., a few mW). Having a large link margin for the test system allowed the collection of data under strong fade conditions, and hence permitted the calculation of link performance over a range of conditions.

2.3 SHORT-RANGE (V-BAND) LINK

A diagram of a short-range data link transmitter is shown in Fig. 2.4. The transmitter utilized 60.0 GHz (transmitter) and 58.5 GHz (local oscillator in the receiver) free-running Gunn oscillators that provided 50 mW (17 dBm) of power. The Gunn oscillators were powered through bias regulator circuits. Each bias circuit included a modulation input that was used to modulate the bias and correspondingly the Gunn frequency. The transmitted frequency was chosen because it fell within the oxygen absorption band centered at 60 GHz. This frequency and low power level gave these links a low probability of intercept over a shorter range than the long-range links.

The frequency of 60 GHz was used because the atmospheric attenuation reduces the detectability of the transmitted signal. It also prevents signals generated far away from interfering with the data link. The atmospheric attenuation creates a limited area zone over which the signal can be detected. This provides optimal security for the signal transmissions.

Standard gain horn antennas with a gain of 24 dB were used for testing at Eglin AFB, and 34 dB dielectric-lens horns were used at Minot and Davis Monthan AFBs. These antennas, along with a block diagram of the receivers

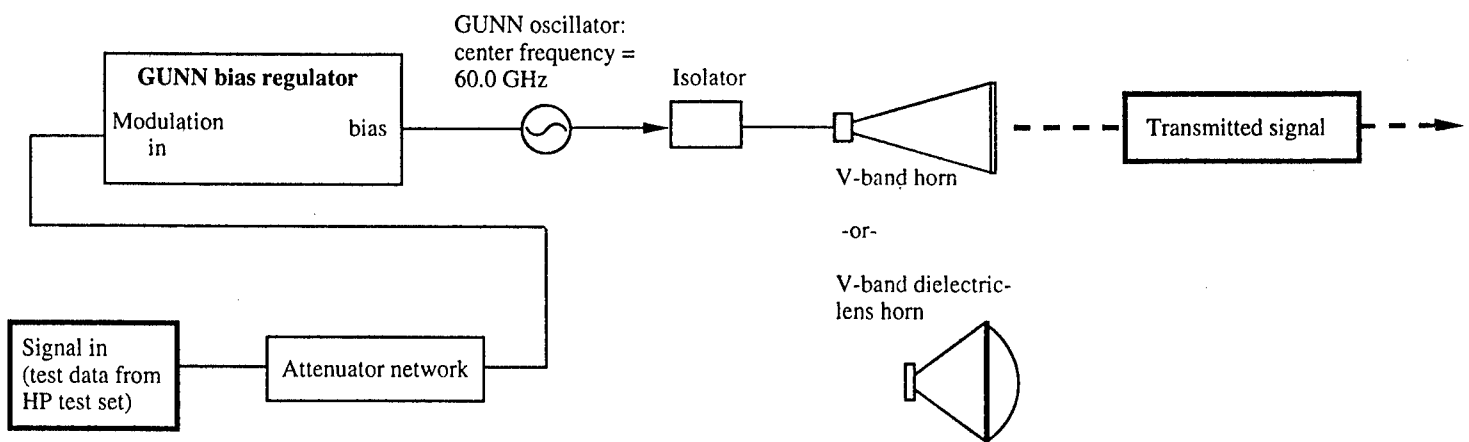


Figure 2.4
Short-range transmitter block diagram.

and transmitters, are shown in Figs. 2.4 and 2.5. The standard gain horns were barely adequate for testing at Eglin AFB, so the dielectric-lens horns were used in the other locations to improve the link margins. Thus, the effective radiated power from the transmitter was approximately 41 dBm at Eglin and 51 dBm at Minot and Davis Monthan.

A block diagram of a short-range receiver is shown in Fig. 2.5. This receiver was almost identical to the long-range receiver shown in Fig. 2.3 except for the front-end RF components. The incoming RF signal was not amplified before the mixer in the short-range receiver. The local oscillator was a free-running Gunn oscillator as in the transmitter; the oscillator ran nominally at 58.5 GHz. After the mixer, the IF was amplified and sent to an IF controller board that was identical to the circuit used in the long-range receiver. The free-running Gunn oscillators used in the transmitter and as the receiver local oscillator are not nearly as stable as the DROs used in the long-range link. Thus the tracking circuit played a very critical role in the short-range link. The tracking circuit allows the receiver to tune from 59.4 GHz up to 60.3 GHz. Characteristics of the short-range data links are given in Table 2.2.

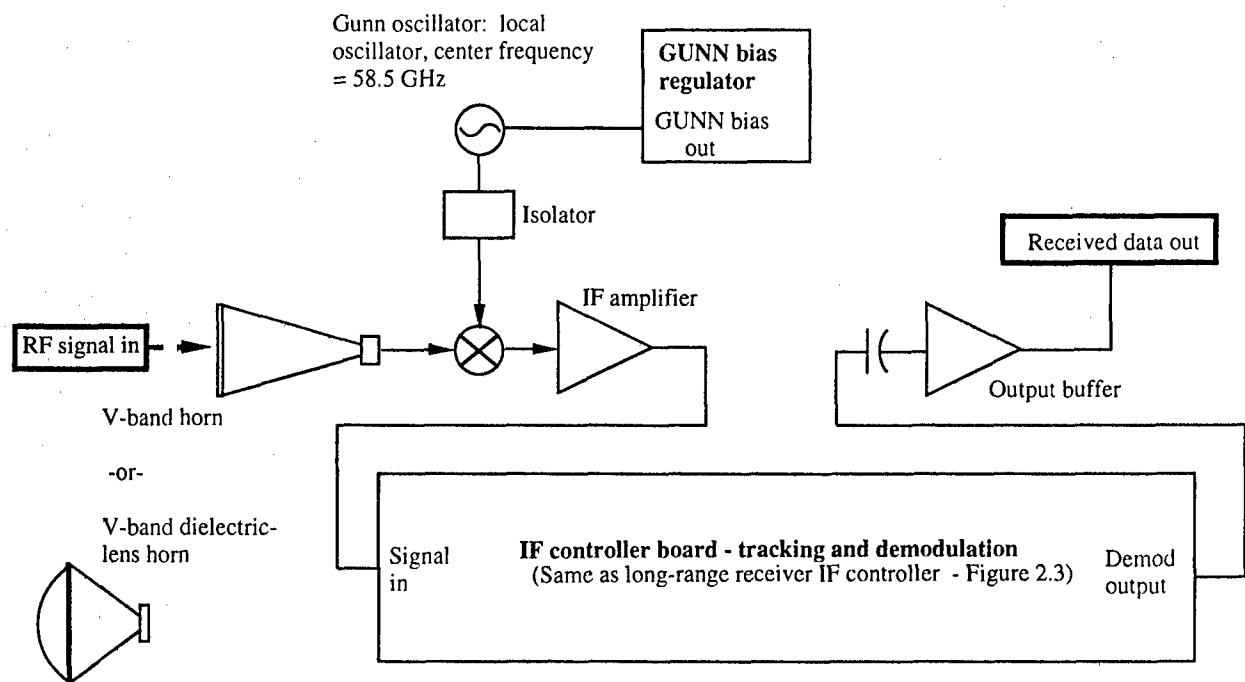


Figure 2.5
Short-range receiver block diagram.

Table 2.2
Characteristics of the short-range data links.

Transmitter Power	17 dBm nominal
Transmit Antenna Gain	24 dB standard gain horn, 34 dB dielectric-lens horn
Modulation Type	FSK
Receiver Noise Figure	10 dB (max.)
Receiver Bandwidth (IF)	7 MHz / 17 MHz (7 MHz used for testing)
Optimum Link Margin at 1 km	16 dB with standard gain horn / 36 dB with dielectric-lens horn
Data Rate: Tested / Max	1.5 Mbps / 3.6 Mbps (extrapolated from filter bandwidths)

2.4 DESCRIPTION OF TEST SEQUENCE

A block diagram of the general test setup and data collection system is shown in Fig. 2.1. This figure illustrates a long-range transmitter and receiver only for graphical purposes; the setup is indicative of all the tests. A Hewlett-Packard 37701B T1/Datacom tester with a 15901A Datacom module was used at the transmitter to generate the transmitted digital test pattern. The pattern and bit-rate were set on the test set's front panel. The RS-232 output of the test set was cabled directly to the transmitter when data were sent at 19.2 Kbps. At 1.5 Mbps the test set only produced synchronous data, so that the clock and data from the test set's RS-449 output port were Manchester-encoded before being transmitted. The demodulated data at the receiver were first sent to an RS-232 driver/buffer or a Manchester decoder, depending on the data rate, and then to the receiving HP test set.

At the receiver the test sequence and data collection were orchestrated by a National Instruments Labview program running on a BSI laptop PC. This

program, or Virtual Instrument (VI) in Labview terminology, was written specifically to coordinate these tests. The VI allowed the user to pick the length of a test period (one minute, for example) and specify the bit-rate and pattern of the data sent to the receiver. The VI then configured the receiving test set to expect data of the type being transmitted. The test set would then produce an accumulated statistic that included the block count, error count, bit error rate, and percent error-free seconds over the test period. The test set and PC were connected through a serial communications port.

Analog signals consisting of the DBS tuner's tuning voltage, AGC voltage, and AFT voltage, along with the receiver's lock indicator, and a voltage from the background RF meter were sampled by a National Instruments NI-DAQ Card 700, A/D PCMCIA card at 100 samples/s. After each second, the mean of these 100 samples from each analog signal were stored in an array. At the end of a test period, the mean, median, and standard deviation of these arrays were calculated. These averages and standard deviations computed over one test period were referred to as "short-term" averages and standard deviations.

Weather data were sampled once per test period and consisted of wind speed, wind direction, outside humidity, barometric pressure, and accumulated rain over a test period. The weather data were measured with a Davis Weather Monitor II that connected to the PC through a serial communications port. The weather monitor consisted of the weather computer that interfaced to the PC and peripherals that included an anemometer, rain gauge, and an external temperature and humidity sensor.

At the end of a test period the date and time, data statistics from the telecommunications test set, analog signal statistics from the receiver and background RF meter, and weather data from the weather monitor were recorded onto a Hewlett-Packard 1300T magneto-optical drive connected to the computer through a PCMCIA SCSI adapter. The data from a test period were saved sequentially in one file until the file grew to a size specified by a

user-chosen parameter in the VI. Once the file reached the specified size, the VI started saving data in a new file. This kept the files at a reasonable size for data analysis. Once the data were stored, the VI reset the statistics on the HP test set and started another test sequence. A typical test setup, showing the data acquisition computers, the test sets, and the UPS units, is shown in Fig. 2.6.

Each test system was designed to run automatically for a period of time that terminated only when the user stopped the VI. Unfortunately, dropouts in supply power to the test sets and PC would cause the system to fail and require user intervention to restart. It was not feasible to keep someone close by to assess problems caused by a power outage and restart the test system. To solve this problem, uninterruptable power through small UPS units designed for powering desktop computers was used. The energy stored in UPS units was increased by paralleling external deep-cycle marine batteries with the UPS units' internal batteries.

Power outages were rarely a problem after suitable UPS units with sufficient battery life were used, but component failure often became a problem due to the extreme conditions in which the test equipment was set up. The test locations were chosen to test the millimeter wave RF equipment and the quality of the path in extreme conditions. The RF equipment faired well in most conditions, but the data collection systems were not as robust and measures had to be taken to ensure the reliability and integrity of the test sets and computers. Unfortunately, the choice of test sites was limited. Without using an extreme amount of cable and modifying structures to run the cables into a controlled environment, the data collection equipment had to endure environmental conditions similar to those experienced by the radio equipment.

2.5 DESCRIPTION OF TEST LOCATIONS

The testing for long-range and short-range data links was carried out at Eglin, Minot, and Davis Monthan AFBs. The maps identifying the locations of the



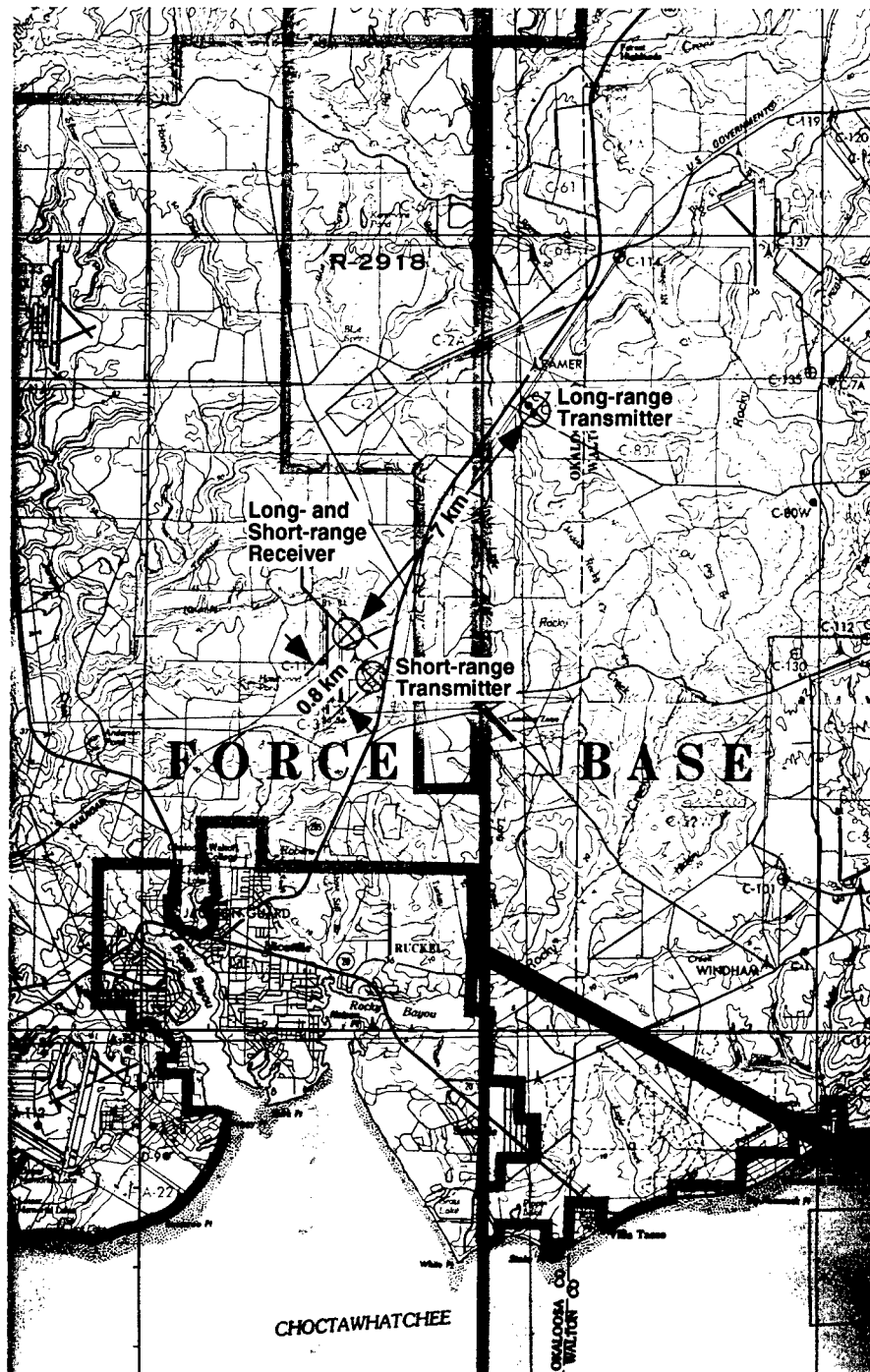
Figure 2.6

Typical installation in a utility room or tower. The photo was taken at Davis Monthan AFB. The computers are on the top rack, the power supplies and test sets are on the middle rack, and the UPS units are on the bottom rack.

tests are shown in Figs. 2.7, 2.8, 2.9, and 2.10. The locations were selected to maximize the operational data link exposure to adverse environmental and electronic environments. The sites also differed in their geographic features. The long-range link paths were typically "barely-line-of-sight" so that the boundary effects of the ground clutter and atmospheric phenomena encountered by the data link could be effectively evaluated.

2.6 EGLIN AFB, C-3 TO C-10

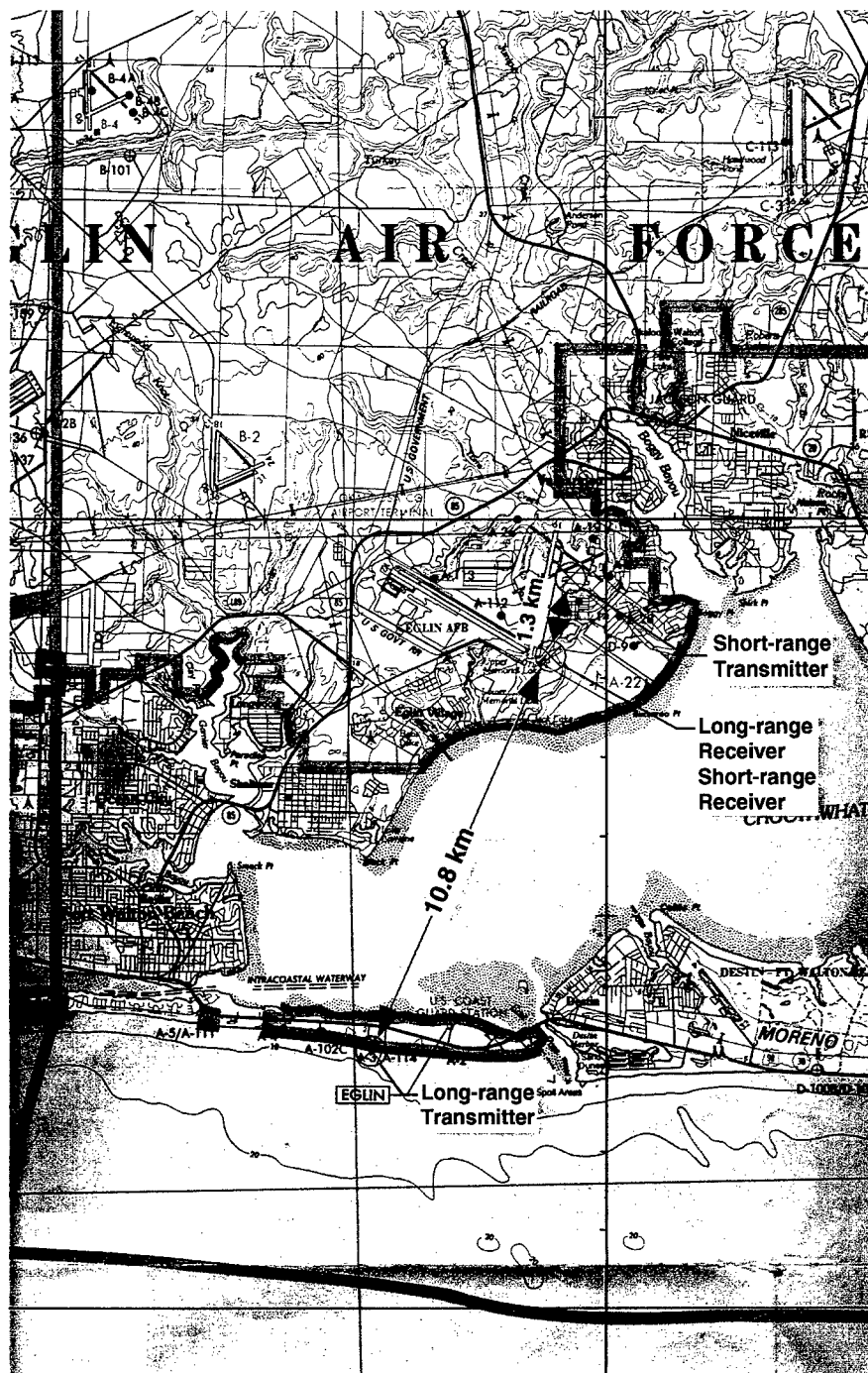
The first test site was at Eglin AFB. This site showed how well the data link would perform over a forested area. This was also an opportunity to test how well the data link would work in a high RF traffic and high rainfall environment. Figure 2.7 shows the map of the relative location of the short- and long-range data links. Figure 2.11 shows how the short- and long-range receivers were positioned on the tower. Although it was desirable to have links as low as possible for a realistic test, the tree tops were approximately 30–35 ft above ground level. The receivers were located on a tower that was 44 ft above ground level. The elevation of ground level at the transmitter was about 30 ft higher than at the receiver. The transmitter antenna, as shown in Fig. 2.12, was about 26 ft above ground level. The sighting camera on the large radar antenna was used to verify the accuracy of pointing the transmitter antenna. The path length was 7 km for the long-range link, and the direct line between the transmitter and the receiver was estimated to be 5–10 ft above the tree tops. The radius of the first Fresnel zone at the midpoint of the path is about 14 ft. At 1000 m from either the transmitter or receiver, the radius of the first Fresnel zone is about 10 ft. Therefore, the trees are within the first and second Fresnel zone over most of the propagation path. Although these clearances were within the standard guidelines of 0.6 Fresnel zone clearances, some of the propagation effects seen did not correspond with expected propagation phenomena. If possible, it is desirable to keep terrain and objects completely clear of the first Fresnel zone. However, as in this case, such a restriction may require the transceivers to be elevated higher than may be convenient or possible in this application.



Non-RF Non-Hardwire Link Test
Eglin AFB: Site 1

Figure 2.7

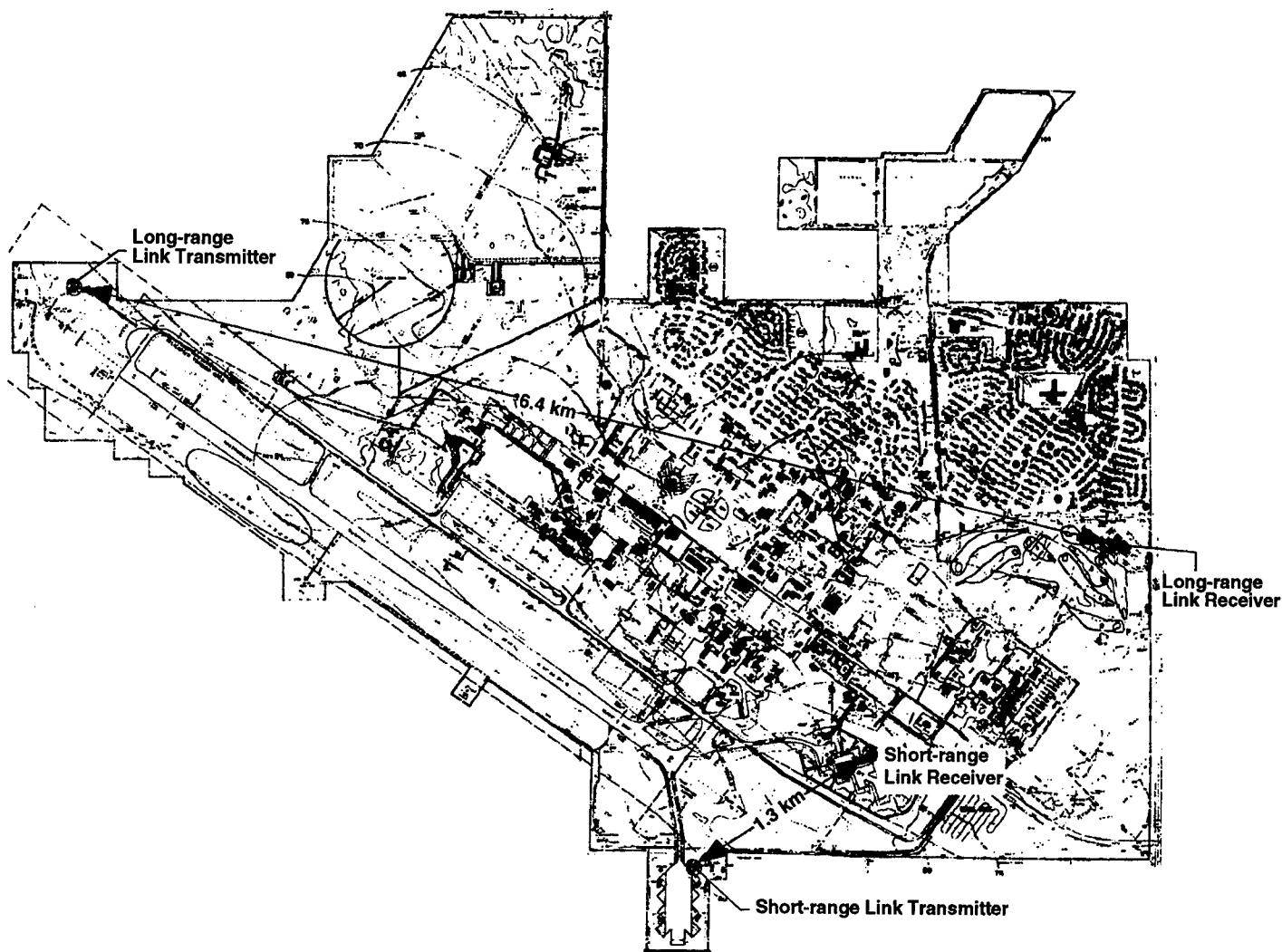
Test site 1 at Eglin AFB. Long-range link and short-range link receivers are located at the C-3 test area on tower 2. The long-range link transmitter is located at the C-10 test area on top of the radar building. The short-range link transmitter is located on a telephone pole at the edge of the test area.



Non-RF Non-Hardwire Data Link Test
Eglin AFB: Site 2

Figure 2.8

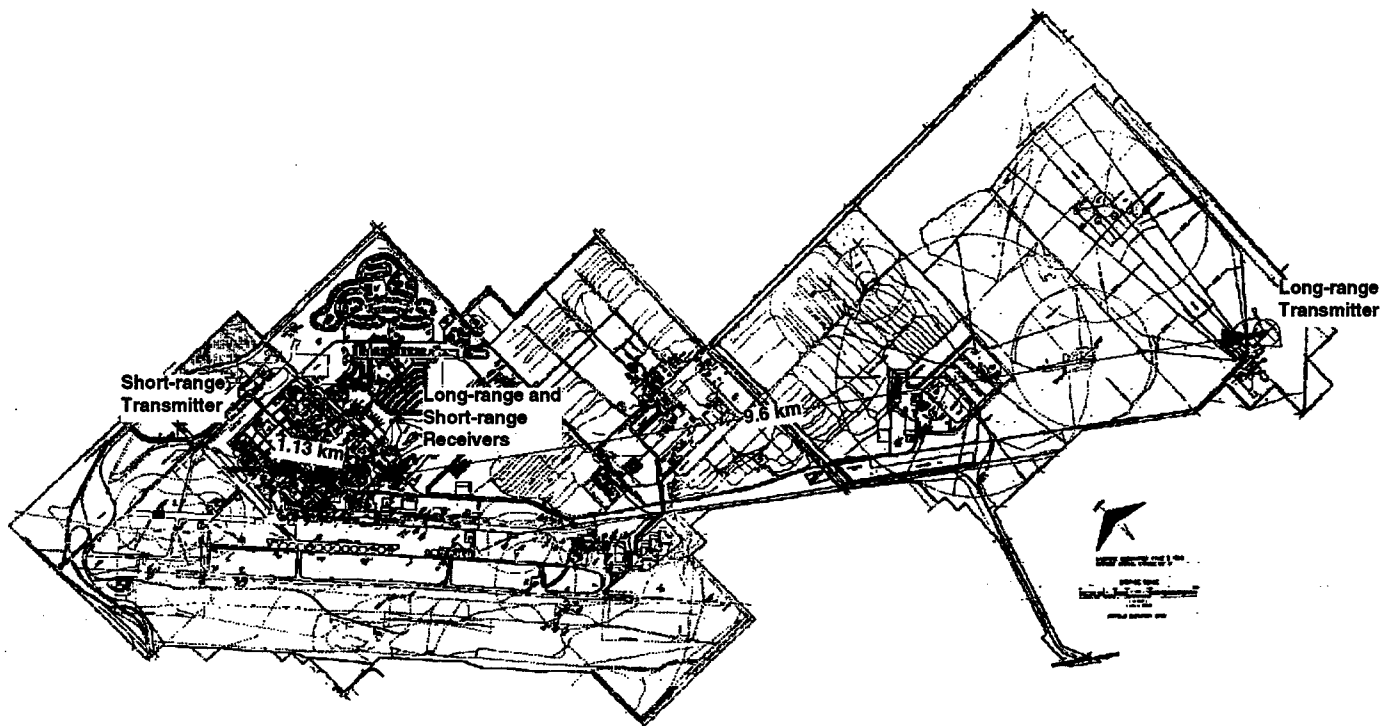
Test site 2 at Eglin AFB. Long-range link receiver is located at King Hangar and the long-range link transmitter is located at test area A-3.



**Non-RF Non-Hardwire Data Link Test
Minot AFB**

Figure 2.9

Test site at Minot AFB. Long-range link receiver is located at the base hospital, and the long-range link transmitter is located on a small building at the far end of the runway.



**Non-RF Non-Hardwire Data Link Test
Davis-Monthan AFB**

Figure 2.10

Test site at Davis Monthan AFB. Long-range and short-range link receivers are located on top of the law enforcement building in the main base area, and the long-range link transmitter is located on small building at the combat arms test range. The short-range link transmitter is located on the communications building.



Figure 2.11
Photograph of Eglin tower at C-3, showing short- and long-range receivers.



Figure 2.12
Photograph of long-range transmitter at C-10, showing top of building with large antenna for the tracking radar.

For acceptable quality signal transmission, the antennas must be above the tree tops. Both the short-range and long-range link require line-of-sight paths to operate. However, the interfering objects, trees in this case, can be close to the line-of-sight path. The difficulty with this circumstance is that boundary effects, such as scattering off terrain or other objects that occur in close proximity to the ground, can substantially affect the signal quality as will be shown by the data presented in Section 3.0.

The large radar antenna operated at 5 GHz with 1 MW peak power. For an interference test, the radar was pointed at the receiver. The direction was adjusted until the echo from the tower could clearly be identified on the radar receiver, and the radar was operated at full power for an hour. At no time was any interference detected from the radar transmission or any of the harmonics. The radar signal was clearly evident on a wideband receiver that was also placed in the tower.

The short-range link was tested over 840 m of path length. The transmitter was located on a telephone pole about 12 ft above the ground at the entrance to the C-3 test area. The propagation path was partially obscured by trees and power lines. The path was not heavily obstructed, however, and this scenario was believed to be representative of what would be commonly encountered in the field. No electronic interference was observed on the short-range link during normal operation. The short-range link was also operated during Hurricane Erin.

2.7 EGLIN AFB, KING HANGAR TO A-3

This was the longest path tested and is shown in Fig. 2.8. It was also over water and initially expected to be a difficult path for propagation because water is a good reflector of electromagnetic waves. Thus, both the direct-path arrival and the first-bounce off the surface of the water would be strong signals. Also,

because of the wave action, the first bounce would have a time-varying nature, so the signal at the antenna was expected to fluctuate in time. However, this was a reliable transmission path with good performance, even during the late summer when heavy thunderstorms frequently occurred in the area. These storms caused wind and waves on the water and fading on the link due to the rain. The initial setup was performed in October 1995, but was damaged by Hurricane Opal. The tests were suspended until the damaged components could be replaced or repaired. The test was restarted in late May 1996 and operated until November 1996. The receiver was mounted on the flightline telemetry building, which contained a large number of UHF and microwave transceivers. No interference was observed on the long-range data link. The data link did not interfere with any of the flightline communications, either. Furthermore, no strong fades were observed other than those believed to be caused by thunderstorms.

The short-range link was the same link that was tested over a 1.3-km path. Unfortunately, the system gain was too low for this link, so most of the data were not usable. However, no RF interference was observed.

2.8 MINOT AFB, NW END OF RUNWAY TO TOP OF BASE HOSPITAL

This link was tested in a cold weather environment at Minot AFB. Figure 2.11 shows where the links were located. The longest path that could be found was from the "Localizer Building" (building 1062). The antenna was elevated about 15 ft above the ground. The land topography was very flat, but the receiver was mounted on the service room of the hospital, which was about 40 ft above the ground. This provided a very reliable transmission path. Testing the transmission path with the remote end at a low elevation and the receiver at a higher elevation is important because this configuration is anticipated to be present in the physical security applications.

The short-range link was set up between two security towers near the flight line, as shown in Fig. 2.9. The nominal signal strength over the 1.3-km path

was satisfactory and 1.5 Mbps were easily transmitted across the path at 60 GHz with the test link. Unfortunately the receiver had a defective mixer that only failed under the coldest temperatures. Furthermore, the failure could not be reproduced in laboratory cold test chambers. It was not until the link was retrieved and tested for the next exercise that the defect was isolated. Therefore, the short-range data gathered were limited and were not analyzed for this report. However, after the mixer was replaced this problem was resolved during subsequent tests.

2.9 DAVIS MONTHAN AFB, SKEET RANGE TO LAW BUILDING

The data links were tested in a desert environment at Davis Monthan AFB in Tucson, Arizona. Figure 2.12 shows the relative locations of the long-range and short-range receivers and transmitters. Figure 2.13 shows both the long-range and short-range link receivers located on top of the security police (SPS) office building (building 4413) at a height of 47 ft above ground level. The transmitter was located at the skeet range on the southwest corner of the base. The range from the transmitter to the receiver was 9.6 km, and the elevation of the transmitter above the ground was about 21 ft. Figure 2.14 shows the installation at the skeet range on the small building. The ground elevation at the transmitter was estimated to be about 30 ft higher than the ground elevation at the receiver. The radius of the first Fresnel zone was about 16 ft. There were no trees between the transmitter and the receiver, but there was considerable ground clutter. The path traversed the areas where aircraft were stored in large numbers. Furthermore, several tails of abandoned B-52 aircraft were taller than the line-of-sight path, but were not directly in the path. The ground clutter consisted mostly of aircraft and buildings that were between 10–15 ft in height. This path, more than any other tested, qualified as “barely-line-of-sight.” The building on which the receiver was mounted was visible from the transmitter but was extremely difficult to see.

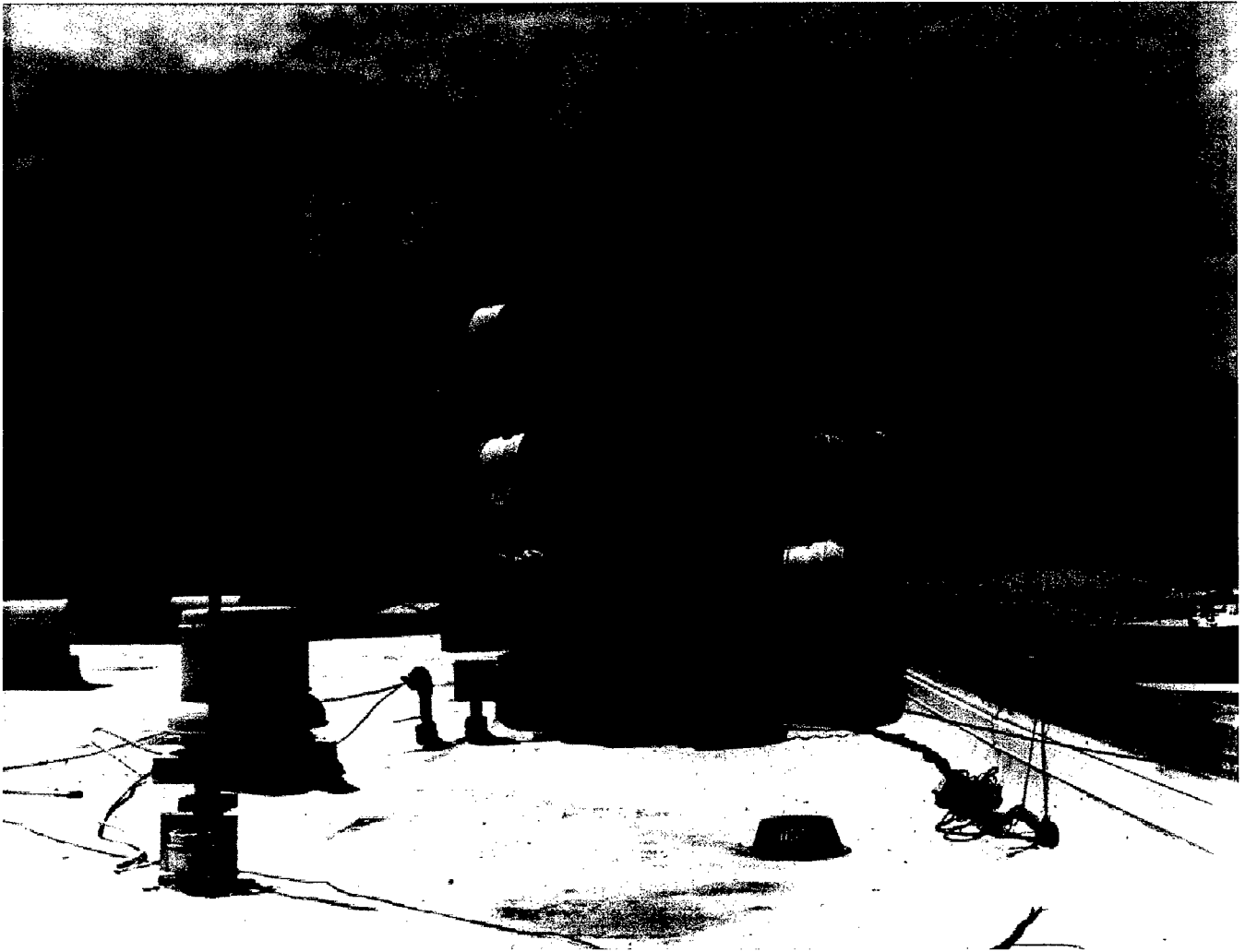


Figure 2.13

Setup of the short- and long-range receivers on top of the SPS office building (building 1540) at Davis Monthan. Note the presence of multiple microwave, VHF, and UHF antennas. No RF interference was experienced during testing.

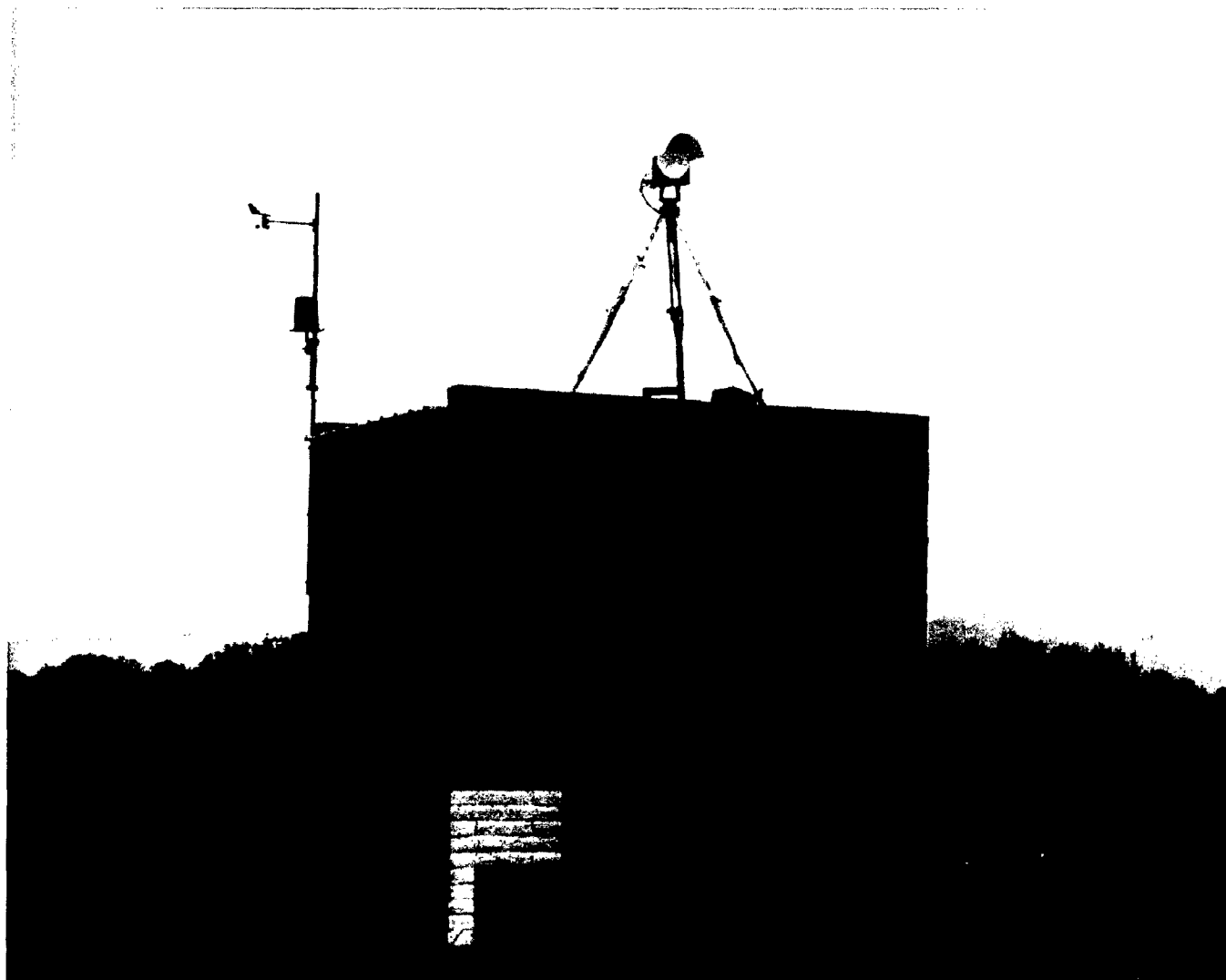


Figure 2.14
Setup of the short- and long-range transmitter on top of the skeet building at Davis Monthan. Note the presence of the weather station used to measure and log conditions at the transmitter.

The mounting of the receivers on the top of building 4413 is shown in Fig. 2.13. Clearly evident are other microwave links, as well as UHF antennas that were in continuous operation during the entire test conducted at Davis Monthan. No interference was detected on the link from these other transmitters, and no interference from the link on any other systems was observed.

The short-range link transmitter was located on the communications building (building 1540). The path was a relatively clear line-of-sight path over 1.13 km. The maximum radius of the first Fresnel zone for this path was 1.2 m, with no obstructions except for one tree that was within the first Fresnel zone.

This page intentionally left blank.

3.0 LONG-RANGE TEST RESULTS

3.1 EGLIN, C-3 TO C-10 TEST, 1995

It was of interest to test the millimeter wave data link over trees in a forest environment. During this early test period, a number of improvements in the data acquisition system were identified and implemented. First, it was apparent that the original data acquisition computers' operating system was unreliable. This caused frequent losses of data collection. Second, the UPS unit at the transmitter did not have enough battery power to sustain the transmitter and test set during the frequent power outages at C-10. This made it impossible to interpret the link data in terms of channel reliability, since any given outage can be caused by either a power outage or a transmission path fade. Therefore, only a limited number of data sets can be analyzed with reasonable certainty. Tables 3.1 and 3.2 show the link characteristics and some of the information about the propagation environment.

Figures 3.1 and 3.2 show the data collected from Eglin during a week in June 1995. The data set corresponds to file 51630819 in the test data archives. The data were recorded after every 5-min test interval. These data show a clear diurnal cycling of the temperature, as well as signal fluctuations of nearly 20 dB that seem to follow the day-night cycle. No rainfall was recorded for this data set. A scatter plot shown in Fig. 3.3 of signal strength versus wind speed shows that the signal strengths were generally high for the low wind speeds. Averages of 1 h were used to generate each point. The plot shows that the higher signal levels occurred during the times of low wind speeds. This does not mean, however, that the low wind speeds caused the high signal levels, merely that the two were concurrent. Because both low temperatures and low wind speeds occurred at the same time, a scatter plot of temperature versus signal strength would provide similar results. Data recorded during days 4–6 in the data set suggest that wind speed might be more important for a signal enhancement

Table 3.1
Long-range data link characteristics.

Transmit Power	20 dBm
Transmitter Antenna Gain	34.5 dB
Receiver Antenna Gain	34.5 dB
Mixer Loss	-13 dB
Front-End LNA Gain	27 dB
IF Amplifier Gain	18 dB
Frequency / Wavelength	27.1 GHz / 0.011 m
Range	7 km
Free Space Spreading Loss	-138 dB
Receiver Noise Figure/Noise Floor at 7-MHz Bandwidth	3.5 dB / -105 dBm
Data Rate	19.2 Kbps
Average Signal Level (Vertical / Horizontal)	-22 dBm / -26 dBm average
Calculated Signal Level	-14 dBm
Average Excess Signal Loss	7 dBm / 12 dBm
Climate Classification	N (Tropical)
Path Length Reduction Factor	0.67

Table 3.2
Statistics from the two data sets shown, transmitted bit pattern:
QRSS, 1024 bits/block.

Data Type	Vertical Polarization Data Set 51630819	Horizontal Polarization Data Set 52211111
Average Bit Error Rate	3.8e-8	8.0e-5
Average Percent Error-Free Seconds	99.9993	99.81
Average Signal Level	-21.9 dBm	-26.17 dBm
Peak Signal Level	-12.1 dBm	-11.3 dBm
Average Temperature	74.39°F	81.6°F
Average Wind Speed	5.9 mph	2.3 mph
Total Rainfall	0 in.	1.54 in.

event than the temperature. At the beginning of day 5, the temperature was low and the wind was higher than usual. No signal enhancement was observed during this time. This was also true at the beginning of day 6, while the beginning of day 7, which had lower wind speeds, shows a signal enhancement.

The signal variations observed may be due to previously studied phenomena. However, some initial estimates were made to see if vertical atmospheric refraction gradients and the accompanying focusing were possible candidates. Unfortunately, these calculations showed that unrealistically large gradients had to be assumed to make the calculations match the measured results. Therefore, the explanation for the origin of the signal fluctuations and their correlation with wind speed and temperature is still open. A partial, speculative explanation is given in Section 3.5.

Table 3.2 shows that the excess path loss is slightly higher for the horizontal polarization. The August data set (file 52211111) in Figs. 3.4, 3.5, and 3.6 showed that a sharp drop in exterior temperature occurred in the afternoons. (Note: The test periods were decreased to 1 min earlier in the summer. These

Eglin, C-3, long-range receiver, file 51630819, 6/12 - 6/19 1995

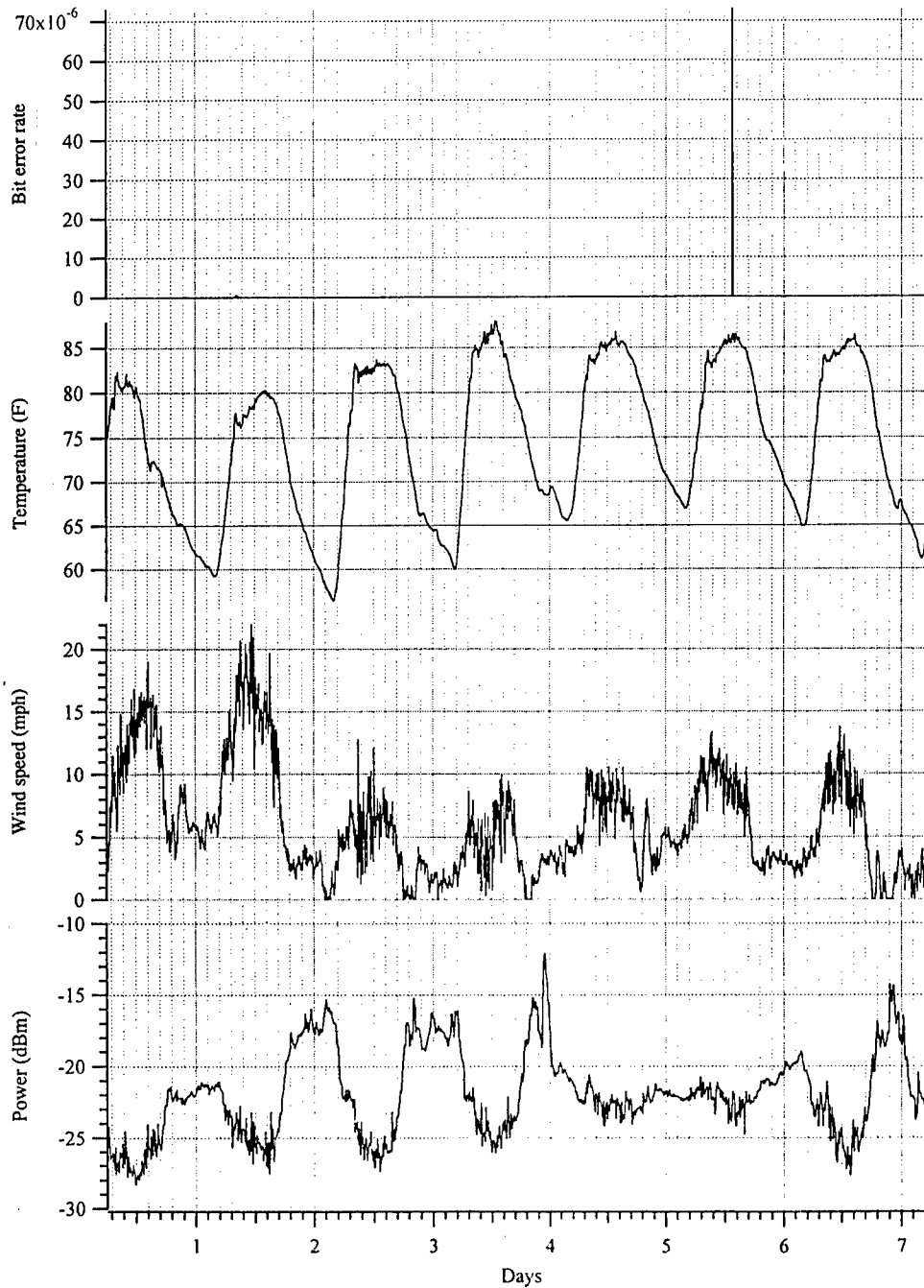


Figure 3.1

Vertical polarization time series data from 51630819: bit error rate, temperature at the receiver, wind speed, and measured signal strength.

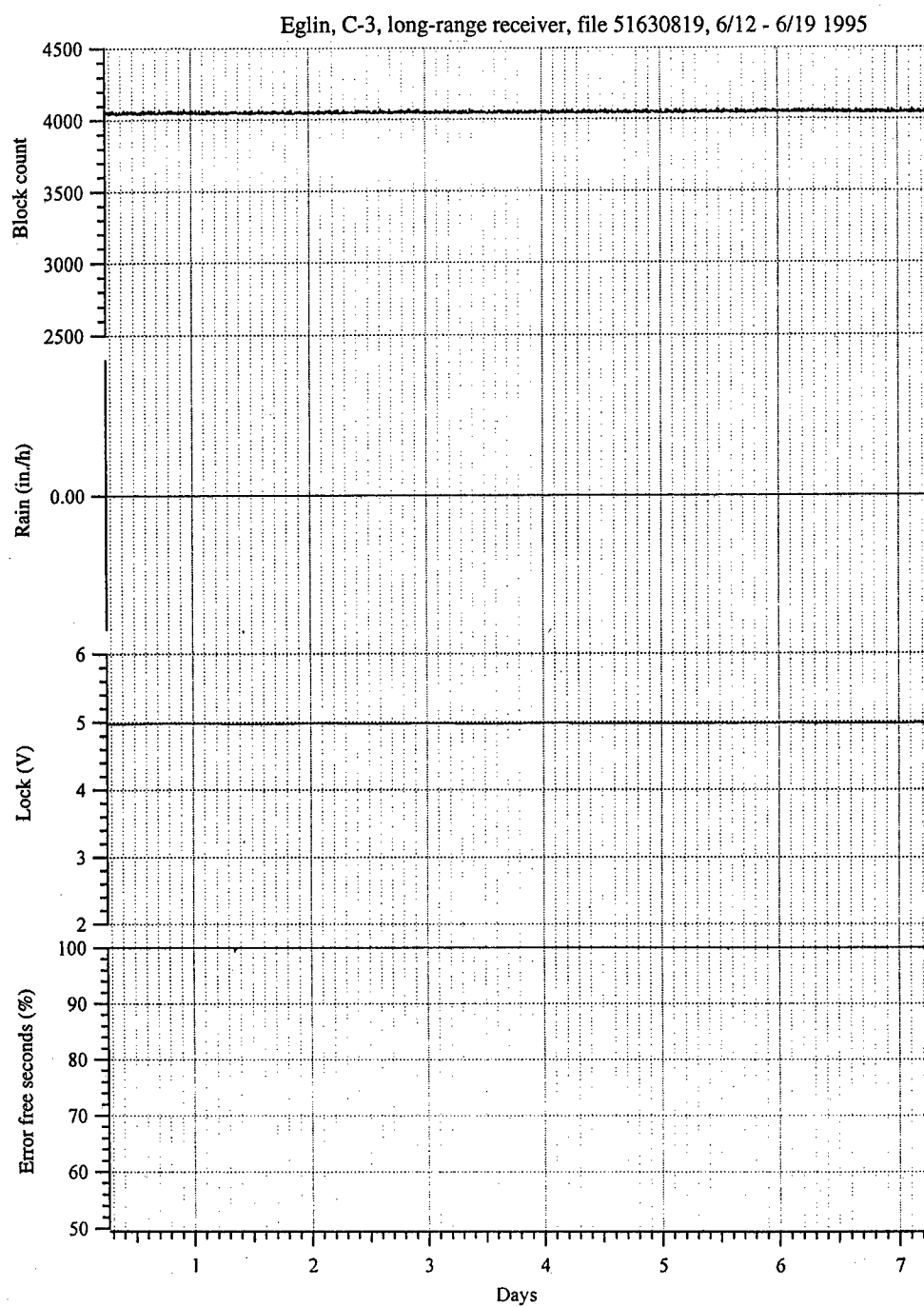


Figure 3.2
Vertical polarization time series data from 51630819: block count, rainfall rate, sweep/lock indicator, and percent error-free seconds of transmission.

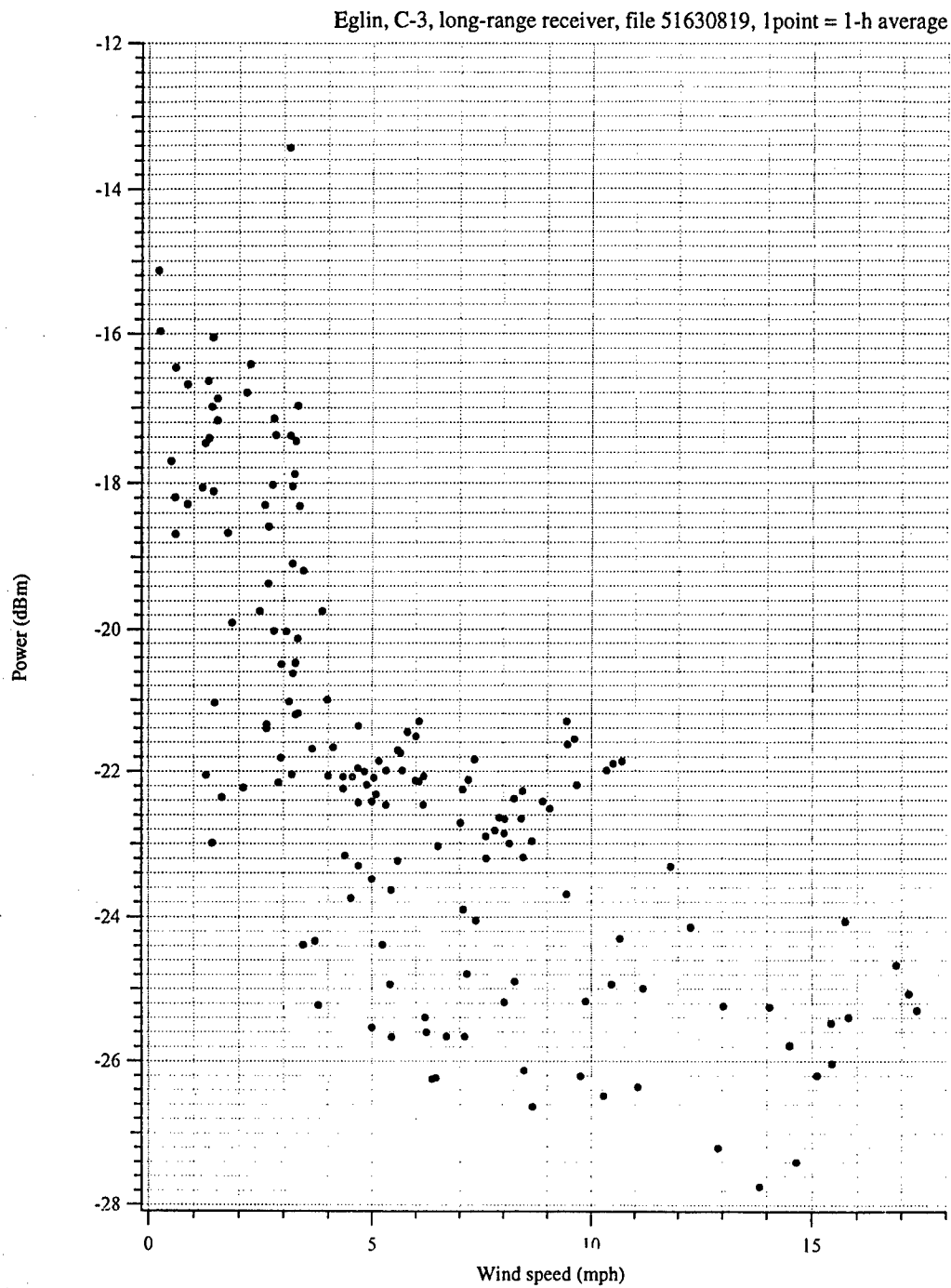


Figure 3.3
Scatter plot of signal strength versus wind speed for 51630819. Each data point is an average of 12 data points.

Eglin, C-3, long-range receiver, file 52211111, 8/9 - 8/14 1995

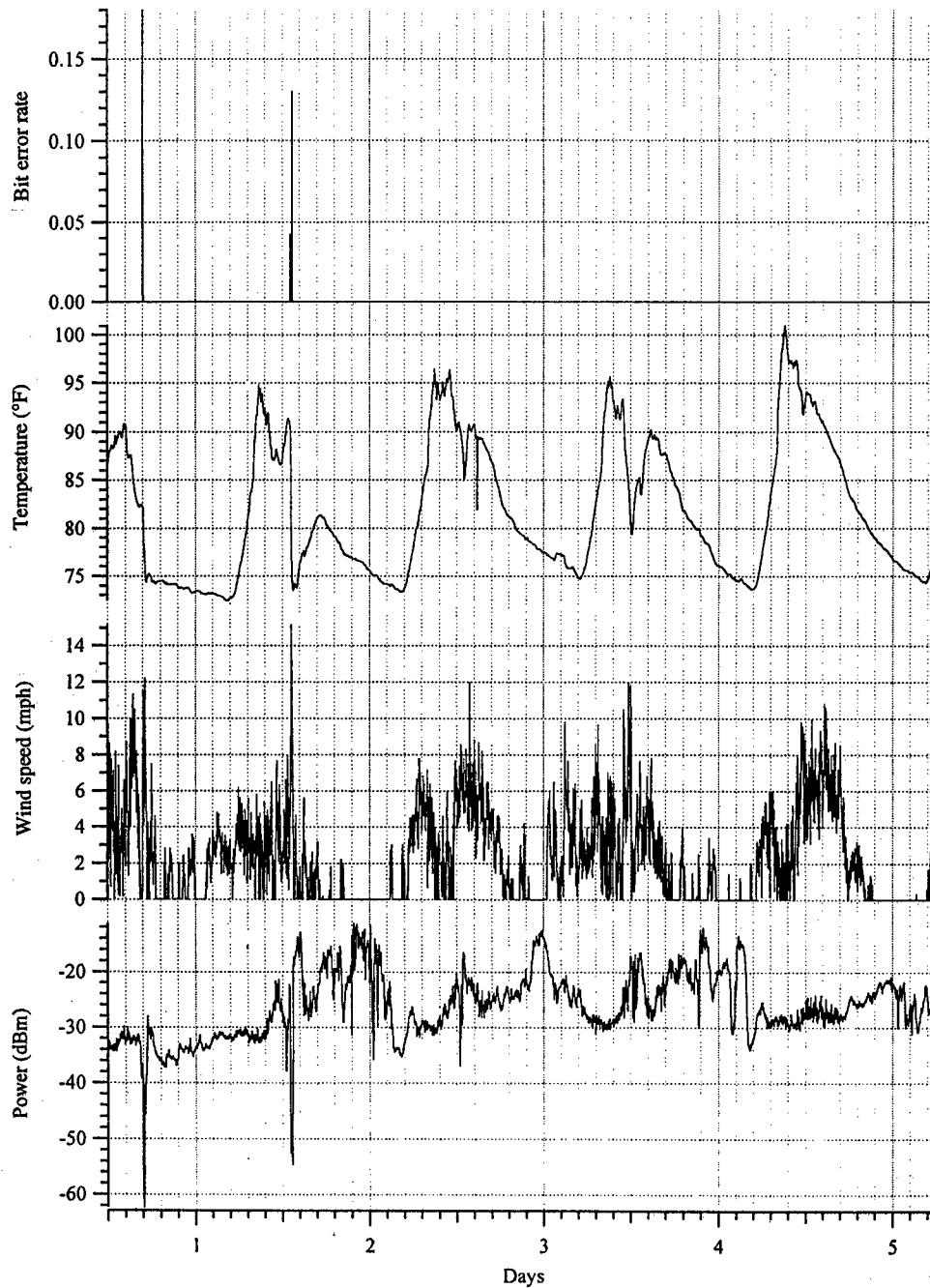


Figure 3.4

Horizontal polarization time series data from 52211111: bit error rate, temperature at the receiver, wind speed, and measured signal strength.

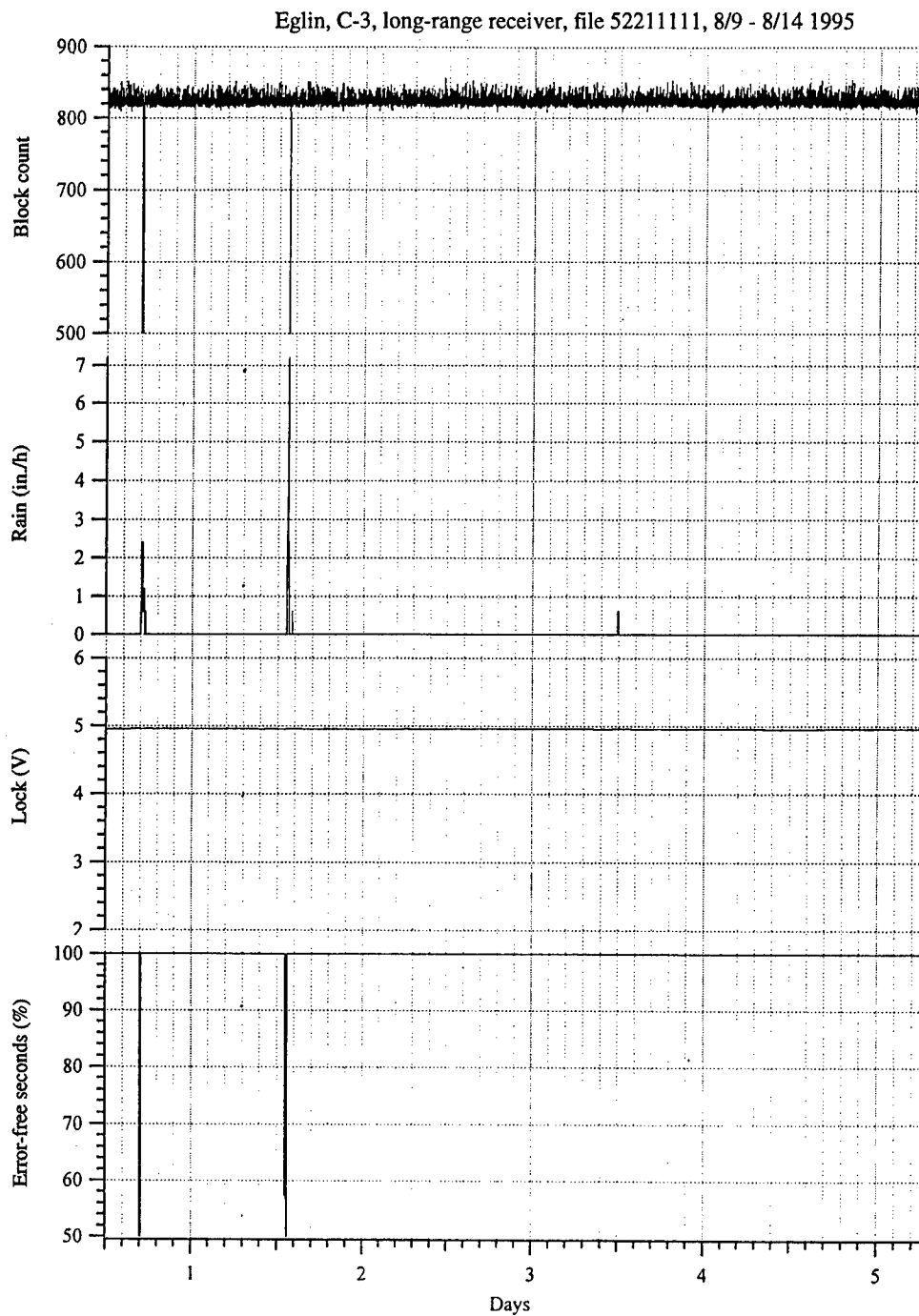


Figure 3.5
Horizontal polarization time series data from 52211111: block count, rainfall rate, sweep/lock indicator, and percent error-free seconds of transmission.

Eglin, C-3, file 52211111, 1 point = 1-hr average

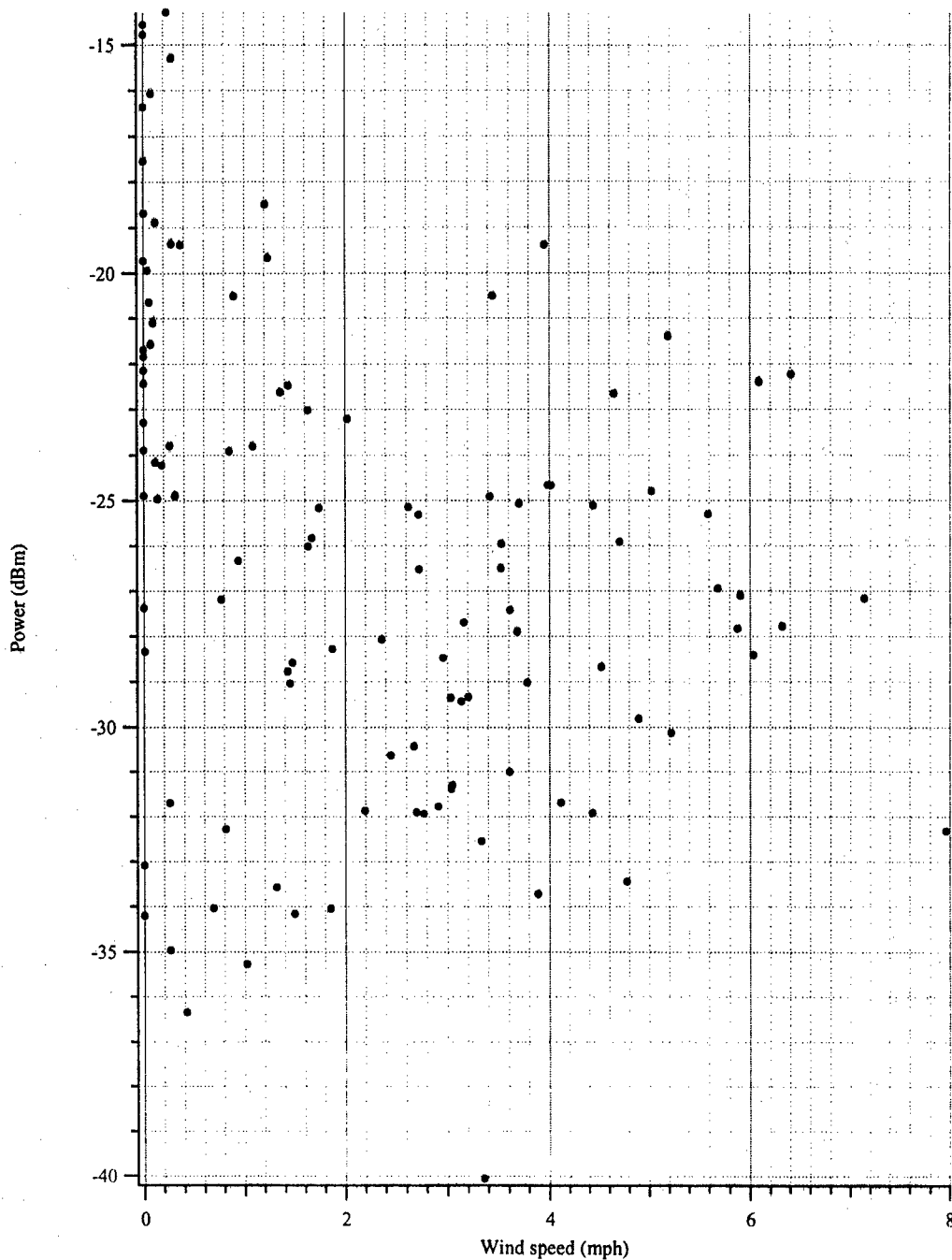


Figure 3.6

Scatter plot of signal strength versus wind speed for 52211111. Each data point is an average of 53 data points.

data and the data in the remainder of the tests were recorded at this rate.) This drop in temperature was indicative of a thunderstorm moving through the area. At approximately 1.6 days into the data set, a sharp spike in the bit error rate accompanied by a sharp, rapid drop in signal level indicated a fade due to rain. The rain bucket recorded a large portion of the total rainfall at a high rainfall rate during this time. The receiver maintained lock on the transmitted signal, but the bit error rates were high. The curious feature was that the fade was followed in time by a rapid increase in signal to about 10 dB above the mean value. At the same time, the wind speed dropped to a very low value. This event lasted nearly the entire night. During the time the wind speed dropped to a low value, the strength of the signal remained high. When sunrise occurred the next morning and the wind picked up, the signal dropped back down about 10–12 dB. The signal increase seemed to occur whenever the wind speed dropped to zero, or near zero. Also, thunderstorms seemed to occur every afternoon and were easily detected in the data set by the sharp drop in temperature that was apparent when clouds and moist air moved into the area.

The scatter plot of 1-h averaged signal strength versus 1-h averaged wind speed shown in Fig. 3.6 does not as clearly show the relationship between low wind speed and signal strength as do Figs. 3.4 and 3.5. Nevertheless, the cluster of the largest values of signal measured were near 0 mph. If low elevation data links are going to be used in deployed systems and systems such as LMDS, then a better understanding of this phenomenon is necessary. (Note: 1-h averages correspond to the average over 53 data points in Fig. 3.6. All the test periods were slightly longer than 1 min due to the overhead involved with storing the data and starting a new test period.)

3.2 EGLIN, KING HANGAR TEST

The high rainfall environment was expected to be a difficult environment for millimeter wave data links because of the attenuation problems caused by rainfall. However, the test results here showed that the pattern and intensity of

rainfall also determined the duration and severity of signal loss. Most of the very intense storms were short-lived and the corresponding fades of signal were also short-lived. For physical security applications, short-lived fades due to rainfall are acceptable, since average data rates can still be quite high.

The characteristics of the data link are summarized in Table 3.3. The results are summarized in Table 3.4. These results showed that relatively high degrees of reliability were available, even for this environment. Although the data link was a 19.2 Kbps link, the low excess path loss suggested that the multipath components were not a major problem and that higher data rates would have been possible. If rapid deep fades were present, periodic bursts of bit errors on the receiver would be expected. Furthermore, the short-term standard deviation would have shown large spikes. This was not observed. Figures 3.7–3.10 show the monthly average received power and standard deviation, rainfall, temperature, and wind speed. The average power received was difficult to correlate with the seasonal averaged temperature, wind, or rainfall. However, the standard deviation of the power measured at the receiver appeared to be well correlated with the cumulative rainfall for each month.

Initially, it was expected that the over-water path would present a difficulty for propagation because the ducting and multipath components would be very strong. In fact, the over-water path was the one of most reliable paths tested. Using standard charts, the link margin needed for 99.9% availability in the Florida panhandle climate was determined. Table 3.5 shows the measure error and dropout statistics for the data link. Table 3.6 shows the calculated rainfall statistics for this link. Calculations indicated that this link should have faded only about 0.1% of the total acquisition time. A total fade time (receiver unlocked from transmit signal) of 0.2% was measured. However, the data acquisition time was limited to months during which the highest rainfalls occurred, which might account for this discrepancy.

Table 3.3
Data link characteristics.

Transmit Power	20 dBm
Transmitter Antenna Gain	34.5 dB
Receiver Antenna Gain	34.5 dB
Mixer Loss	-13 dB
Front-End LNA Gain	27 dB
IF Amplifier Gain	25 dB
Frequency / Wavelength	27.3 GHz / 0.011 m
Range	10.8 km
Free Space Spreading Loss	-143 dB
Receiver Noise Figure/Noise Floor at 7-MHz Bandwidth	3.5 dB / -105 dBm
Data Rate	19.2 Kbps
Average Signal Level	-18 dBm average
Calculated Signal Level	-16 dBm
Average Excess Signal Loss	2 dB
Climate Classification	N (Tropical)
Path Length Reduction Factor	0.67

Table 3.4
Summary of Eglin AFB tests
(King Hangar to A-3) (high RF traffic environment).

Total Test Time	3985 hr
Percentage of Good Data Acquisition Time	92.3%
Average BER	2.7e-4
Percent Error-Free Time	99.5%
Total Rainfall Recorded at the Receiver	25.15 in.

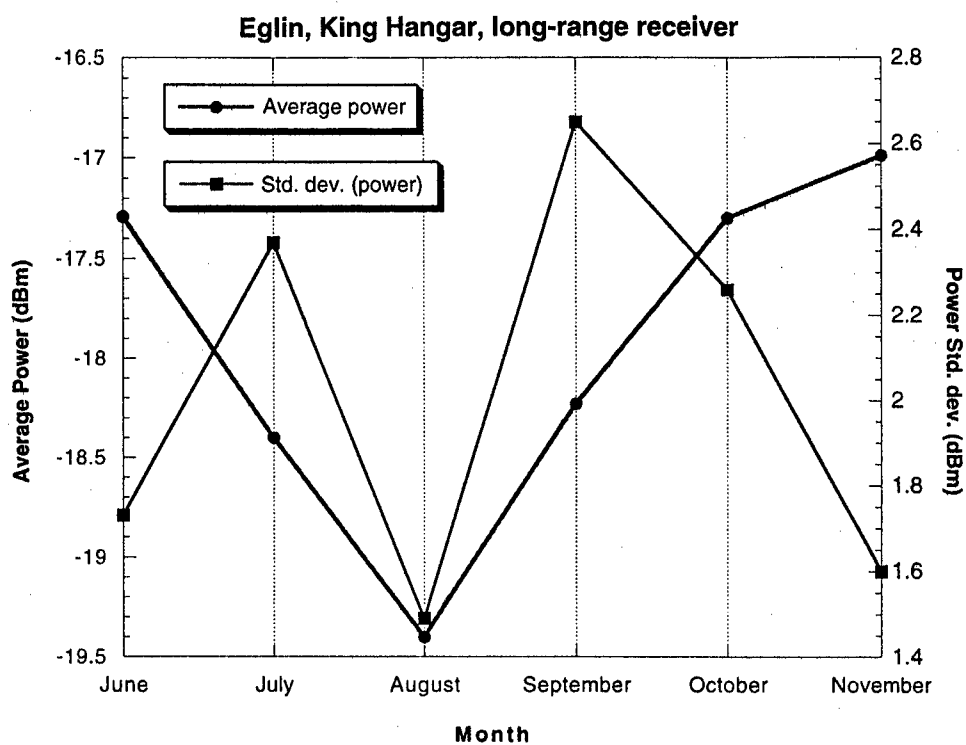


Figure 3.7
Seasonal average power.

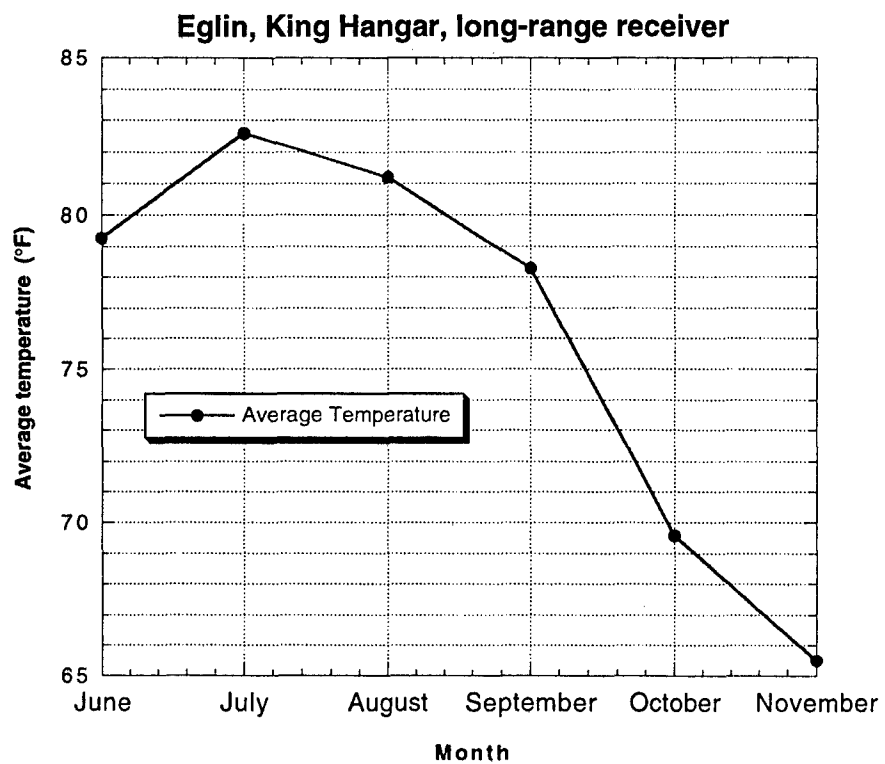


Figure 3.8
Seasonal average temperature.

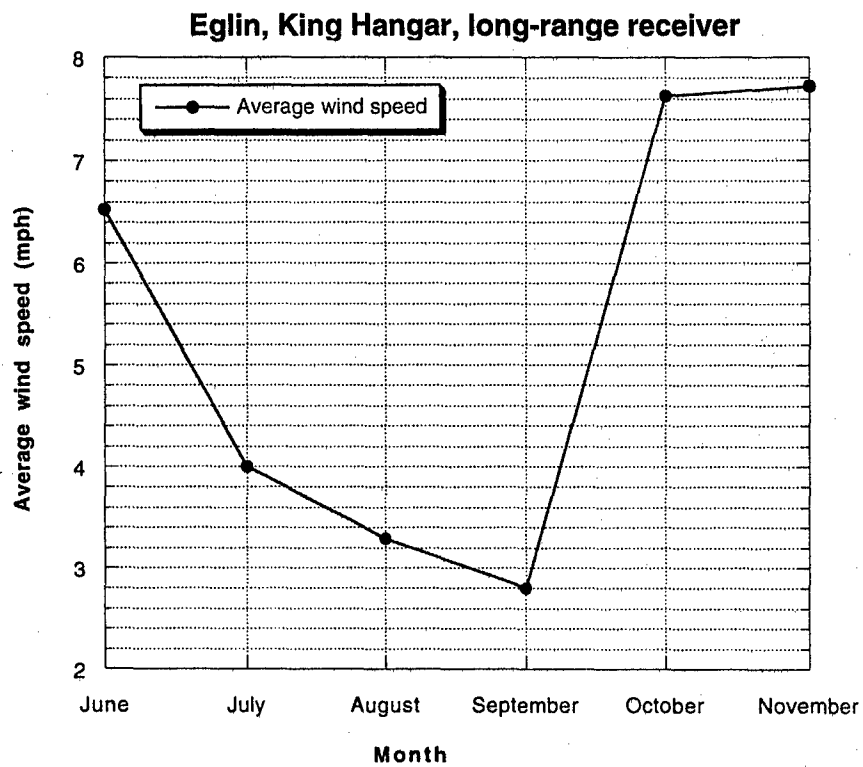


Figure 3.9
Seasonal average wind speed.

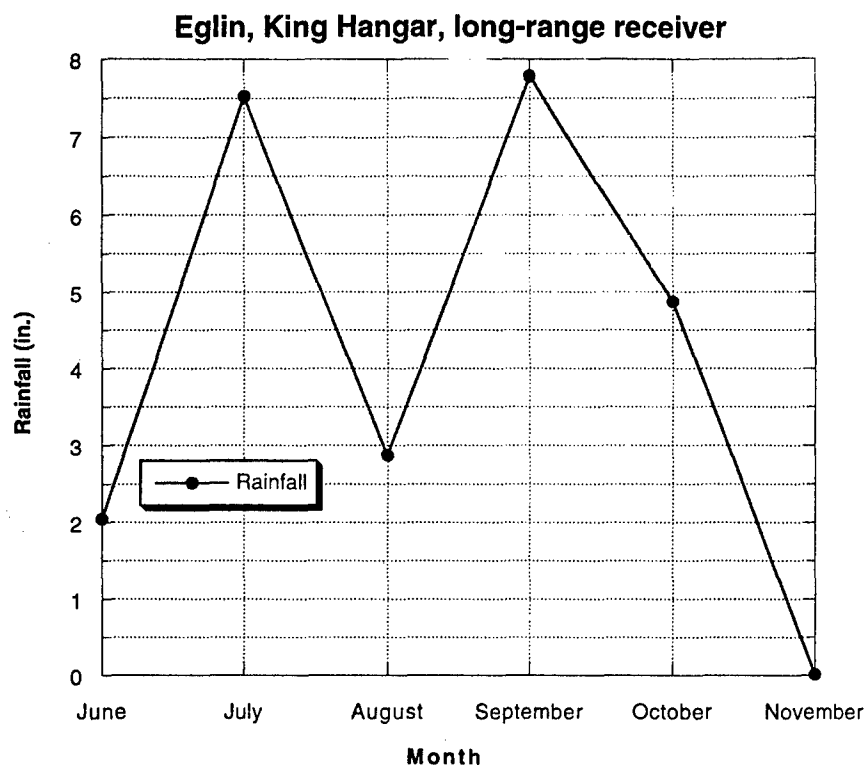


Figure 3.10
Seasonal cumulative rainfall.

Table 3.5

**Statistics from two 1-week data sets shown,
transmitted bit pattern: QRSS, 1024 bits/block.**

Data Type	Summer Data Set 62060635	Fall Data Set 62831341
Average Bit Error Rate	1.77e-3	0.0
Average Percent Error-Free Seconds	96.5	99.98
Average Block Count	811	820
Average Signal Level	-18.7 dBm	-16.5 dBm
Peak Signal Level	-12.9 dBm	-12.7 dBm
Average Temperature	81.3°F	68.6°F
Average Wind Speed	4.3 mph	6.7 mph
Total Rainfall	2.28 in.	0.0 in.

Table 3.6

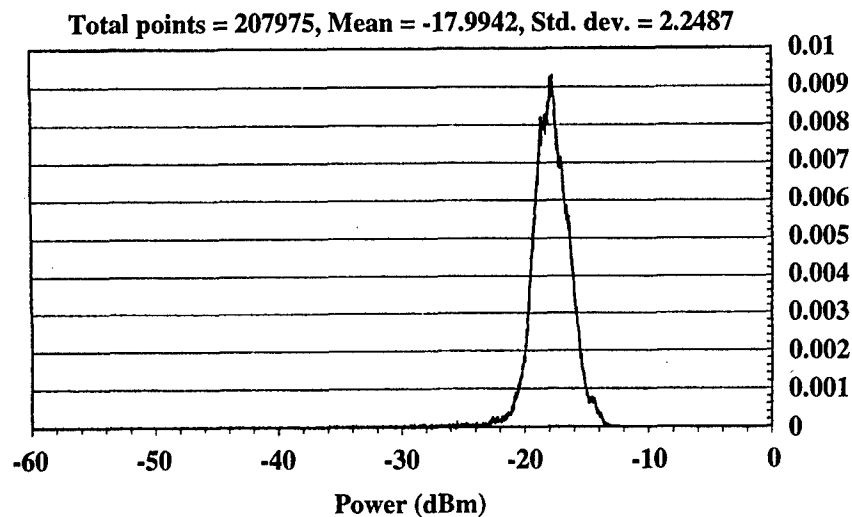
Calculated rainfall statistics for Eglin King Hangar to A-3 path.

Frequency	27.3 GHz
Physical Path Length	10.8 km
Reduction Factor	0.67
Rainfall Rate Exceeded 0.1% of the Time	35 mm/hr
Attenuation Vertical Polarization	5.2 dB/km
Total Attenuation	37.8 dB
Signal-to-Noise Ratio Required during Fade Event	10 dB
Total Signal Excess Required	47.8 dB
Climate Classification	N
Average Link Margin from Measured Signal Level	46.3 dB
Percentage of Time Receiver Unlocked (i.e., fade greater than 40 dB)	0.2%

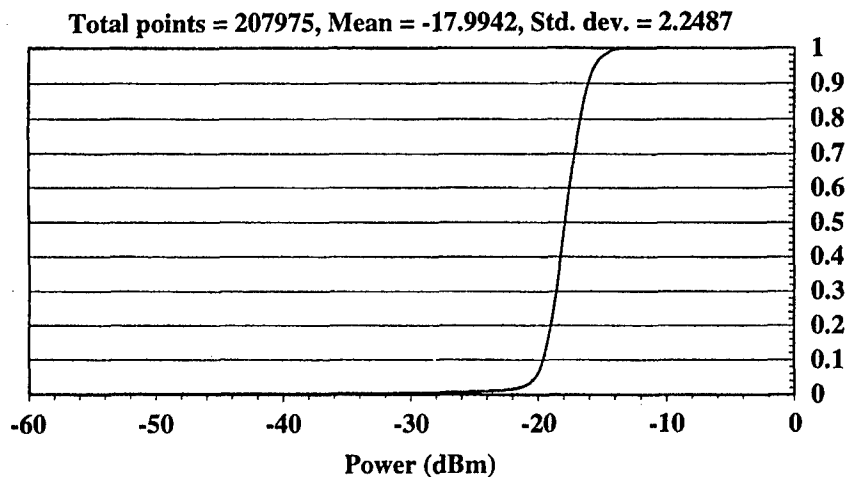
Figure 3.11 (top) is the received power histogram and Fig. 3.11 (bottom) is the received power cumulative distribution. The histograms for the monthly intervals are also shown in Figs. 3.12–3.15. Although some variation was apparent in the monthly distributions, no radical variations occurred.

Figures 3.16 and 3.17 show the data set started 24 July 1996, file 62060635. These data were collected during the peak of the thunderstorm season in the Florida panhandle region. During this collection, a major thunderstorm system moved through the area and lasted for about 18 h. Both the transmitter and receiver showed a maximum rainfall rate of 4.8 in. (130 mm) per hour during this very intense storm with about 2 in. of total rainfall. During the storm, the receiver was locked onto the transmitter signal for more than half the time. The receiver was unable to lock onto the transmitter signal for only 93 min total time, with the longest period lasting for 13 min. The average length of signal fade that caused the receiver to unlock during the storm was about 5 min. The fades were very sporadic and unpredictable during storm events. The bit error rate exceeded $1e-1$ (one errored bit for every 10 received) for about 43 min, with an average length of 1.2 min, and a maximum period of 3 min. Inspection of other data sets showed similar behavior during large storms, but this data set was recorded during the highest intensity and longest duration storms, which resulted in one of the worst fades recorded. During large storms, comparable amounts of rainfall were recorded at the transmitter and the receiver, although at different times. This was indicative of several intense thunderstorm cells moving through the link path.

Figures 3.18 and 3.19 show a fall data set, file 62831341, in which no storms occurred. The data transmission during this time frame was essentially perfect. The importance of these data is that there was no evidence of ducting or other interfering mechanisms in the transmission path, indicating a highly reliable data link.



(a) Eglin, King Hangar, long-range receiver
Received power histogram, May through November 1996



(b) Eglin, King Hangar, long-range receiver
Received power cumulative distribution
May through November 1996

Figure 3.11
Histogram of signal strength data from May 1996 through November 1996.

Eglin, King Hangar, long-range receiver
received power histogram , July 1996

Total points = 46210, Mean = -18.4048, Std. dev. = 2.3747

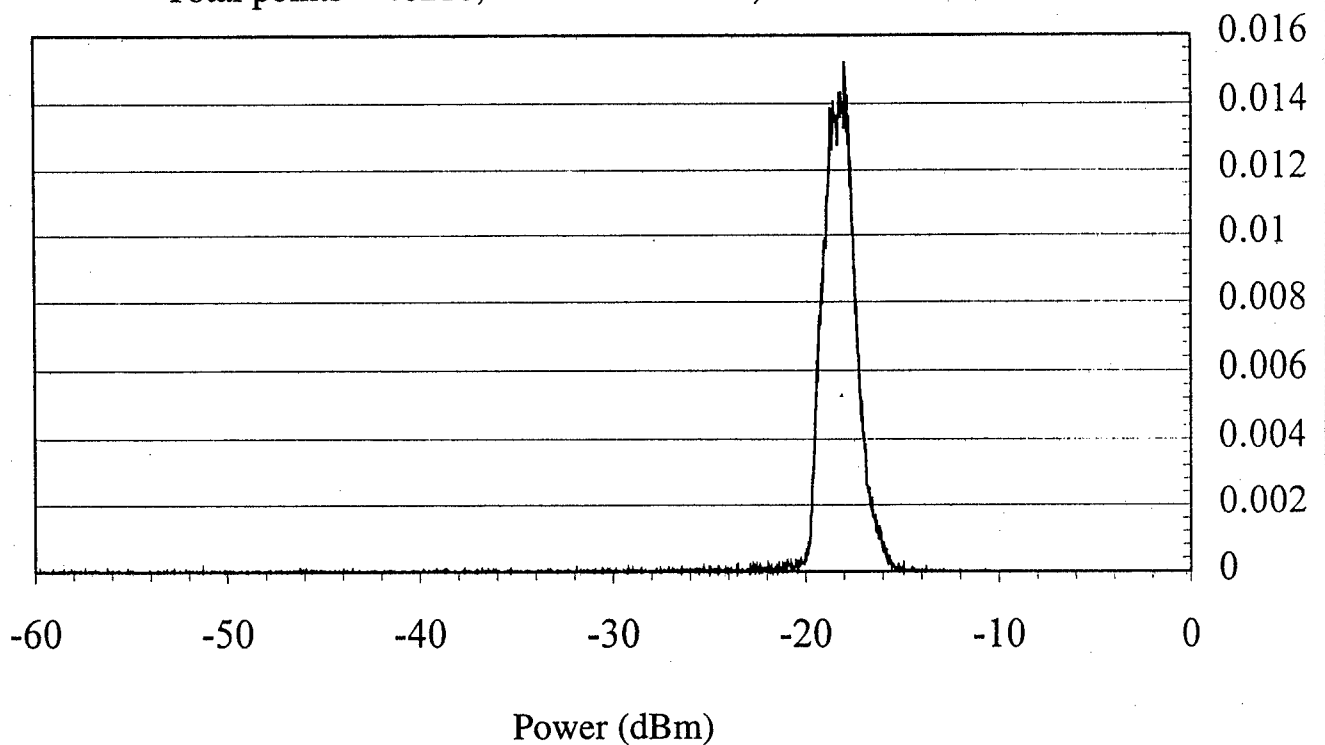


Figure 3.12

Histogram of signal strength data from July 1996.

Eglin, King Hangar, long-range receiver
received power histogram , August 1996

Total points = 36167, Mean = -19.0411, Std. dev. = 1.4908

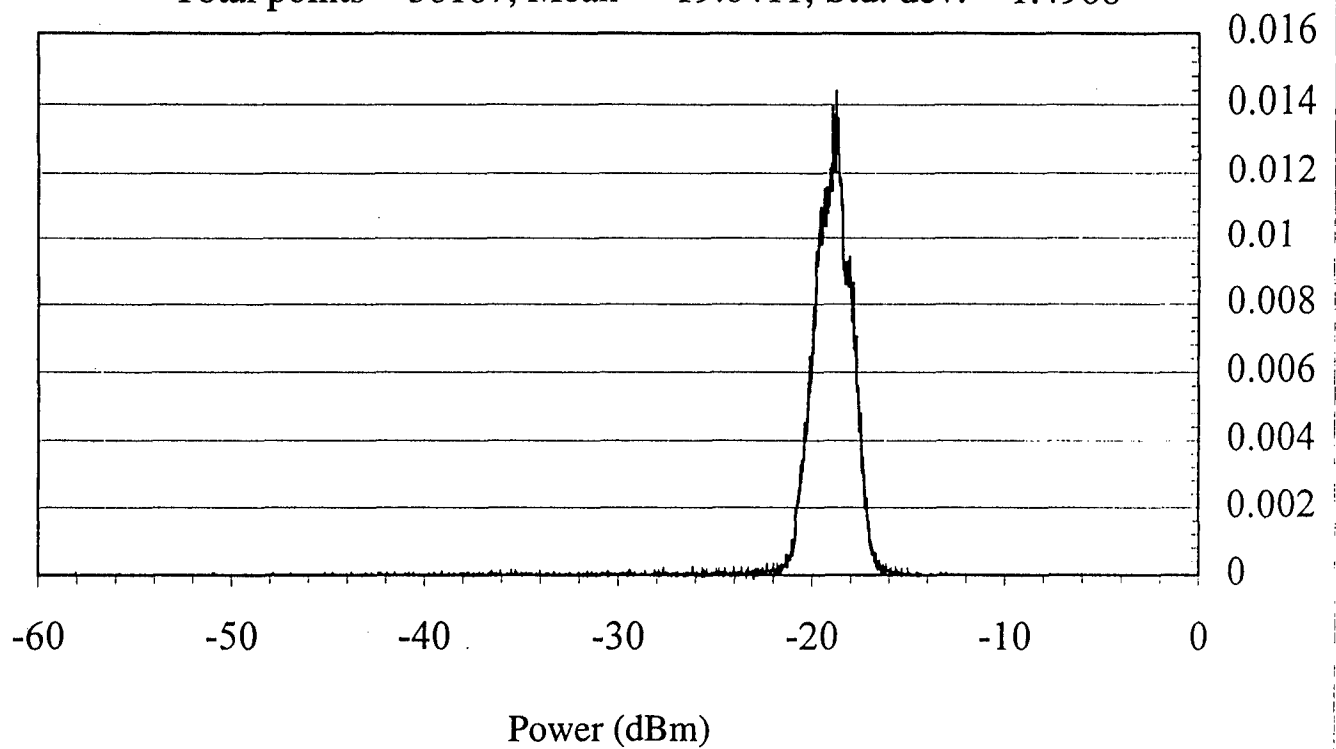


Figure 3.13

Histogram of signal strength data from August 1996.

Eglin, King Hangar, long-range receiver
received power histogram, September 1996

Total points = 35911, Mean = -18.2301, Std. dev. = 2.6533

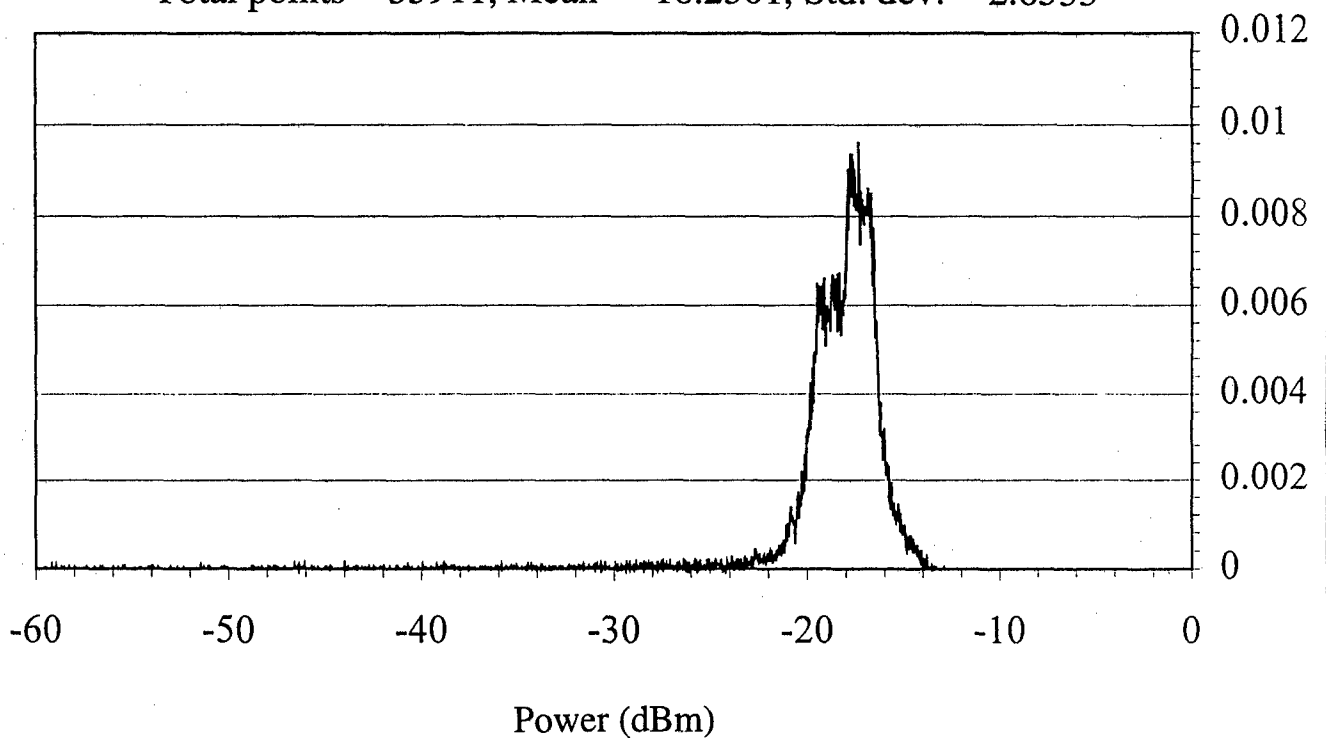


Figure 3.14

Histogram of signal strength data from September 1996.

Eglin, King Hangar, long-range receiver
received power histogram, October 1996

Total points = 43991, Mean = -17.3179, Std. dev. = 2.2611

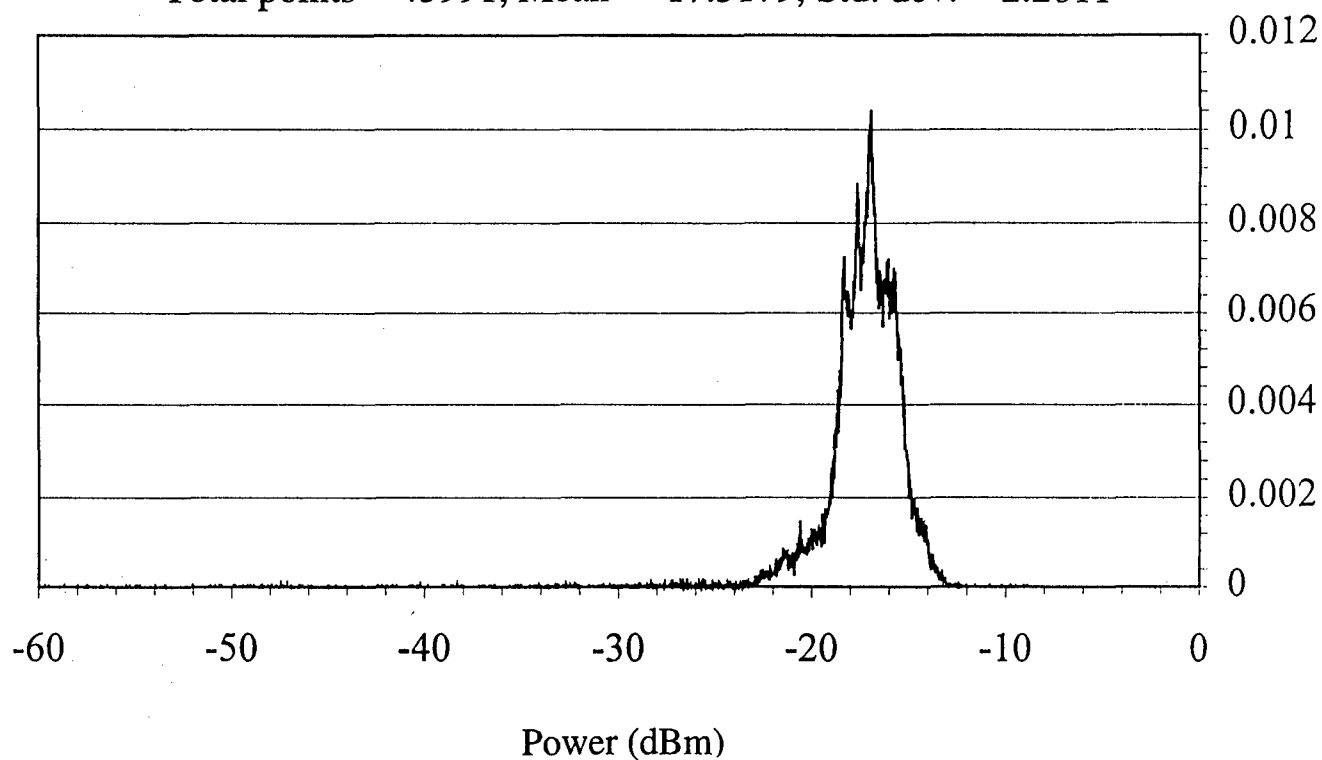


Figure 3.15
Histogram of signal strength data from October 1996.

Eglin, King Hangar, long-range receiver, file 62060635, 7/24 - 7/31 1996

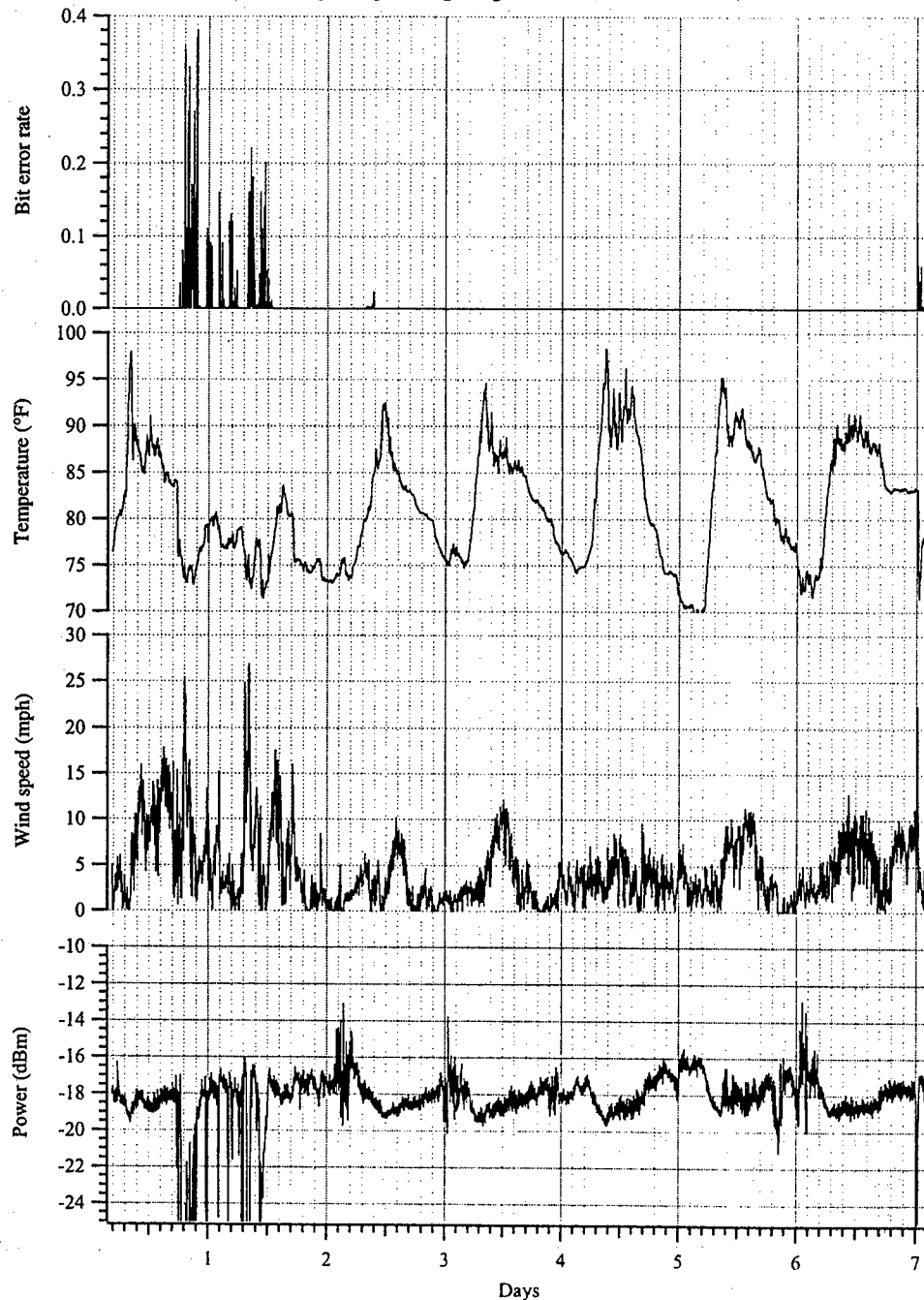


Figure 3.16

Vertical polarization time series data from 62060635: bit error rate, temperature at the receiver, wind speed, and measured signal strength.

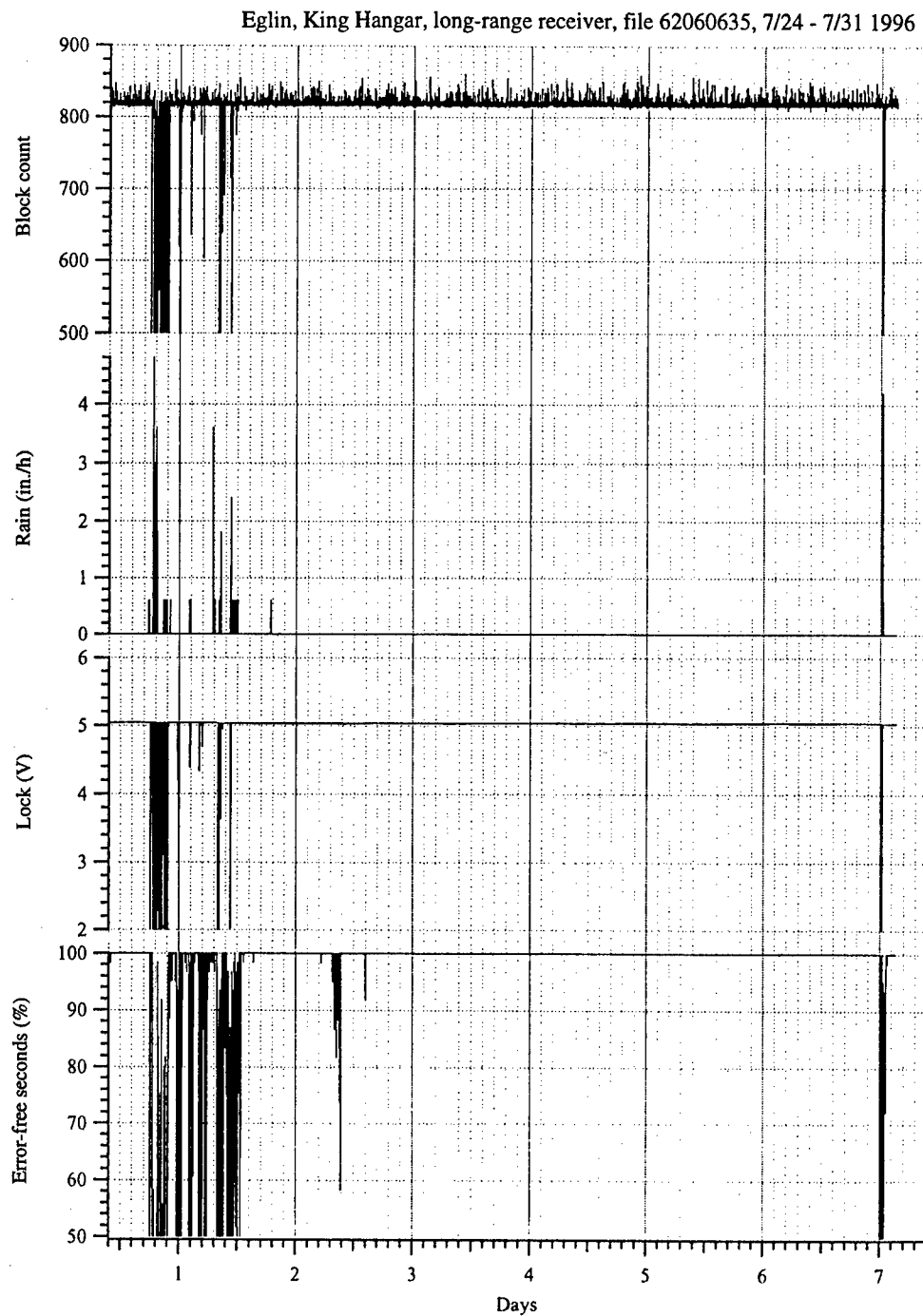


Figure 3.17

Vertical polarization time series data from 62060635: block count, rainfall rate, sweep/lock indicator, and percent error-free seconds of transmission.

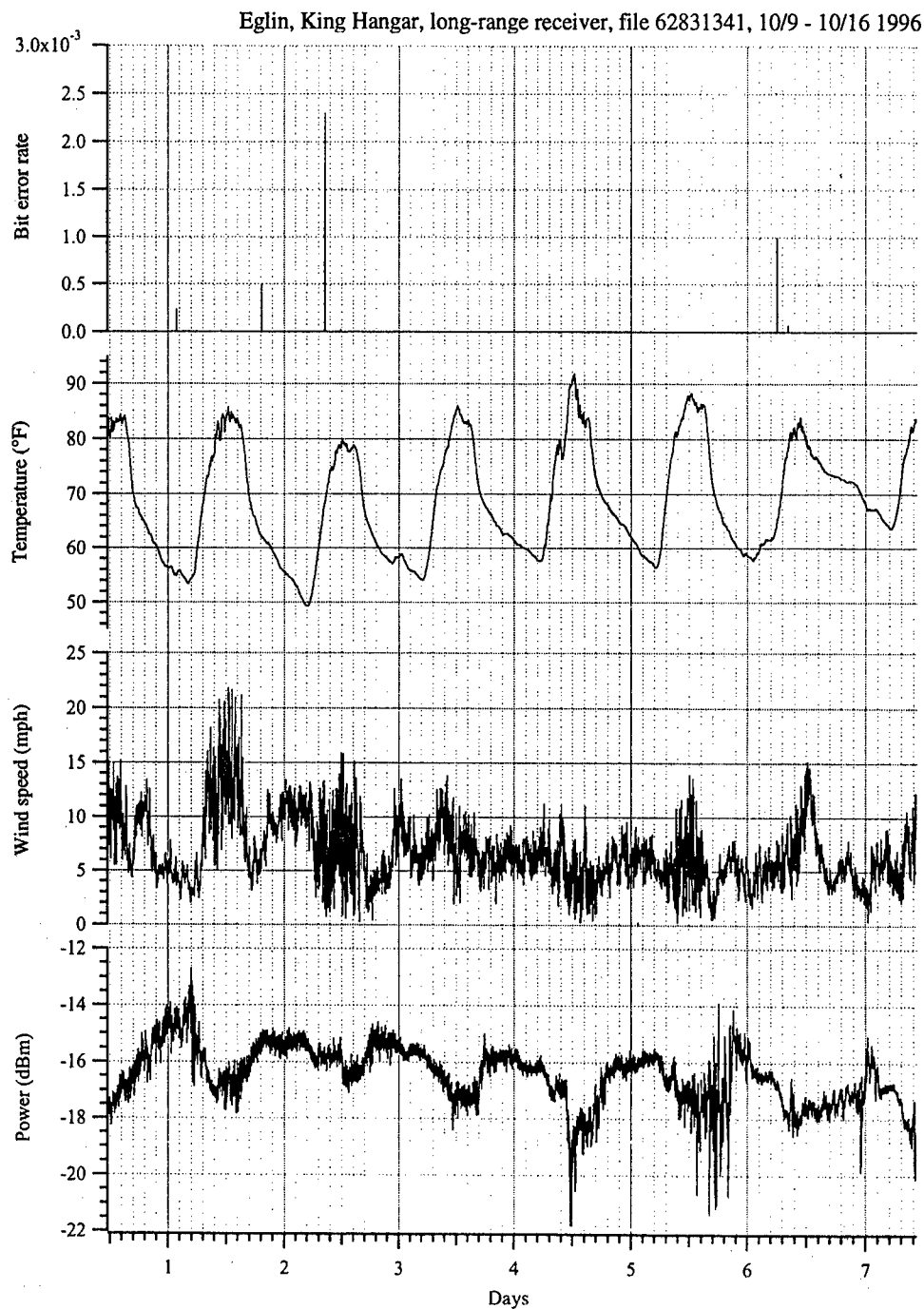


Figure 3.18

Vertical polarization time series data from 62831341: bit error rate, temperature at the receiver, wind speed, and measured signal strength.

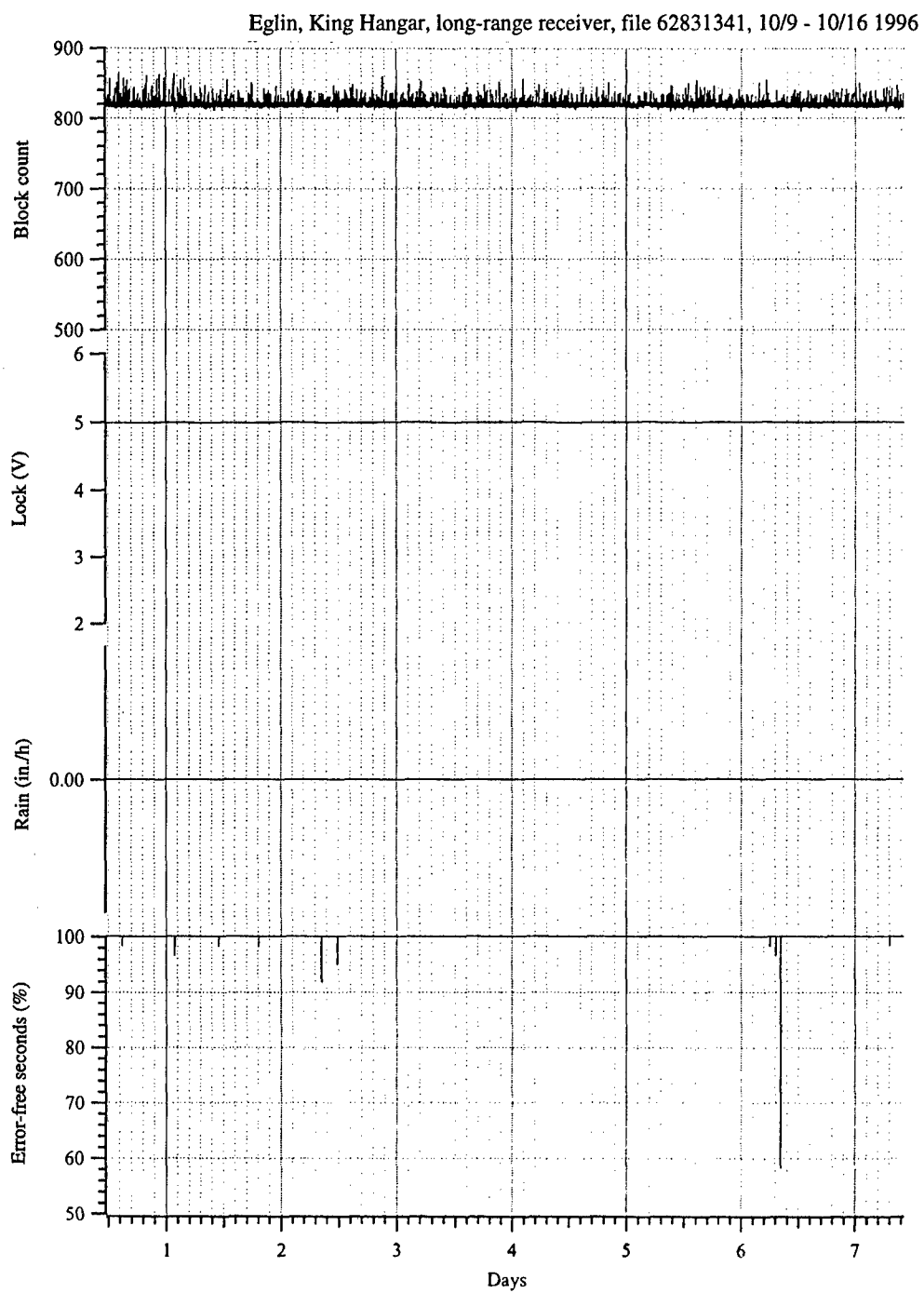


Figure 3.19
Vertical polarization time series data from 62831341: block count, rainfall rate, sweep/lock indicator, and percent error-free seconds of transmission.

3.3 MINOT AFB TEST, NOVEMBER 1995 THROUGH MARCH 1996

This test was conducted at Minot AFB, North Dakota, over a 6.7-km path to assess the effects of cold weather with significant temperature swings on low elevation propagation paths. The transmitter was elevated about 50 ft above the terrain, and the receiver was elevated about 20 ft above the terrain. A clear line-of-sight was available between the transmitter and the receiver. The monthly averages are shown in Fig. 3.20–3.23. Very few episodes of dropout and signal loss were observed. The overall performance of the data link was nearly perfect for this test period in this environment.

Figure 3.20 shows that very little variation of average power was observed. The standard deviation of power was also quite low. The average temperatures shown in Fig. 3.21 indicated that January was the coldest month measured. The average wind speed measured is shown in Fig. 3.22. These were the highest average wind speeds measured during the testing. Although no confirmed rain occurred during the entire test period at Minot, some moisture was recorded because of the melting snow in the buckets. A total of 0.5 in. of “rain” was recorded by the rain bucket, all of it believed to be from melting frozen rain or snow.

The histogram of the total data has a more regular shape than the histograms measured in high excess path loss environments. The histogram of the total accumulated data set is shown in Fig. 3.23. The average power was estimated to be about 1.5 dB below the free space value. The low excess path loss was curious because the path elevation was not much higher than those at Eglin and Davis Monthan AFB. Figures 3.24–3.27 show the histograms of the individual months. Although a number of these histograms show multiple peaks, the widths of the histograms are narrow. The standard deviation of the overall signal histogram was 1.3 dB, and less than 1 dB during December, March, and April.

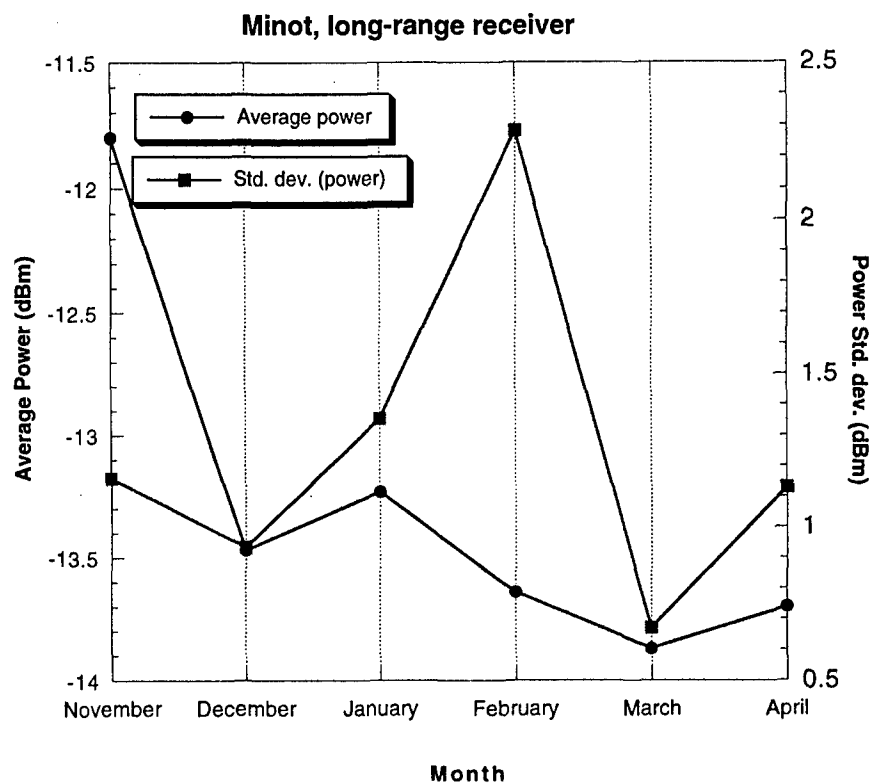


Figure 3.20
Seasonal average power.

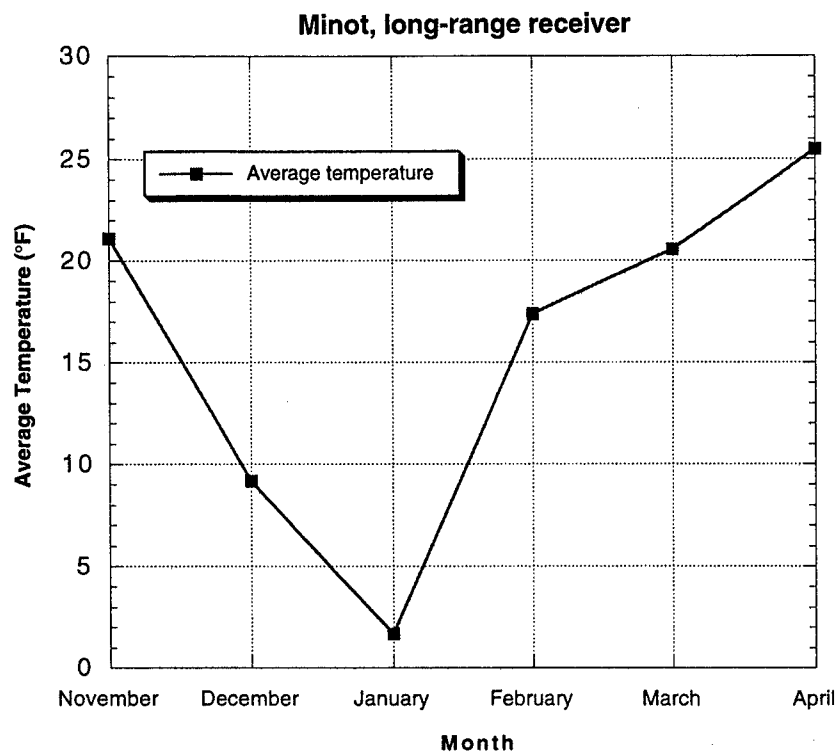


Figure 3.21
Seasonal average temperature.

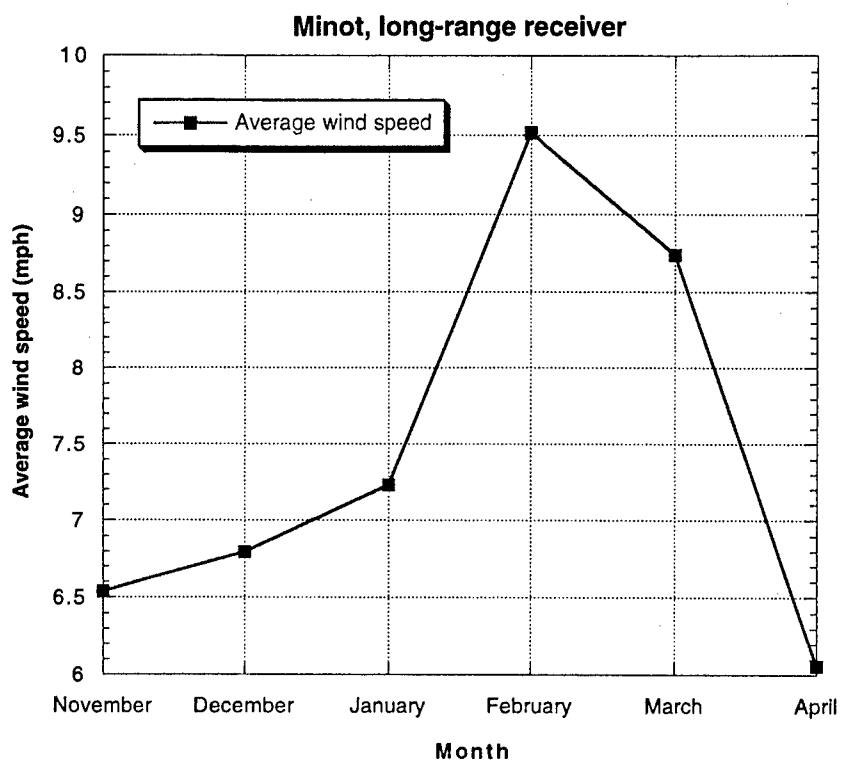
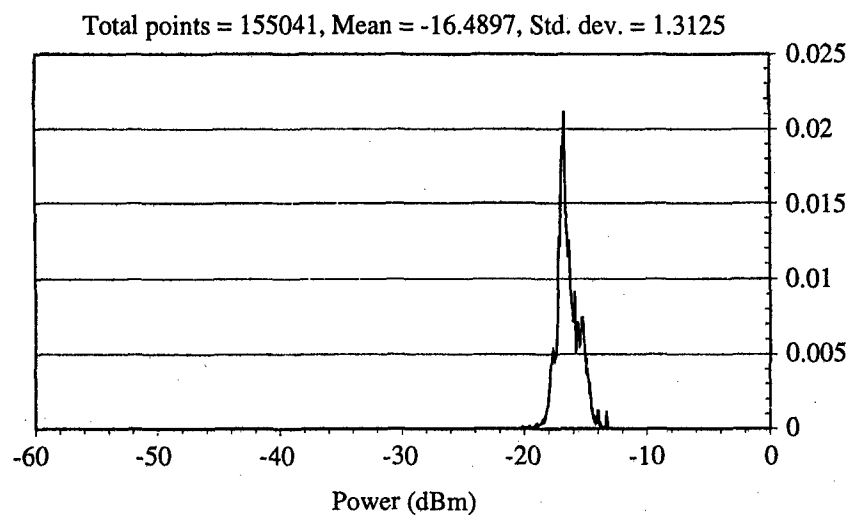
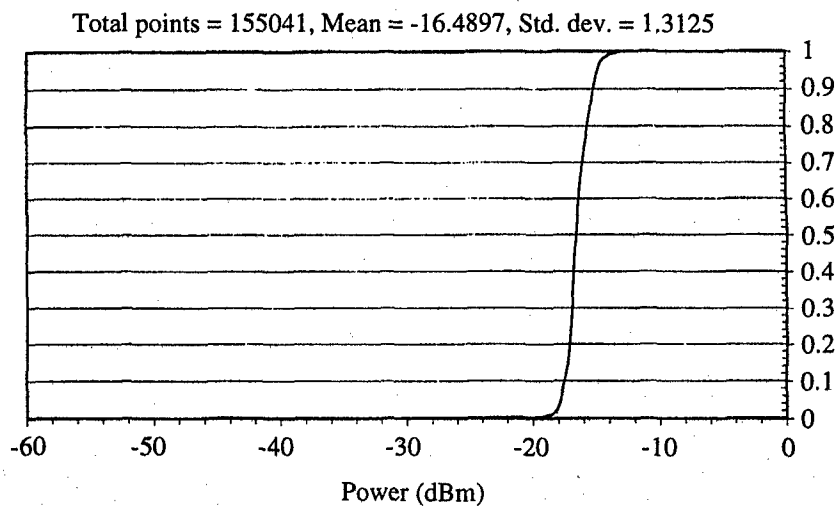


Figure 3.22
Seasonal average wind speed.



(a) Minot long-range receiver
received power histogram
November 1995 through April 1996



(b) Minot long-range receiver
received power cumulative distribution
November 1995 through April 1996

Figure 3.23
Histogram of signal strength data from November through April 1996.

Minot long-range receiver
received power histogram, December 1995

Total points = 23707, Mean = -16.4970, Std. dev. = 0.7173

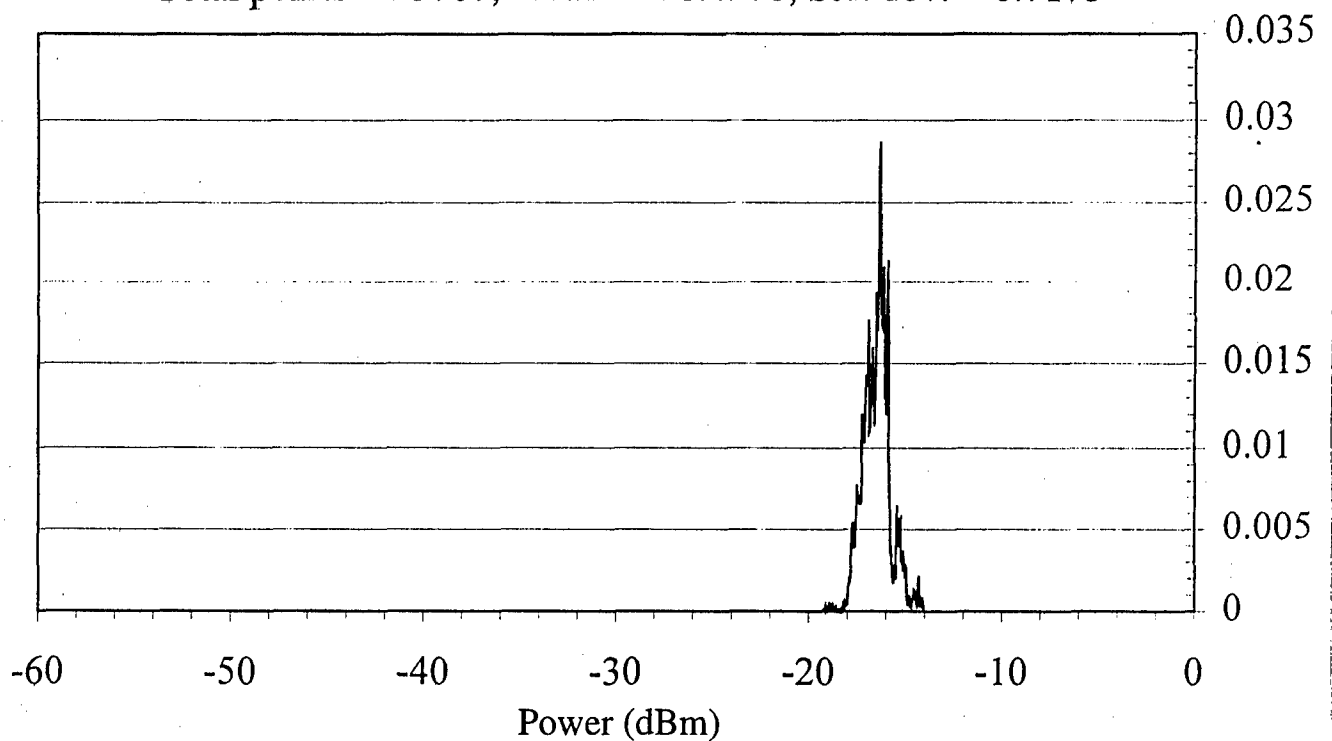


Figure 3.24

Histogram of signal strength data for December 1995.

Minot long-range receiver
received power histogram, January 1996

Total points = 29636, Mean = -16.2956, Std. dev. = 1.0274

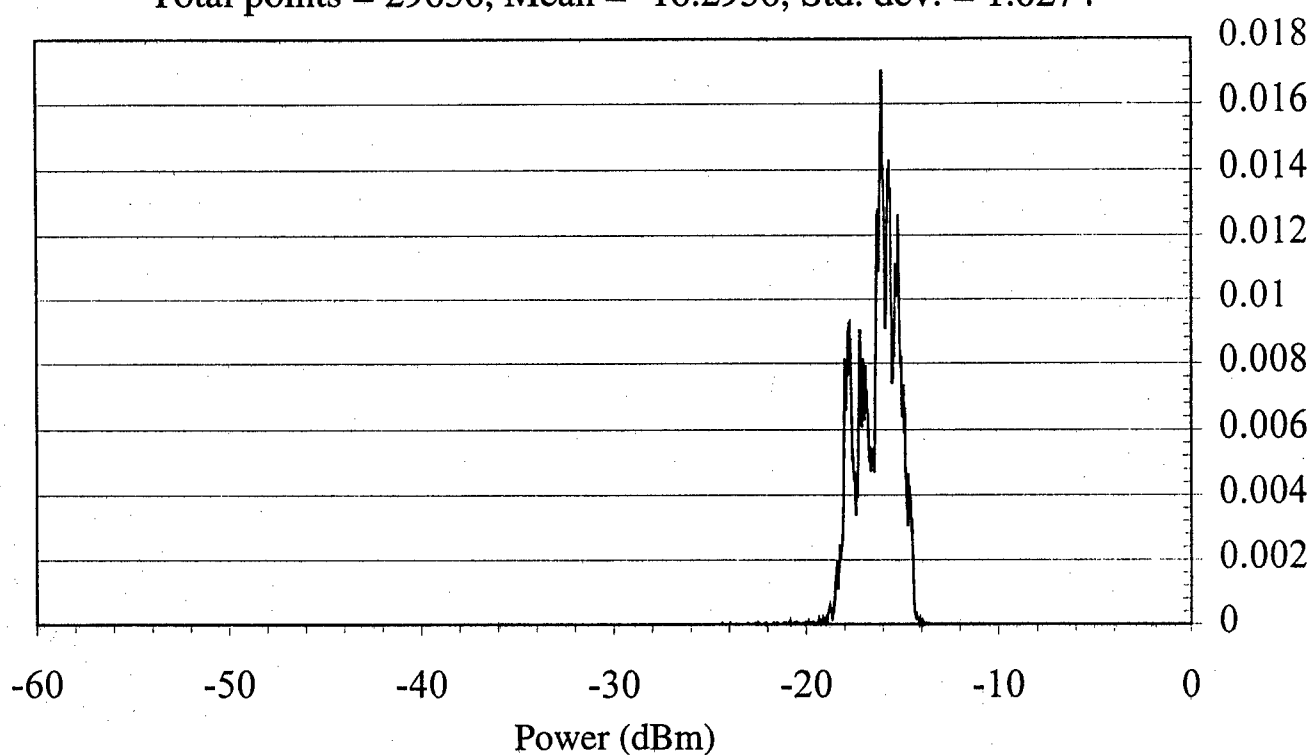


Figure 3.25

Histogram of signal strength data for January 1996.

Minot long-range receiver
received power histogram, February 1996

Total points = 35575, Mean = -16.6457, Std. dev. = 2.1469

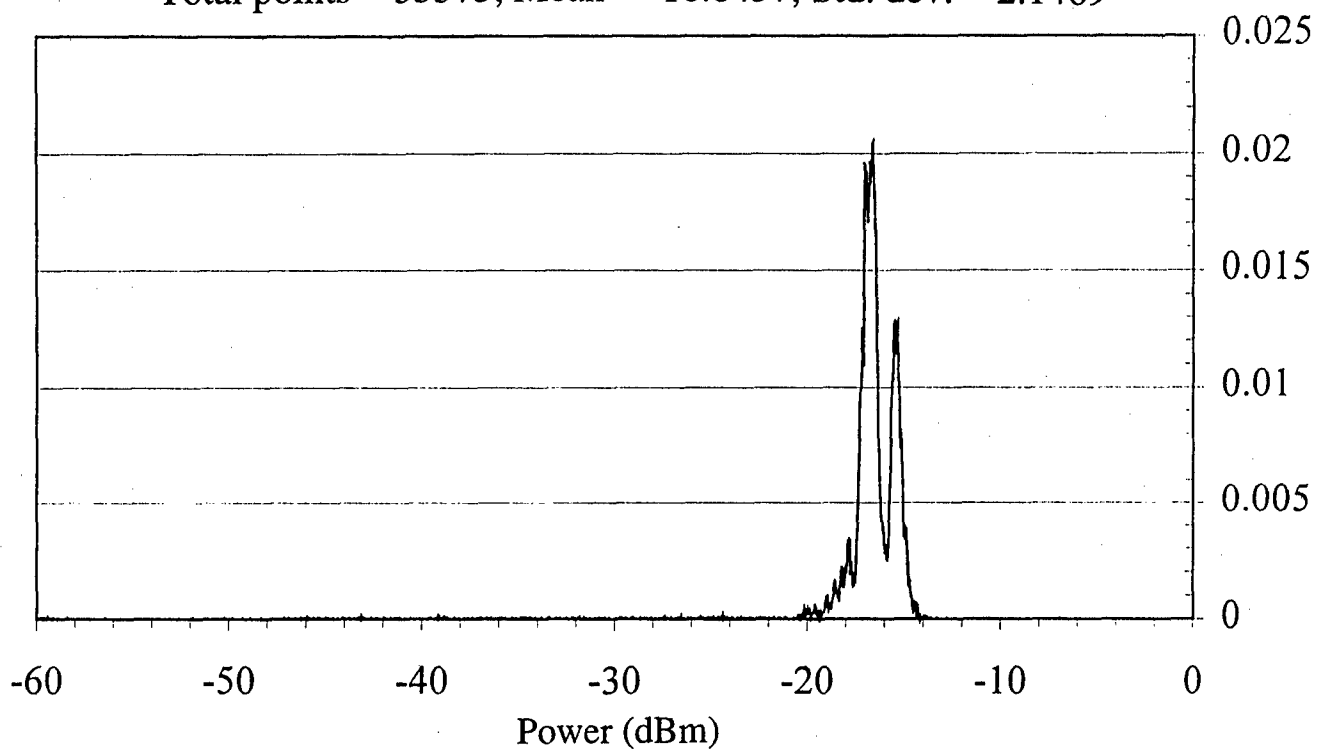


Figure 3.26

Histogram of signal strength data for February 1996.

Minot long-range receiver
received power histogram, March 1996

Total points = 36004, Mean = -16.809, Std. dev. = 0.5018

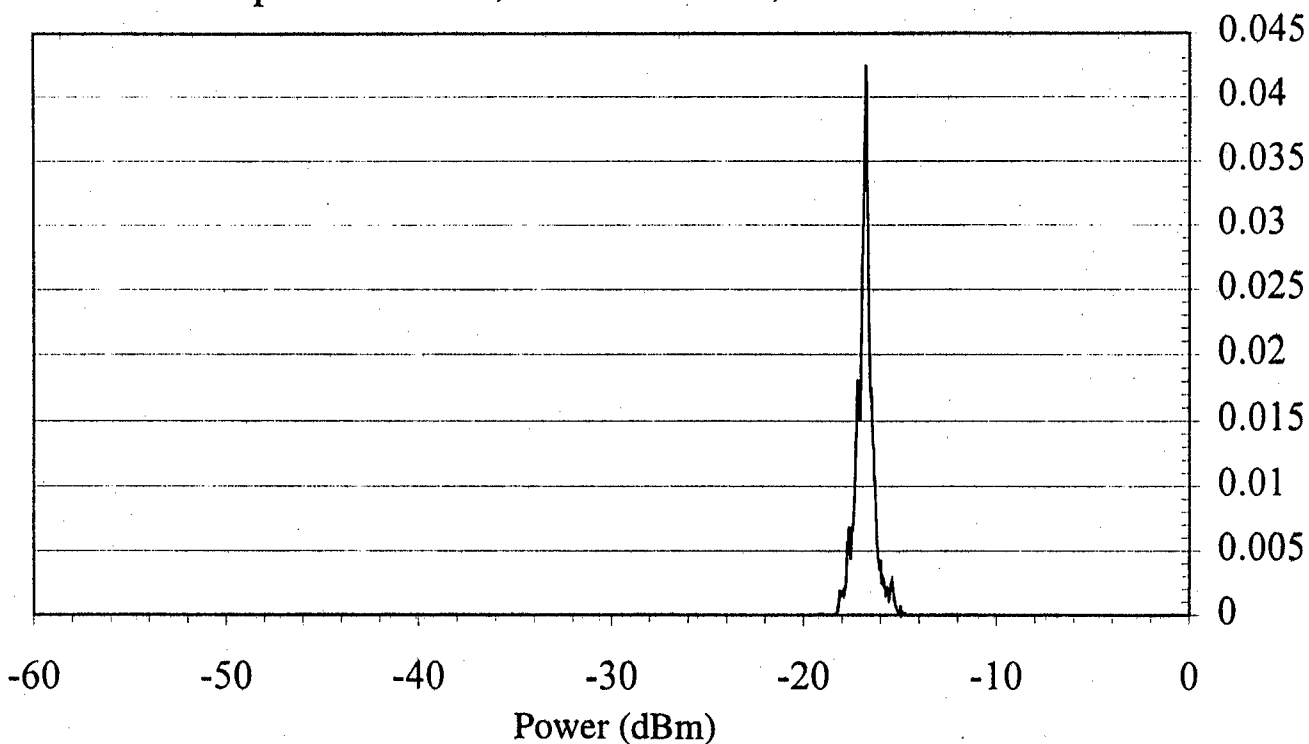


Figure 3.27

Histogram of signal strength data for March 1996.

Table 3.7 gives the data link characteristics for the Minot test. Table 3.8 gives a summary of the performance statistics of the data link. These data clearly show that the transmission path is very reliable, even for this low power system.

Table 3.7
Data link characteristics.

Transmit Power	18 dBm
Transmitter Antenna Gain	29 dB
Receiver Antenna Gain	35 dB
Mixer Loss	-12 dB
Front-End LNA Gain	27 dB
IF Amplifier Gain	26 dB
Frequency / Wavelength	27.3 GHz / 0.011 m
Range	6.7 km
Free Space Spreading Loss	-138 dB
Receiver Noise Figure / Noise Floor at 7-MHz Bandwidth	3.5 dB / -105 dBm
Data Rate	1.5 Mbps
Average Signal Level	-16.5 dBm average
Calculated Signal Level	-15 dBm
Average Excess Signal Loss	1.5 dB
Climate Classification	Transition from E to K
Path Length Reduction Factor	0.67

Table 3.8
Summary of Minot AFB long-range link information.

Total Test Time	2248 h
Percentage of Good Data Acquisition Time	84.51%
Average BER	6.8e-6
Percent Error-Free Time	99.92%
Total Rainfall Recorded at the Receiver	0.51 in.

The two data sets, 60341059 and 60660520, were collected in February and March 1996. Data set 60341059, shown in Figs. 3.28 and 3.29, indicated that extreme cold did not adversely affect the transmission path or hardware. It was curious that the signal amplitude actually dipped slightly during the coldest period of the data set, but did not show any increase in the short-term deviation of the AGC voltage. The digital data transmission was essentially perfect, with only one brief episode of signal error, lasting only for 1 min. Also, there were no diurnal temperature fluctuations during this data collection period.

Figures 3.30 and 3.31 show data set 60660520, which indicated a cold front moving through the area. This is evidenced by high winds primarily from the north and associated cooler temperatures. The lowest temperature recorded during this data collection period was -12°F. The link performance was also essentially perfect for this period. The signal variation was very small. Table 3.9 gives a summary of the statistics for the two sets of data. Except for average wind speed, both sets of data were similar in their average characteristics. The average signal level was slightly higher for the second data set. It could not be determined if this was due to the same effects that caused the signal enhancements in the Eglin and Davis Monthan data.

Minot long-range receiver, file 60341059, 2/3 - 2/10 1996

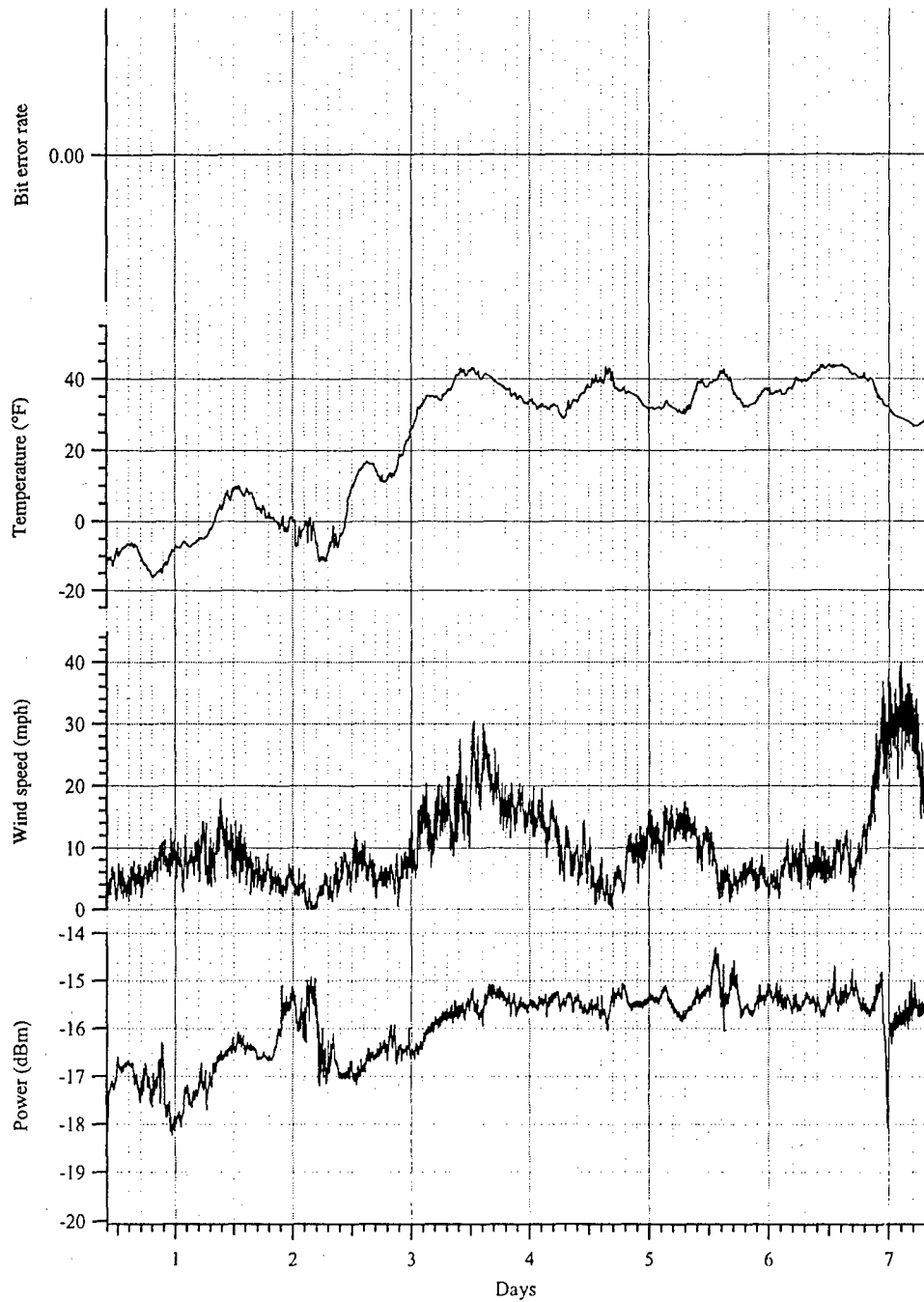


Figure 3.28

Vertical polarization time series data from 60341059: bit error rate, temperature at the receiver, wind speed, and measured signal strength.

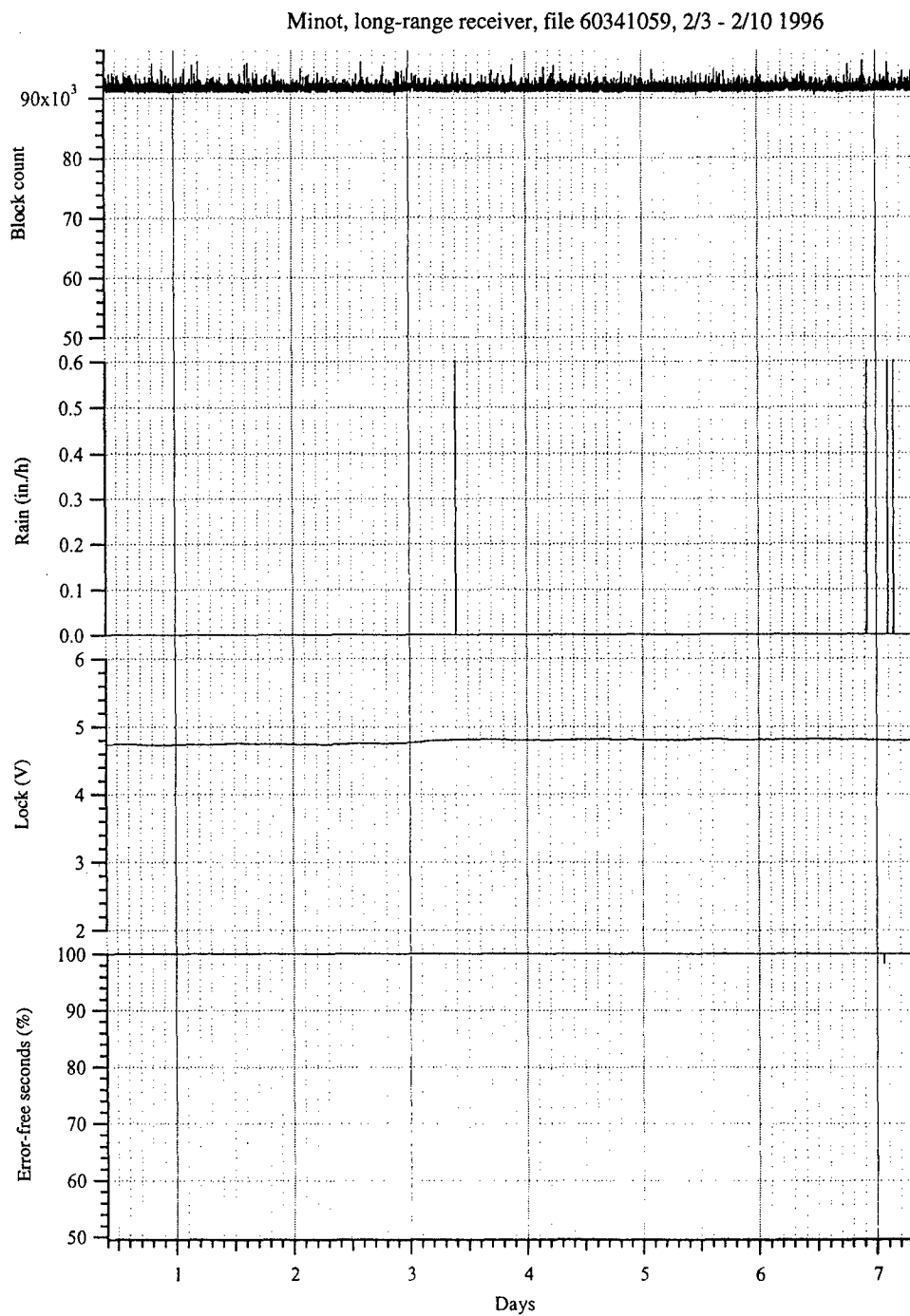


Figure 3.29

Vertical polarization time series data from 60341059: block count, rainfall rate, sweep/lock indicator, and percent error-free seconds of transmission.

Minot, long-range receiver, file 60660520, 3/6 - 3/13 1996

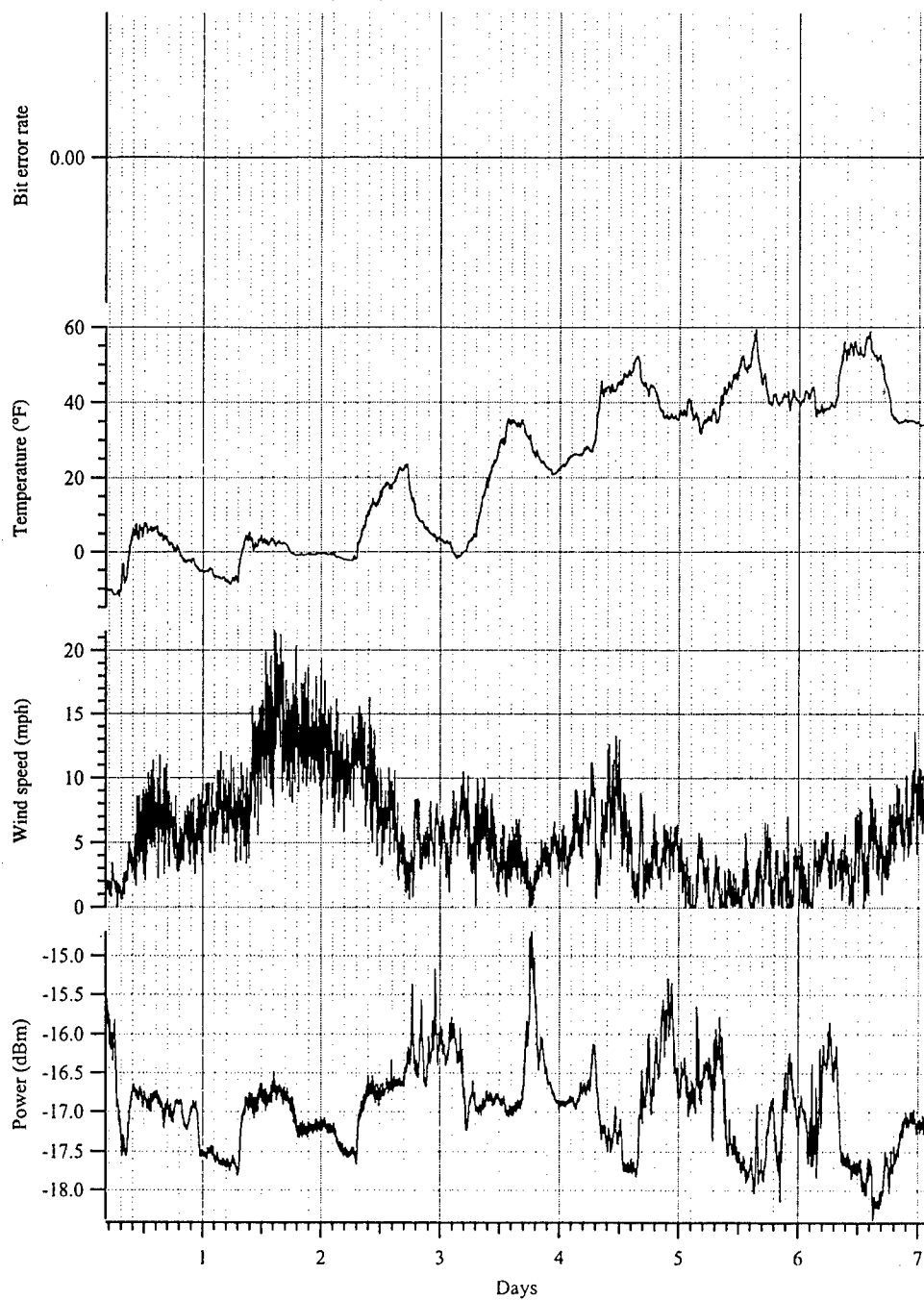


Figure 3.30

Vertical polarization time series data from 60660520: bit error rate, temperature at the receiver, wind speed, and measured signal strength.

Minot, long-range receiver, file 60660520, 3/6 - 3/13 1996

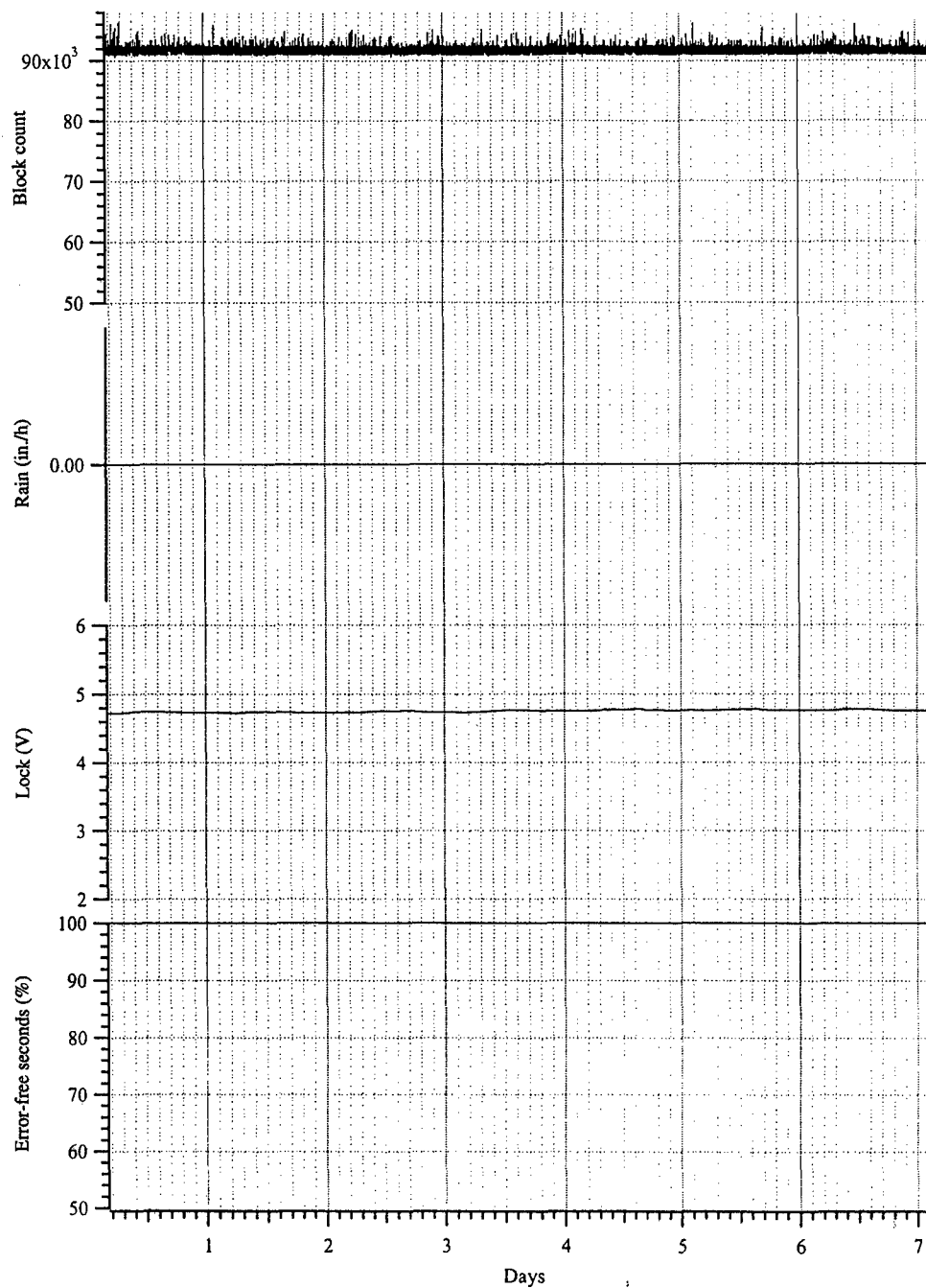


Figure 3.31

Vertical polarization time series data from 60660520: block count, rainfall rate, sweep/lock indicator, and percent error-free seconds of transmission.

Table 3.9
Statistics from the two data sets shown,
transmitted bit pattern: QRSS, 1023 bits/block.

Data Type	Data Set 60341059	Data Set 60660520
Average Bit Error Rate	0.0	0.0
Average Percent Error-Free Seconds	100.0	100.0
Average Block Count	91800	91857.3
Average Signal Level	-15.9 dBm	-16.9 dBm
Peak Signal Level	-14.3 dBm	-14.6 dBm
Average Temperature	22.7°F	22.0°F
Average Wind Speed	10.2 mph	5.77 mph
Recorded Rainfall	0.05 in.	0.0 in.

These data showed fewer signal fluctuations than the Eglin and Davis Monthan data. The path at Minot was shorter and less cluttered than the paths tested at Eglin and Davis Monthan.

3.4 DAVIS MONTHAN TEST

Special attention was given to this test due to military interest in using a deployable link of this type in a desert climate. The site chosen was across the aircraft storage area at Davis Monthan AFB. This path proved to be a difficult environment and provided a good test of the system's capability. The elevation of the transmitter was only 22 ft above ground level, while the receiver was elevated 47 ft above ground level. The ground elevation was slightly higher at the transmitter, estimated to be about 30 ft higher than ground level at the receiver. The separation between the transmitter and the receiver was 9.6 km. Although the path was line-of-sight, it was difficult to actually sight the far end of the link. The clutter on the terrain and the long path distance made it necessary to get a mechanical "cherry picker" to elevate an observer high enough (about

50 ft above ground level) so that the building the receiver was mounted on was clearly identifiable from other buildings. Furthermore, a reflective balloon was attached to the roof of this building to insure positive identification. The elevation of the observer was then reduced to the transmitter level and the transmitter was aimed.

3.4.1 Seasonal Average Statistics

This path contained many metal scatterers (aircraft in storage) between the transmitter and the receiver. The effect of these scatterers and the low elevation of the path significantly attenuated the signal from the transmitter. The signal was reduced by approximately 20 dB below the calculated free space value.

The tests were conducted at Davis Monthan for a longer period than at any other site. Long periods (up to 20 weeks at a time) of unattended data collection provided a low-cost means of collecting data for determining seasonal behavior. The seasonal changes can be evaluated by looking at the received power in Fig. 3.32. The seasonal dependence of the received signal power is clearly evident. The 2-month received power is shown along with the standard deviation computed from the 2-month accumulated histograms. The exception to this is the June 1996 data, which is only one month of accumulated data. The standard deviation did not seem to have as clear a dependence on season as on the average power. Figure 3.33 shows seasonal average temperature, which indicated a possible negative correlation with the average received power. In order to assure that this effect is not simply due to the system electronics, measurements of the test equipment were made and showed only about 1 dB of variation in the transmitter for the power amplifier temperature of 90°F up to 150°F. The receiver output seemed relatively insensitive to temperature over the range to which the system was exposed. Figure 3.34 shows seasonal average wind speed, which suggests a possible negative correlation with average signal level. Figure 3.35 shows the cumulative rainfall recorded for each 2-month

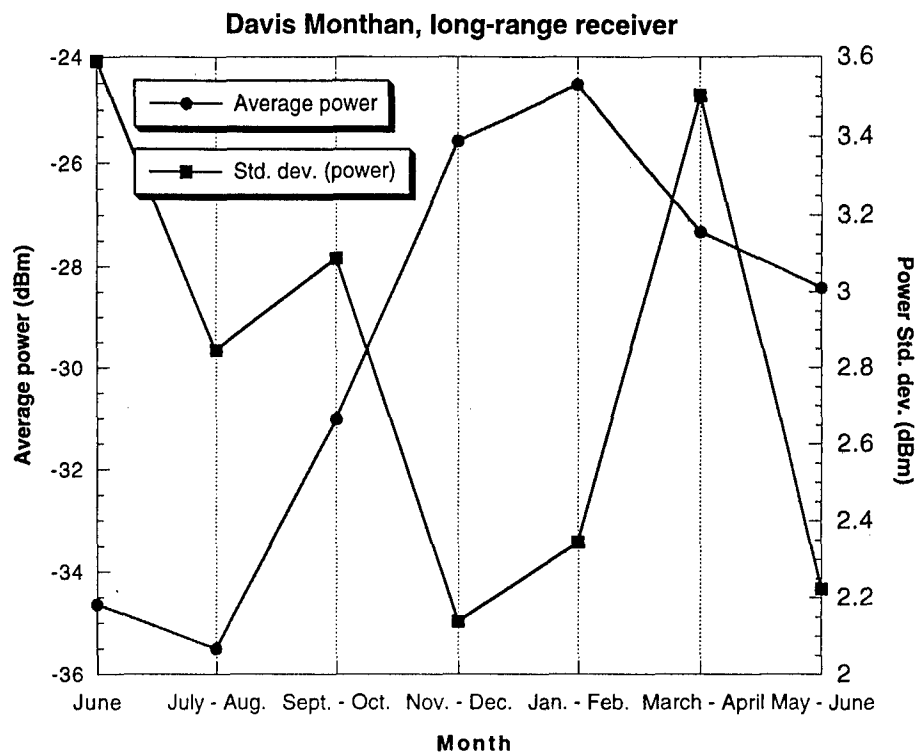


Figure 3.32
Bimonthly average power.

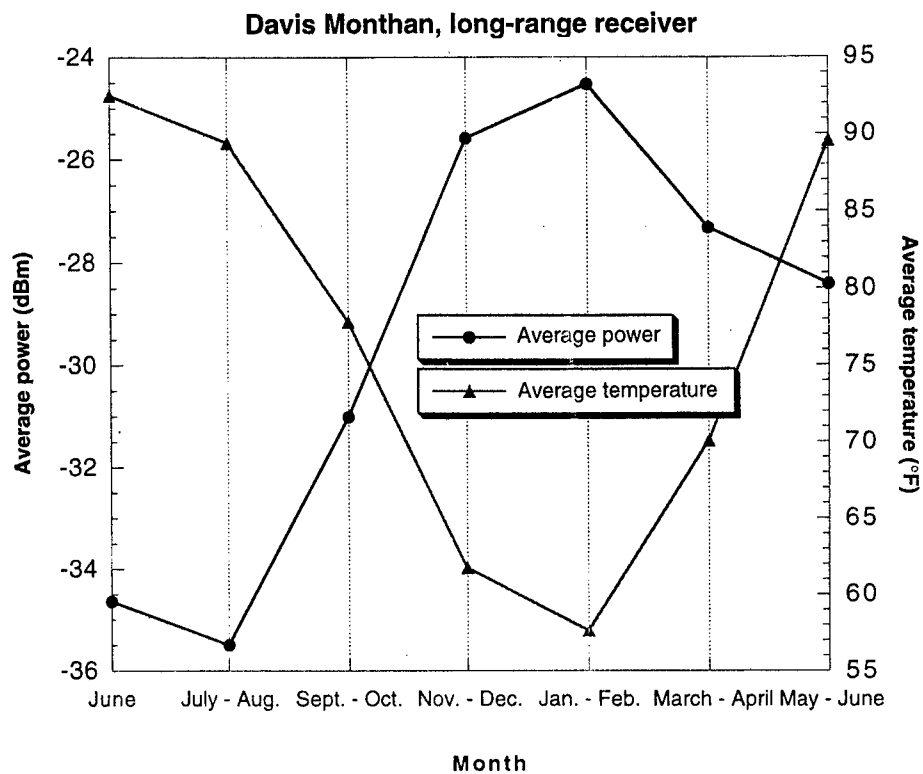


Figure 3.33
Bimonthly average temperature and power.

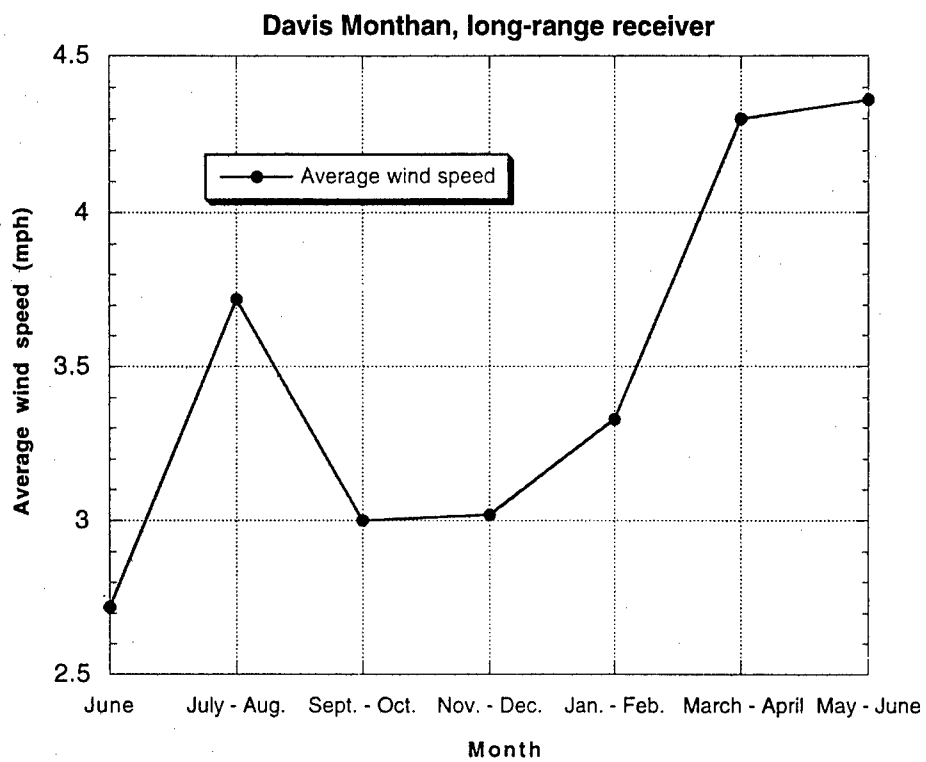


Figure 3.34
Bimonthly average wind speed.

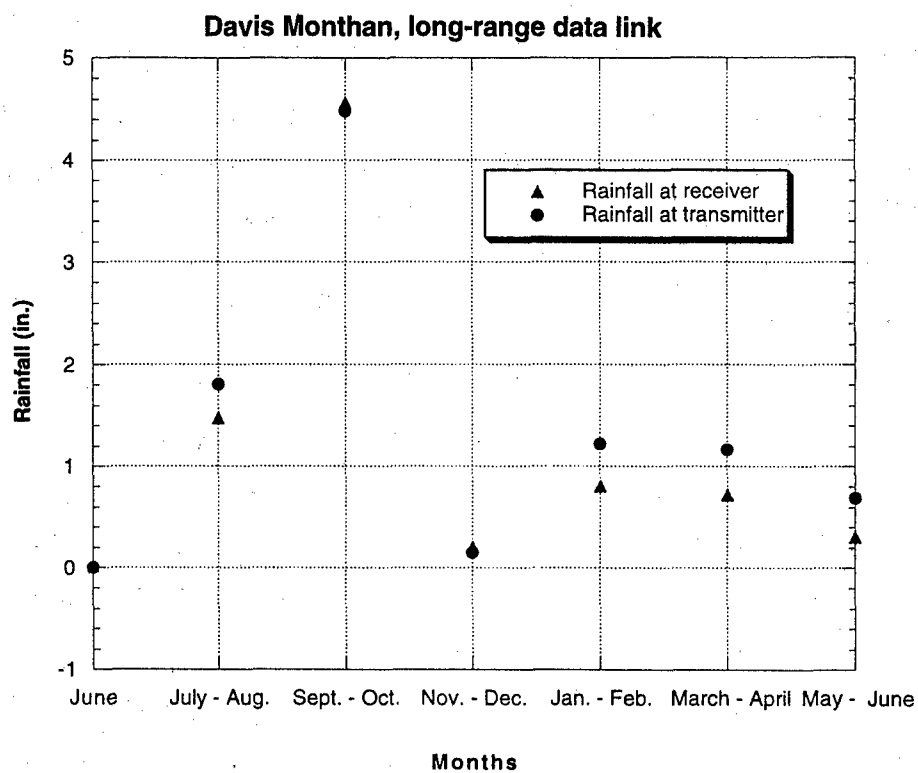


Figure 3.35
Bimonthly cumulative rainfall at the transmitter and receiver.

interval at the transmitter and the receiver. There did not appear to be a strong correlation between the cumulative rainfall amounts and the average signal levels. Representative averages from each month of average bit error rate and percent error-free seconds are shown in Fig. 3.36. These data showed that, except for September, the average percentage of error-free seconds was greater than 99% for the entire test period.

Table 3.10 shows a summary of the link characteristics for this test. The summary bit error rate statistics are shown in Table 3.11. Several important features are apparent from these data. First, the excess signal loss was quite high and was 21 dB in the summer months. The fact that the received signal is corrupted by multipath and diffracted components makes this transmission path sensitive to small variations in the atmospheric properties.

Knowledge of the relationship between seasonal dependence and the high excess path loss is very important from a deployment and system design standpoint. Data links for these low elevation paths should be designed with as large a system gain as possible. The exact signal reduction for any given site may be difficult to predict. However, it is also significant that the data link functioned reliably for more than a year, with an average BER of about $5e-4$ at 1.5 Mbps even over this difficult propagation path.

The change in the behavior of the propagation path can be seen in the histograms of the received signal power. Figure 3.37 shows the histogram of the cumulative data collected (vertical polarization). Note the large spikes evident in the cumulative histogram. The July and August 1996 histogram is shown in Fig. 3.38. The general shape of the July/August histogram is considerably smoother than that of the cumulative. However, the November and December 1996 data in Fig. 3.39 showed a substantially different shape, with less standard deviation and a higher mean. The March and April 1997 histogram, Fig. 3.40, shows a very non-Gaussian appearance, with a higher standard deviation than for the winter months. Furthermore, there is a substantial "tail" to the distribution

Table 3.10
Davis Monthan data link characteristics.

Transmit Power	17 dBm
Transmitter Antenna Gain	34.6 dB
Receiver Antenna Gain	35.4 dB
Mixer Loss	-12 dB
Front-End LNA Gain	27 dB
IF Amplifier Gain	26 dB
Frequency / Wavelength	27.3 GHz / 0.011 m
Range	9.6 km
Free Space Spreading Loss	-141 dB
Receiver Noise Figure	3.5 dB
Data Rate	1.5 Mbps
Average Signal Level August / February	-34 dBm / -23 dBm
Calculated Signal Level	-13 dBm
Average Excess Signal Loss August / February	21 dB / 10 dB
Climate Classification	E (Desert)
Path Length Reduction Factor	0.6983

Table 3.11
Summary of Davis Monthan AFB tests.

Total Test Time	9017 h
Percentage of Good Data Acquisition Time	94.53%
Average BER	5.4e-4
Average Percent Error-Free Time	99.7%

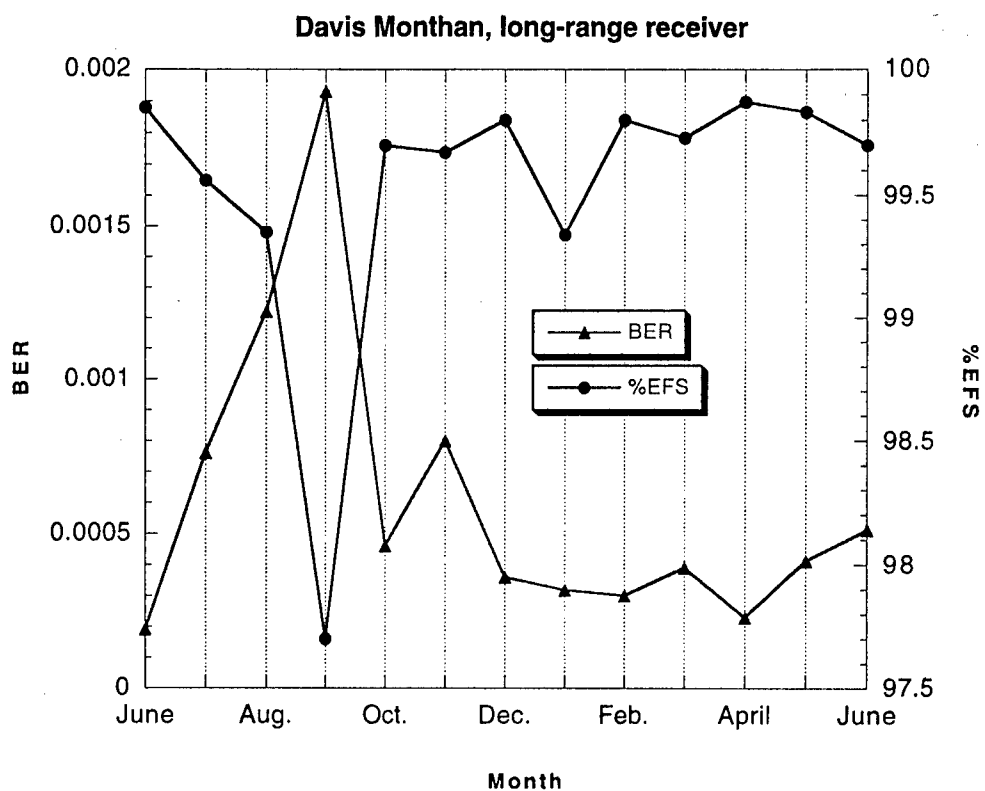
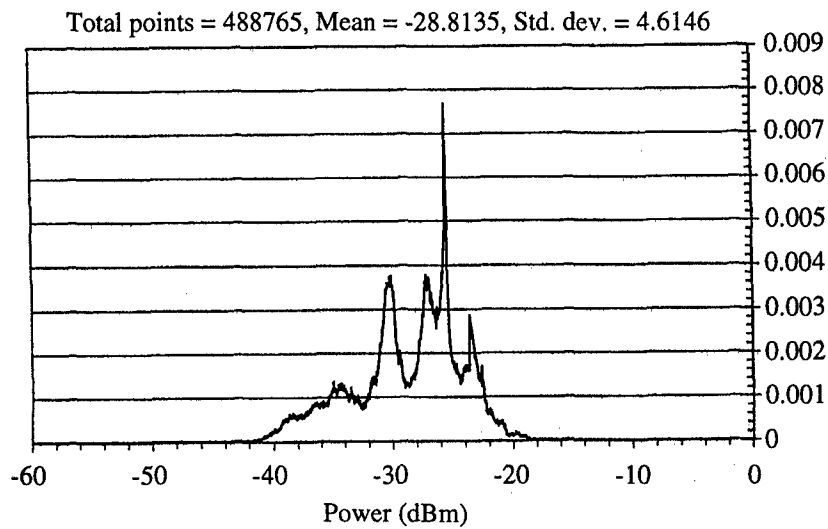
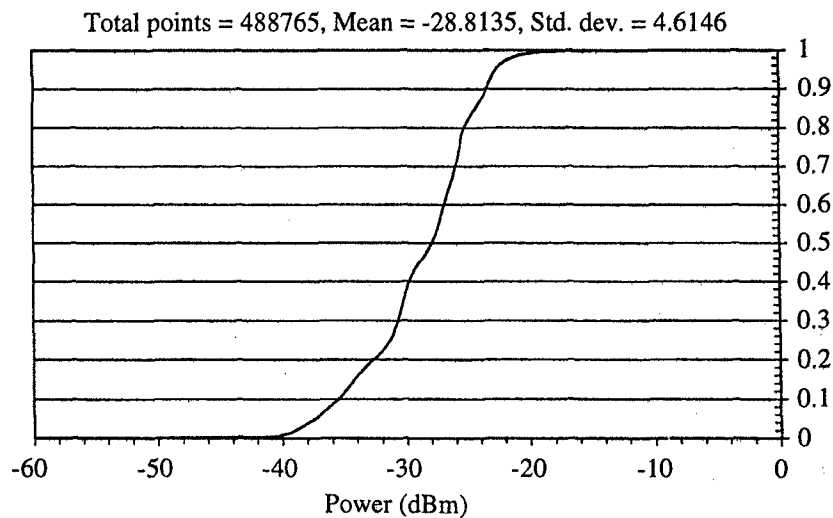


Figure 3.36
Representative averages of bit error rate (BER) and percent error-free
seconds (% EFS).



(a) Davis Monthan, long-range receiver
received power histogram
June 1996 through June 1997



(b) Davis Monthan, long-range receiver
received power cumulative distribution
June 1996 through June 1997

Figure 3.37
Histogram of signal strength data from June 1996 through June 1997.

Davis Monthan, long-range receiver
received power histogram, July and August 1996

Total points = 72368, Mean = -35.4952, Std. dev. = 2.8457

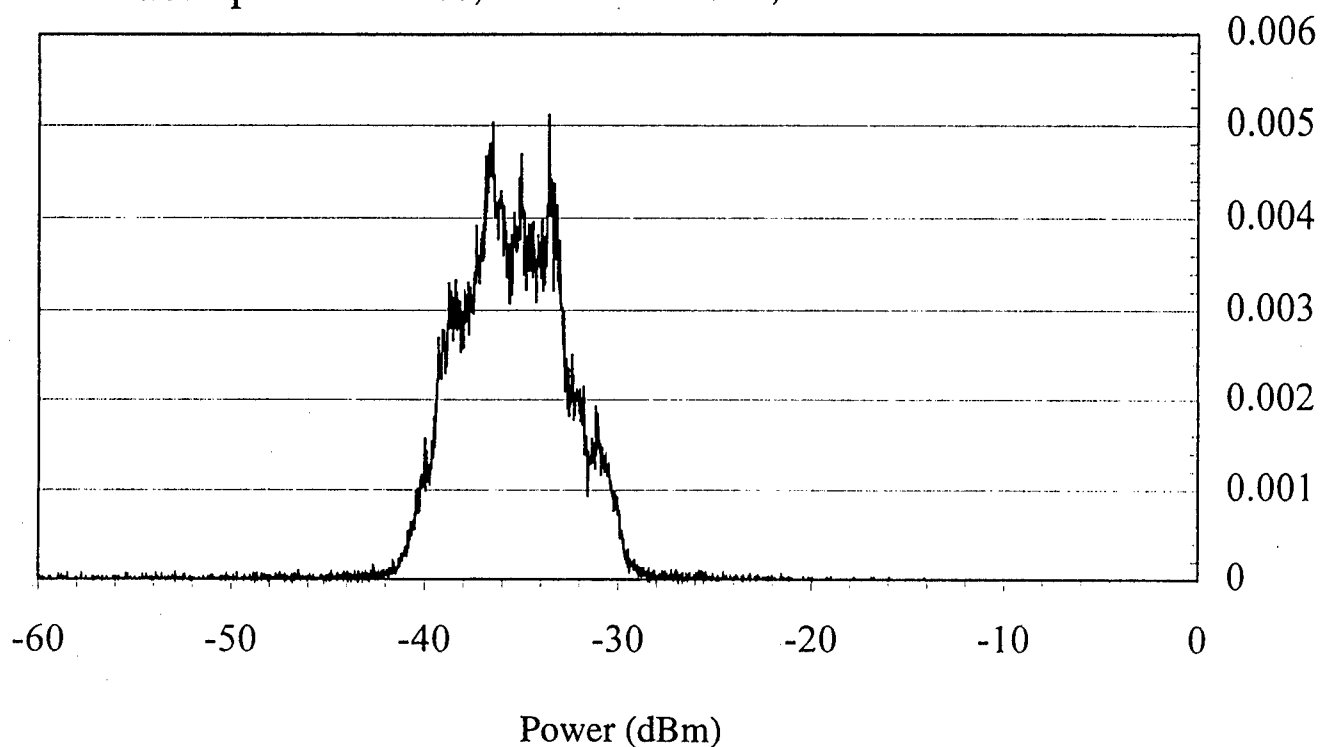


Figure 3.38

Histogram of signal strength data for July and August 1996.

Davis Monthan, long-range receiver
received power histogram, November and December 1996

Total points = 71993, Mean = -25.5869, Std. dev. = 2.1374

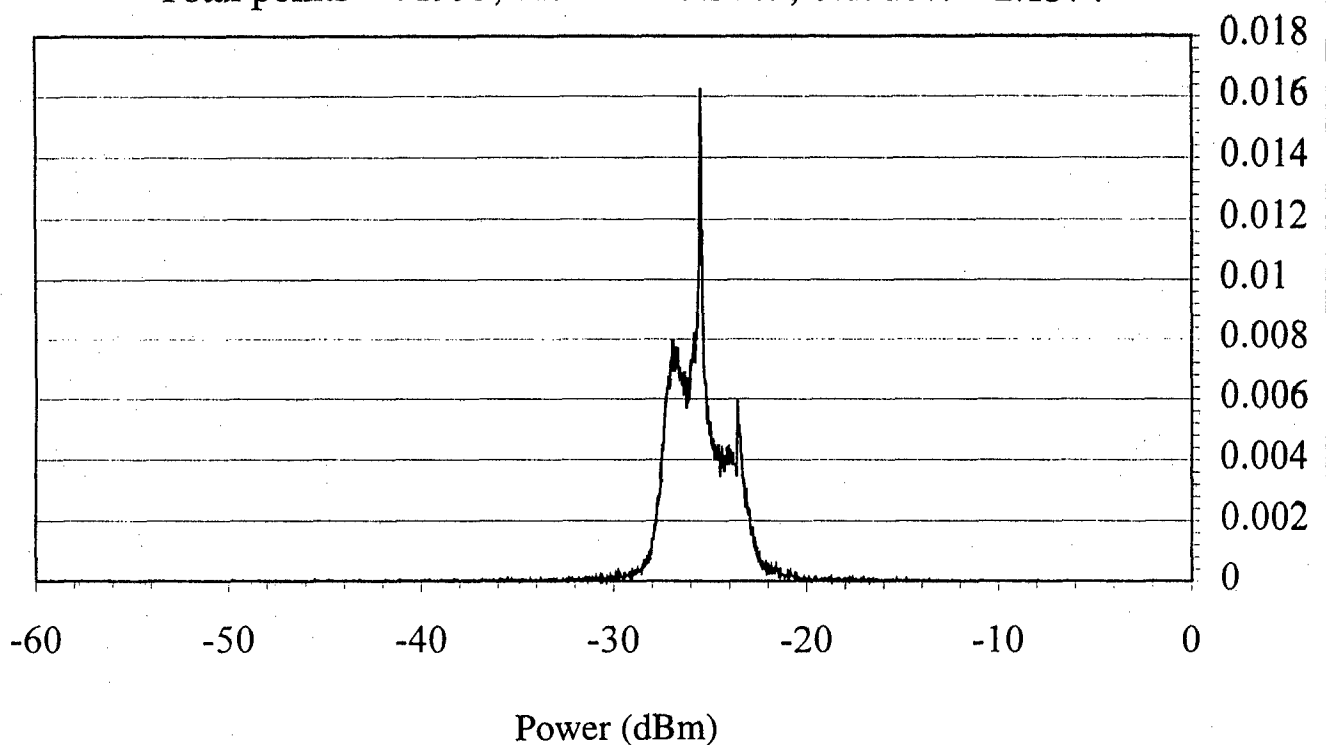


Figure 3.39

Histogram of signal strength data for November and December 1996.

Davis Monthan, long-range receiver
received power histogram, March and April 1997

Total points = 77648, Mean = -27.3294, Std. dev. = 3.5030

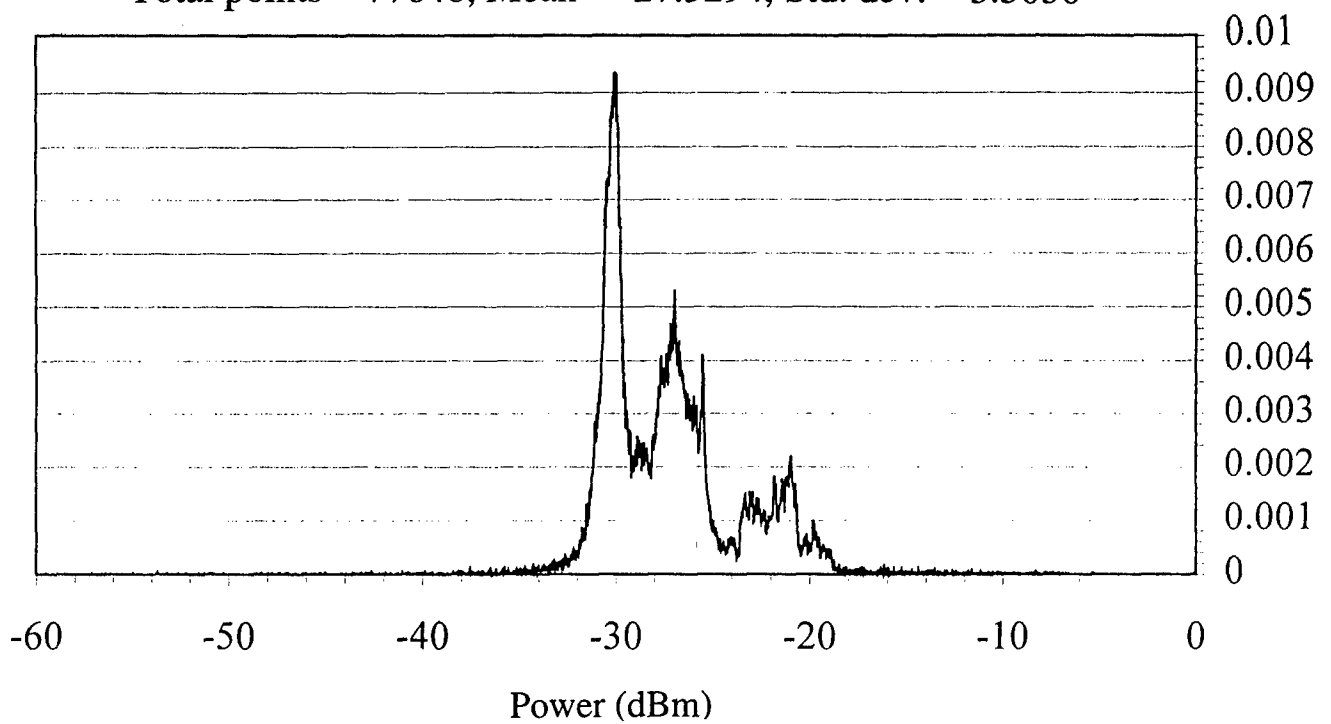


Figure 3.40

Histogram of signal strength data for March and April 1997.

that is 6–8 dB above the mean. It is not clear what caused these seasonal changes.

To better understand in detail the average features of the data link previously discussed, Table 3.12 shows selected statistics for three example data sets from 14–21 August (summer), 26 September–3 October (early fall), and a data set from 20–27 February (winter). There are three categories of statistics in this table: (1) the digital data and error rate statistics generated by the test set; (2) the signal strength statistics from the output of the receiver; and (3) the weather statistics from the weather station.

Table 3.12
Statistics from the three data sets shown,
transmitted bit pattern: QRSS, 1024 bits/block.

Data Set	Summer 62271158	Fall 62701448	Winter 70512036
Average Bit Error Rate	982.9e-6	464.7e-6	184.8e-6
Average Percent Error-Free Seconds	99.37	99.77	99.86
Average Block Count	91.7e3	91.82e3	92e3
Average Signal Level	-34.098 dBm	-28.86 dBm	-22.6 dBm
Peak Signal Level	-22.0 dBm	-13.1 dBm	-13.0 dBm
Average Temperature	87.96°F	81.97°F	55.58°F
Average Wind Speed	3.4 mph	2.6 mph	4.2 mph

The average bit error rate was computed by averaging the bit error rates measured from the received test data for each interval (read at approximately one per minute). The block count is the number of blocks that were received and decoded by the receiving test set, approximately 92,000 blocks per interval. Errors in the received signal will generally tend to reduce this number. The average percentage of error-free seconds was the percent error-free seconds measured in each interval, averaged over one data set. Note that in all the data sets considered, the percentage of error-free seconds exceeded 99%.

3.4.2 Summer Data Set 62271158

Figures 3.41 and 3.42 show a data set collected from 14–21 August. Summer data showed the effects of high temperature during the day and the monsoon rains that occurred during late July and August 1996. The average signal level measured from the data set was -34.1 dBm. The data starting on 14 August showed the effects of the afternoon storms. Early in the data set, a heavy rainstorm occurred that produced multiple fades. During this event, 0.17 in. of rainfall were recorded at the transmitter, and 0.16 in. at the receiver. The rain cells were separated so that signal loss was sporadic and short-lived. Between the rain cells, the signal strength was sufficient for the receiver to reacquire the signal and continue operation. This is important with respect to transmission of alarm and video data because the fades occurred in very short and unpredictable intervals. Therefore, it would be unwise for an intruder to assume that the system would not be operating properly in a heavy rainstorm simply because of the dropout in the communication link. The statistics in Table 3.12 for the summer data set showed that the link was still performing with 99.37% error-free seconds and a bit error rate of less than $1e-3$ averaged over the data set. The longest period of time that the receiver could not acquire the signal was 10 min. There were 14 intervals 1 min long where the receiver was unlocked for more than half of the interval. The total data set is 9001 intervals, or slightly longer than 1 week. The diurnal signal fluctuations appeared to be about

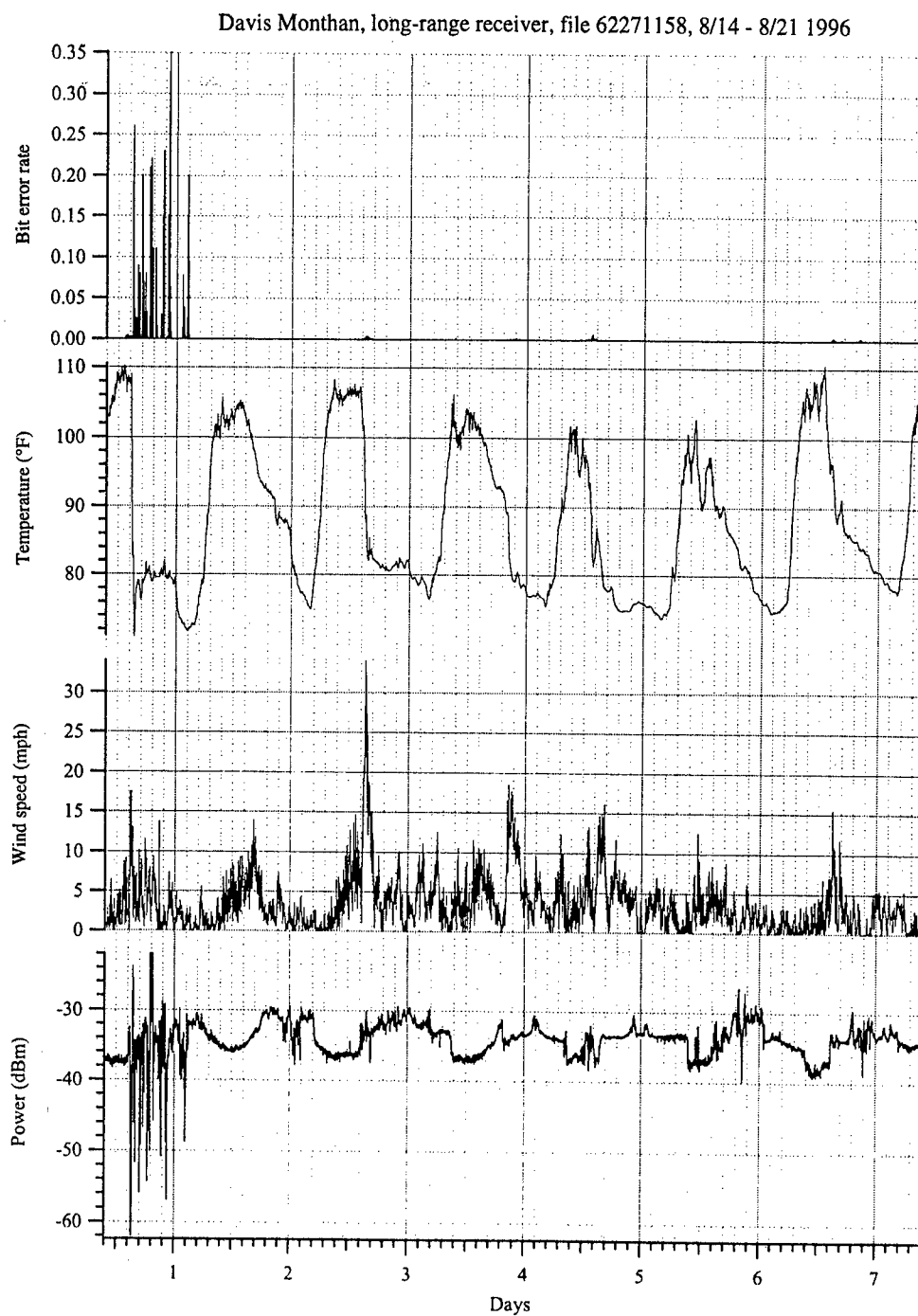


Figure 3.41
Vertical polarization time series data from 62271158: bit error rate,
temperature at the receiver, wind speed, and measured signal strength.

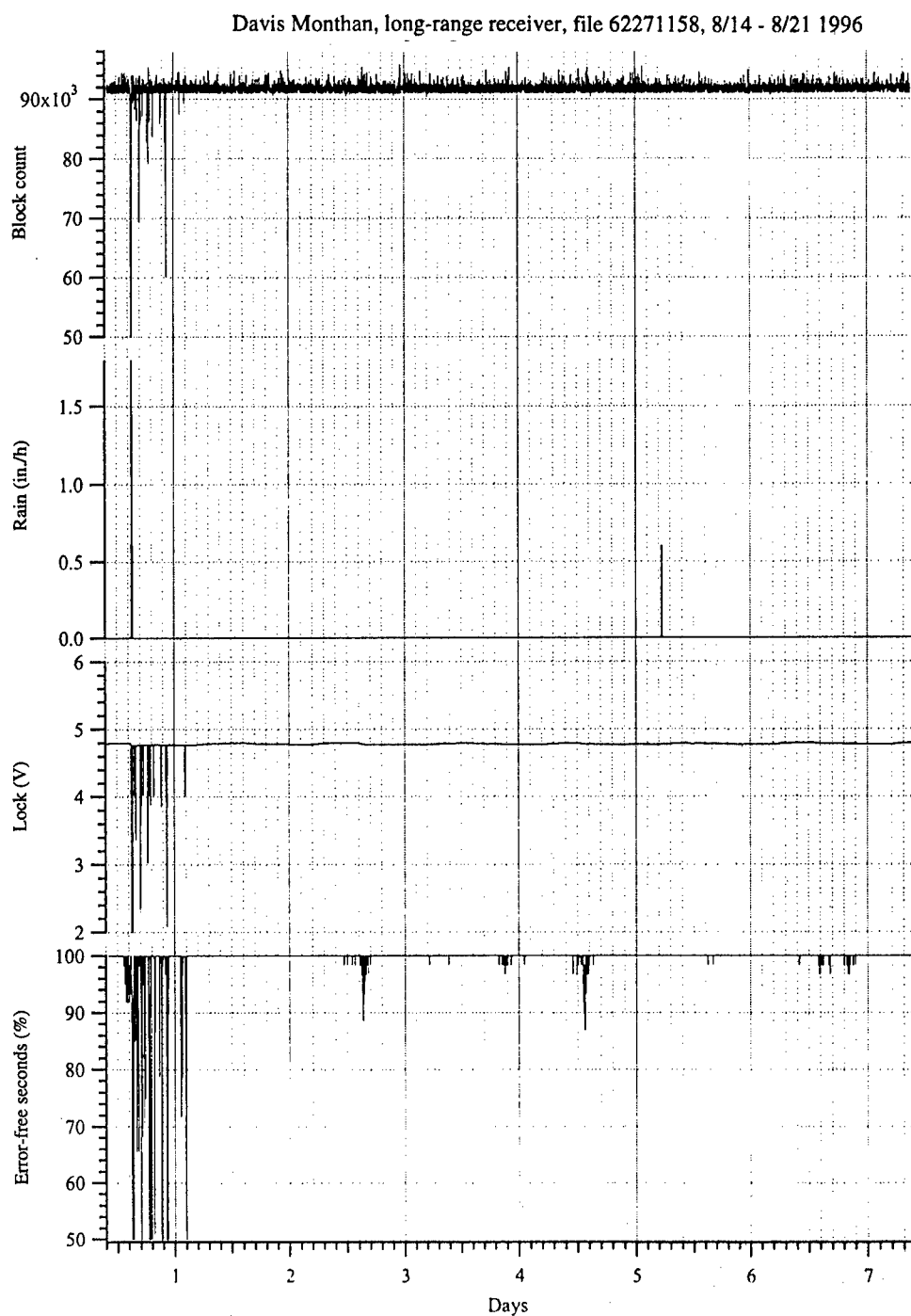


Figure 3.42
Vertical polarization time series data from 62271158: block count, rainfall rate, sweep/lock indicator, and percent error-free seconds of transmission.

5–6 dB when there were no storms present. The peak value measured was during a signal enhancement event.

The rapid temperature drop shortly after noon strongly indicated the occurrence of a storm. During days with no storms, the temperature drop was gradual. There were two more storm events during this data set that did not affect the data link, and rainfall was recorded at both the transmitter and receiver during these events. Neither event caused significant fades.

3.4.3 Fall Data Set 62701448

The weather patterns, and thus the behavior of the data link, were different during the transition months. Figures 3.43 and 3.44 show a data set for 26 September–3 October 1996, which indicates how the system behaved during the transition from summer to fall. This data set showed that the boundary effects due to the low elevation of propagation through the atmosphere caused very significant signal fluctuations, even during calm weather conditions. Fortunately, the signal loss resulting from these fluctuations was small, i.e., the amount of time that dropouts occurred was relatively small. This data set is summarized in the second column of Table 3.12.

The temperature data at the receiver clearly shows that the diurnal temperature patterns were strongly evident. No storm events or fronts are evident in this data. This data set also shows diurnal shifts in the wind direction. Daily the wind shifted from the south at night to the northwest during daytime with a corresponding change in wind speed. The wind speeds were stronger during the day than at night. Significant signal enhancement events occurred at days 1.0, 2.0, 3.0, 4.0, 5.0, and 6.0. These events corresponded to the shift in wind direction and to periods when the wind speeds were low. The shift in wind direction that occurred during the daylight hours did not produce the same large swings in signal amplitude. However, during the day, the upwelling thermal drafts probably provided a mixing of the atmosphere boundary layers through

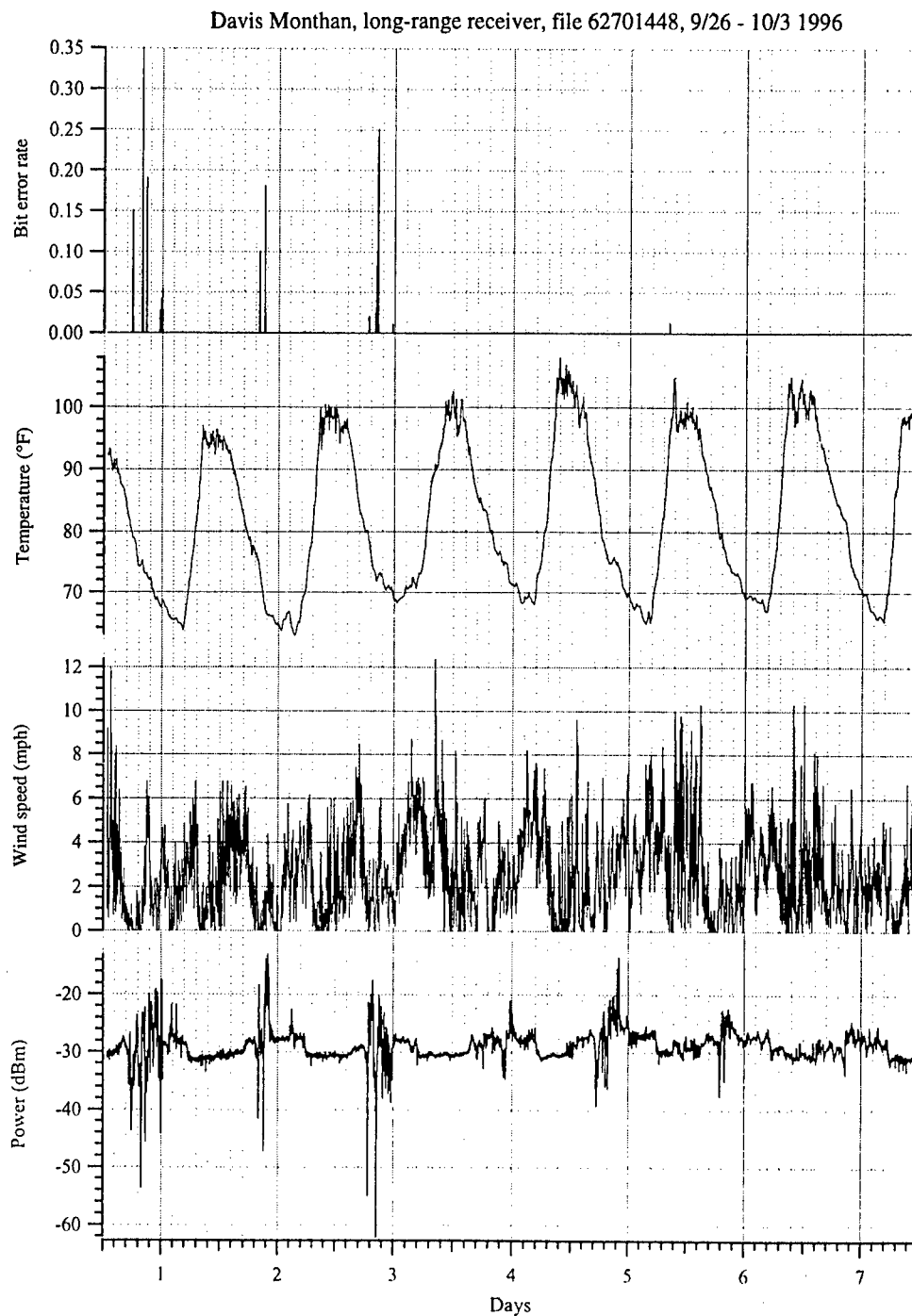


Figure 3.43

Vertical polarization time series data from 62701448: bit error rate, temperature at the receiver, wind speed, and measured signal strength.

Davis Monthan, long-range receiver, file 62701448, 9/26 - 10/3 1996

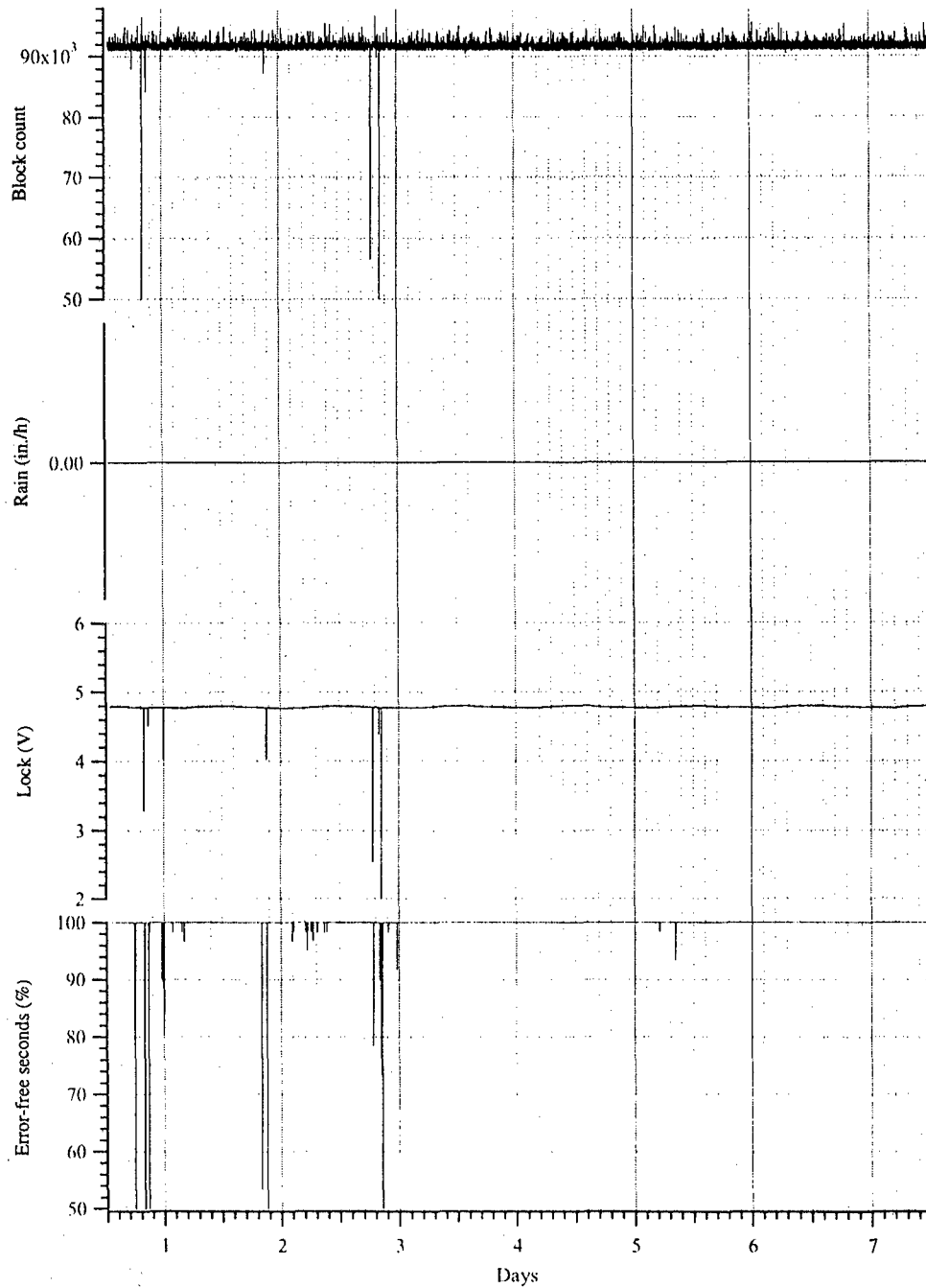


Figure 3.44

Vertical polarization time series data from 62701448: block count, rainfall rate, sweep/lock indicator, and percent error-free seconds of transmission.

which the path passed, so that no large vertical atmospheric structures occurred in the atmosphere that could cause substantial refraction of the transmitted signal.

At midnight, however, there were no thermal updrafts to mix the atmosphere, so that significant stratification could exist near the ground. The events that had high values of short-term standard deviations showed more bit errors than the events which had low values. This was probably because the bit errors were caused by the rapidity of the signal change as opposed to a simple fade. The AGC compensation of the phase-locked loop demodulator did not respond quickly enough during one of these events to prevent errors in the demodulation of the data. Curiously, no signal enhancement event occurred at 7.0 days.

Although these events occurred nearly every night during this data sequence, the average percentage of error-free seconds was 99.8%, with 8927 error-free 1-min intervals out of 9001 intervals tested. Furthermore, there were only 4 min during this data set where the receiver actually lost lock on the transmitted signal for more than 30 s at a time. Therefore, the quality of signal was quite high for most of this period.

The standard deviation of the signal strength was computed over 1-h intervals, and plotted against average temperature and wind speed in Figs. 3.45 and 3.46. There were many episodes of high standard deviation at wind speeds below 4 mph, and no episodes of standard deviations greater than 2 dB for wind speeds greater than 5 mph. Similarly, the episodes of time with high standard deviations occurred at lower temperatures. This is understandable because wind and temperature were linked together in the diurnal cycling in this data set.

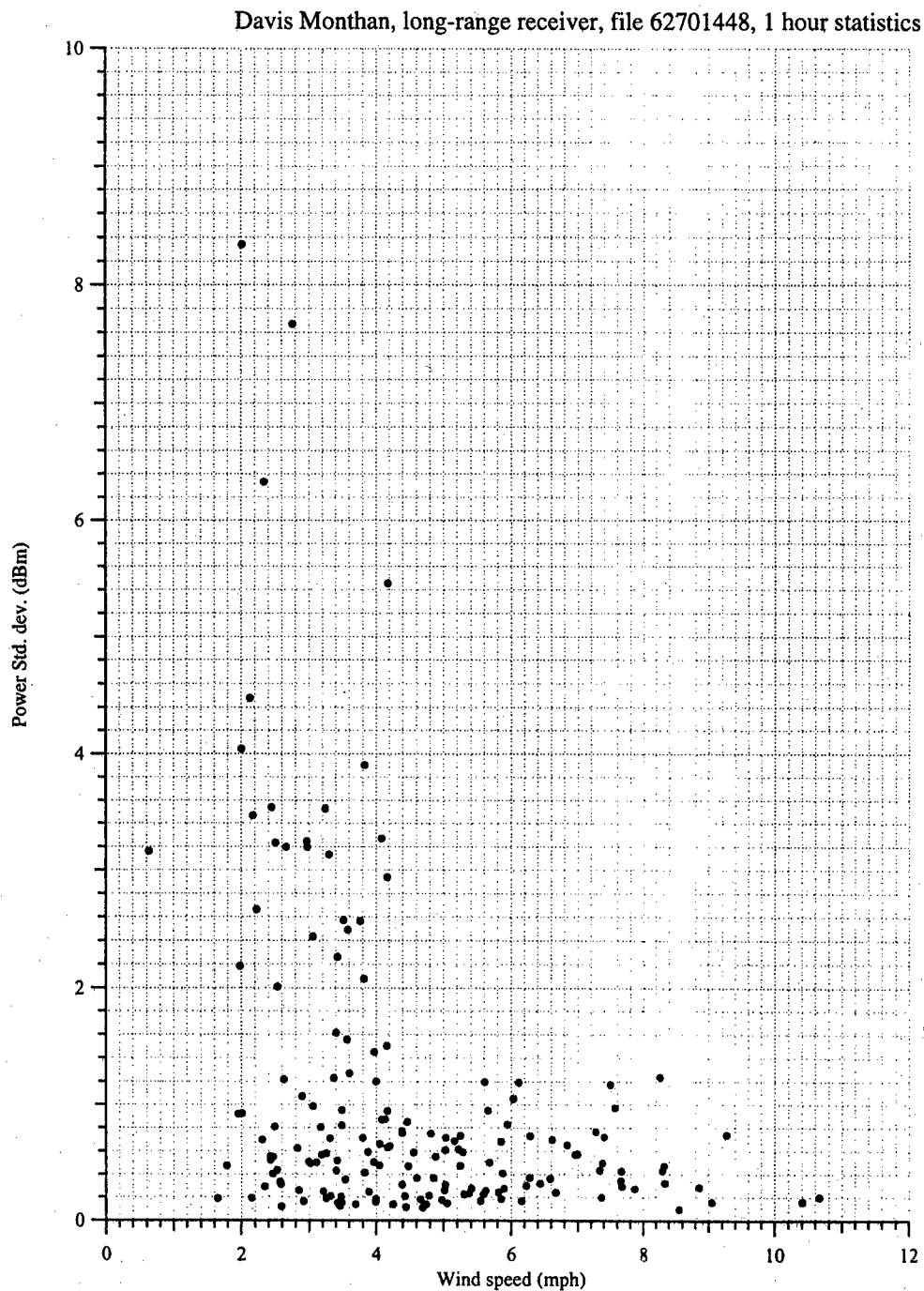


Figure 3.45

Scatter plot of signal power standard deviation versus average temperature for data set 62701448. Statistics calculated over 53 time series data points.

Davis Monthan, long-range receiver, file 62701448, 1 hour statistics

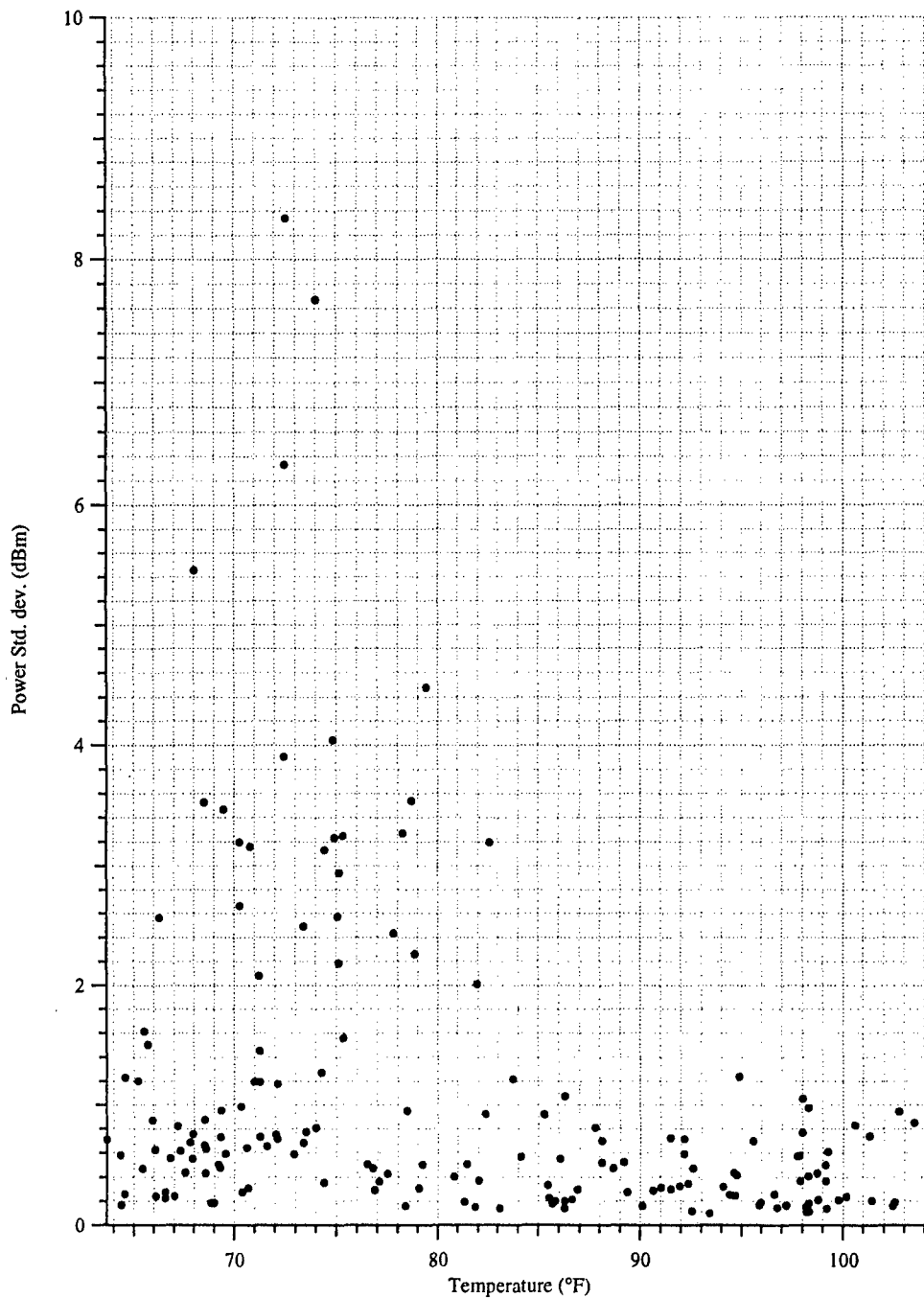


Figure 3.46

Scatter plot of signal power standard deviation versus average wind speed for data set 62701448. Statistics calculated over 53 time series data points.

3.4.4 Winter Data Set 70512036

Figures 3.47 and 3.48 show time series data for a data set 70512036. The time period of this data set is from 20–27 February 1997. The data link performed with an average bit error rate of $1.85e-4$. The average signal level measured at the receiver was -22.58 dBm. This is 11 dB higher than the average signal level measured in the August data set. There were a few dropout events which were very short-lived, with only two events causing the receiver to lose lock on the signal. There were three periods of signal enhancement observed at approximately 2.25 days, 2.8 days, and 6.5 days. The diurnal temperature fluctuations were strongly evident on the temperature and humidity data. The winds usually increased during the evening hours. There was also an apparent diurnal shift in the direction of the wind, with the winds out of the south during the night, shifting to the north during the daytime hours. The signal enhancement events seemed to occur immediately following a period of high wind. The event at 2.25 days brought the level up only about 5 dB above the average. The peak lasted for nearly 6 h. The event at 2.8 days had a much higher peak, 9 dB above the average signal level.

The actual enhancement occurred typically when the wind was below 10 mph, but did not always occur. For example, the low wind period at 6.5 days did not have any enhancement events. Further examination of the data, and perhaps further investigation, will be needed to fully understand these enhancement events.

A scatter plot of the standard deviation of the received signal power and the average wind speed measured at the transmitter calculated over 1-h intervals is shown in Fig. 3.49. This plot shows the highest level of signal standard deviation occurring at wind speeds below 5 mph. A similar scatter plot of standard deviation versus temperature measured at the transmitter is shown in Fig. 3.50. Although the relationship was not as strong, the highest average signal fluctuations occurred in the lower half of the spread of temperatures.

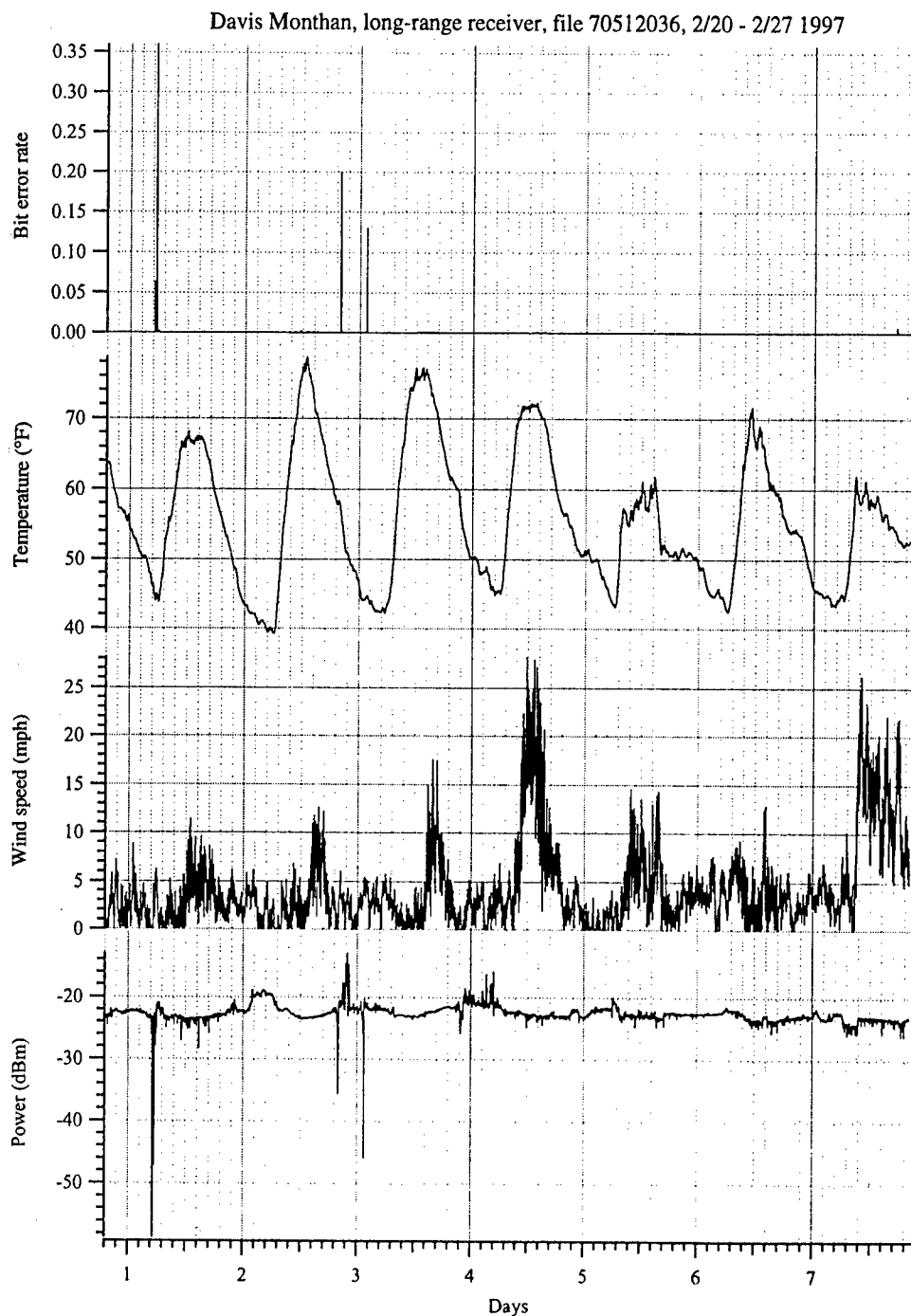


Figure 3.47

Vertical polarization time series data from 70512036: bit error rate, temperature at the receiver, wind speed, and measured signal strength.

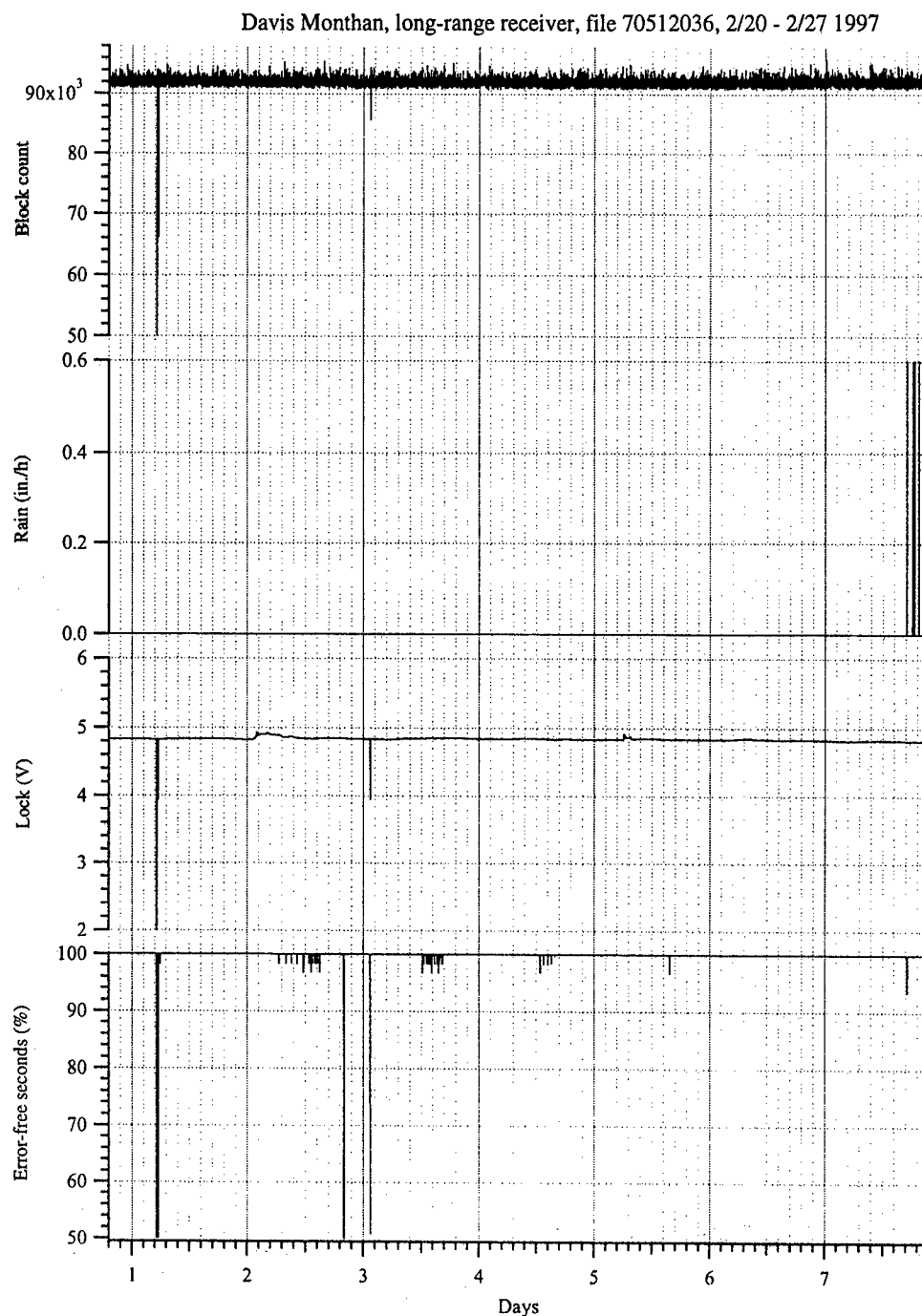


Figure 3.48
Vertical polarization time series data from 70512036: block count, rainfall rate, sweep/lock indicator, and percent error-free seconds of transmission.

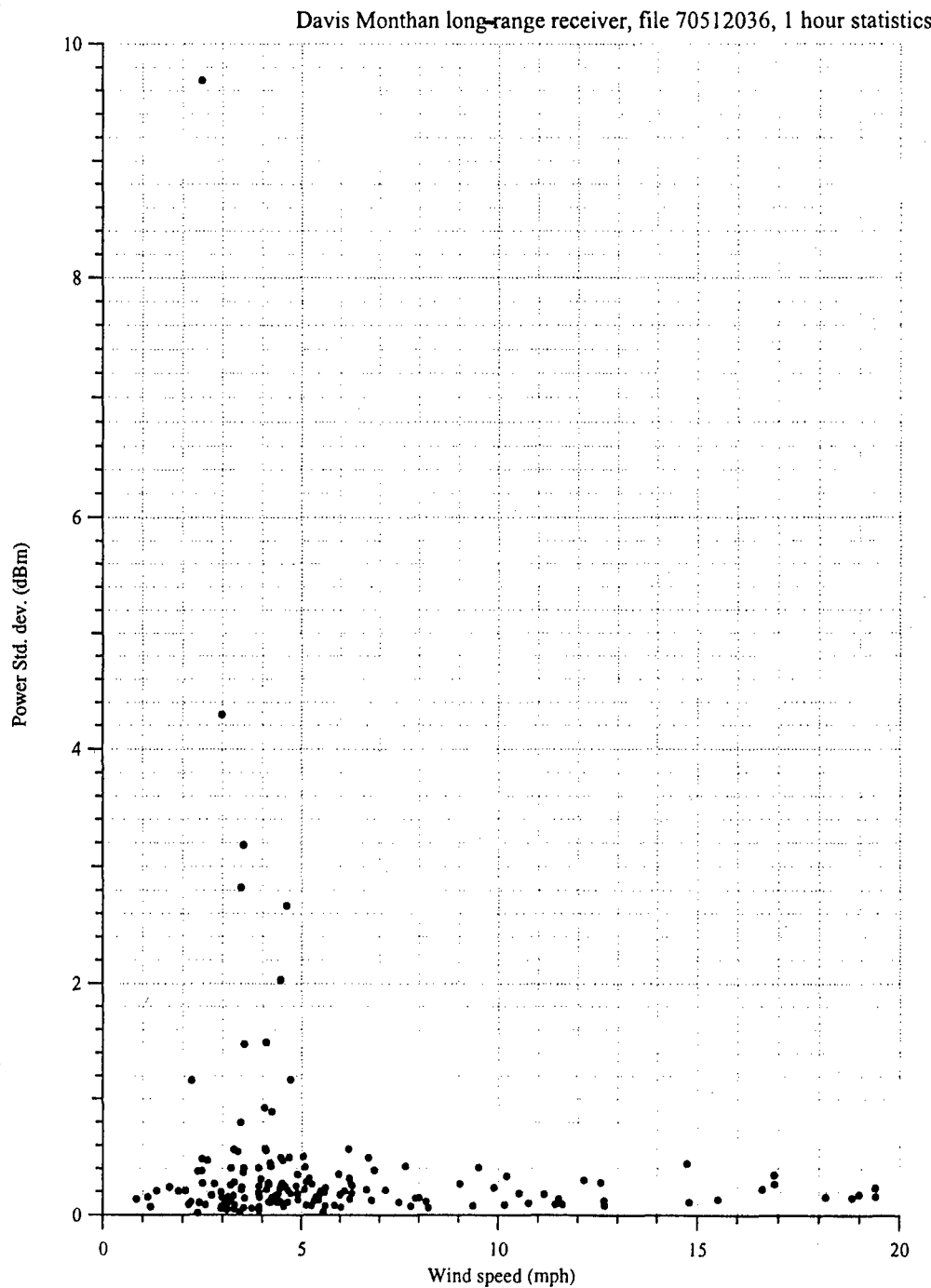


Figure 3.49

Scatter plot of signal power standard deviation versus average wind speed for data set 70512036. Statistics calculated over 53 time series data points.

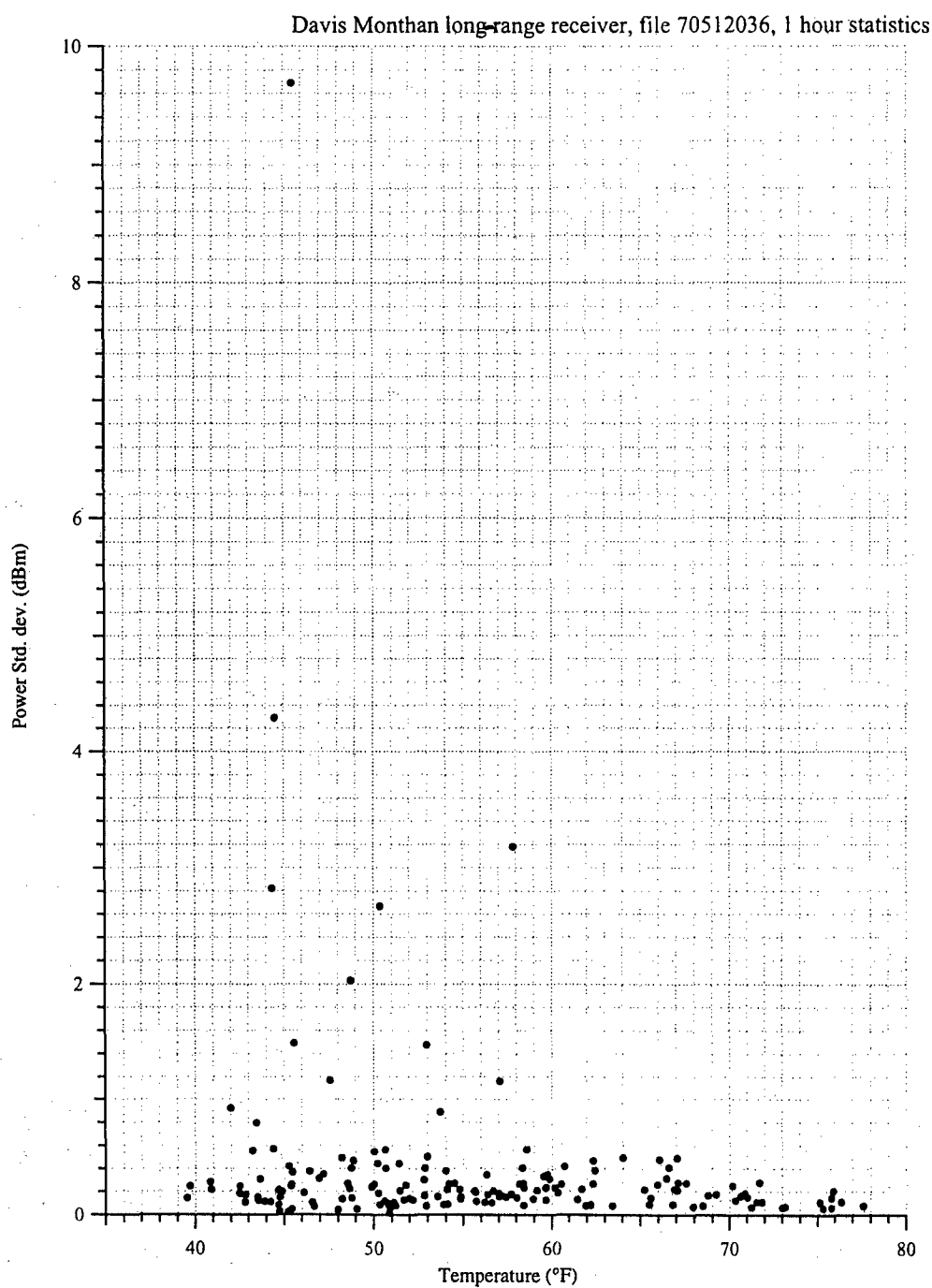


Figure 3.50
Scatter plot of signal power standard deviation versus average temperature
for data set 70512036. Statistics calculated over 53 time series data points.

3.5 NONPRECIPITATION-INDUCED SIGNAL FLUCTUATIONS

A possible explanation for the enhancement events observed that do not appear to be related to precipitation is as follows: the total path length from the transmitter to the receiver was approximately 10^6 wavelengths. Forward scattering from the objects on the ground provided multiple arrivals at the receiver. The relative phases of the multiple arrivals depended on the average index of refraction of the paths traversed. The index of atmospheric refraction changes of 1 part in 10^6 could cause phase shifts of the order of 2π radians of the scattered components at the receiver. Changes in average atmospheric temperature of the order of about 1°C could cause changes in the atmosphere of this magnitude.

This means that slight but stable horizontal variations in atmospheric temperature could have caused major phase shifts of the arriving components. This could have resulted in large signal fluctuations, since the scattered signals comprised a major portion of the arriving energy. This was evident in the data when very calm conditions occurred. It is important to understand this effect when selecting sites and trying to determine the potential reliability of a given deployed link.

At present, there is not an adequate hypothesis for the diurnal fluctuations in signal level that were evident, especially in the Davis Monthan data collected during the summer. One speculation is that signal loss could be caused by the scintillation induced by thermal updrafts occurring during daylight hours. These thermal updrafts are driven by the heating of the ground. More detailed measurements of ground temperature in conjunction with more accurate signal measurements would help identify the cause. The seasonal variations in signal level also observed at Davis Monthan AFB may have a similar origin. Further efforts to develop models for these effects are needed if detailed quantitative predictions are to be obtained.

4.0 SHORT-RANGE TESTS

4.1 EGLIN, SHORT-RANGE C-3 TEST

The ability of a 60-GHz data link to transmit data securely and its immunity to interfering signals are enhanced by atmospheric absorption. At the same time, absorption limits the applicability of the link to short transmission paths of approximately 1 km or less. However, it is possible to set up a short-range wireless network with virtually no probability of unwanted detection or interference from other systems. This is advantageous if wireless video transmission of sensitive data is desired, or if covertness is a critical factor in the system. Another advantage of 60-GHz systems is antenna size. The dimensions of high gain antennas at 60 GHz are very small. The system tested at Eglin used standard gain pyramidal horns that were approximately 2 in. by 1.5 in. in aperture size and that provided 24 dB of gain and a beamwidth of about 9° . The system at Davis Monthan had 3 in. diameter dielectric lens conical horns that each had approximately 33 dB of gain and a beamwidth of approximately 2° .

Because of hardware problems with the short-range data links and difficulties with the data acquisition computers (not related to the data link problems), only a limited amount of data were available to compute reliability. Furthermore, one objective of these tests was to determine if free-running Gunn diodes were adequately stable for the receivers to operate and track the transmitted signal. Because of the frequency and power drift of the free-running Gunn diode, the signal strength had some dependence on the ambient temperature. The relative drift between the local oscillator of the receiver and the transmitter was 50–100 MHz. The histograms of signal strength were slightly less useful from these tests than from the long-range link tests. However, it was determined that free-running Gunn diodes were suitable in a wide range of the environments and could be used for low-cost data links. Wider channel spacing would be required if multiple channels were used than if more stable frequency sources were used. It might be necessary to have only a few channels due to

the highly directional nature of the signal and the atmospheric absorption, even if a large number of data links were operating in close proximity.

Table 4.1 gives the link characteristics of the Eglin short-range data link. The link margins were much smaller on the Eglin short-range link than on the long-range links. The link margin was only approximately 15 dB, which was insufficient to overcome substantial fades. This was due mainly to limitations in available hardware. At the time the links were built and the tests were conducted, V-band DROs and low noise amplifiers were not readily available. Currently, a number of efforts are underway to develop these components for wireless local area networks, as well as high speed digital modulation and demodulation circuits for fiber-optic data transmission. Therefore, the difficulties experienced due to hardware limitations in these tests may not be as significant an issue in future systems. The link margin was later increased to acceptable levels during the Davis Monthan short-range link by using higher gain antennas.

4.1.1 Description of Data Set 52010850

The data set shown in Figs. 4.1 and 4.2 ran for over 10 days and provided an accurate sample of the performance of the data link as well as the problems associated with the data collection. The transmitter test set that generated the bit patterns was damaged by lightning at about 7.5 days into the data set. This was shown by the abrupt dropout of the block count in Fig. 4.2. The data statistics recorded in Table 4.2 reflect averages taken from the portion of the data set recorded when the test set was working. The rainfall rates recorded were quite high during these events. The longest time period that the receiver was unlocked was 20 min. The thunderstorms were clearly indicated by the peaks in wind speed, the rapid drops in temperature, and the rainfall and accompanying signal drops. The total rainfall recorded for this data set was 6.48 in., and the maximum estimated rainfall rate was about 5.5 in./h.

Table 4.1
Link characteristics of short-range link at Eglin AFB.

Transmit Power	17 dBm (Nominal)
Transmitter Antenna Gain	23 dB
Receiver Antenna Gain	23 dB
Mixer Loss	-8 dB
Atmospheric Loss	-13 dB
IF Amplifier Gain	39 dB
Frequency / Wavelength	60 GHz / 0.005 m
Range	0.84 km
Free Space Spreading Loss	-126 dB
Receiver Noise Figure / Noise Floor at 7-MHz Bandwidth	11 dB / -95 dBm
Data Rate	19.2 Kbps
Average Signal Level (Horizontal Pol.)	-45 dBm
Calculated Signal Level	-44 dBm
Average Excess Signal Loss	1 dB
Climate Classification	N (Tropical)
Path Length Reduction Factor	0.67

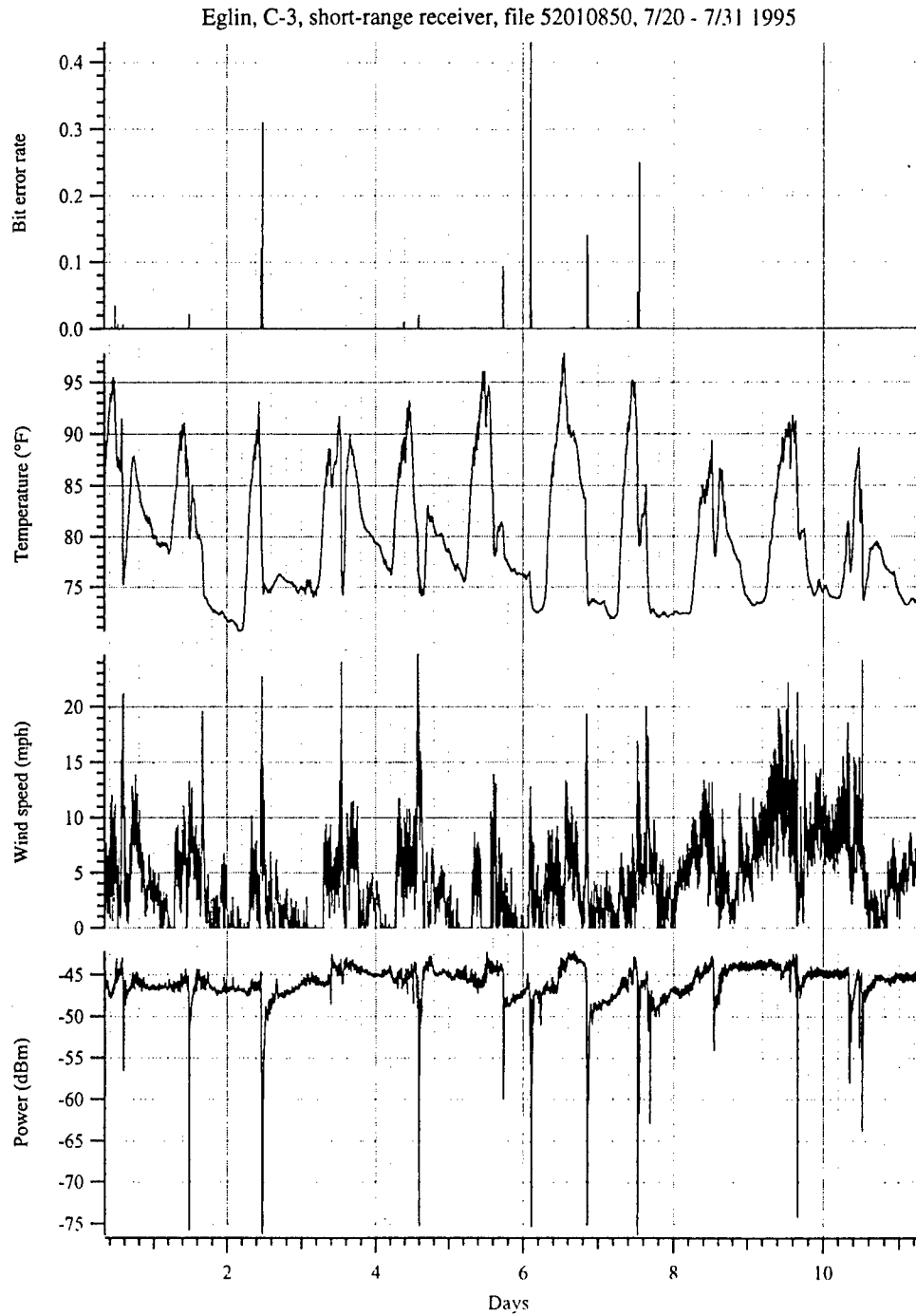


Figure 4.1
Horizontal polarization time series data from 52010850: bit error rate, temperature at the receiver, wind speed, and measured signal strength.

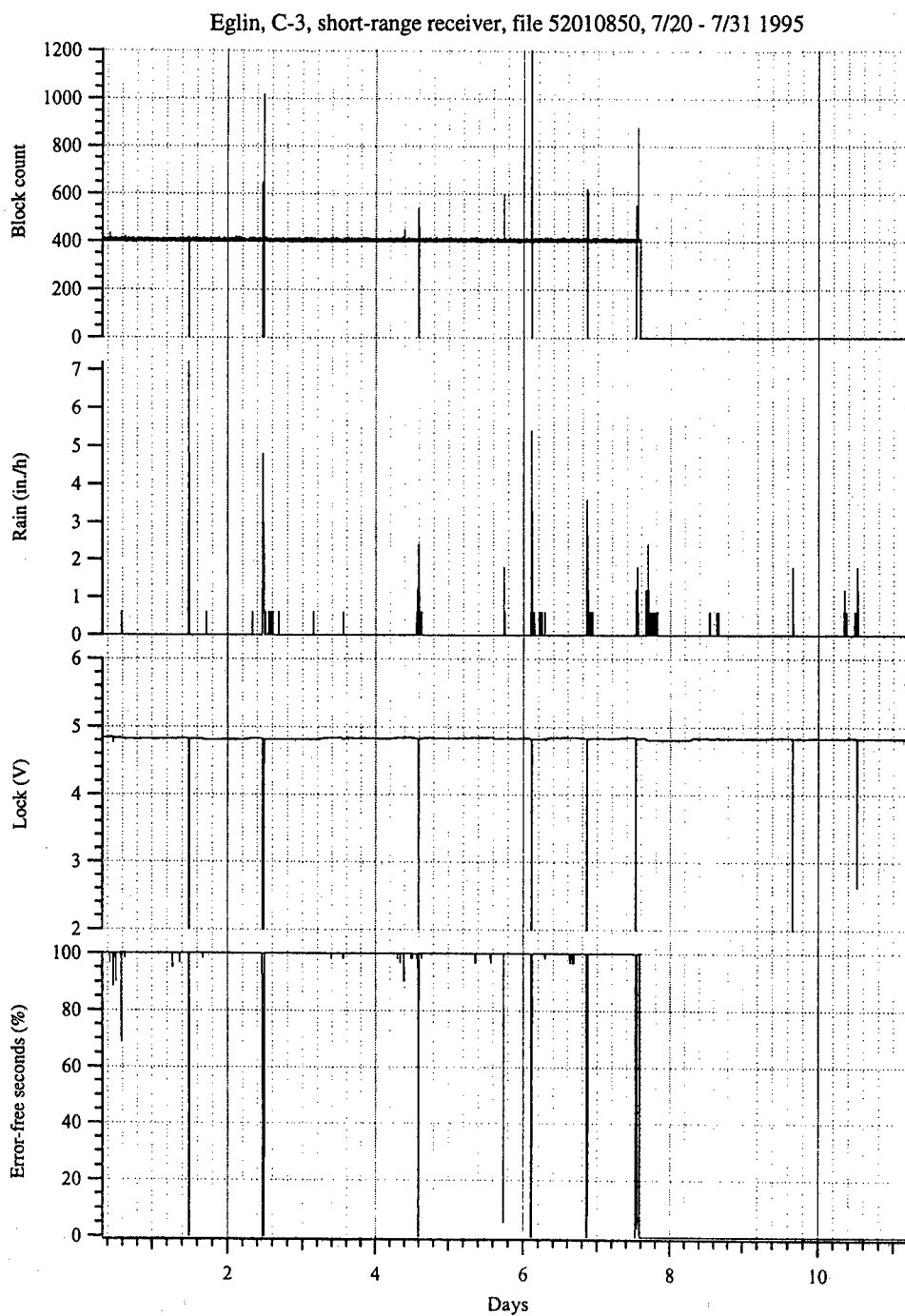


Figure 4.2
Horizontal polarization time series data from 52010850: block count,
rainfall rate, sweep/lock indicator, and percent error-free seconds of
transmission.

Table 4.2
Statistics from the two data sets shown,
transmitted bit pattern: 2047 bits/block.

Data Set	52010850	52120806
Average Bit Error Rate	2.4e-4	1.68e-3
Average Percent Error-Free Seconds	99.076	97.15
Average Signal Level	-46.04 dBm	-47.7 dBm
Peak Signal Level	-42.3 dBm	-43.05 dBm
Average Temperature	79.8°F	80.8°F
Average Wind Speed	4.3 mph	9.6 mph
Total Rainfall	6.48 in.	3.58 in.

Overall, the link performance appeared to be reliable and the RF components (i.e., transmitter and receiver) did not suffer damage due to lightning strikes. There appeared to be no outside RF source interference during this data collection or any other data set recorded at Eglin. The fade events were isolated, rapid, and usually short-lived.

4.1.2 Description of Data Set 52120806

Data set 52120806 was interesting because it provided data on how well the short-range link performed during a hurricane. The average statistics are shown in Table 4.2. The average percent error-free seconds was still over 97% for this data set, and the average bit error rate was less than $2e-3$. The loss of data between 1.4 and 1.5 days on the block count and the slightly lower percent error-free seconds recorded were not due to weather conditions. Rather, the receiver test set probably malfunctioned and then recovered. The signal strength and the sweep-lock indicators showed no evidence of signal interruption. The weather data indicated the typical hurricane signature of high wind, dropping

barometric pressure, and accompanying wind shift as the eye of Hurricane Erin passed near the C-3 test site. The data in Figs 4.3, 4.4, and 4.5 showed that the weather pattern was unusual. Diurnal cycling was evident on the outside temperature recorded for the first two days, but then disappeared at the end of the data set. Furthermore, the wind speed showed a peculiar shape during a long period of time when the wind remained constant, then peaked, and finally, gradually diminished. Also evident was a thunderstorm at 2.6 days that probably was an entrained storm on one of the spiral arms of the hurricane. The signal strength was reduced at the peak of the hurricane and the bit error rates were high. However, the rainfall indicators showed a steady rain rate, with a cumulative total for this data set of 3.58 in. The peak rainfall rates were estimated to be about 2.5 in./h.

The sweep-lock indicator showed that the maximum time of signal loss was only about 6 min, and that most of the fades and signal losses were of very short duration. This is helpful to know when transmitting alarm data because the fade is not a long duration event, so that the data can still be transmitted. Furthermore, multipath diversity could help in alleviating some of the data loss problems. The average bit error rate for these data is somewhat higher than that in other data sets, but the length and strength of this storm showed how well this system operated during a prolonged rain. The block count in Fig. 4.4 shows that there were a number of times when the block count was highly erroneous, but there was also a substantial period where the count was correct.

Finally, Fig. 4.5 shows the wind speed, direction, barometric pressure, and rainfall rate, clearly indicating the unique hurricane-like signature of this particular weather event. This is especially evident in the wind direction data, which showed a constant wind direction and then a clear shift in wind direction at the minimum barometric pressure. Curiously, intense thunderstorm rainfall frequently exceeded the rainfall rates recorded during this hurricane. The principal difference was the duration of the event. The effects of the hurricane lasted several days, while thunderstorms usually lasted a few minutes to an hour.

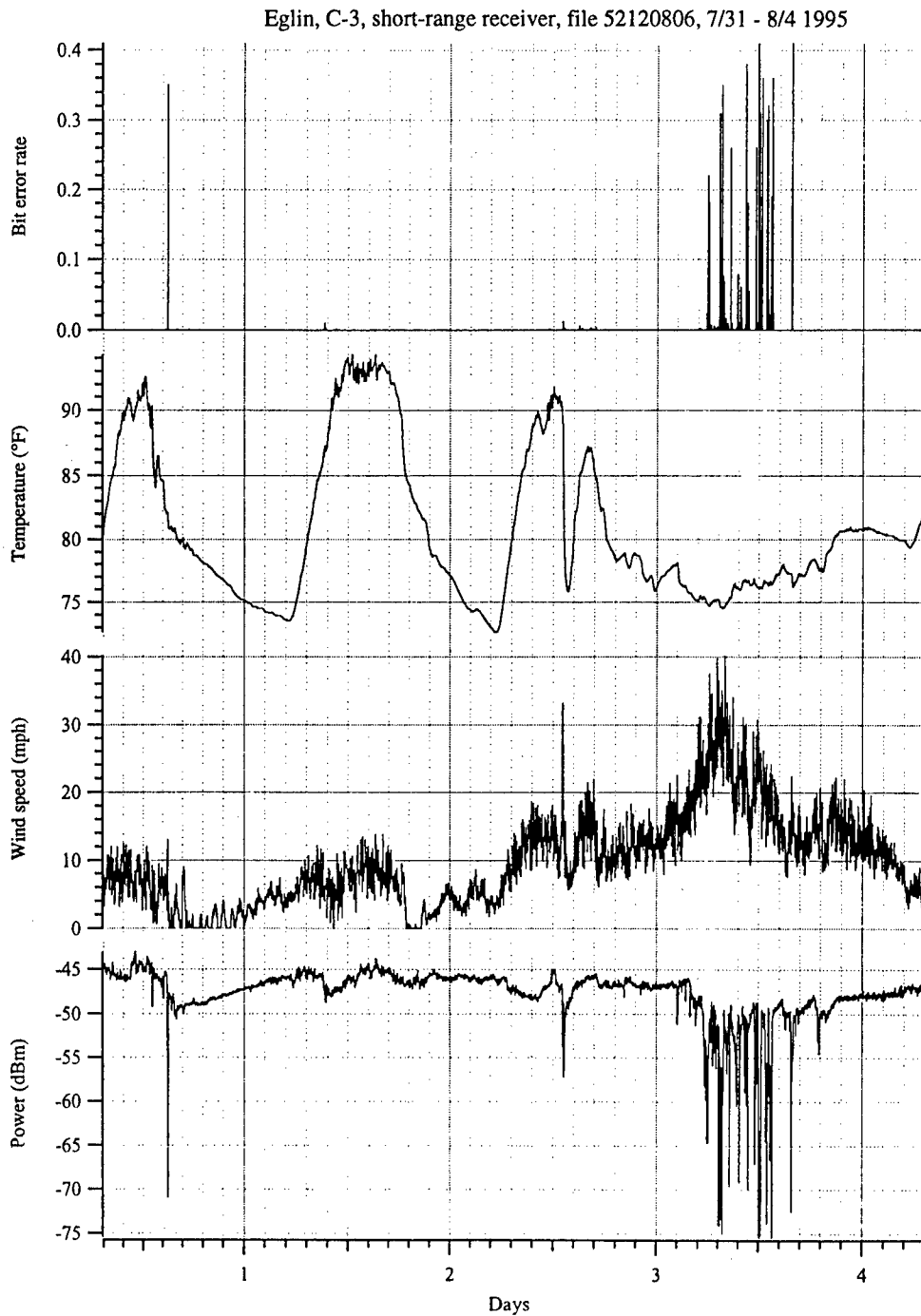


Figure 4.3
Horizontal polarization time series data from 52120806 (Hurricane Erin data set): bit error rate, temperature at the receiver, wind speed, and measured signal strength.

Eglin, C-3, short-range receiver, file 52120806, 7/31 - 8/4 1995

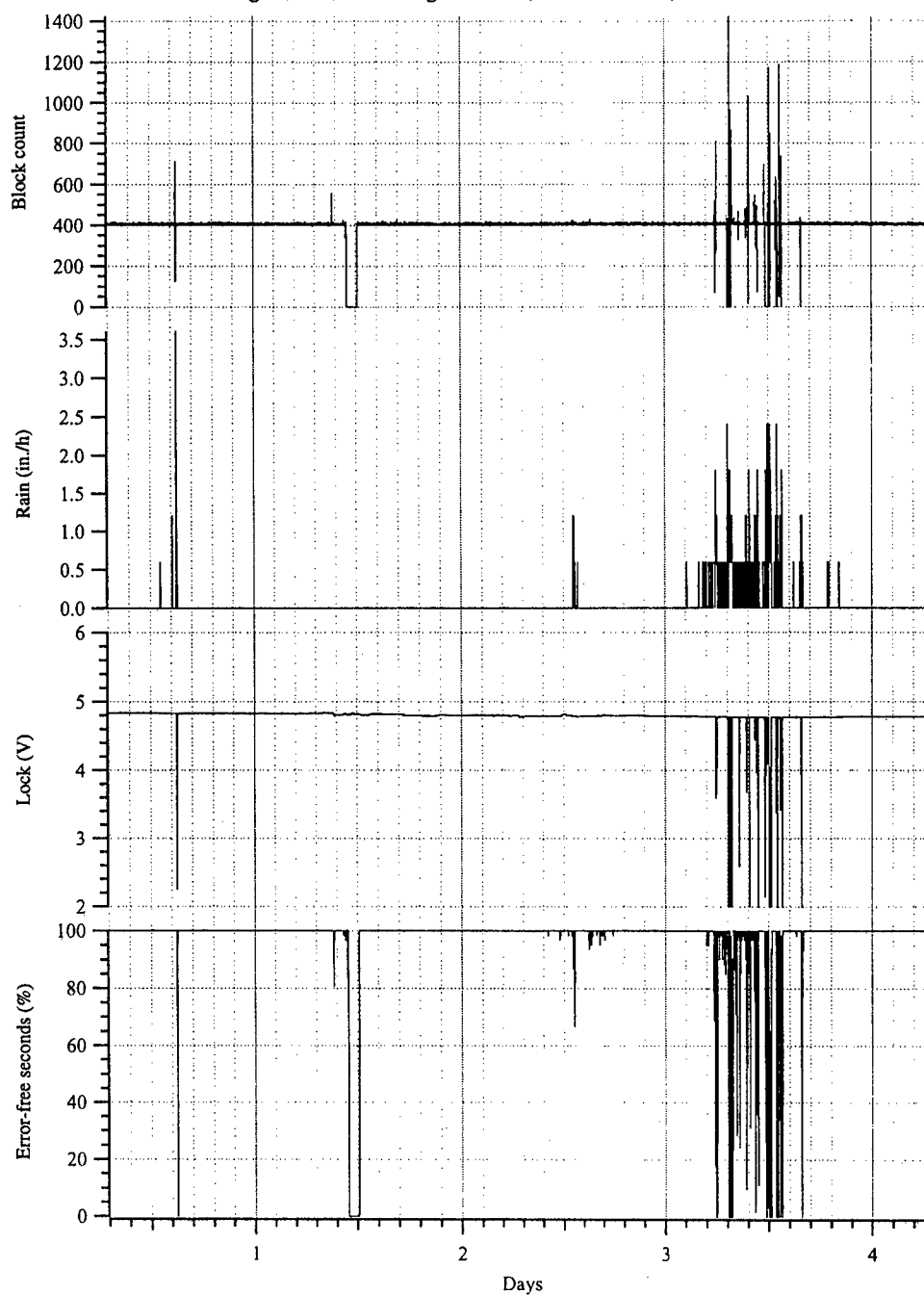


Figure 4.4

Horizontal polarization time series data from 52120806 (Hurricane Erin data set): block count, rainfall rate, sweep/lock indicator, and percent error-free seconds of transmission.

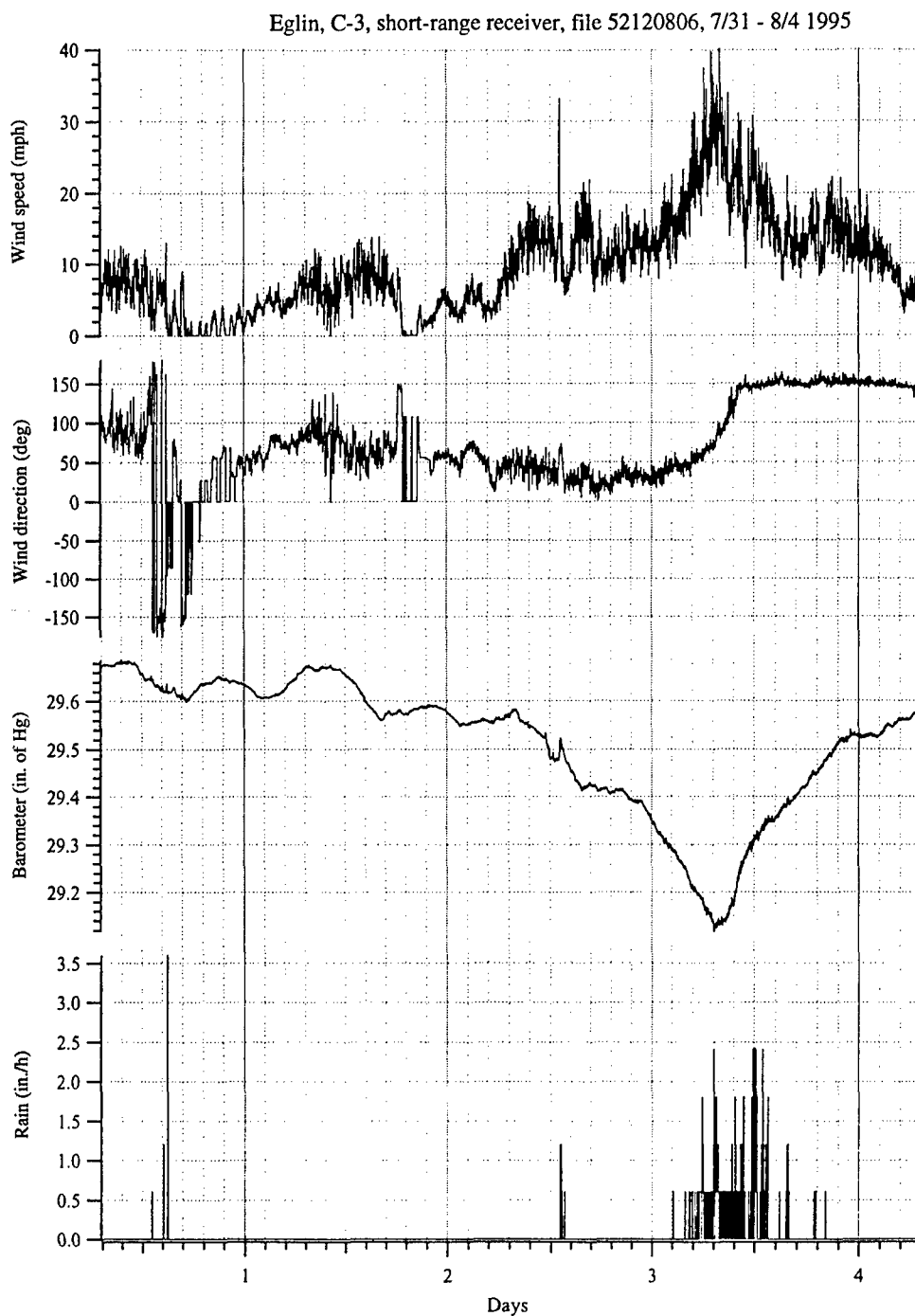


Figure 4.5
Horizontal polarization time series data from 52120806 (Hurricane Erin data set): wind speed, wind direction, barometric pressure, and rainfall.

4.2 DAVIS MONTHAN, SHORT-RANGE LINK TEST

The short-range link was tested at Davis Monthan AFB to check its performance in a desert environment. It was found that the performance of this data link was adequate. Unfortunately, during the period of the hottest months at Davis Monthan, the data link did not function properly. Portions of this data are usable, but data analysis will be more difficult than for the data sets with properly working equipment. All indications were that this was a random failure of a standard electronic component (a voltage regulator) with no relationship to the 60-GHz hardware. The reliable data sets did not show any anomalous behavior, except for higher standard deviations of signal strength during the hottest hours of the day. The problem was remedied during October 1996, and the link continued to function until March 1997. The data reported here is from that time. The results for the link properties, the summaries of the two data sets shown in this section, and the summary statistics for the period of reliable data collected are given in Tables 4.3–4.5, respectively.

The signal levels measured at the receiver corresponded closely with the calculated signal levels shown in Table 4.3. The disagreement between calculated and measured signal levels was within the uncertainty in the system gain. An important difference between the Davis Monthan short-range link and the Eglin link was that higher gain antennas were used at Davis Monthan. Dielectric lens antennas were used instead of pyramidal standard gain horns at Davis Monthan AFB. These antennas had a gain of 33.5 dB. Because of the short wavelength at 60 GHz (5 mm), these antennas were only 3 in. in diameter and approximately 6 in. long. The overall link margin was approximately 32 dB. For the desert environment, this link margin appeared to provide reliable performance.

Table 4.3**Link characteristics of short-range link at Davis Monthan AFB.**

Transmit Power	17 dBm (Nominal)
Transmitter Antenna Gain	33.5 dB
Receiver Antenna Gain	33.5 dB
Mixer Loss	-7 dB
Atmospheric Loss	-18.1 dB
IF Amplifier Gain	53 dB
Frequency / Wavelength	60 GHz / 0.005 m
Range	1.13 km
Free Space Spreading Loss	-129 dB
Receiver Noise Figure / Noise Floor at 7-MHz Bandwidth	10 dB / -95 dBm
Data Rate	1.5 Mbps
Average Signal Level (Horizontal Pol.)	-16.8 dBm
Calculated Signal Level	-17 dBm
Average Excess Signal Loss	-0.2 dB
Climate Classification	E (Desert)
Path Length Reduction Factor	0.95

Table 4.4
Statistics from the data sets shown,
transmitted bit pattern: 1023 bits/block.

Data Set	63100384	70070845
Average Bit Error Rate	5.4e-9	6.5e-5
Average Percent Error-Free Seconds	99.999%	99.98%
Average Signal Level	-17.2 dBm	-17.3 dBm
Peak Signal Level	-15.57 dBm	-15.1 dBm
Average Temperature	66.6°F	46.9°F
Average Wind Speed	3.47 mph	4.2 mph
Total Rainfall	0.0 in.	0.04 in.

Table 4.5
Summary of Davis Monthan AFB short-range link information,
November 1996–March 1997.

Total Test Time	2525 h
Percentage of Good Data Acquisition Time	99.99%
Average BER	1.54e-5
Percent Error-Free Time	99.98%
Total Rainfall Recorded at the Receiver	1.36 in.

The first data set shown here is 63100834, which covered the period from 5–12 November. The bit error rate, temperature, wind speed, and received power level are shown in Fig. 4.6. The diurnal temperature changes were clearly evident, and the power levels seemed to correspond with the temperature fluctuations. Interpretation of these data should be done with caution since transmitter and receiver local oscillator were free-running Gunn diodes.

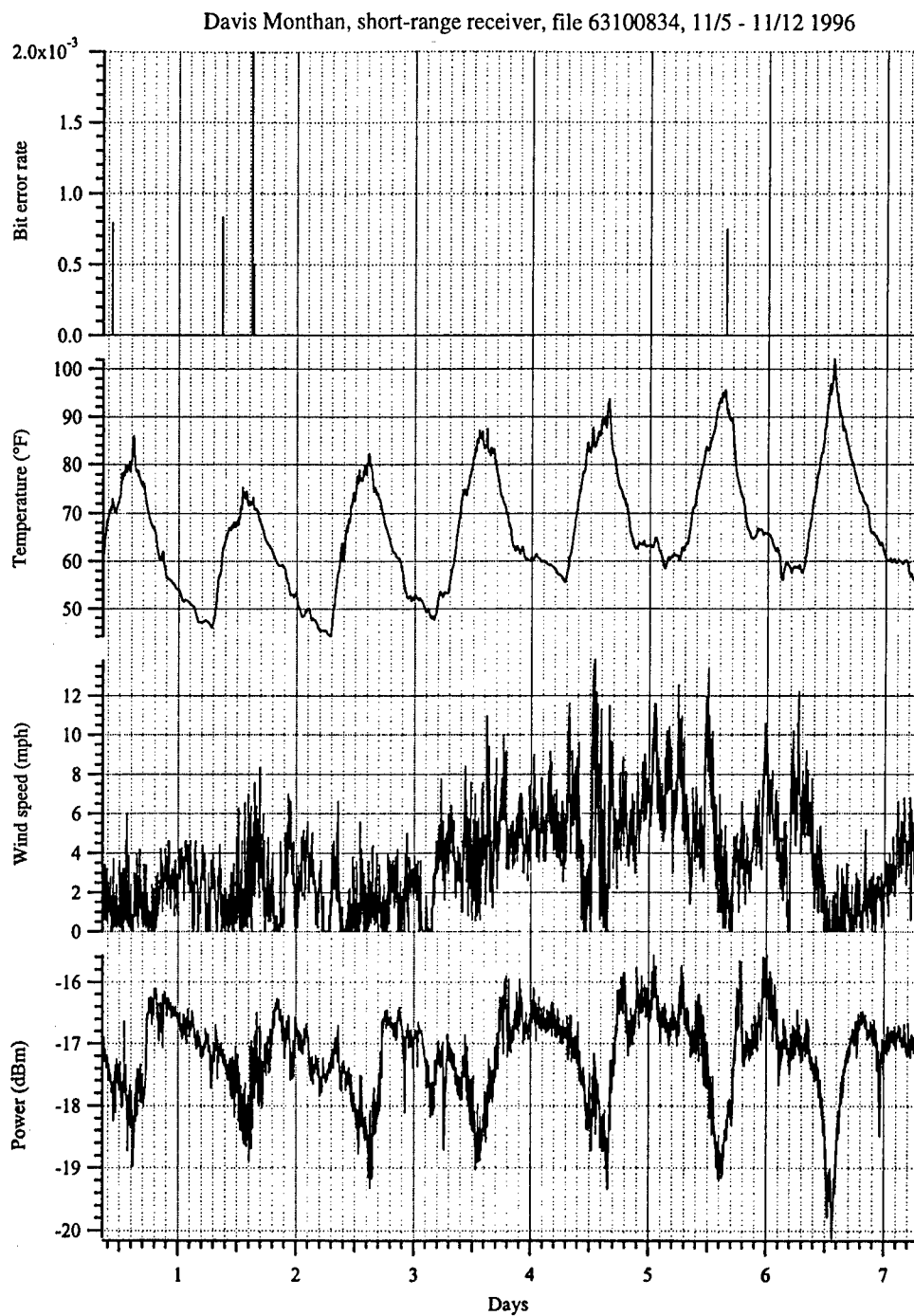


Figure 4.6

Vertical polarization time series data from 63100384 (5–12 November, autumn-winter data): bit error rate, temperature at the receiver, wind speed, and measured signal strength.

The received power level varied only about 3 dB maximum over the week. The system gain variability may be significant on this scale. Although the bit errors were very small, it was interesting to note that they occurred during the high temperature portion of the day. Figure 4.7 shows that there was no recorded rainfall during this time and that the data transmission was uninterrupted.

Figures 4.8 and 4.9 show the second data set, 70070845, which covers the time period from 7–14 January. A very slight amount of rainfall was recorded at 6.5 days, and a momentary increase in the BER was evident. The receiver sweep-lock indicator remained locked for the entire data set. The brief periods of errors appeared to occur during daylight hours of mildly disturbed conditions but with no recorded rainfall. From the observed data, it appeared that the errors were probably due to signal fluctuations causing errors on the phase locked loop (PLL) demodulator, rather than actual fades.

These data showed that the 60-GHz data link performed reliably and with little difficulty in the desert environment. The 60-GHz hardware appeared to be robust in this environment. Even with a mixer front-end, the small units had sufficient system gain to provide transmission of data at very low bit error rates and with extremely brief periods of errors. No anomalous signal fluctuations during calm weather periods were observed on the short-range link.

4.3 INTERCEPT TESTS

Measurements were made to determine the difficulty and possibility of detecting the signal of the 60-GHz transmitter. These tests were conducted at the C-3 test facility where the short-range link was set up. Included in our tests were the two most likely scenarios, which were: (a) the intercept of a signal behind the transmitter; and (b) the intercept of the signal in the main beam of the antenna, but at ranges greater than the intended receiver. In a perimeter sensor configuration, the first configuration corresponds to an intercept receiver outside the perimeter looking at a nearby transmitter. The transmitter will normally be

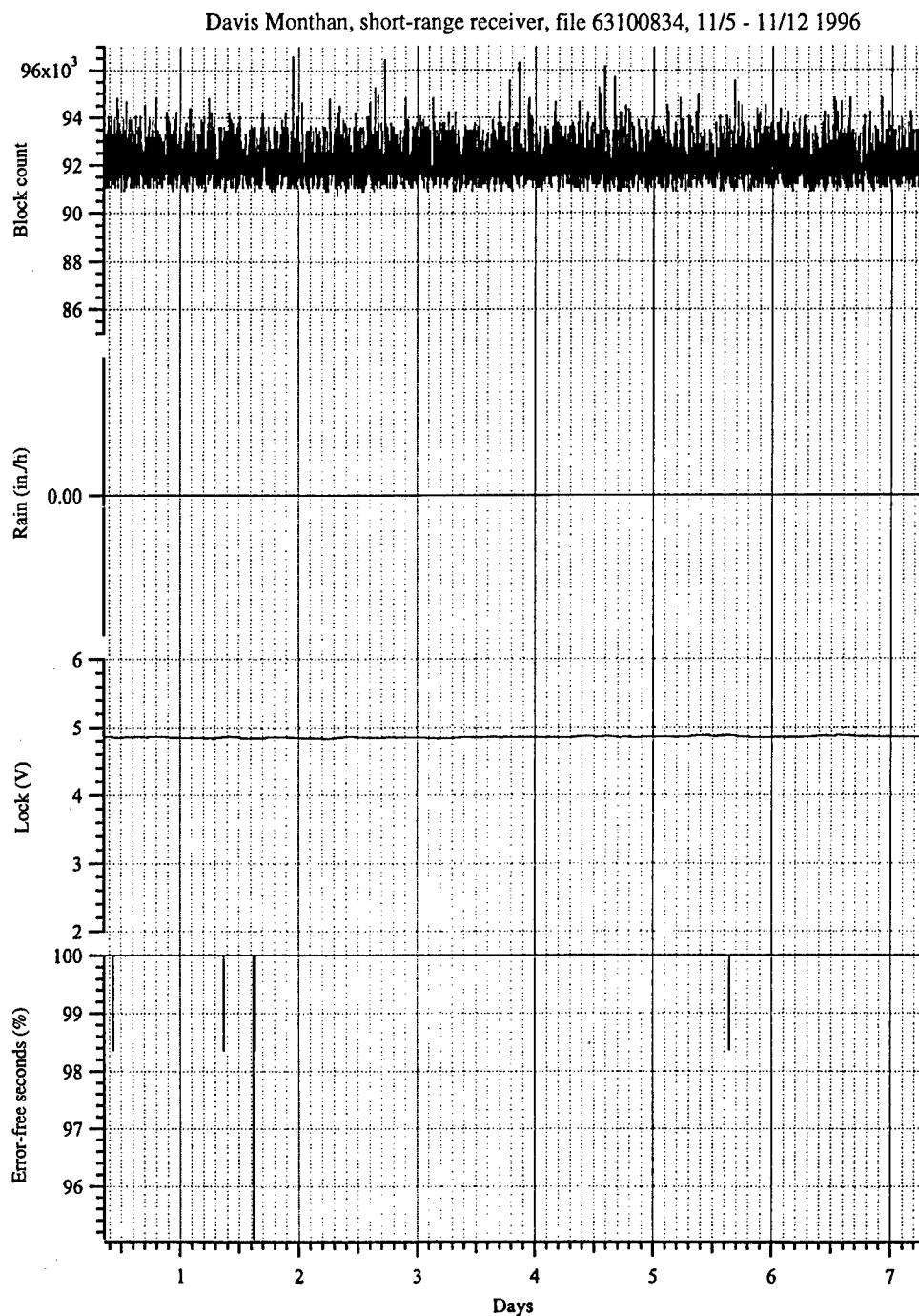


Figure 4.7

Vertical polarization time series data from 63100384 (5–12 November, autumn-winter data): block count, rainfall rate, sweep/lock indicator, and percent error-free seconds of transmission.

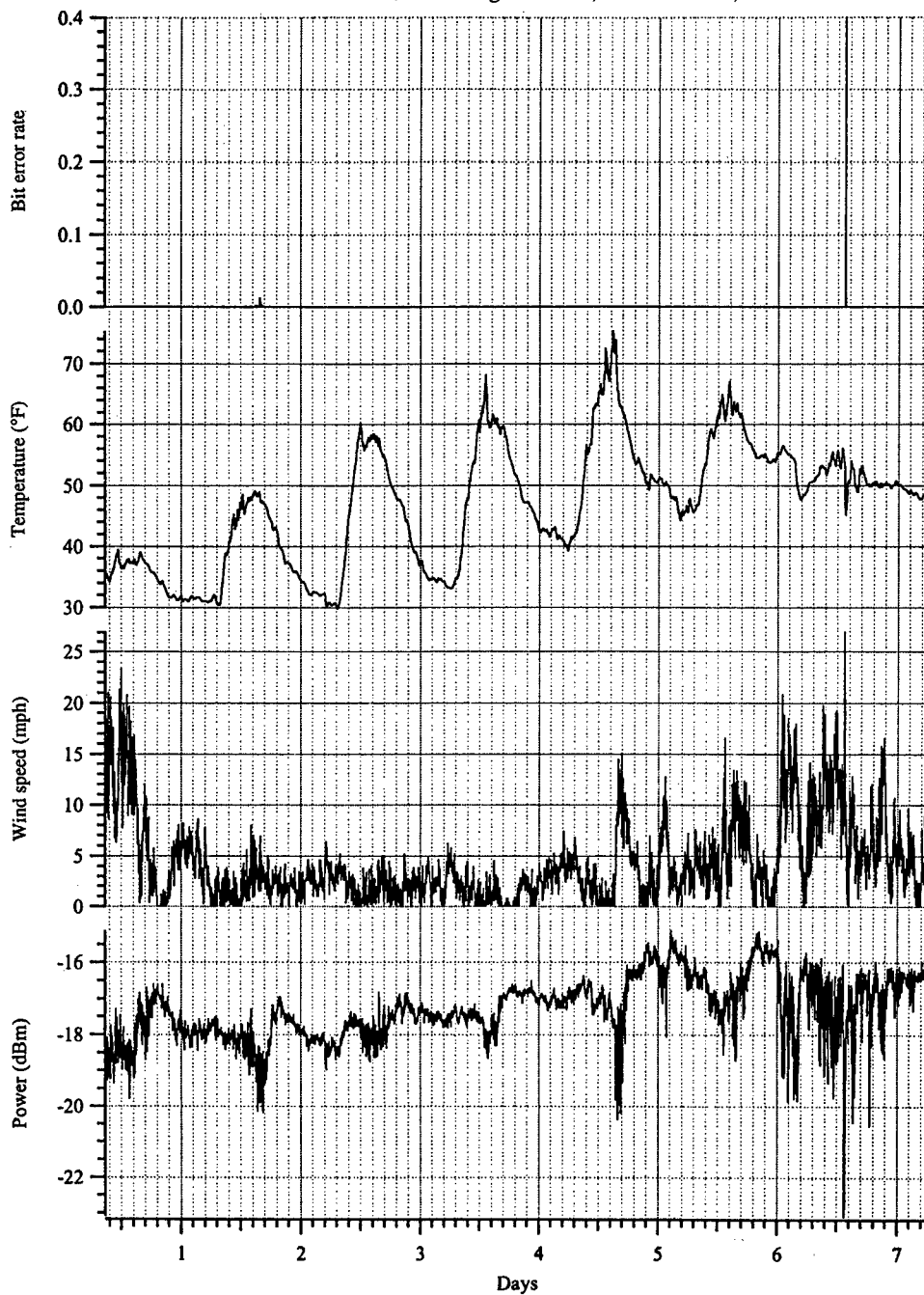


Figure 4.8

Vertical polarization time series data from 70070845 (7–14 January, autumn-winter data): bit error rate, temperature at the receiver, wind speed, and measured signal strength.

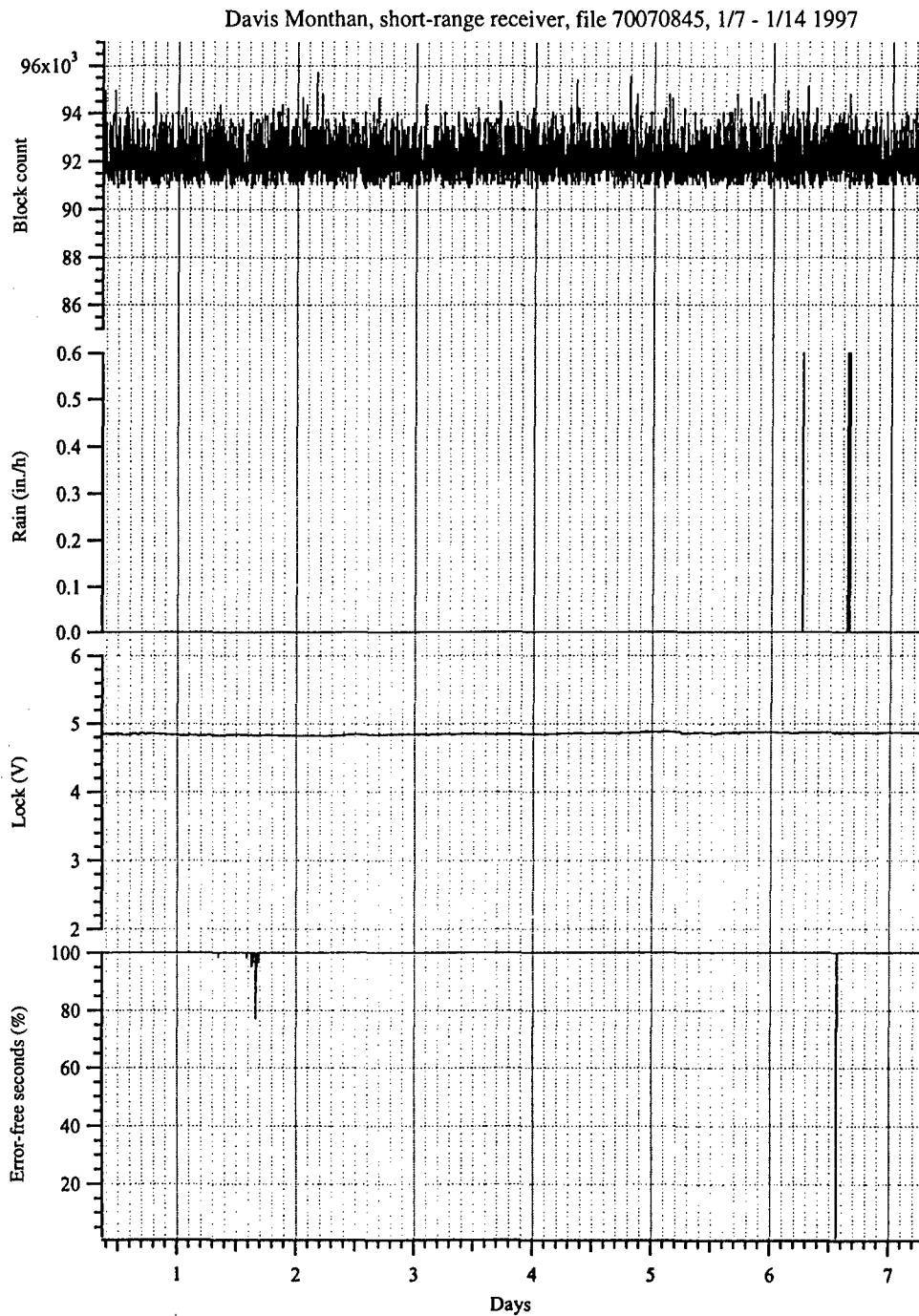


Figure 4.9
Vertical polarization time series data from 70070845 (7–14 January,
autumn-winter data): block count, rainfall rate, sweep/lock indicator, and
percent error-free seconds of transmission.

pointed toward the interior of the perimeter. The second scenario represents the intercept receiver looking across a secured area to detect a transmitter pointed toward the center of the secured area, but spilling across the far side of the secured area.

Measurements were made by a receiver that consisted of a down-converter circuit similar to the type that was used for the primary test receiver discussed in Section 2.0. The output was displayed on a spectrum analyzer that displayed the frequency spectrum of the transmitted signal. The signal was modulated with test data, and the signal strength was measured by looking at the spectrum analyzer. The minimum power level detectable by the receiver and analyzer was about -90 dBm.

The transmitter was held fixed and the receiver was moved to various locations, and the signal strength was read. In most cases, the receiver was not directly in the line-of-sight of the transmitter at ranges from less than 40 m to ranges greater than 2000 m. Furthermore, signals were measured behind the transmitter at approximately 33 m of range. The transmitter remained mounted on the telephone pole in the same configuration as that used for the reliability testing. In the main lobe of the transmitter beam on the ground, no signals were detectable at ranges greater than the receiver antenna range. Both the transmitter and the intercept receiver used the same standard gain horn antennas. In general, the signal was very difficult to detect because of its low level. With this configuration, it was found that no reliable detections could be made outside of the 3-dB beamwidth cone of the transmitter, or within the cone beyond a range of 1800 m from the transmitter.

This page intentionally left blank.

5.0 BAFFLED PYRAMIDAL HORN ANTENNA

The Cassegrain reflectors used in the long-range system were compact, high-gain antennas. These reflectors were fairly expensive and had to be handled very carefully. The small subreflectors constituting the Cassegrain configuration could be easily misaligned with a slight inadvertent bump, and realignment had to be performed by the manufacturer. The dielectric lens horns used in the Davis Monahan and Minot short-range tests were also compact, high-gain antennas. They were more robust than the Cassegrain reflectors, but were also quite expensive due to the cost of the lens.

Reflectors and lensed horns may currently be the most practical antennas for systems needing high-gain antennas; but size, cost, simplicity, and robustness may be more important than antenna gain in many cases. In such cases, a simple antenna such as a pyramidal horn may be adequate. Unfortunately, even medium-gain pyramidal horns can be too long to be practical; thus, horn lenses are often used. In an effort to improve the performance of a wide-flare pyramidal horn without the added cost and complexities associated with lenses, metal horn baffles were developed for this project. When these baffles are placed inside the horn near its throat, the antenna's performance is improved significantly. The metal baffles are simple, planar structures that reduce phase curvature at the aperture, like a lens. They were developed through calculations with two-dimensional models of the horn's E- and H-planes. This loading technique is economical and very easy to implement.

This section will focus on one particular set of baffles that greatly enhance the performance of a wide-flare, X-band pyramidal horn. The set contains two baffles that were designed independently through two-dimensional numerical modeling. One baffle was designed to enhance E-plane characteristics of the antenna and the other was designed to enhance H-plane characteristics. The two-dimensional numerical results approximate the true measured behavior of

the antenna in the corresponding planes. When the two baffles are used together as a combination-baffle, their performance becomes additive.

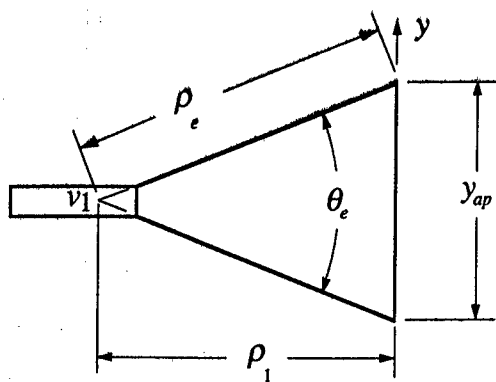
In Section 5.1, the pyramidal horn is reviewed to identify its critical parameters and their effects on the antenna's performance. The review describes the horn's radiating characteristics and why phase-correcting devices must be used with short, wide-flare horns. In Section 5.2, a description of the wide-flare X-band horn is given along with those of the two-dimensional models used to analyze the horn and simple horn loads. The two-dimensional numerical results for the baffle-loaded X-band antenna are presented and discussed in Section 5.3. Metal baffles for the E- and H-planes are described, and performances of the antenna with and without the baffles are compared. Measured performances of the antenna fitted with physical interpretations of the metal baffles are analyzed in Section 5.4. Measurements of the antenna loaded with each baffle independently and together as a combination-baffle are presented.

5.1 THE PYRAMIDAL HORN

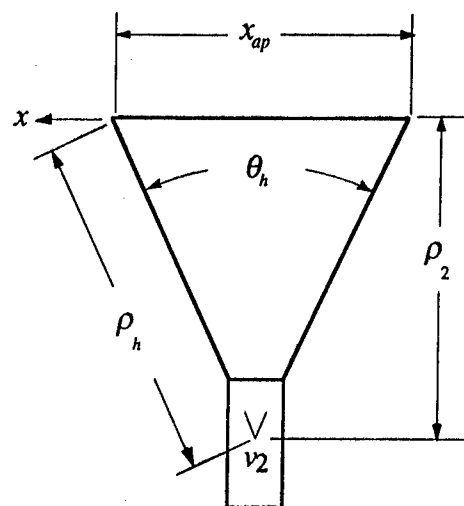
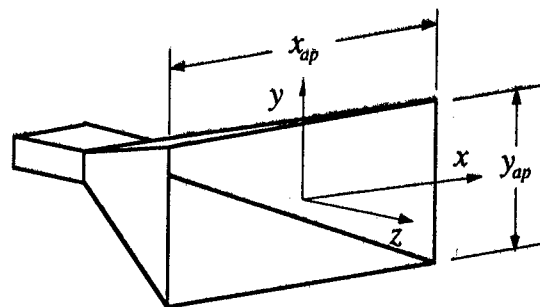
The pyramidal horn is a directional antenna that is widely used in microwave and millimeter wave systems. It is most commonly used as a calibration standard due to its robustness and predictability. Its simplicity makes it easy to construct, easy to use, and less expensive than most microwave antennas. The pyramidal horn's intrinsic utility has also been complemented by extensive research.⁸

5.1.1 Pyramidal Horn Configuration

The pyramidal horn is a rectangular aperture antenna that has the geometry shown in Fig. 5.1. The conventions in Fig. 5.1 are commonly used and are very similar to those used in Balanis.⁹ The antenna is simply an extension of



(a) E-plane



(b) H-plane

Figure 5.1
Pyramidal horn.

the feeding waveguide. It transitions the waveguide aperture to a suitable size for directional transmission or reception of electromagnetic energy. The horn flares with flare angles θ_e in the E-plane and θ_h in the H-plane. Directivity is provided in the E- and the H-planes by the rectangular, planar aperture. The aperture's dimensions are x_{ap} in the x-direction and y_{ap} in the y-direction. The slant heights, ρ_e and ρ_h , describe the length of the horn's sides from imaginary vertices at v_1 and v_2 , respectively, to the aperture.

5.1.2 Aperture Field Effects

For lossless rectangular apertures, the aperture efficiency equals 100% when the aperture electric fields are vertically polarized with a uniform amplitude distribution and a flat phase distribution.¹⁰ The aperture fields for pyramidal horns have a TE_{10} amplitude distribution.⁹ This mode effectively applies a tapered shading function to the aperture that reduces the sidelobes and broadens the main beam in the H-plane. With a flat phase distribution and a TE_{10} amplitude distribution, the aperture efficiency of a rectangular aperture is reduced to 81%.¹⁰

The horn's flare angles cause the distance from the waveguide to different locations on the aperture to vary. Increasing the flare angles causes more variance between these paths. Figure 5.1 shows that the greatest path difference in the E-plane is $\rho_e - \rho_1$, and the greatest difference in the H-plane is $\rho_h - \rho_2$. These differences cause the wave front at the aperture to be curved with a quadratic phase distribution. The fields across an aperture with a flat phase distribution add constructively in the direction of the main beam; a quadratic distribution weakens this constructive interference. Thus, increasing the flare angles increases phase curvature and lowers the aperture's directivity and aperture efficiency. The TE_{10} amplitude taper in the H-plane reduces the fields near the aperture edges where the phase deviates most from a flat distribution.

Therefore, most of the benefit from reducing phase curvature in pyramidal horn antennas is realized in the E-plane.

The flare angles of a pyramidal horn can be chosen to optimize directivity for a given set of slant heights. A horn with optimized flare angles is termed an optimum-gain horn. An optimum-gain horn is the most size-efficient, unaided pyramidal horn antenna. However, optimum-gain horns can be too large for small systems needing a high-gain antenna. To increase the gain of a pyramidal horn, the slant heights must be extended to increase the aperture area and the flare angles must be reduced to offset the added phase curvature. Adding 3 dB to the gain of an optimum-gain horn requires increasing the aperture area and slant heights of the horn by a factor of two.¹¹

Since the directivity of an aperture antenna is proportional to its aperture area, a short, compact, high-gain pyramidal horn would have to employ wide flare angles. However, the flare angles of a pyramidal horn cannot be larger than the angles describing an optimum-gain horn, or the antenna directivity will be adversely effected. Therefore, some type of phase-correcting device must be used with wide-flare pyramidal horns to improve their performance.

5.2 WIDE-FLARE, PYRAMIDAL X-BAND HORN AND MODELS

5.2.1 Construction

A wide-flare horn was constructed using an M/A-Com MA-86551 X-band antenna as a base antenna. The MA-86551 is a simple, inexpensive (\$20), metal-coated-plastic antenna with a nominal gain over the X-band of 17 dB. The walls of the antenna were extended with single-clad printed-circuit board to enlarge the aperture area. The extensions were secured to each other and to the base antenna with copper foil tape. Constructing an experimental horn in this fashion is quick, simple, and inexpensive. The flare angles of the experimental

antenna are greater than optimum, so the antenna performance is very limited. The dimensions of the antenna are shown in Table 5.1.

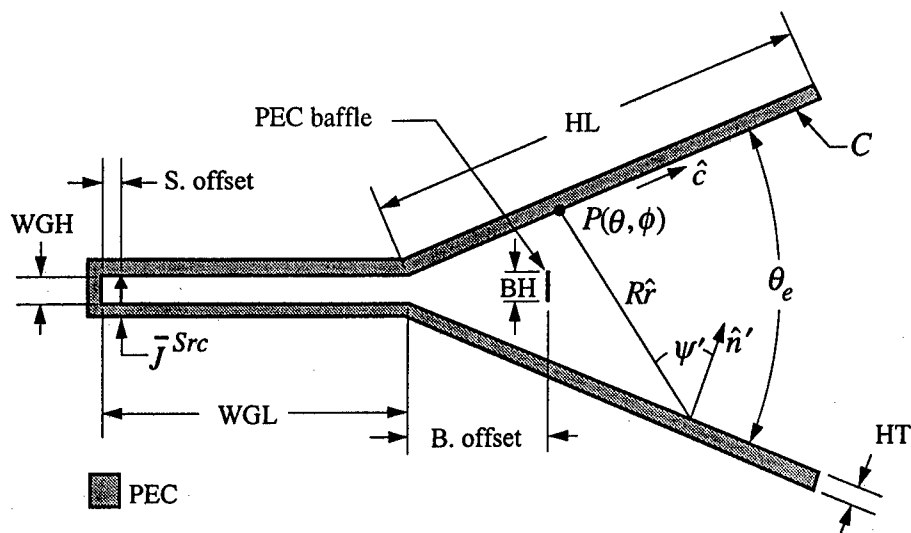
Table 5.1
Dimensions of wide-flare X-band pyramidal horn.

E-Plane Dimensions	H-Plane Dimensions
$y_{ap} = 14.0 \text{ cm}$	$x_{ap} = 16.7 \text{ cm}$
$\rho_e = 18.5 \text{ cm}$	$\rho_h = 20.2 \text{ cm}$
$\rho_1 = 17.1 \text{ cm}$	$\rho_2 = 18.4 \text{ cm}$
$\theta_e = 45^\circ$	$\theta_h = 49^\circ$

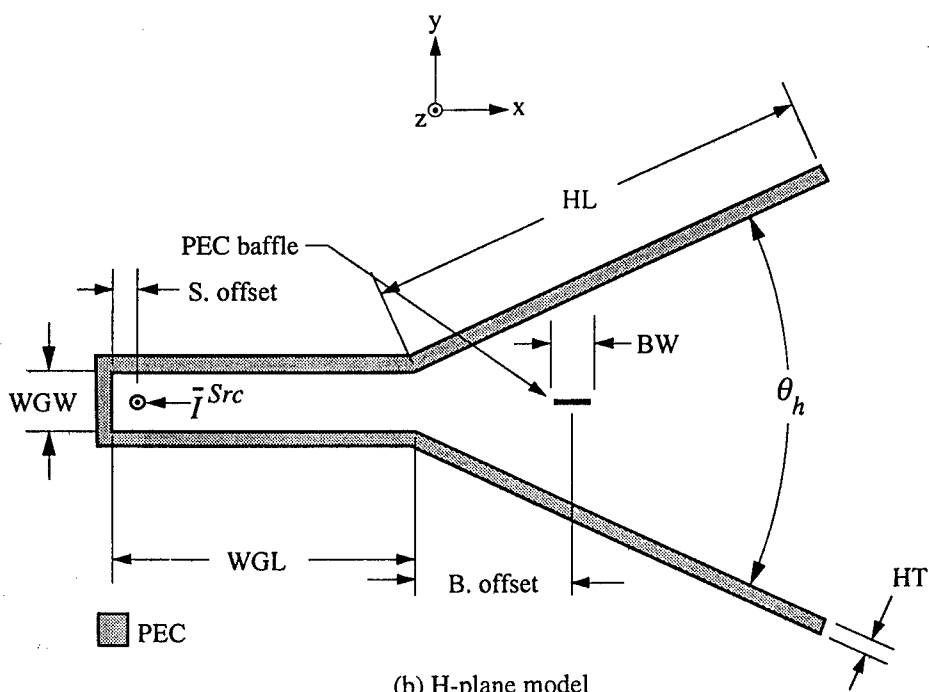
5.2.2 Two-Dimensional Numerical Models

The E-plane and H-plane two-dimensional models of the pyramidal horn are based on a moment method solution to the magnetic field integral equation (MFIE) and the electric field integral equation (EFIE), respectively.¹²⁻¹⁴ Both models allow simple metal objects to be placed inside the antenna. A three-dimensional model is necessary to correctly analyze the pyramidal horn; however, the rigorous analysis of a three-dimensional pyramidal horn is much more complex than the two-dimensional analysis, especially when scattering structures are loaded into the antenna. Although the pyramidal horn is not separable into E-plane and H-plane solutions, the two two-dimensional solutions do approximate the real behavior of the antenna in the respective planes.

Figure 5.2 pictures the E- and H-plane two-dimensional models. The horn and metal baffles in both models are described as perfect-electric-conductor (PEC) structures that have infinite length in the z-direction. The infinite direction is chosen as z to follow radial waveguide conventions. An MFIE in the E-plane



(a) E-plane model



(b) H-plane model

Figure 5.2
Two-dimensional models.

model is formed from the boundary conditions along the PEC surfaces in Fig. 5.2, top,

$$J_c(\rho, \phi)|_{PEC} + \frac{jk_o}{4} \int_C J_c(\rho', \phi') \cos(\psi') H_1^{(2)}(k_o R) dc' \Big|_{PEC} = -H_z^i|_{PEC} \quad (5.1)$$

Equation 5.1 relates the total magnetic field at a point $P(\rho, \phi)$ on a PEC surface (C in Fig. 5.2, top) to equivalent electric current densities, J_c . In Eq. 5.1, H_z^i is the incident field produced by the source, \bar{J}^{src} , the primed coordinates indicate the source location, and $H_1^{(2)}$ is the first-order Hankel function of the second kind. The equivalent currents are all polarized in the c -direction defined by the unit vector, $\hat{c} = -\hat{n} \times \hat{z}$, where \hat{n} is the outward pointing normal to C . Similarly, an EFIE in the H-plane model is formed that relates the electric field to equivalent surface currents along the PEC surfaces in Fig. 5.2, bottom.

$$\frac{\omega\mu_o}{4} \int_C J_z(\rho', \phi') H_0^{(2)}(k_o R) dc' \Big|_{PEC} = E_z^i|_{PEC} \quad (5.2)$$

In Eq. 5.2, the equivalent currents are all polarized in the z -direction, E_z^i is the electric field produced by the source, \bar{I}^{src} , and $H_0^{(2)}$ is the zero-order Hankel function of the second kind.

The equivalent currents are then calculated by solving Eqs. 5.1 and 5.2 using the moment method. A pulse-expansion and point-matching moment method solution was chosen in which the currents are expanded into rectangular basis functions and the boundary conditions are matched at the center of each basis. The integral over each basis was calculated using a rectangular approximation except for the self-terms, where limiting approximations were necessary. See Appendix B for a more detailed description of the two-dimensional models and their moment method solutions.

In order to calculate results over the entire X-band in the E-plane model, the dimensions of the E-plane horn and E-plane baffle (shown in Fig. 5.2, top) were entered in units of wavelength at 10.3 GHz and scaled appropriately for calculations at other frequencies. The basis functions along the horn were chosen to be 0.1λ (10.3 GHz) long everywhere except on the waveguide end. The bases on the waveguide end are 0.025λ long to resolve the waveguide height. The E-plane baffle is a thin, vertically oriented, PEC strip placed near the horn's throat. The length of the bases forming the baffle are 0.05λ long in order to resolve the small structure. The baffle is only one-basis-function thick, representing a thin object. Dimensions of the horn and baffle used for numerical results are shown in Table 5.2.

The H-plane baffle, shown in Fig. 5.2, bottom, is a thin PEC object centered horizontally in the narrow end of the horn. The size of the horn basis functions in this model are all 0.1λ (10.3 GHz) long and the baffle basis functions are 0.05λ . Table 5.2 lists the H-plane horn and baffle's dimensions.

Table 5.2.
Dimensions used in two-dimensional models.

E-Plane Model Dimensions	H-Plane Model Dimensions
WGH = 0.35λ (10.3 GHz)	WGW = 0.8λ
WGL = 4.0λ	WGL = 4.0λ
S. Offset = 0.25λ	S. Offset = 0.25λ
HL = 5.9λ	HL = 6.0λ
HT = 0.2λ	HT = 0.2λ
BH = 0.5λ	BW = 0.5λ
B. Offset = 2.1λ	B. Offset = 2.0λ
$\theta_e = 45^\circ$	$\theta_h = 49^\circ$

Field values, directivity, gain, reflection efficiency, and beam patterns in both models are calculated from the equivalent currents.¹⁴ The far-fields are

calculated directly from the equivalent currents and source using far-field approximations, and the beam patterns and directivity are calculated from the far-fields. The gain is related to the directivity by $G = \epsilon_r D_o$, where ϵ_r is the total antenna efficiency.¹⁵ In the following numerical results, only reflection-losses are considered and ϵ_r is equal to the reflection efficiency, $(1 - |\Gamma|^2)$, where the current reflection coefficient, Γ , is calculated from the current standing wave pattern in the waveguide. See Appendix B for a detailed description of the antenna parameter calculations.

5.3 NUMERICAL RESULTS

5.3.1 E-Plane Numerical Results

The E-plane directivity and gain of the X-band horn were calculated at 100-MHz intervals from 8.2 GHz to 12.4 GHz using the two-dimensional E-plane model. The results are plotted in Fig. 5.3. The figure displays results for the unloaded antenna and the antenna loaded with the E-plane baffle. The calculations show that the baffle increases the antenna gain by 3 dB over the frequency range from 10.0 GHz to 11.1 GHz. This enhancement band corresponds to a bandwidth of 11.3%. The directivity is increased by 3 dB from 9.7–11.2 GHz.

The antenna's performance is dependent upon the baffle's electrical distance from the horn's throat along the antenna's axis. Figure 5.3 shows that the reflection efficiency and the directivity begin to decrease near 8.8 GHz, reach a null at 9.4 GHz, and recover by 10.0 GHz. At 8.8 GHz, the distance from the horn throat to the baffle is 1.8λ . The distance at 10.0 GHz is 2.0λ . The enhancement band (10.0–11.1 GHz) corresponds to throat-to-baffle distances

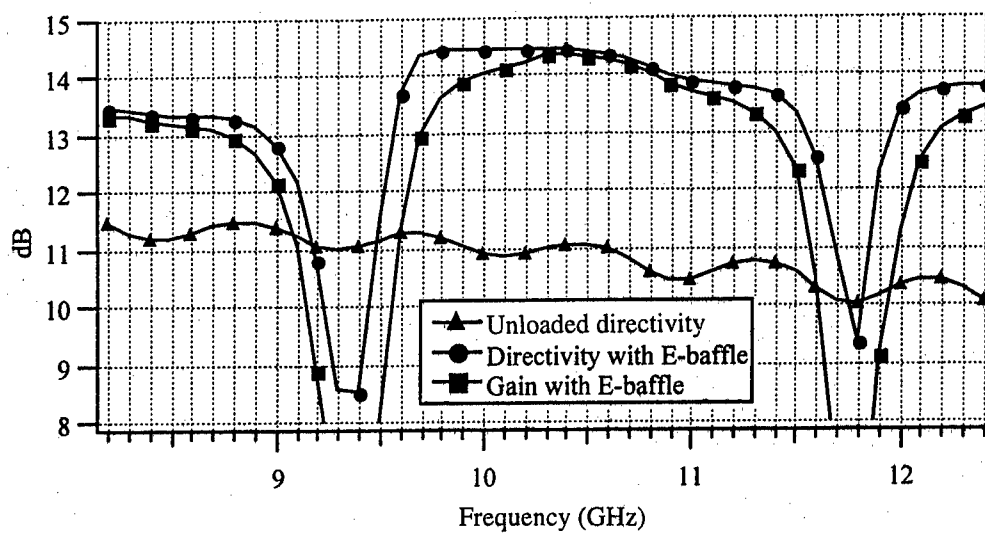


Figure 5.3
E-plane, calculated on-axis directivity and gain.

ranging from 2.0λ to 2.26λ , and the second null band (11.1–12.4 GHz) corresponds to distances ranging from 2.26λ to 2.5λ . The center frequency of the enhancement band corresponds to a baffle placement of approximately 2.15λ ; thus, the center frequency can be adjusted by adjusting the baffle's throat-to-baffle location. The lengths of the enhancement and null bands correspond to throat-to-baffle distances ranging over approximately one-quarter of a wavelength. In the null regions, standing wave patterns form nulls in the slots on either side of the baffle and a maximum in front of the baffle. Most of the energy appears to radiate from the maximum in front of the baffle in the null bands, resulting in poor antenna performance.

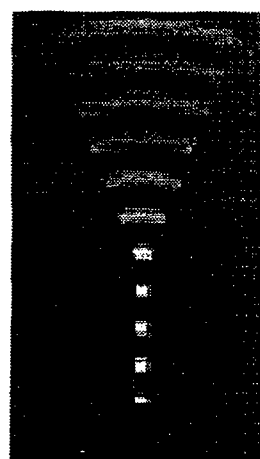
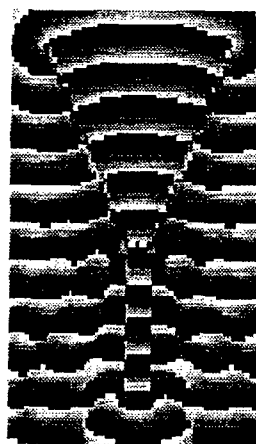
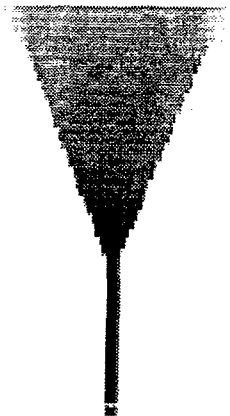
The enhancement band is centered at 10.5 GHz. At this frequency the loaded horn's input impedance is well matched to the waveguide and the baffle adds 3.2 dB to the antenna gain. (A small reflection loss and a consequently small difference between directivity and gain indicate a good impedance match.) The interior magnetic fields are plotted in Fig. 5.4 for the loaded and unloaded antennas at this frequency. The fields are sampled at 0.1λ intervals in the x- and y-directions. The gray scale used in the amplitude plots is a relative scale where black signifies 1 A/m and white signifies 0 A/m. In the phase plot, white to black bands correspond to 360° of phase shift (white and black equal zero degrees). The third field plot pictures the total field at time zero, or $\text{Re}\{H_z(x, y)e^{j\omega t}\}_{t=0} = H_o(x, y)\cos(\theta(x, y))$, where $H_o(x, y)$ is the amplitude and $\theta(x, y)$ is the phase of the magnetic field at the location x,y.

The aperture amplitude distribution of the unloaded horn is fairly uniform, but a quadratic phase distribution is revealed in the phase plot. The phase at the edge of the aperture differs from the phase at the center by approximately 180° . The loaded field plots show that the baffle corrects the phase curvature and has little effect on the amplitude distribution. Fields emitted from the waveguide impinge upon the baffle and are forced to travel around either side of it. There appear to be two radiating slots next to the baffle feeding the remainder of the

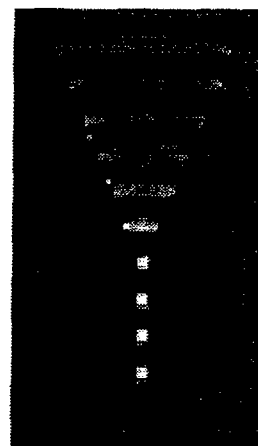
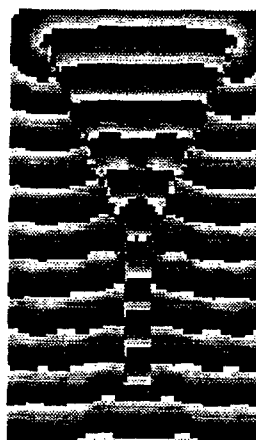
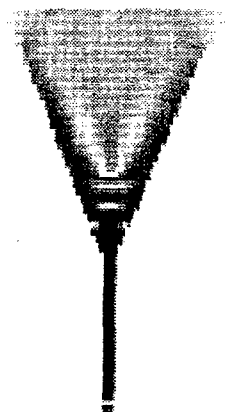
Amplitude = $H_0(x, y)$

Phase = $\theta(x, y)$

Total = $H_0(x, y) * \cos(\theta(x, y))$



(a) Unloaded E-plane horn



(b) E-plane horn loaded with E-plane baffle

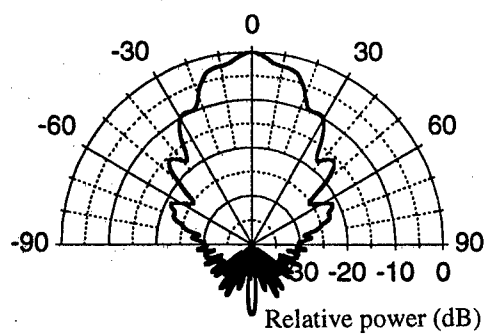
Figure 5.4
Calculated E-plane, interior magnetic fields at 10.5 GHz.

antenna. The fields from the two slots interfere to produce a relatively flat phase distribution and uniform amplitude distribution at the aperture. An alternate way of interpreting this phenomenon is that the baffle appears to delay the fields in the central region of the horn.¹⁴ It appears that the baffle delays the fields in the central region of the horn. The delay adds length to the central path so that this path is equivalent to the paths near the edges of the horn. As the fields spread past the baffle, the central and edge fields reach the aperture in phase.

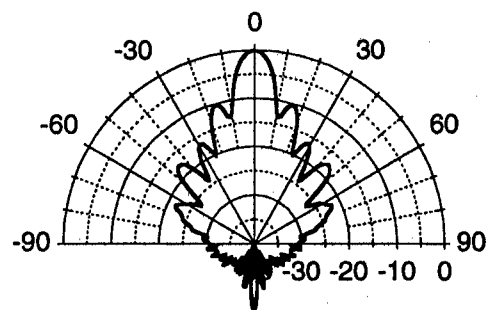
The E-plane beam patterns of the loaded and unloaded antennas at 10.5 GHz are shown in Fig. 5.5. The effects of phase curvature are apparent in the unloaded beam pattern. The main beam is very broad and the sidelobes are not distinct. Loading the antenna with the E-plane baffle decreases the aperture phase curvature resulting in more on-axis constructive interference. The main lobe is narrowed and the nulls between sidelobes become deeper. The 3-dB beamwidth of the loaded horn is 10° and the unloaded horn's beamwidth is 28° . Additionally, the first sidelobes of the loaded horn are 10 dB down from the main beam and the remaining sidelobes are all 15 dB below the main beam.

5.3.2 H-Plane Numerical Results

Figure 5.6 shows that the H-plane baffle increases the antenna gain and directivity 1.9 dB over an 700-MHz band centered around 10.6 GHz. The gain and directivity are very similar, implying that the loaded horn's input impedance is well matched to the waveguide over the entire X-band. The H-plane baffle does not provide as much performance enhancement as the E-plane baffle, but this baffle configuration can be combined with the E-plane baffle to improve the overall antenna performance. This will be shown through the measured results. A baffle parallel to the aperture in the H-plane will produce results similar to those produced by the E-plane baffle. However, no baffle configuration was found to enhance the antenna's performance with both baffles parallel to the aperture.



(a) Unloaded E-plane



(b) Loaded E-plane

Figure 5.5
Calculated E-plane beam patterns at 10.5 GHz.

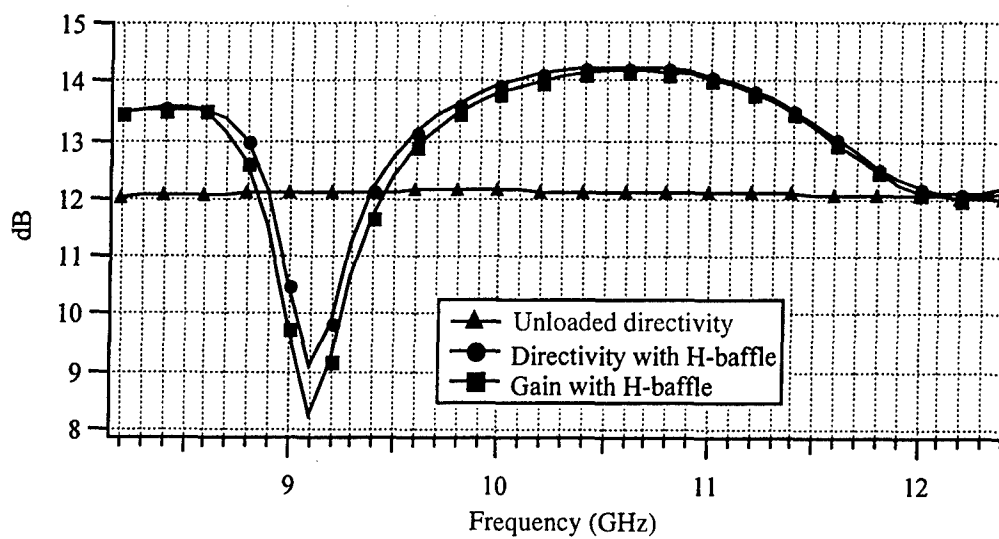


Figure 5.6
H-plane, calculated on-axis directivity and gain.

The null in directivity centered at 9.1 GHz corresponds to the center of the baffle being placed 1.75λ in front of the horn's throat. At the frequencies near 9.1 GHz, energy radiating through the antenna does not flow smoothly around the baffle. The fields around the baffle produce an aperture distribution with a phase reversal in its central region. The distribution resembles a TE_3 mode with an added quadratic phase term.

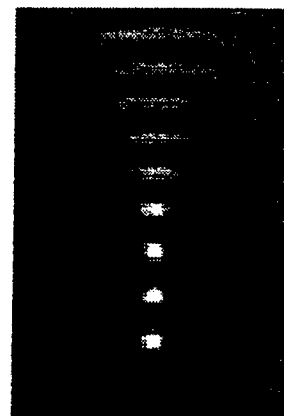
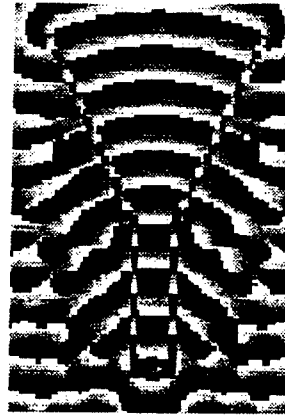
The antenna reaches its peak directivity near 10.5 GHz. The interior electric fields at this frequency are plotted in Fig. 5.7. The aperture amplitude distribution of the unloaded horn appears to be the half period of a sinusoid indicative of the TE_1 parallel-plate waveguide mode, and the phase distribution is quadratic due to spreading inside the horn. The TE_1 mode is analogous to the TE_{10} mode in a three-dimensional rectangular waveguide. A new mode is set up when the baffle is added, which appears to be the combination of odd-ordered modes. The new mode illuminates the aperture more evenly than the TE_1 mode. The baffle also flattens the phase by forcing the energy to diffract around the baffle, similar to the effect produced by the E-plane baffle.

The calculated beam patterns at 10.5 GHz of the unloaded and loaded H-plane horns are shown in Fig. 5.8. Like the TE_{10} distribution in a three-dimensional horn, the unloaded horn's TE_1 amplitude distribution effectively reduces the size of the aperture and limits phase curvature effects. This distribution produces one broad beam with a 3-dB beamwidth of 20° . Since the H-plane baffle redistributes the amplitude and reduces the phase curvature, the beam pattern of the loaded horn has a narrow main lobe and distinctive sidelobes. The beamwidth of the main lobe is 10° and the sidelobes are 9 dB down from the main lobe.

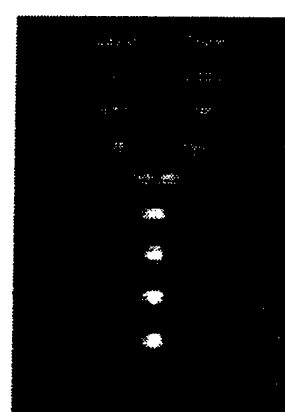
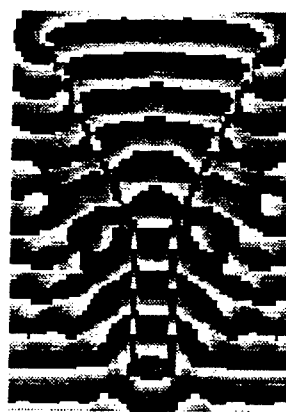
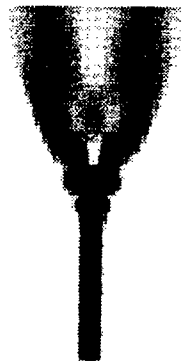
Amplitude = $H_0(x, y)$

Phase = $\theta(x, y)$

Total = $H_0(x, y) * \cos(\theta(x, y))$

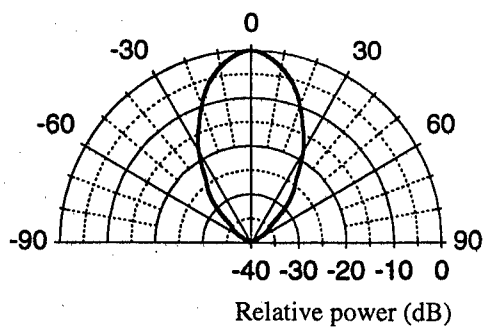


(a) Unloaded H-plane horn

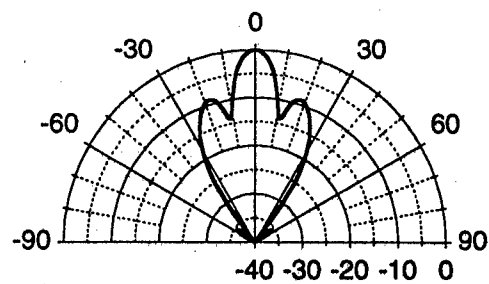


(b) H-plane horn loaded with H-plane baffle

Figure 5.7
Calculated H-plane, interior electric fields at 10.5 GHz.



(a) Unloaded H-plane



(b) Loaded H-plane

Figure 5.8
Calculated H-plane beam patterns at 10.5 GHz.

5.4 EXPERIMENTAL RESULTS

5.4.1 Setup

To measure the loaded horn's performance, baffles were fabricated from 0.7-mm copper sheet. The E-plane baffle was cut to extend completely across the horn in the direction (x in Fig. 5.1) corresponding to the infinite direction, z , in the E-plane model. Similarly, the H-plane baffle was cut to extend across the horn in the direction corresponding to z (y in Fig. 5.1) in the H-plane model. In order to make measurements with both baffles inside the horn, a slot was cut in the H-plane baffle so the E-plane baffle could intersect it. This physical implementation of the combination E- and H-plane baffles is pictured in Fig. 5.9.

An M/A Com MA-86551 pyramidal horn was used as the transmitting antenna. Both the transmitting antenna and the test antenna (wide-flare X-band horn) were set 4.5 ft off the ground on plastic stands. The largest dimension of the test antenna's aperture, D , is its diagonal. The test antenna was placed 20 ft from the transmitter, corresponding to a distance of $3.6D^2/\lambda$ at 10.5 GHz. The transmitting antenna was fed through an X-band coax-to-waveguide feed with a HP-8350B sweep oscillator. The test antenna's received power was measured through an X-band coax-to-waveguide feed using an Anritsu ML83A power meter and an Anritsu MA73A power sensor. For gain versus frequency measurements, the transmitting and test antennas were directed on-axis and the received power was recorded at 100 MHz intervals from 8.2–12.4 GHz. The gain of the test antenna was then determined using the Friis transmission equation. The gain of the transmitting antenna was determined using an MA-86551 horn as the receiving antenna.

Beam pattern measurements were measured at 10.5 GHz. The antenna stands rotated freely in the azimuth direction only. Therefore, the antennas were oriented so their E- or H-planes were parallel to the ground when making the

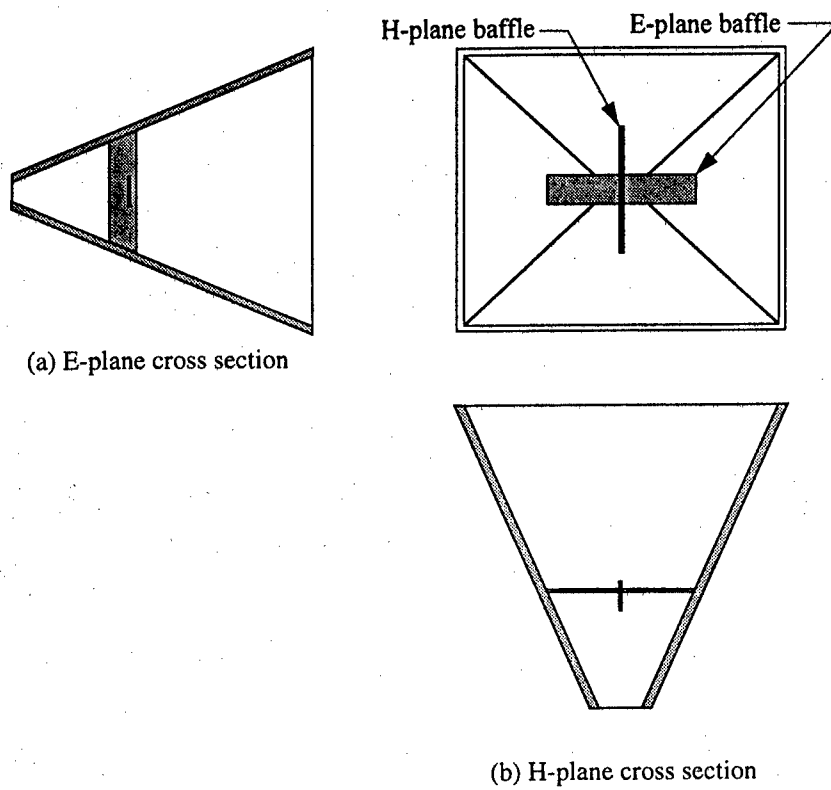


Figure 5.9
Pyramidal horn loaded with combination baffle.

respective beam pattern measurement. The test antenna was turned in 2.5° increments from -90° to 90°, and the received power was measured at each increment.

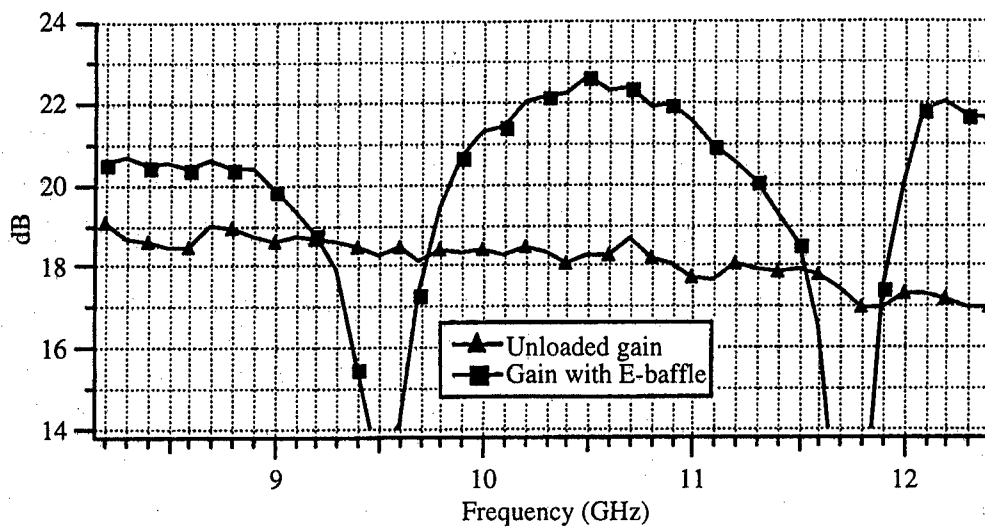
5.4.2 Measurements

The on-axis gain of the horn loaded with the E-plane baffle is shown in Fig. 5.10, top. The measurements agree with the two-dimensional calculated results plotted in Fig. 5.3. The E-plane baffle enhances the gain 3 dB over the unloaded horn in a 1.1-GHz band from 10.1–11.1 GHz. The bandwidth of this enhancement band is 10.4%. The peak gain in the enhancement band is 22.5 dB at 10.5 GHz and the average gain is 21.9 dB.

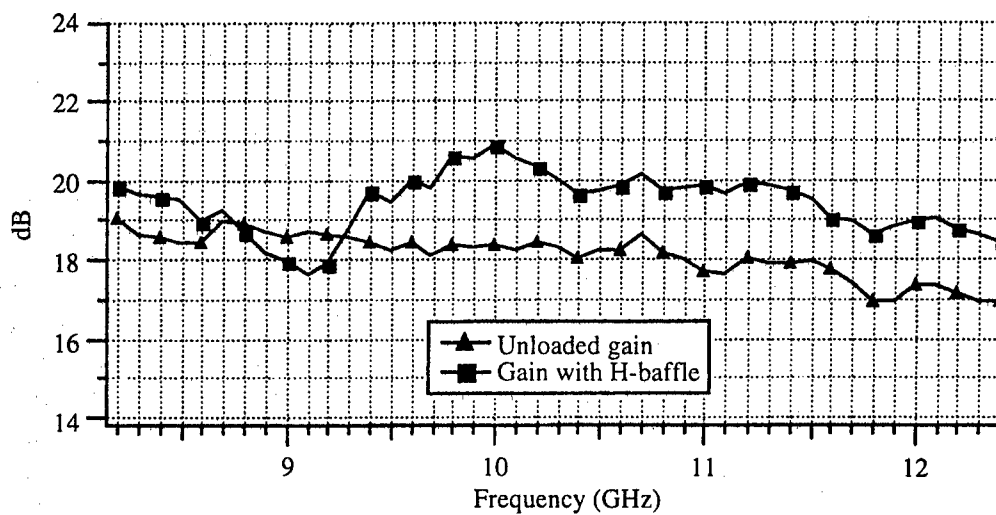
H-plane calculations shown in Fig. 5.6 also agree with the measured results shown in Fig. 5.10, bottom. The performance improvement of this baffle is not as significant as that of the E-plane baffle, but the baffle increases the antenna gain by nearly 2 dB over the E-plane enhancement band.

In Fig. 5.11, top, the measured gain of the horn loaded with the combined baffles shows that the antenna gain is increased by 4.5 dB over a 1-GHz frequency band. Over the 4.5-dB enhancement band, the gain peaks to 23.4 dB, and the average gain is 23.1 dB. In addition, the baffles improve the antenna's gain by 5 dB over a 700-MHz band from 10.4–11.0 GHz. The gain remains greater than 23 dB over the entire 5-dB enhancement band. The loaded horn's aperture efficiency,* shown in Fig. 5.11, bottom, is greater than 50% from 10.2–11.0 GHz. The aperture efficiency stays above 55% from 10.2–10.9 GHz and peaks to 60.9%.

* aperture efficiency = $100 \times \frac{\text{Gain}}{4\pi(\text{ApertureArea}) / \lambda^2}$.

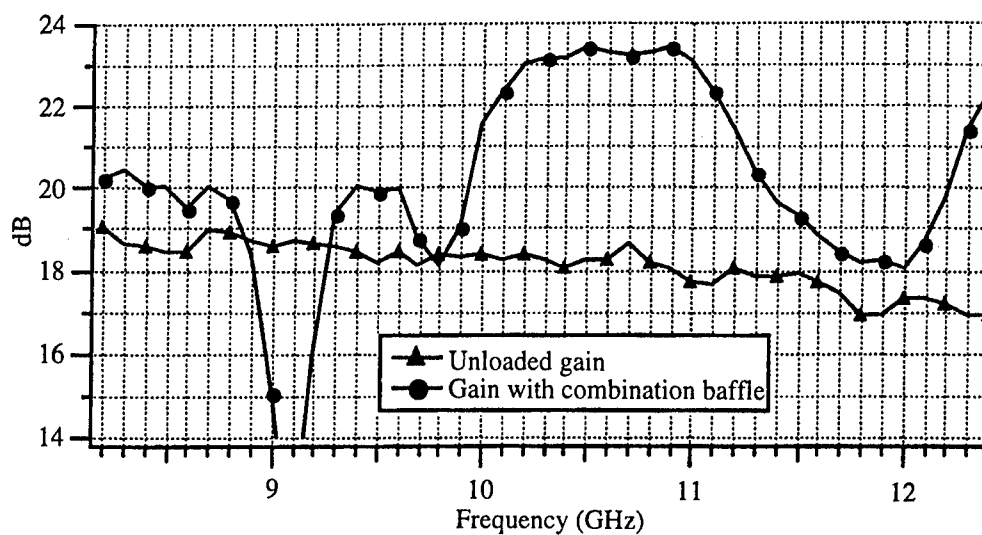


(a) Gain with E-baffle

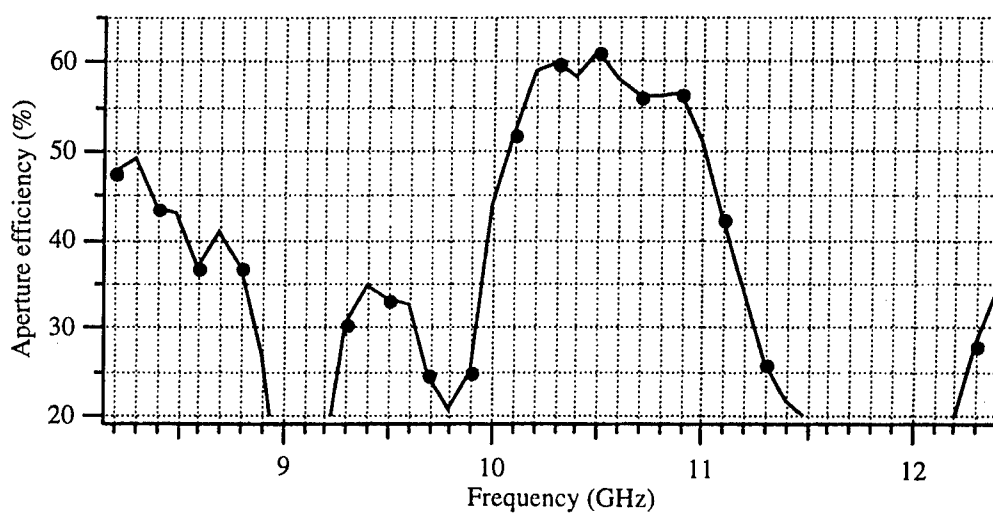


(b) Gain with H-baffle

Figure 5.10
Measured on-axis gain versus frequency for E-plane and H-plane baffles.



(a) Gain of horn with combination baffle



(b) Aperture efficiency with combination baffle

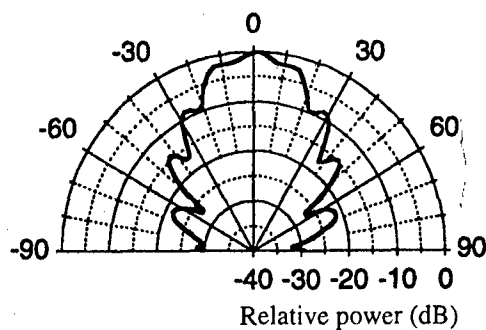
Figure 5.11
Measured gain and aperture efficiency of horn with combination baffle.

The E- and H-plane beam patterns of the unloaded horn and the horn loaded with the combination baffle are shown in Fig. 5.12. The E- and H-plane beam patterns are very similar to those calculated and plotted in Figs. 5.5 and 5.8, respectively. The unloaded horn suffers from the effects of phase curvature and the TE_{10} waveguide mode. The half-power beamwidths of the unloaded horn are approximately 20° in both planes. The baffles produce a very symmetric main beam that has half-power beamwidths in the E- and H-planes equal to 10° .

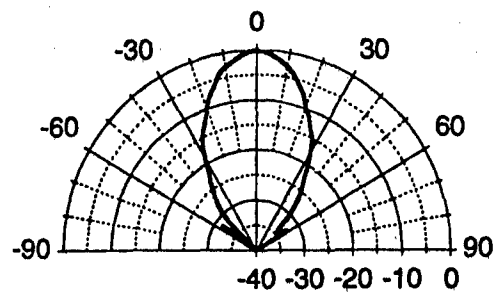
The E- and H-plane beam patterns of the unloaded horn and the horn loaded with the combination baffle are shown in Fig. 5.12. The E- and H-plane beam patterns are very similar to those calculated and plotted in Figs. 5.5 and 5.8, respectively. The unloaded horn suffers from the effects of phase curvature and the TE_{10} waveguide mode. The half-power beamwidths of the unloaded horn are approximately 20° in both planes. The baffles produce a very symmetric main beam that has half-power beamwidths in the E- and H-planes equal to 10° .

5.4.3 Comparison to an Optimum-Gain Horn

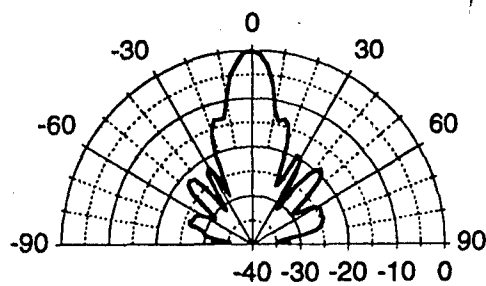
Without the use of a horn load, the most compact horn design is an optimum-gain horn. Using the Braun¹¹ design equations, the dimensions of an optimum-gain horn were calculated to give the antenna a gain of 23.1 dB. This gain value corresponds to the average gain of the wide-flare X-band horn with the combined baffles over the 4.5 dB enhancement band. The optimum-gain horn's dimensions are shown in Table 5.3. The optimum-gain horn's calculated on-axis length (distance from the throat to the aperture) is 11.5λ and its aperture area is $35.5\lambda^2$. Comparatively, at 10.5 GHz (the center of the enhancement band) the wide-flare horn's length is 5.5λ (see Table 5.1) and its aperture area is $28.6\lambda^2$. These dimensions show that the wide-flare X-band horn is 52% shorter than the optimum-gain horn, and its aperture area is 19% smaller than that of the optimum-gain horn. The wide-flare horn is not only considerably smaller than the optimum-gain horn, its aperture efficiency is also greater; the wide-flare horn's



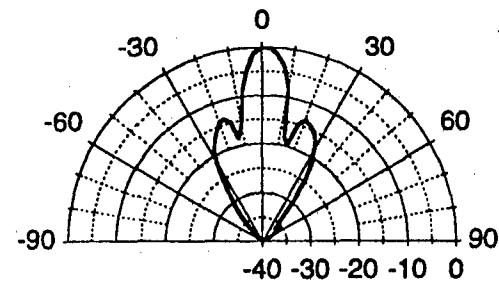
(a) Unloaded E-plane



(b) Unloaded H-plane



(c) E-plane with combination baffle



(d) H-plane with combination baffle

Figure 5.12
Measured beam patterns at 10.5 GHz.

aperture efficiency is over 55% and the optimum-gain horn's aperture efficiency is only 46%.

Table 5.3
Calculated dimensions of optimum-gain horn.

$y_{ap} = 5.1 \lambda$	$x_{ap} = 6.9 \lambda$
$\rho_e = 12.6 \lambda$	$\rho_h = 13.5 \lambda$
$\theta_e = 23^\circ$	$\theta_h = 30^\circ$

5.5 APPLICATION OF BAFFLED PYRAMIDAL HORN

A baffled pyramidal horn would be well-suited for medium-range installations where small, inexpensive, robust antennas are necessary. The antenna has enough gain to provide the necessary link margin over a medium-range path to combat fading, and the antenna's beam pattern will help to reduce multipath effects due to scattering objects. If installed on the long-range transmitter and receiver used in these tests, the system would have 30 dB of link margin at a range of approximately 1.5 km. However, multipath effects increase as the range increases. Thus, 30 dB of link margin may not be necessary over medium-range paths. Therefore, the reliable range using baffled horns would most likely extend past 1.5 km.

The baffled X-band horn presented in this section could be scaled to the Ka-band by reducing its dimensions by a factor of approximately 2.8. So a Ka-band baffle-loaded horn would be approximately 6 cm (2.7 in.) long and have an aperture with dimensions of 5 cm by 6 cm (2.2 in. by 2.7 in.). Comparatively, an optimum-gain Ka-band horn would have to be approximately 12 cm (5.3 in.) long with a 25% larger aperture than the baffle-loaded horn.

Ease of alignment is another benefit provided by using the baffle-loaded pyramidal horn. The Cassegrain parabolic reflectors used for testing had a gain

of approximately 35 dB and beamwidths of approximately 2° . Aligning two antennas to each other over a 10-km path proved to be difficult and time-consuming. The broader beam pattern of the baffle-loaded horn allows for easier alignment at the expense of antenna gain. In deployable systems, fast, reliable, installation may be an issue, and small, manageable antennas may be best suited for the situation.

6.0 CONCLUSIONS

This investigation confirmed that millimeter wave data links in physical security systems could be used for high speed data transmission. Statistical analysis for data links in locations that represent realistic climates where this link is likely to be deployed show very high link availability, especially for the 27-GHz link. Seven key elements were successfully demonstrated in this test:

- 1) Established the feasibility of low elevation (overland links up to 9.6 km, over water up to 10.8 km), low power millimeter wave data transmission of highly reliable data.
- 2) Millimeter wave data transmission reliability was tested at V-band for up to 1.3 km ranges in high RF traffic environments. No identifiable interference was observed in any of the test data.
- 3) Millimeter wave data links are insensitive to electronic interference, even when the electronic interference is near or in band, because of the highly directional nature of the antennas.
- 4) Reliable performance with commercial low-cost components was demonstrated under a wide variety of weather conditions.
- 5) Long-range, high speed data transmission with low power transmitters was accomplished. The long-range transmitter had an output power of 100 mW, the short-range transmitter had an output power of 50 mW, and data rates of 1.5 Mbps were transmitted with low bit error rates.
- 6) A low-cost two-way K-band (24 GHz) link was constructed and demonstrated with very low-cost parts. A similar Ka-band link can be constructed. Low-cost, commercially available antennas with gains greater than 37 dB were implemented with this link. This link was also demonstrated to be battery-operable with a small battery pack. The battery lifetime was about 24 h with continuous operation. Many of the components in this low-cost link were essentially the same as the 27-GHz test link. No special power-conserving electronics or

power management devices were used. It is possible that the battery life could be greatly improved.

- 7) A low-cost horn antenna was designed and tested at X-band (10 GHz), which can provide moderate gain (20–24 dB) with compact, low-cost, rugged antenna design. This design is scaleable to Ka-band (27 GHz) or V-band (60 GHz).

The effort documented in this report can be an effective demonstration for determining parameters of future data link designs. Furthermore, the present availability of low-cost components for the 27-GHz data link makes this link an economical choice. The rapid development of low-cost components for the 60-GHz link will make this an economical option, possibly within two years. The low-cost antenna design presented in this report should be extremely useful for both the 27-GHz and 60-GHz data links. The inherent line-of-sight nature of millimeter waves, as well as the directionality of the antennas and the large bandwidth availability, should allow use of the millimeter wave frequency bands with little or no interference.

This data link could provide a considerable added functionality to physical security systems. It could be possible to have two-way data transmissions with realtime video signals. High speed networking and repeater operations are also possible, allowing communications over obstructing hills or buildings.

Although Gunnplexers were used in the low-cost data link described in Appendix A, it could be possible to build fully-independent transmit and receive modules with DRO oscillators in the near future. Currently, Ka-band down-converters that have DRO oscillators, such as MDC28L by Microwave Devices Technology, are commercially available. Transmitters could be low power and still function at long ranges, as was demonstrated in this work.

APPENDIX A

LOW-COST DEMONSTRATION LINK

This page intentionally left blank.

A low-cost demonstration data link was developed to demonstrate the feasibility of building an inexpensive working system with operational parameters similar to those of the test links. The low-cost data link is a working system in the sense that it was designed for communications and not for testing. The link is compact and can be operated from a relatively small battery pack, making it easily deployable. The link can operate in full duplex mode and supports data rates high enough for realtime video. Since the test links described in Section 2.0 were designed to be as economical as possible, many of their components were already suited for the low-cost link. These components included most of the IF section, which transferred virtually intact from the test receivers to the low-cost link.

A Gunn oscillator-driven transceiver, called a Gunnplexer, was chosen to provide the low-cost link with K-band transmission and reception capabilities. The Gunnplexer is the least expensive transceiver currently available for microwave and millimeter wave systems. The Gunnplexer consists of a Gunn oscillator and a waveguide section that contains a mixer diode. The Gunn oscillator acts as the transmitter and the local oscillator for the mixer. Thus, the transmitted signal is always added to the received signal because of the dual role of the Gunn oscillator. These transceivers can be operated in full duplex mode if the transmitted signal is removed from the received signal. A differencing circuit is used to subtract the transmitted signal from the received signal after demodulation in the low-cost link to remedy this problem.

The Gunnplexer's frequency drifts with temperature. The drift rate will vary depending on the frequency and type of Gunn oscillator used. Sample testing of the Gunnplexers used in the low-cost link showed total drifts of less than 10 MHz over the expected temperature operating range. This frequency drift is dealt with in the low-cost link as it was in the test links; a wideband IF is used for tracking the received signal as it drifts. Time variations of the frequency drift are much longer than the time constant associated with the data. Thus, the

frequency tracking circuitry can track the slow changes in frequency caused by temperature variations while correctly demodulating the signal. The frequency tracking ability of the IF circuitry is well in excess of the expected maximum drift of the oscillators. The current techniques for frequency stabilization use ovens to hold the Gunn oscillator at a fixed temperature. This technique is very effective but consumes a significant amount of power, making it incompatible with a portable battery-powered unit. The Gunn oscillator bias can also be adjusted to compensate frequency drift caused by temperature variations if small drifts are unacceptable.

A block diagram of a low-cost transceiver module is shown in Fig. A.1. The signal to be transmitted first enters a transmitter buffer. The buffer adjusts the signal before it is applied to the tuning pin of the Gunnplexer. This adjustment consists of modifying the signal amplitude to acquire the proper frequency modulation index and adding a dc offset to set the Gunnplexer's center frequency. The received signal is mixed down to the IF frequency and then amplified before the IF controller board. This controller is the same as those used in the test links. The controller tracks the IF frequency and demodulates the signal. A block diagram of the IF controller is shown in Fig. 2.3. The transmitted signal is then subtracted from the received signal by a differencing circuit. Again, the subtraction must be performed because the transmitted signal modulates the Gunn oscillator, and the Gunn oscillator also acts as the local oscillator for the mixer.

One very important component used in the low-cost link is the DSS satellite antenna. This antenna is inexpensive, portable, and increases the system performance substantially. The DSS antenna is an offset-paraboloid reflector that was designed for satellite TV reception around 12 GHz, and also functions very well at 24 GHz. The antenna gain was found to be in excess of 38 dB with an aperture efficiency of approximately 50% at 24 GHz. In order to make a transceiver module and DSS reflector compatible, the reflector mounting bracket was modified to hold the transceiver at the focal point of the reflector,

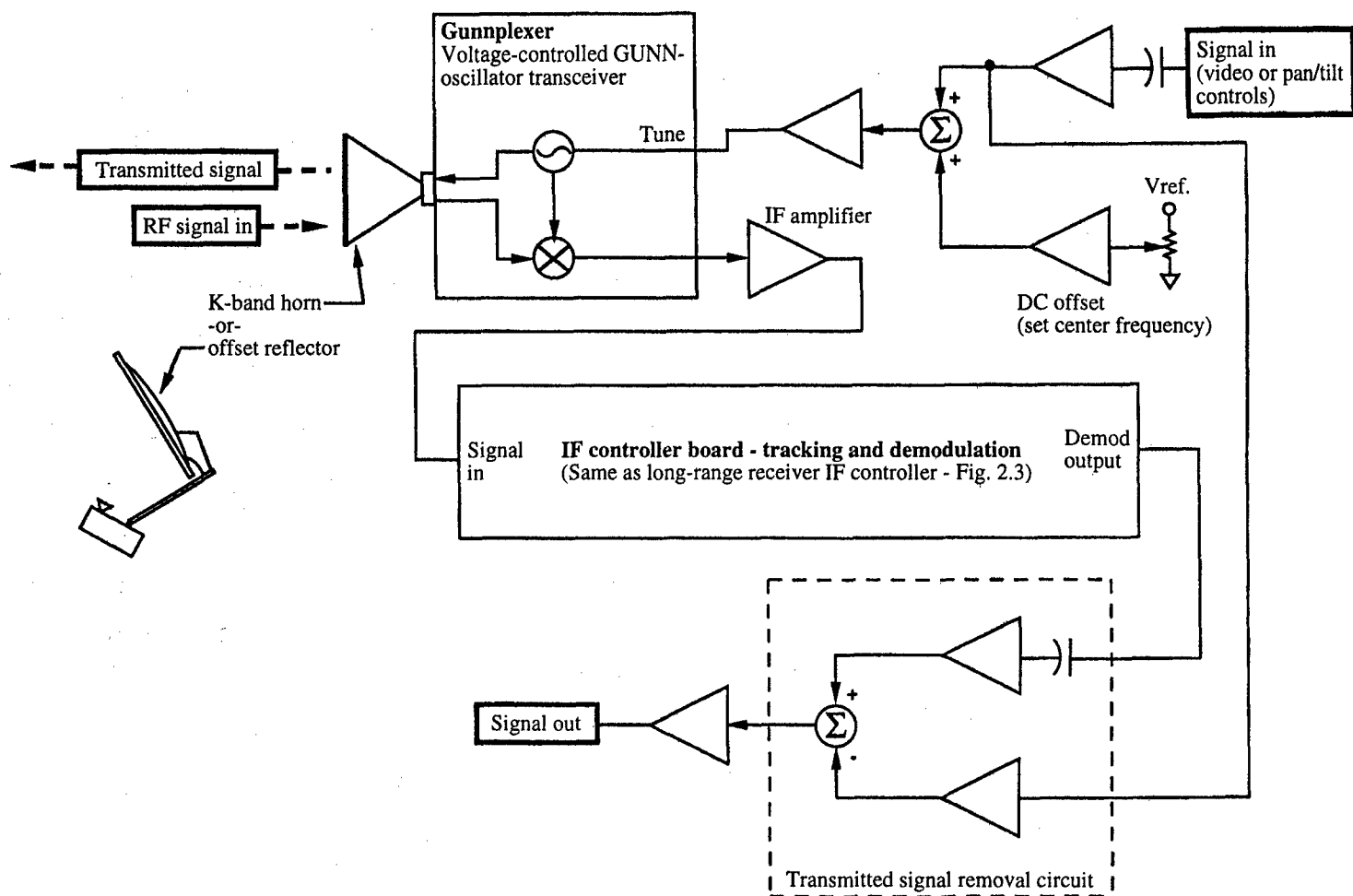


Figure A.1
Low-cost transceiver block diagram.

and a feed horn was attached to the Gunnplexer. Each feed horn is a small, inexpensive pyramidal horn that was shortened to reduce its aperture area. This modification produces a beam pattern that is sufficient to feed the reflector.

To demonstrate its functionality, the low-cost link was set up to transmit color NTSC video from a remote camera on a pan/tilt mount to a monitoring location where an operator could simultaneously send pan/tilt controls back to the camera. This system arrangement is shown in Fig. A.2. The system used two transceiver modules—one at the camera end and one at the monitoring end. The camera module transmitted NTSC video and received pan/tilt controls, and the monitoring module received the video and transmitted the controls. The NTSC signal was sent directly into the camera module for transmission. The pan/tilt controls were DTMF (dual tone multiple frequency) encoded and the tones were sent to the monitoring module. This was a full duplex arrangement with high data rate video going one direction and low rate tones coming back. Phase errors in the differencing circuit on the monitoring end were not a problem due to the low data rate of the transmitted DTMF signal. Therefore, the transmitted signal subtraction was performed with a simple operational amplifier circuit. Phase errors in the differencing amplifier could be an issue at the camera end if the entire spectrum of the video signal had to be subtracted. However, the same simple operational amplifier circuit was sufficient when followed by a low-pass filter because the received signal was at a much lower data rate than the video.

The data link was operated on batteries during the demonstration for periods of 8–10 h with no difficulty. It is estimated that, without changing the batteries, the unit will continuously transmit and receive for approximately 24 h. The circuits used were prototype circuits only, using standard parts, and no effort was made to minimize or manage power consumption in the transceiver modules.

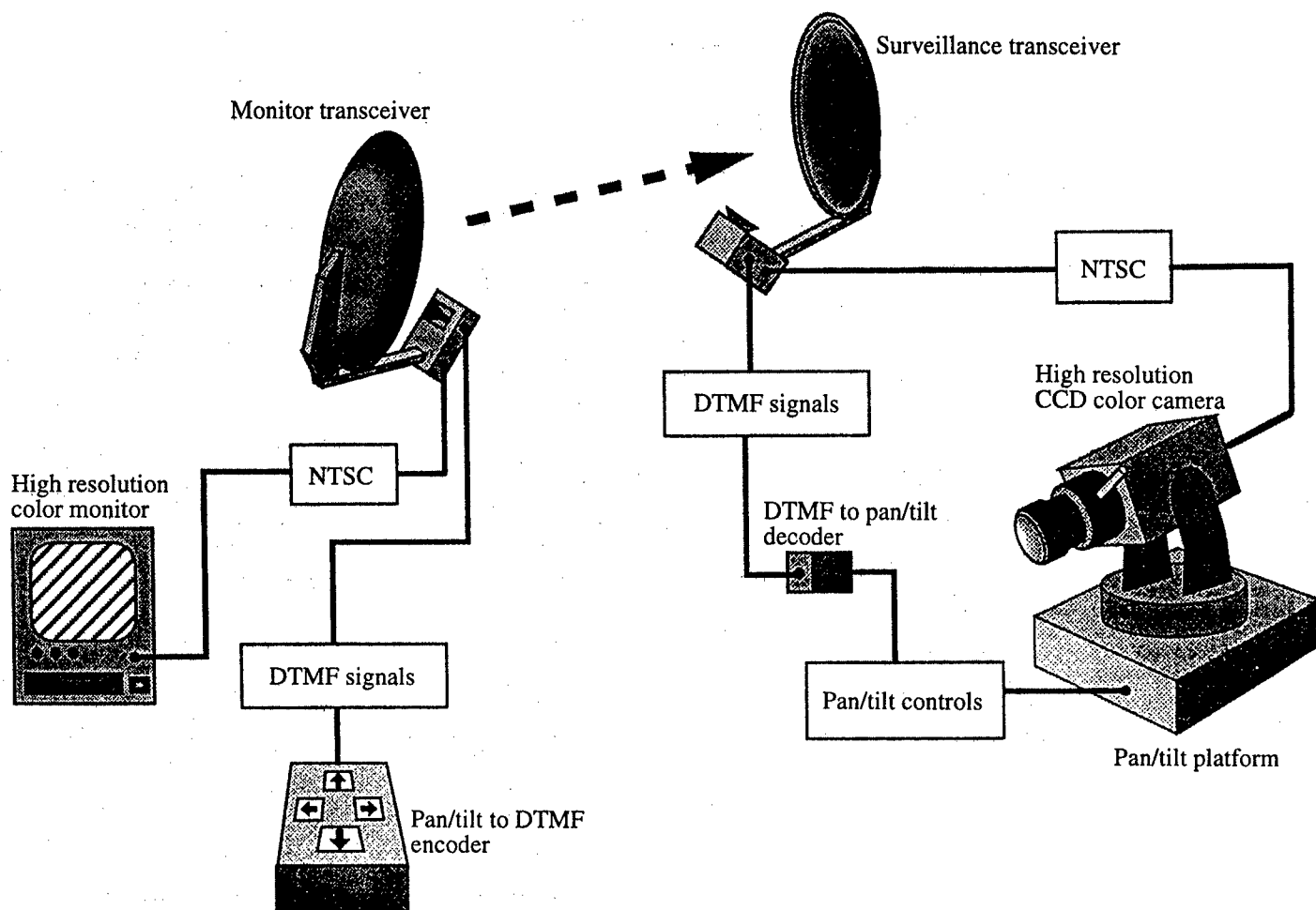


Figure A.2
Low-cost data link functional diagram.

New millimeter wave components are now becoming available that will not require the use of Gunnplexers. An example is the L-band to Ka-band upconverters and down-converters that are now available. The availability of these units will substantially increase in the next several years as the LMDS market expands. An estimated link budget for the low-cost data link is given in Table A.1. This table shows that even with the low-cost components, the line still has enough margin (over 40 dB) to allow high reliability transmissions. Table A.2 gives detailed specifications of the low-cost demonstration link. Table A.3 gives the physical characteristics of the low-cost data link. The entire assembly, with batteries and the large reflector antenna, weighs under 40 lb, making this data link very portable and useful for deployed security systems where realtime video is needed.

Table A.1
Link budget.

Transmitter Power	17 dBm
Transmit Antenna Gain	38 dB
Modulation Type	FM
Receiver Noise Figure	17 dB Max.
Receiver Bandwidth	7 MHz–17 MHz
Optimum Link Margin at 7 km	42 dB
Test Data Transmitted	NTSC Realtime Video

Table A.2
Specifications of the low-cost demonstration link.

Typical Transmitter Power	17 dBm
Typical Receiver Noise Figure	17 dB
Frequency of Operation of Prototype	23.5 GHz / 24.5 GHz
Modulation Type	FM/FSK
Oscillator Type	Gunn Diode
IF Bandwidth	Selectable, 7 MHz/17 MHz
Data Rate (With Present IF Circuits)	3.6 Mbps Max.
Receiver Tuning Bandwidth	1 GHz
Demodulation Type	Phase Locked Loop

Table A.3
Low-cost data link features.

- Battery-powered (24 h with no power management on current prototypes)
- Maximum range with 30 dB; signal-to-noise ratio is 20 km; typical operation is expected to be 7 km
- Antenna type: offset-fed reflector for long range/small horn for short range
 - 18 in. diameter dish
 - 2 in. x 2 in. small horn
- Modulation type
 - FM
 - FSK
- Data Transmission: Digital (4.5 MB/s max. with current prototypes)
 - NTSC color video, one-way with current prototypes
- Link type
 - Two-way, full duplex (current prototype)
- Line-of-sight
- Narrowbeam pattern transmission and reception
 - Low probability of intercept/interference
- Hand-portable

— Transceiver:	6 lb
— Antenna with mounting bracket:	9 lb
— Battery weight:	24 lb
- 24 h operation with camera and pan-tilt
- Improvements:
 - Can be made to transmit video both directions in full duplex
 - Can add data transmission channels

APPENDIX B

NUMERICAL ANTENNA ANALYSIS

This page intentionally left blank.

B.1 E-PLANE, TWO-DIMENSIONAL PEC MFIE

The two-dimensional E-plane horn and E-plane baffle are modeled as PEC scattering objects in Fig. 5.2, top. All objects in the model are infinite in the direction perpendicular to the E-plane. This direction is denoted z to follow the conventions of radial wave propagation. The source, J^{src} , is positioned near the end of the waveguide. It is a thin sheet of current, infinite in z , with x - and y -components only ($J_z^{src} \hat{z} = A_z \hat{z} = 0$). This is a TE^z polarized model due to the configuration of the scattering objects and source; thus, the only fields that exist¹⁶ are $E_x \hat{x}$, $E_y \hat{y}$, and $H_z \hat{z}$.

A relatively simple solution can be formulated for $H_z \hat{z}$ in the E-plane model. First, an integral equation is formed from the boundary conditions along the scattering surfaces that relates the total magnetic field to equivalent electric current densities. The integral equation is then solved for the equivalent currents, and $H_z \hat{z}$ is calculated from the currents.

The equivalent electric surface currents are all parallel to the x - y plane and lie along the contour, C , of the PEC objects (see Fig. 5.2, top). The equivalent currents are represented as $J_c(\rho, \phi) \hat{c}$, where the unit vector $\hat{c} = -\hat{n} \times \hat{z}$ is directed along C and \hat{n} is the outward pointing normal to C . $H_z(\rho, \phi) \hat{z}$, at some point $P(\rho, \phi)$, is now expressed in terms of these currents radiating into an unbounded medium:^{13,14}

$$H_z(\rho, \phi) \hat{z} = \hat{z} \frac{jk_o}{4} \int_C J_c(\rho', \phi') \cos(\psi') H_1^{(2)}(k_o R) dc' \quad . \quad (B.1)$$

The primed coordinates in Eq. (B.1) indicate the location of the current, and the unprimed coordinates designate the observation location. The angle between

\hat{r} and \hat{n}' is ψ' , where \hat{r} is the unit vector directed from the equivalent current to $P(\rho, \phi)$ and \hat{n}' is the normal vector to the current.¹⁴ The function $H_1^{(2)}$ in the integral is the first-order Hankel function of the second kind.

The electric surface current densities along the PECs are equivalent to the total magnetic field just outside of the PECs. This is expressed by the following boundary condition:¹³

$$\hat{c} J_c(\rho, \phi)|_{PEC} = \hat{n} \times \hat{z} H_z^{total}|_{PEC} = \hat{n} \times \hat{z} (H_z^i + H_z^s)|_{PEC} \quad (B.2)$$

The incident magnetic field, H_z^i , is the component of the total field produced by the source, and the scattered magnetic field, H_z^s , is produced by the equivalent currents along the PEC scattering surfaces. When Eq. (B.1) is substituted for the scattered fields in Eq. (B.2), (B.2) becomes¹³

$$J_c(\rho, \phi)|_{PEC} + \frac{jk_o}{4} \int_C J_c(\rho', \phi') \cos(\psi') H_1^{(2)}(k_o R) dc' \Big|_{PEC} = -H_z^i|_{PEC} \quad (B.3)$$

Equation (B.3) is the two-dimensional, TE^z, magnetic field integral equation (MFIE) for the equivalent electric currents along the PEC surfaces.

B.2 H-PLANE, TWO-DIMENSIONAL PEC EFIE

The two-dimensional H-plane model, pictured in Fig. 5.2, bottom, is very similar to the E-plane model. The source is an infinitely thin wire of current that is infinite in the z-direction and centered near the end of the waveguide ($I_x^{src} \hat{x} = A_x \hat{x} = I_y^{src} \hat{y} = A_y \hat{y} = 0$). Only $H_x \hat{x}$, $H_y \hat{y}$, and $E_z \hat{z}$ exist,¹⁶ making this a TM^z polarized model. $E_z \hat{z}$ is calculated by formulating an integral equation that

relates the equivalent electric current densities to the electric field along the PEC boundaries as $H_z \hat{z}$ is calculated in the E-plane model.

The surface current densities are all perpendicular to the x-y plane. $E_z(\rho, \phi) \hat{z}$, at some point $P(\rho, \phi)$, can be expressed in terms of these currents radiating into an unbounded medium¹³ as

$$E_z(\rho, \phi) \hat{z} = -\hat{z} \frac{\omega \mu_o}{4} \int_C J_z(\rho', \phi') H_0^{(2)}(k_o R) dc' \quad (B.4)$$

The function $H_0^{(2)}$ is the zero-order Hankel function of the second kind. The tangential electric field must be zero on the surface of the PECs. This boundary condition is expressed as

$$\hat{z} E_z^s(\rho, \phi) \Big|_{PEC} + \hat{z} E_z^i(\rho, \phi) \Big|_{PEC} = 0 \quad (B.5)$$

where E_z^s is the scattered field produced by the equivalent currents and E_z^i is the incident field produced by the source. When Eq. (B.4) is substituted for the scattered field in Eq. (B.5), (B.5) becomes¹³

$$\frac{\omega \mu_o}{4} \int_C J_z(\rho', \phi') H_0^{(2)}(k_o R) dc' \Big|_{PEC} = E_z^i \Big|_{PEC} \quad (B.6)$$

Equation (B.6) is the electric field integral equation (EFIE) for the equivalent electric surface currents.

B.3 MOMENT METHOD

The moment method is applied to numerically solve the MFIE, Eq. (B.3), and the EFIE, Eq. (B.6), for the equivalent surface currents in the separate models.¹²⁻¹⁴ The moment method involves expanding the unknown current in the integral equation into N linearly independent basis functions with unknown coefficients resulting in one equation with N unknowns. To resolve the system, N linearly independent equations are needed. Therefore, the inner products of N linearly independent weighting functions are taken with the integral equation resulting in N equations with N unknowns.

The basis function chosen to expand the unknown current densities, J_c in Eq. (B.3) and J_z in Eq. (B.6), is a pulse function of length Δ so that

$$J_c(\rho', \phi') = J_c(c') = \sum_{n=1}^N J_{cn} P\left(c' - c'_n, \frac{\Delta}{2}\right) \quad (\text{B.7a})$$

for the MFIE, and

$$J_z(c') = \sum_{n=1}^N J_{zn} P\left(c' - c'_n, \frac{\Delta}{2}\right) \quad (\text{B.7b})$$

for the EFIE. The pulse function is defined as

$$P\left(x - x_n, \frac{\Delta}{2}\right) = \begin{cases} 1: & |x_n - x| < \frac{\Delta}{2} \\ 0: & \text{otherwise} \end{cases} \quad (\text{B.8})$$

The set of weighting functions used to resolve the unknowns in each model is the set of Dirac delta functions,

$$[w_m] = [\delta(c - c_m)] \quad m = 1 \dots N \quad , \quad (B.9a)$$

where

$$\delta(c - c_m) = \begin{cases} 1: & c = c_m \\ 0: & \text{otherwise} \end{cases} \quad . \quad (B.9b)$$

The points where the weighting functions are non-zero are where the boundary conditions are enforced or tested. Each test point is centered on a basis function.

When each unknown current density is expanded and the boundary conditions are matched according to the weighting functions, each integral involving the unknown forms a parameter matrix.¹⁴ The MFIE for the E-plane becomes

$$[P_{mn}][J_{cn}] = [-H_{zn}^i] \quad , \quad (B.10)$$

and the EFIE for the H-plane becomes

$$[P_{mn}][J_{zn}] = [E_{zn}^i] \quad . \quad (B.11)$$

The parameter matrices are found by calculating the integrals over the appropriate basis and test point, and the incident fields are calculated from the known sources.

B.4 INTEGRATION

A number of numerical integration techniques can be used to evaluate the integrals in the parameter matrices of Eqs. (B.10) and (B.11). For our analysis, the integrals are calculated quickly and easily using a rectangular approximation. The integral over each basis is approximated by multiplying the value of the function at the center of the basis by the length of the basis, Δ . This is a crude approximation, but the results become accurate for small values of Δ .

The integration is straightforward except for the cases where a basis and a test point coincide. This occurs in the matrix self-terms where the test point is on the basis current from which the radiated fields are being calculated. In the MFIE and the EFIE, the self-term integration is over a line where the Hankel function has a singularity. These integrals do not have to be calculated in the MFIE. It can be shown¹²⁻¹⁴ that the tangential magnetic field along a basis produced by the equivalent current on the same basis can be expressed as

$$H_z^{J_{cb}} \Big|_{\Delta} = -\frac{J_{cb}\Delta}{2} \Big|_{\Delta} \quad , \quad (B.12)$$

and Eq. (B.3) becomes

$$\frac{J_c(\rho, \phi)}{2} \Big|_{\Delta} = -H_z^i \Big|_{\Delta} \quad . \quad (B.13)$$

A simple relationship between the electric field at a basis and the equivalent currents along the same basis for the EFIE does not exist, and the integral must be calculated. The Hankel function is replaced by a small argument approximation,

$$\lim_{u \rightarrow 0} H_o^{(2)}(u) = \lim_{u \rightarrow 0} [J_0(u) - jN_0(u)] \approx 1 - j \frac{2}{\pi} \left[\ln \frac{u}{2} + \gamma \right] \quad , \quad (\text{B.14})$$

where γ is Euler's constant. The scattered field on the left-hand side of Eq. (B.6) becomes

$$E_z^{J_{z\Delta}} \Big|_{\Delta} \approx J_{z\Delta} \frac{\omega \mu_o}{4} 2 \int_0^{\frac{\Delta}{2}} \left[1 - j \frac{2}{\pi} \left[\ln \frac{\Delta}{2} + \gamma \right] \right] dc' = \quad (\text{B.15})$$

$$J_{z\Delta} \frac{\omega \mu_o}{2} \Delta \left[1 - j \frac{2}{\pi} \left[\ln \left(\frac{k_o \Delta}{4} \right) - 1 + \gamma \right] \right]$$

B.5 INTERIOR-FIELDS AND FAR-FIELDS

The magnetic field and the electric field in the E- and H-plane models, respectively, are found by summing the fields radiated from the equivalent current densities and the source. The horn's interior fields are found by solving Eqs. (B.1) for the magnetic field and (B.4) for the electric field using the integration techniques discussed previously. The far-fields are found similarly using large-argument approximations of the Hankel functions.^{14,17}

B.6 DIRECTIVITY, DIRECTIVE GAIN, AND BEAM PATTERNS

Directivity is the on-axis directive gain, and directive gain in two-dimensions (no z-variations) is defined as

$$D_g(\phi) = \frac{2\pi \rho z W_{rad}(\phi)}{P_{rad}} \quad , \quad (\text{B.16})$$

where $W_{rad}(\phi)$ is the radiation density, and P_{rad} is the total radiated power from the antenna. In the far-field, the directive gain becomes

$$D_g(\phi_m) = \frac{2\pi |H_z(\phi_m)|^2}{\int_0^{2\pi} |H_z(\phi)|^2 d\phi} \quad , \quad (B.17)$$

for the E-plane calculations. The integral in Eq. (B.17) can be approximated by summing incremental values of the far-field and multiplying by the incremental arc lengths. When the far-fields are calculated at 1° increments and each arc length is approximated as a straight line, Eq. (B.17) becomes¹⁴

$$D_g(\phi_m) \cong \frac{2\pi |H_z(\phi_m)|^2}{2\pi/360 \sum_{n=0}^{359} |H_z(\phi_n)|^2} = \frac{360 |H_z(\phi_m)|^2}{\sum_{n=0}^{359} |H_z(\phi_n)|^2} \quad (B.18)$$

Similarly, directive gain in the H-plane model is calculated by

$$D_g(\phi_m) \cong \frac{2\pi |E_z(\phi_m)|^2}{2\pi/360 \sum_{n=0}^{359} |E_z(\phi_n)|^2} = \frac{360 |E_z(\phi_m)|^2}{\sum_{n=0}^{359} |E_z(\phi_n)|^2} \quad (B.19)$$

Beam patterns are produced by plotting the directive gain at 1° intervals and normalizing the values.

B.7 INPUT IMPEDANCE AND GAIN

When the waveguide dimensions are chosen so that only the fundamental parallel-plate waveguide mode propagates (TEM for the E-plane and TE_1 for the H-plane), transmission line principles can be used to calculate

the antenna's input impedance and reflection efficiency.¹⁸ The current reflection coefficient

$$\Gamma = |\Gamma|e^{j\theta} \quad (\text{B.20})$$

is found from the current standing wave pattern in the waveguide antenna feed. The magnitude of Γ is calculated from the standing wave ratio (SWR)

$$|\Gamma| = \frac{SWR - 1}{SWR + 1}, \quad (\text{B.21})$$

where SWR is defined as

$$SWR = \frac{J_{max}}{J_{min}} \quad (\text{B.22})$$

J_{max} and J_{min} are the maximum and minimum amplitudes of the electric current density on the waveguide walls. These current extremes are found by examining the current amplitudes starting at the antenna-waveguide junction and searching back toward the source through at least one wavelength of distance along the upper waveguide conductor. The phase of the reflection coefficient is defined as

$$\theta = \pi + 2\beta l_{min} \quad (\text{B.23})$$

where l_{min} is the distance from the antenna-waveguide junction to the first current minimum.

The relative input impedance is the ratio of the antenna's input impedance to the characteristic impedance of the waveguide; it can be calculated from the current reflection coefficient,

$$Z_{rel} = \frac{Z_{in}}{Z_0} = \frac{1 - \Gamma}{1 + \Gamma} \quad (B.24)$$

Assuming there are no conductor losses in the antenna and waveguide, the total power radiated by the antenna is equivalent to the input power minus the reflected power. Thus, the total radiated power is related to the input power by

$$P_{rad} = (1 - |\Gamma|^2) P_{in} \quad (B.25)$$

The antenna gain then becomes¹⁵

$$G(\phi) = \frac{P_{rad} D_g(\phi)}{P_{in}} = (1 - |\Gamma|^2) D_g(\phi) \quad (B.26)$$

The coefficient, $(1 - |\Gamma|^2)$, is termed the reflection efficiency. The total antenna efficiency, ϵ_r , is equal to the reflection efficiency if there are no other losses in the antenna.

APPENDIX C

DD FORM 1494

This page intentionally left blank.

APPLICATIONS FOR EQUIPMENT FREQUENCY ALLOCATION	CLASSIFICATION UNCLASSIFIED	DATE 18 Sep 95	Form Approved OMB No. 0704-0188 Page 1 of <u>7</u> Pages
DOD GENERAL INFORMATION			
TO Headquarters AF Frequency Management Agency Washington, D.C. 20330-6340	FROM Applied Research Laboratories The University of Texas at Austin P.O. Box 8029 Austin, TX 78713-8029		
1. APPLICATION TITLE Millimeter Wave Non-rf Non-Hardware Data Link			
2. SYSTEM NOMENCLATURE Short Range Non-rf Non Hardware Data Link AN/TKC			
3. STAGE OF ALLOCATION (x one) <div style="display: flex; justify-content: space-around; align-items: flex-end;"> <div><input type="checkbox"/> a. STAGE 1 CONCEPTUAL</div> <div><input checked="" type="checkbox"/> b. STAGE 2 EXPERIMENTAL</div> <div><input type="checkbox"/> c. STAGE 3 DEVELOPMENTAL</div> <div><input type="checkbox"/> d. STAGE 4 OPERATIONAL</div> </div>			
4. FREQUENCY REQUIREMENTS a. FREQUENCY (IES) 60 GHz. See Remark (1) b. EMISSION DESIGNATORS 7M00F2D (Experiments System) See Remarks (2) and (3)			
5. TARGET STARTING DATE FOR SUBSEQUENT STAGES <div style="display: flex; justify-content: space-between;"> <div style="width: 30%;">a. STAGE 2 November 1995 (estimated)</div> <div style="width: 30%;">b. STAGE 3 January 1997 (estimated)</div> <div style="width: 30%;">c. STAGE 4 January 1999 (estimated)</div> </div>			
6. EXTENT OF USE 24 hrs/day, 7 days/week			
7. GEOGRAPHICAL AREA FOR a. STAGE 2 Eglin AFB, Minot AFB, Davis Monthan AFB, Lackland AFB, Randolph AFB b. STAGE 3 N/A c. STAGE 4 N/A			
8. NUMBER OF UNITS <div style="display: flex; justify-content: space-between;"> <div style="width: 30%;">a. STAGE 2 2 Transmitter Receiver Pairs (ea pair at different location)</div> <div style="width: 30%;">b. STAGE 3 Navail</div> <div style="width: 30%;">c. STAGE 4 Navail</div> </div>			
9. NUMBER OF UNITS OPERATING SIMULTANEOUSLY IN THE SAME ENVIRONMENT Stage 2: One transmitter and one receiver in the same environment			
10. OTHER J/F 12 APPLICATION NUMBER(S) TO BE <div style="display: flex; justify-content: space-between;"> <div><input type="checkbox"/> a. SUPERSEDED J/F</div> <div><input type="checkbox"/> b. RELATED J/F N/A</div> </div>		11. IS THERE ANY OPERATIONAL REQUIREMENT AS DESCRIBED IN THE INSTRUCTIONS FOR PARAGRAPH 11? <div style="display: flex; justify-content: space-around;"> <input type="checkbox"/> a. YES <input checked="" type="checkbox"/> b. NO <input type="checkbox"/> c. NAail </div>	
12. NAMES AND TELEPHONE NUMBERS <div style="display: flex; justify-content: space-between;"> <div style="width: 40%;">a. PROGRAM MANAGER William Witter</div> <div style="width: 20%;">(1) COMMERCIAL (703) 325-1002</div> <div style="width: 20%;">(2) AUTOVON 221-1002</div> </div> <div style="display: flex; justify-content: space-between;"> <div style="width: 40%;">b. PROJECT Robert L. Rogers</div> <div style="width: 20%;">(1) COMMERCIAL (512) 835-3307</div> <div style="width: 20%;">(2) AUTOVON</div> </div>			
13. REMARKS (1) From item 4: Free running Gunn diodes will be used for the transmitter and first local oscillator. These devices drift substantially in frequency, and no simple fix is available. This problem is under consideration at present and suitable modifications will be made for the final systems to improve this characteristic at later stages. Frequency drift is thermally induced and for operating temperatures that will be experienced is expected to be less than ± 200 MHz (± 3300 ppm). (2) From item 4: More channels are expected to be used in the later stages. The tests for this stage are for evaluation of transmission channel quality and reliability. The emission designator for the later stages will be: 7M00F7D. The number of channels, channel spacing, and bandwidth will be determined by frequency availability and technological limitations. (3) From item 4: There is a possibility phase modulation may be used in the later stages as well as frequency modulation.			
DOWNGRADING INSTRUCTIONS N/A		CLASSIFICATION UNCLASSIFIED	

CLASSIFICATION UNCLASSIFIED		PAGE 2 of 7
TRANSMITTER EQUIPMENT CHARACTERISTICS		
1. NOMENCLATURE, MANUFACTURER'S MODEL NO. Short Range Non-rf Non Hardwire Data Link Transmitter AN/TKC	2. MANUFACTURER'S NAME Gunn diodes, isolator, and bias control were manufactured by Millitech Corporation	
3. TRANSMITTER INSTALLATION Deployed at Air Base	4. TRANSMITTER TYPE FSK Digital Data Transmission	
5. TUNING RANGE for Stage 2: 59.5 GHz to 60.5 GHz	6. METHOD OF TUNING Combination of cavity tuning and bias tuning	
7. RF CHANNELING CAPABILITY N/A for Stage 2	8. EMISSION DESIGNATOR(S) 7M00F2D See Remark (1)	
9. FREQUENCY TOLERANCE -67ppm/°C change of oscillator temp from 25°C ambient; expected total drift < ±3300ppm	10. FILTER EMPLOYED (x one) <div style="display: flex; justify-content: space-around;"> <input type="checkbox"/> a. YES <input checked="" type="checkbox"/> b. NO </div>	
11. SPREAD SPECTRUM (x one) <div style="display: flex; justify-content: space-around;"> <input type="checkbox"/> a. YES <input checked="" type="checkbox"/> b. NO </div>	12. EMISSION BANDWIDTH (x and complete as applicable) <div style="display: flex; justify-content: space-around;"> <input type="checkbox"/> CALCULATED <input checked="" type="checkbox"/> MEASURED </div>	
13. MAXIMUM BIT RATE 1.5 MB/s See Remark (3)	14. MODULATION TECHNIQUES AND CODING FSK modulation Manchester encoding for data (except at 19.2 Kb/s where no coding is used)	
16. PRE-EMPHASIS (x one) <div style="display: flex; justify-content: space-around;"> <input type="checkbox"/> a. YES <input checked="" type="checkbox"/> b. NO </div>	15. MAXIMUM MODULATION FREQUENCY Navail	
19. POWER a. MEAN 100 mW b. PEP 100 mW	17. DEVIATION RATIO <small>Deviation ratio ranges from 0.1 to 4 (higher deviation ratios only apply to lower data rates; minimum data rate is 19.2kb/s)</small>	
20. OUTPUT DEVICE Gunn diode for Stage 2	18. PULSE CHARACTERISTICS a. RATE N/A b. WIDTH N/A c. RISE TIME N/A d. FALL TIME N/A e. COMPRESSION N/A	
22. SPURIOUS LEVEL Navail	21. HARMONIC LEVEL a. 2nd Navail b. 3rd Navail c. OTHER Navail	
23. FCC TYPE ACCEPTANCE NO. Navail	24. REMARKS (1) From item 8: Some applications in later stages may require more bandwidth, such as the transmission of video data. (2) From item 11: Later stages may employ spectral spreading depending on the results of present testing. (3) From item 13: Stage 2 tests will be at varying data rates of 19.2 kb/s, 64 kb/s, and 1.5 MB/s.	
CLASSIFICATION UNCLASSIFIED		

CLASSIFICATION

UNCLASSIFIED

PAGE

3 of 7

RECEIVER EQUIPMENT CHARACTERISTICS

1. NOMENCLATURE, MANUFACTURER'S MODEL NO.

Short Range Non-rf Non Hardwire Data Link Receiver
AN/TKC

2. MANUFACTURER'S NAME

Gunn diodes, isolator, bias control and filters were
manufactured by Millitech Corporation

3. RECEIVER INSTALLATION

Deployed at Air Base

4. RECEIVER TYPE

Double conversion FSK

5. TUNING RANGE

59 GHz to 61 GHz

6. METHOD OF TUNING

Combination of cavity tuning, bias tuning, and vacator tuning

7. RF CHANNELING CAPABILITY

N/A for Stage 2

8. EMISSION DESIGNATOR(S)

7M00F2D See Remark (1)

9. FREQUENCY TOLERANCE

-67ppm/°C change of oscillator temp from 25°C ambient; expected total drift $\leq \pm 3300$ ppm

10. IF SELECTIVITY

1st

2nd

3rd

a. -3 dB

1.2 GHz

7MHz/17MHz

N/A

b. -20 dB

Navail

Navail

Navail

c. -60 dB

Navail

Navail

Navail

12. IF FREQUENCY

a. 1st 1.5 GHz

b. 2nd 479 MHz

c. 3rd N/A

15. OSCILLATOR TUNED

1st

2nd

3rd

a. ABOVE TUNED FREQUENCY

479MHz

b. BELOW TUNED FREQUENCY

1.5 GHz

c. EITHER ABOVE OR
BELOW

N/A

18. DE-EMPHASIS (x one)

☐

a. YES

☒

b. NO

19. IMAGE REJECTION

Estimated to be more than 30 dB

11. RF SELECTIVITY (x and complete as applicable)

☒

CALCULATED

☐

MEASURED

a. -3 dB 3.9 GHz

b. -20 dB Navail

c. -60 dB Navail

d. Preselection Type

Waveguide filter

13. MAXIMUM POST DETECTION FREQUENCY

Navail

14. MINIMUM POST DETECTION FREQUENCY

N/A

16. MAXIMUM BIT RATE

1.5 MB/s See Remark (2)

17. SENSITIVITY.

a. SENSITIVITY -90 dBm at 7 MHz, -86 dBm at 17 MHz

b. CRITERIA Signal acquisition by Phase
Locked Loop Demodulator

c. NOISE FIG 8.5 dB to 10 dB dB

d. NOISE TEMP 2000 K to 2600 K Kelvin

20. SPURIOUS REJECTION

NAvail

20. REMARKS

(1) From item 8: Some applications in later stages may require more bandwidth, such as the transmission of video data.

(2) From item 16: Stage 2 tests will be at varying data rates of 19.2 kb/s, 64 kb/s, and 1.5 MB/s.

CLASSIFICATION

UNCLASSIFIED

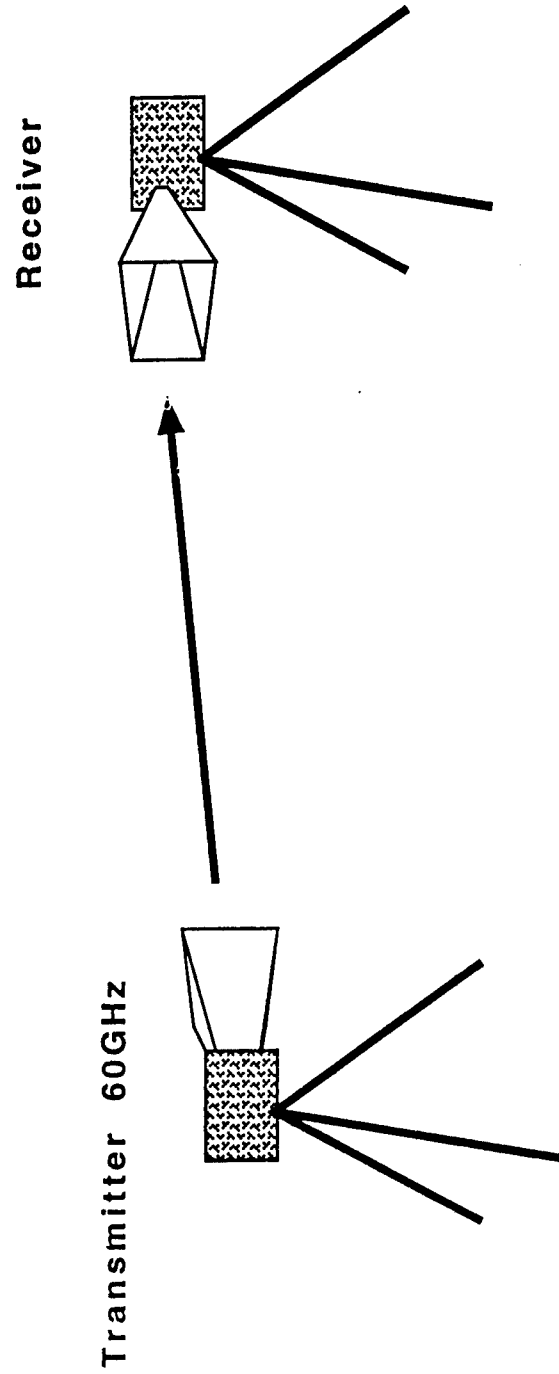
CLASSIFICATION UNCLASSIFIED		PAGE 4 of 7
ANTENNA EQUIPMENT CHARACTERISTICS		
<div style="display: flex; justify-content: space-between;"> <input type="checkbox"/> a. TRANSMITTING <input type="checkbox"/> b. RECEIVING <input checked="" type="checkbox"/> c. TRANSMITTING AND RECEIVING </div>		
2. NOMENCLATURE, MANUFACTURER'S MODEL NO. DLH-141-R415 Dielectric Horn Antenna	3. MANUFACTURER'S NAME Millitech Corporation	
4. FREQUENCY RANGE Navail	5. TYPE Horn antenna with dielectric lens	
6. POLARIZATION Linear, horizontal or vertical	7. SCAN CHARACTERISTICS	
8. GAIN	a. TYPE N/A	
a. MAIN BEAM 33 dB nominal	b. VERTICAL N/A	
b. 1st MAJOR SIDE 17 dB to 20 dB below main beam	(1) Max Elev N/A	
9. BEAMWIDTH	(2) Min Elev N/A	
a. HORIZONTAL H-Plane for vertical polarization: 3.5°	(3) Scan Rate N/A	
b. VERTICAL E-Plane for vertical polarization: 4°	c. HORIZONTAL SCAN	
d. SECTOR BLANKING (x one)		<input type="checkbox"/> (1) Yes <input checked="" type="checkbox"/> (2) No
10. REMARKS Dielectric lens horn antenna is interchangeable with standard gain horn antenna.		
CLASSIFICATIONS UNCLASSIFIED		

CLASSIFICATION UNCLASSIFIED		PAGE 5 of 7
ANTENNA EQUIPMENT CHARACTERISTICS		
<div style="display: flex; justify-content: space-between;"> <input type="checkbox"/> a. TRANSMITTING <input type="checkbox"/> b. RECEIVING <input checked="" type="checkbox"/> c. TRANSMITTING AND RECEIVING </div>		
2. NOMENCLATURE, MANUFACTURER'S MODEL NO. SGH-15 Standard Gain Horn Antenna	3. MANUFACTURER'S NAME Millitech Corporation	
4. FREQUENCY RANGE Navail	5. TYPE Pyramidal horn antenna	
6. POLARIZATION Linear, horizontal or vertical	7. SCAN CHARACTERISTICS	
8. GAIN	a. TYPE N/A	
a. MAIN BEAM 24 dB nominal	b. VERTICAL N/A	
b. 1st MAJOR SIDE N/A	(1) Max Elev N/A	
9. BEAMWIDTH	(2) Min Elev N/A	
a. HORIZONTAL H-Plane for vertical polarization: 9.5°	(3) Scan Rate N/A	
b. VERTICAL E-Plane for vertical polarization: 10.5°	c. HORIZONTAL SCAN	
10. REMARKS Standard gain horn antenna is interchangeable with dielectric lens horn antenna.		(1) Sector Scanned N/A
(2) Scan Rate N/A		d. SECTOR BLANKING (x one)
(1) Yes <input type="checkbox"/>		(2) No <input checked="" type="checkbox"/>
CLASSIFICATIONS UNCLASSIFIED		

APPLICATION FOR SPECTRUM REVIEW	CLASSIFICATION UNCLASSIFIED	PAGE 6 of 7
NTIA GENERAL INFORMATION		
1. APPLICATION TITLE Millimeter Wave Non-rf Non-Hardware Data Link		
2. SYSTEM NOMENCLATURE Short Range Non-rf Non Hardware Data Link AN/TKC		
3. STAGE OF ALLOCATION (x one) <div style="display: flex; justify-content: space-around; align-items: flex-start;"> <div style="text-align: center;"> <input type="checkbox"/> a. STAGE 1 CONCEPTUAL </div> <div style="text-align: center;"> <input checked="" type="checkbox"/> b. STAGE 2 EXPERIMENTAL </div> <div style="text-align: center;"> <input type="checkbox"/> c. STAGE 3 DEVELOPMENTAL </div> <div style="text-align: center;"> <input type="checkbox"/> d. STAGE 4 OPERATIONAL </div> </div>		
4. FREQUENCY REQUIREMENTS a. FREQUENCY(IES) 60 GHz See Remark (1) b. EMISSION DESIGNATOR(S) 7M00F2D (Experimental System) See Remarks (2) and (3)		
5. PURPOSE OF SYSTEM, OPERATIONAL AND SYSTEM CONCEPTS (WARTIME USE) (x one) <input checked="" type="checkbox"/> a. YES <input type="checkbox"/> b. NO This system is a data transmission link intended for use in deployable automated security systems. This system will operate as a line of sight data transmission link within and around the perimeter of a forward deployed air base. It may also be used at permanent base facilities.		
6. INFORMATION TRANSFER REQUIREMENTS This system will transfer sensor data, sensor alarm data, and video data.		
7. ESTIMATED INITIAL COST OF THE SYSTEM Navail		
8. TARGET DATE FOR <div style="display: flex; justify-content: space-between;"> <div style="width: 30%;">a. APPLICATION 31 October 1995</div> <div style="width: 30%;">b. SYSTEM ACTIVATION 7 November 1995</div> <div style="width: 30%;">c. SYSTEM TERMINATION 31 December 1996 See Remark (4)</div> </div>		
9. SYSTEM RELATIONSHIP AND ESSENTIALITY The system for this experimental phase is essential to evaluating the viability of the use of 60 GHz for data transmission of security sensor data in an air base environment. The use of a wireless data link that is relatively immune to interference or is not likely to cause interference is essential to the success of the automated system.		
10. REPLACEMENT INFORMATION This system in its final development will replace the current RF transmission system used in the Tactical Automated Security System (TASS).		
11. RELATED ANALYSIS AND / OR TEST DATA <small>Technical Report at the Applied Research Laboratories, The University of Texas at Austin: R.L. Rogers and C.M. Loeffler, "A Feasibility Study for a Non-rf, Non-Hardware Data Link," Report ARL-TR-94-12, May 94, Contract N00039-91-C-0082.</small>		
12. NUMBER OF MOBILE UNITS N/A		
13. GEOGRAPHICAL AREA FOR a. STAGE 2 Eglin AFB, Minot AFB, Davis Montham AFB, Kelly AFB b. STAGE 3 c. STAGE 4		
14. LINE DIAGRAM See page(s) See attached sheet	15. SPACE SYSTEMS See page(s) N/A	
16. TYPE OF SERVICE(S) FOR STAGE 4 Fixed	17. STATION CLASS(ES) FOR STAGE 4 FX, FXD, FXE	
18. REMARKS (1) From item 4: Free running Gunn diodes will be used for the transmitter and first local oscillator. These devices drift substantially in frequency, and no simple fix is available. This problem is under consideration at present and suitable modifications will be made for the final systems to improve this characteristic at later stages. Frequency drift is thermally induced and for operating temperatures that will be experienced is expected to be less than ± 200 MHz (± 3300 ppm). (2) From item 4: More channels are expected to be used in the later stages. The tests for this stage are for evaluation of transmission channel quality and reliability. The emission designator for the later stages will be: 7M00F7D. The number of channels, channel spacing, and bandwidth will be determined by frequency availability and technological limitations. (3) From item 4: There is a possibility phase modulation may be used in the later stages as well as frequency modulation. (4) From item 8: The termination date is intended to apply to the test system used in Stage 2.		
DOWNGRADING INSTRUCTIONS N/A	CLASSIFICATION UNCLASSIFIED	

APPLICATION FOR FOREIGN SPECTRUM REVIEW	CLASSIFICATION UNCLASSIFIED	PAGE 7 of 7
FOREIGN COORDINATION GENERAL INFORMATION		
1. APPLICATION TITLE Millimeter Wave Non-rf Non-Hardware Data Link		
2. SYSTEM NOMENCLATURE Short Range Non-rf Non Hardware Data Link AN/TKC		
3. STAGE OF ALLOCATION (x one) <div style="display: flex; justify-content: space-around; align-items: flex-start;"> <div style="text-align: center;"> <input type="checkbox"/> a. STAGE 1 CONCEPTUAL </div> <div style="text-align: center;"> <input checked="" type="checkbox"/> b. STAGE 2 EXPERIMENTAL </div> <div style="text-align: center;"> <input type="checkbox"/> c. STAGE 3 DEVELOPMENTAL </div> <div style="text-align: center;"> <input type="checkbox"/> d. STAGE 4 OPERATIONAL </div> </div>		
4. FREQUENCY REQUIREMENTS a. FREQUENCY(IES) 60 GHz See Remark (1) b. EMISSION DESIGNATOR(S) 7M00F2D (Experimental System) See Remarks (2) and (3)		
5. PROPOSED OPERATING LOCATIONS OUTSIDE US&P This system is intended to operate wherever an air base is deployed, e.g.: Saudi Arabia, Europe, Asia		
6. PURPOSE OF SYSTEM, OPERATIONAL AND SYSTEM CONCEPTS This system is a data transmission link intended for use in deployable automated security systems. This system will operate as a line of sight data transmission link within and around the perimeter of a forward deployed air base.		
7. INFORMATION TRANSFER REQUIREMENTS This system will transfer sensor data, sensor alarm data, and video data		
8. NUMBER OF UNITS OPERATING SIMULTANEOUSLY IN THE SAME ENVIRONMENT Stage 2: 2 Transmitter Receiver Pairs (ea pair at a different location), Stage 3: Navail, Stage 4: Navail		
9. REPLACEMENT INFORMATION This system in its final development will replace the current rf transmission system used in the Tactical Automated Security System (TASS).		
10. LINE DIAGRAM See page(s) See attached page	11. SPACE SYSTEMS See page(s) N/A	
12. PROJECTED OPERATIONAL DEPLOYMENT DATE January 1996 for Stage 4		
13. REMARKS (1) From item 4: Free running Gunn diodes will be used for the transmitter and first local oscillator. These evce drit substantial in frequency, and so simple fix is available. This problem is under consideration at present and suitable modifications will be made for the final systems to improve this characteric at later stages. Frequency drift is thermally induced and for operating temperatures that will be experienced is expected to be less than ± 200 MHz (± 3300 ppm). (2) From item 4: More channels are expected to be used in the later stages. The tests for this stage are for evaluation of transmission channel quality and reliability. The emission designator for the later stages will be: 7M00F7D. The number of channels, channel spacing, and bandwidth will be determined by frequency availability and technological limitations. (3) From item 4: There is a possibility phase modulation may be used in the later stages as well as frequency modulation.		
DOWNGRADING INSTRUCTIONS N/A	CLASSIFICATION UNCLASSIFIED	

Short Range Non-RF Non-Hardware Data Link



APPLICATIONS FOR EQUIPMENT FREQUENCY ALLOCATION	CLASSIFICATION UNCLASSIFIED	DATE 18 Sep 95	Form Approved OMB No. 0704-0188 Page 1 of <u>6</u> Pages						
DOD GENERAL INFORMATION									
TO Headquarters AF Frequency Management Agency Washington, D.C. 20330-6340		FROM Applied Research Laboratories The University of Texas at Austin P.O. 8029 Austin, TX 78713-8029							
1. APPLICATION TITLE Millimeter Wave Non-rf Non-Hardwire Data Link									
2. SYSTEM NOMENCLATURE Long Range Non-rf Non Hardwire Data Link AN/TKC									
3. STAGE OF ALLOCATION (x one) <div style="display: flex; justify-content: space-around; align-items: flex-end;"> <div><input type="checkbox"/> a. STAGE 1 CONCEPTUAL</div> <div><input checked="" type="checkbox"/> b. STAGE 2 EXPERIMENTAL</div> <div><input type="checkbox"/> c. STAGE 3 DEVELOPMENTAL</div> <div><input type="checkbox"/> d. STAGE 4 OPERATIONAL</div> </div>									
4. FREQUENCY REQUIREMENTS a. FREQUENCY (IES) 27.3 GHz B. EMISSION DESIGNATORS 7M00F2D (Experiments System) See Remarks (1) and (2)									
5. TARGET STARTING DATE FOR SUBSEQUENT STAGES <table style="width:100%; border: none;"> <tr> <td style="width:33%; border: none;">a. STAGE 2 November 1995 (estimated)</td> <td style="width:33%; border: none;">b. STAGE 3 January 1997 (estimated)</td> <td style="width:33%; border: none;">c. STAGE 4 January 1999 (estimated)</td> </tr> </table>				a. STAGE 2 November 1995 (estimated)	b. STAGE 3 January 1997 (estimated)	c. STAGE 4 January 1999 (estimated)			
a. STAGE 2 November 1995 (estimated)	b. STAGE 3 January 1997 (estimated)	c. STAGE 4 January 1999 (estimated)							
6. EXTENT OF USE 24 hrs/day, 7 days/week									
7. GEOGRAPHICAL AREA FOR a. STAGE 2 Eglin AFB, Minot AFB, Davis Monthan AFB, Lackland AFB, Randolph AFB b. STAGE 3 N/A c. STAGE 4 N/A									
8. NUMBER OF UNITS <table style="width:100%; border: none;"> <tr> <td style="width:33%; border: none;">a. STAGE 2 2 Transmitter Receiver Pairs (ea pair at different location)</td> <td style="width:33%; border: none;">b. STAGE 3 NAvail</td> <td style="width:33%; border: none;">c. STAGE 4 NAvail</td> </tr> </table>				a. STAGE 2 2 Transmitter Receiver Pairs (ea pair at different location)	b. STAGE 3 NAvail	c. STAGE 4 NAvail			
a. STAGE 2 2 Transmitter Receiver Pairs (ea pair at different location)	b. STAGE 3 NAvail	c. STAGE 4 NAvail							
9. NUMBER OF UNITS OPERATING SIMULTANEOUSLY IN THE SAME ENVIRONMENT Stage 2: One transmitter and one receiver in the same environment									
10. OTHER J/F 12 APPLICATION NUMBER(S) TO BE <div style="display: flex; align-items: flex-start;"> <div style="margin-right: 20px;"> <input type="checkbox"/> a. SUPERSEDED J/F <input type="checkbox"/> b. RELATED J/F N/A </div> </div>		11. IS THERE ANY OPERATIONAL REQUIREMENT AS DESCRIBED IN THE INSTRUCTIONS FOR PARAGRAPH 11? <div style="display: flex; justify-content: space-around; align-items: flex-end;"> <div><input type="checkbox"/> a. YES</div> <div><input checked="" type="checkbox"/> b. NO</div> <div><input type="checkbox"/> c. NAail</div> </div>							
12. NAMES AND TELEPHONE NUMBERS <table style="width:100%; border: none;"> <tr> <td style="width:40%; border: none;">a. PROGRAM MANAGER William Witter</td> <td style="width:30%; border: none;">(1) COMMERCIAL (703) 325-1002</td> <td style="width:30%; border: none;">(2) AUTOVON 221-1002</td> </tr> <tr> <td style="border: none;">b. PROJECT Robert L. Rogers</td> <td style="border: none;">(1) COMMERCIAL (512) 835-3307</td> <td style="border: none;">(2) AUTOVON</td> </tr> </table>				a. PROGRAM MANAGER William Witter	(1) COMMERCIAL (703) 325-1002	(2) AUTOVON 221-1002	b. PROJECT Robert L. Rogers	(1) COMMERCIAL (512) 835-3307	(2) AUTOVON
a. PROGRAM MANAGER William Witter	(1) COMMERCIAL (703) 325-1002	(2) AUTOVON 221-1002							
b. PROJECT Robert L. Rogers	(1) COMMERCIAL (512) 835-3307	(2) AUTOVON							
13. REMARKS (1) From item 4: More channels are expected to be used in the later stages. The tests for this stage are for evaluation of transmission channel quality and reliability. The emission designator for the later stages will be: 7M00F7D. The number of channels, channel spacing, and bandwidth will be determined by frequency availability and technological limitations. (2) From item 4: There is a possibility phase modulation may be used in the later stages as well as frequency modulation.									
DOWNGRADING INSTRUCTIONS N/A		CLASSIFICATION UNCLASSIFIED							

CLASSIFICATION UNCLASSIFIED		PAGE 2 of 6
TRANSMITTER EQUIPMENT CHARACTERISTICS		
1. NOMENCLATURE, MANUFACTURER'S MODEL NO. Long Range Non-rf Non Hardwire Data Link Transmitter AN/TKC	2. MANUFACTURER'S NAME DRO oscillator manufactured by Delphi Components Inc., output power amplifier manufactured by DBS Microwave or Avantek	
3. TRANSMITTER INSTALLATION Deployed at Air Base	4. TRANSMITTER TYPE FSK Digital Data Transmission	
5. TUNING RANGE for Stage 2: 27.2 GHz to 27.4 GHz	6. METHOD OF TUNING Varactor tuning	
7. RF CHANNELING CAPABILITY N/A for Stage 2	8. EMISSION DESIGNATOR(S) 7M00F2D See Remark (1)	
9. FREQUENCY TOLERANCE $\pm 5 \text{ ppm/}^{\circ}\text{C}$	10. FILTER EMPLOYED (x one) <div style="display: flex; justify-content: space-around;"> <input type="checkbox"/> a. YES <input checked="" type="checkbox"/> b. NO </div>	
11. SPREAD SPECTRUM (x one) <div style="display: flex; justify-content: space-around;"> <input type="checkbox"/> a. YES <input checked="" type="checkbox"/> b. NO </div>	12. EMISSION BANDWIDTH (x and complete as applicable) <div style="display: flex; justify-content: space-around;"> <input type="checkbox"/> CALCULATED <input checked="" type="checkbox"/> MEASURED </div>	
13. MAXIMUM BIT RATE 1.5 MB/s See Remark (3)	14. MODULATION TECHNIQUES AND CODING FSK modulation Manchester encoding for data (except at 19.2 Kb/s where no coding is used)	
15. PRE-EMPHASIS (x one) <div style="display: flex; justify-content: space-around;"> <input type="checkbox"/> a. YES <input checked="" type="checkbox"/> b. NO </div>	16. MAXIMUM MODULATION FREQUENCY N/Avail	
17. POWER a. MEAN 200 mW b. PEP 200 mW	17. DEVIATION RATIO <small>Deviation ratio ranges from 0.1 to 4 (higher deviation ratios only apply to lower data rates; minimum data rate is 19.2kb/s)</small>	
18. OUTPUT DEVICE HEMT Power transistor for Stage 2	18. PULSE CHARACTERISTICS a. RATE N/A b. WIDTH N/A c. RISE TIME N/A d. FALL TIME N/A e. COMPRESSION N/A	
19. SPURIOUS LEVEL N/Avail	21. HARMONIC LEVEL a. 2nd N/Avail b. 3rd N/Avail c. OTHER N/Avail	
20. FCC TYPE ACCEPTANCE NO. N/Avail	24. REMARKS (1) From item 8: Some applications in later stages may require more bandwidth, such as the transmission of video data. (2) From item 11: Later stages may employ spectral spreading depending on the results of present tests. (3) From item 13: Stage 2 tests will be at varying data rates of 19.2 kb/s, 64 kb/s, and 1.5 MB/s.	
CLASSIFICATION UNCLASSIFIED		

CLASSIFICATION

UNCLASSIFIED

PAGE

3 of 6

RECEIVER EQUIPMENT CHARACTERISTICS

1. NOMENCLATURE, MANUFACTURER'S MODEL NO. Long Range Non-rf Non Hardwire Data Link Receiver AN/TKC				2. MANUFACTURER'S NAME NAvail	
3. RECEIVER INSTALLATION Deployed at Air Base				4. RECEIVER TYPE Double conversion FSK	
5. TUNING RANGE 26.5 GHz to 28.3 GHz				6. METHOD OF TUNING Varactor tuning	
7. RF CHANNELING CAPABILITY N/A for Stage 2				8. EMISSION DESIGNATOR(S) 7M00F2D See Remark (1)	
9. FREQUENCY TOLERANCE ± 10 ppm/ $^{\circ}$ C (estimated)					
10. IF SELECTIVITY	1st	2nd	3rd	11. RF SELECTIVITY (x and complete as applicable) <input checked="" type="checkbox"/> CALCULATED <input type="checkbox"/> MEASURED	
a. -3 dB	1.2 GHz	7MHz/17MHz	N/A	a. -3 dB 29 GHz	
b. -20 dB	NAvail	NAvail	NAvail	b. -20 dB N/Avail	
c. -60 dB	NAvail	NAvail	NAvail	c. -60 dB N/Avail	
12. IF FREQUENCY				d. Preselection Type Waveguide cut off	
a. 1st 1.2 GHz				13. MAXIMUM POST DETECTION FREQUENCY NAvail	
b. 2nd 479 MHz				14. MINIMUM POST DETECTION FREQUENCY N/A	
c. 3rd N/A					
15. OSCILLATOR TUNED	1st	2nd	3rd	16. MAXIMUM BIT RATE 1.5 MB/s See Remark (2)	
a. ABOVE TUNED FREQUENCY		479MHz		17. SENSITIVITY.	
b. BELOW TUNED FREQUENCY	1.3 GHz			a. SENSITIVITY -96 dBm at 7 MHz, -92 dBm at 17 MHz	
c. EITHER ABOVE OR BELOW	N/A			b. CRITERIA Signal acquisition by Phase Locked Loop Demodulator	
18. DE-EMPHASIS (x one) <input type="checkbox"/> a. YES <input checked="" type="checkbox"/> b. NO				c. NOISE FIG 3.5 dB dB	
19. IMAGE REJECTION Estimated to be more than 30 dB				d. NOISE TEMP 650 K Kelvin	
20. REMARKS (1) From item 8: Some applications in later stages may require more bandwidth, such as the transmission of video data. (2) From item 16: Stage 2 tests will be at varying data rates of 19.2 kb/s, 64 kb/s, and 1.5 MB/s.				20. SPURIOUS REJECTION NAvail	

CLASSIFICATION

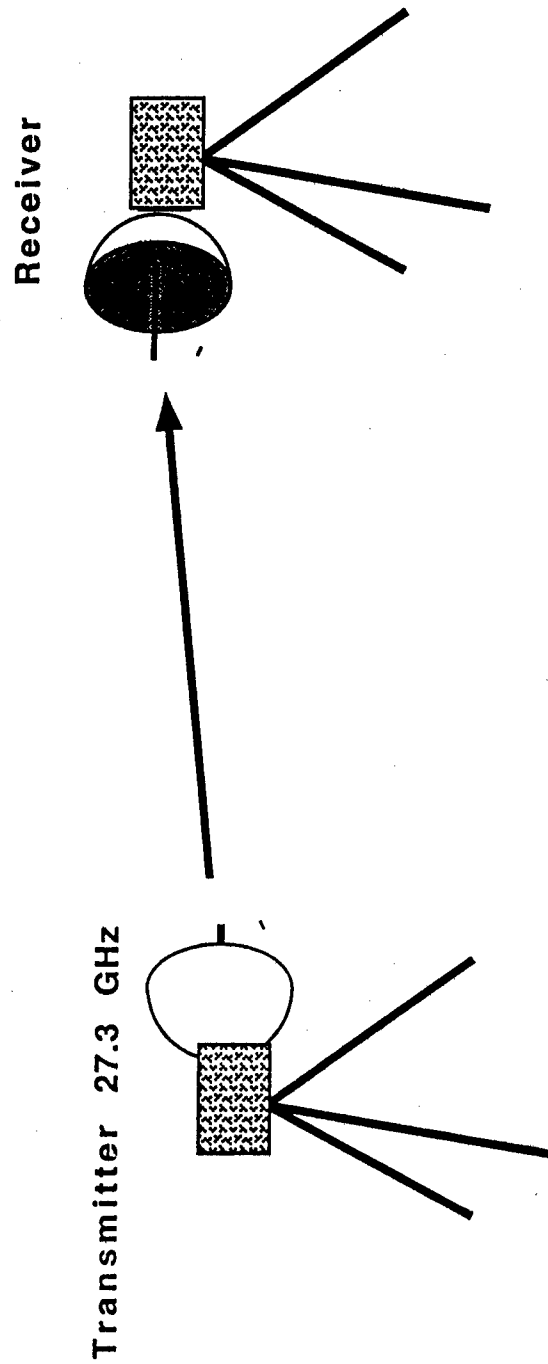
UNCLASSIFIED

CLASSIFICATION UNCLASSIFIED		PAGE 4 of 6
ANTENNA EQUIPMENT CHARACTERISTICS		
<div style="display: flex; justify-content: space-between;"> <input type="checkbox"/> a. TRANSMITTING <input type="checkbox"/> b. RECEIVING <input checked="" type="checkbox"/> c. TRANSMITTING AND RECEIVING </div>		
2. NOMENCLATURE, MANUFACTURER'S MODEL NO. CRA-396-S12A Reflector Antenna	3. MANUFACTURER'S NAME Millitech Corporation	
4. FREQUENCY RANGE N/Avail	5. TYPE Cassegrain reflector antenna	
6. POLARIZATION Linear, horizontal or vertical	7. SCAN CHARACTERISTICS	
8. GAIN	a. TYPE N/A	
a. MAIN BEAM 35 dB nominal	b. VERTICAL N/A	
b. 1st MAJOR SIDE 13 dB to 17 dB below main beam	(1) Max Elev N/A	
9. BEAMWIDTH	(2) Min Elev N/A	
a. HORIZONTAL H-Plane for vertical polarization: 2.5°	(3) Scan Rate N/A	
b. VERTICAL E-Plane for vertical polarization: 2.8°	c. HORIZONTAL SCAN	
10. REMARKS		
CLASSIFICATIONS UNCLASSIFIED		

APPLICATION FOR SPECTRUM REVIEW	CLASSIFICATION UNCLASSIFIED	PAGE 5 of 6						
NTIA GENERAL INFORMATION								
1. APPLICATION TITLE Millimeter Wave Non-rf Non-Hardware Data Link								
2. SYSTEM NOMENCLATURE Long Range Non-rf Non Hardware Data Link AN/TKC								
3. STAGE OF ALLOCATION (x one) <div style="display: flex; justify-content: space-around; align-items: flex-start;"> <div style="text-align: center;"> <input type="checkbox"/> a. STAGE 1 CONCEPTUAL </div> <div style="text-align: center;"> <input checked="" type="checkbox"/> b. STAGE 2 EXPERIMENTAL </div> <div style="text-align: center;"> <input type="checkbox"/> c. STAGE 3 DEVELOPMENTAL </div> <div style="text-align: center;"> <input type="checkbox"/> d. STAGE 4 OPERATIONAL </div> </div>								
4. FREQUENCY REQUIREMENTS a. FREQUENCY(IES) 27.3 GHz b. EMISSION DESIGNATOR(S) 7M00F2D (Experimental System) See Remarks (1) and (2)								
5. PURPOSE OF SYSTEM, OPERATIONAL AND SYSTEM CONCEPTS (WARTIME USE) (x one) <input checked="" type="checkbox"/> a. YES <input type="checkbox"/> b. NO This system is a data transmission link intended for use in deployable automated security systems. This system will operate as a line of sight data transmission link within and around the perimeter of a forward deployed air base. It may also be used at permanent base facilities.								
6. INFORMATION TRANSFER REQUIREMENTS This system will transfer sensor data, sensor alarm data, and video data.								
7. ESTIMATED INITIAL COST OF THE SYSTEM N/A								
8. TARGET DATE FOR <table style="width: 100%; border-collapse: collapse;"> <tr> <td style="width: 33%; border-bottom: 1px solid black;">a. APPLICATION</td> <td style="width: 33%; border-bottom: 1px solid black;">b. SYSTEM ACTIVATION</td> <td style="width: 33%; border-bottom: 1px solid black;">c. SYSTEM TERMINATION</td> </tr> <tr> <td>31 October 1995</td> <td>7 November 1995</td> <td>31 December 1996 See Remark (3)</td> </tr> </table>			a. APPLICATION	b. SYSTEM ACTIVATION	c. SYSTEM TERMINATION	31 October 1995	7 November 1995	31 December 1996 See Remark (3)
a. APPLICATION	b. SYSTEM ACTIVATION	c. SYSTEM TERMINATION						
31 October 1995	7 November 1995	31 December 1996 See Remark (3)						
9. SYSTEM RELATIONSHIP AND ESSENTIALITY The system for this experimental phase is essential to evaluating the viability of the use of 27.3 GHz for data transmission of security sensor data in an air base environment. The use of a wireless data link that is relatively immune to interference or is not likely to cause interference is essential to the success of the automated system.								
10. REPLACEMENT INFORMATION This system in its final development will replace the current RF transmission system used in the Tactical Automated Security System (TASS).								
11. RELATED ANALYSIS AND / OR TEST DATA <small>Technical Report at the Applied Research Laboratories, The University of Texas at Austin: R.L. Rogers and C.M. Loeffler, "A Feasibility Study for a Non-rf, Non-Hardware Data Link," Report ARL-TR-94-12, May 94, Contract N00039-91-C-0082.</small>								
12. NUMBER OF MOBILE UNITS N/A								
13. GEOGRAPHICAL AREA FOR a. STAGE 2 Eglin AFB, Minot AFB, Davis Montham AFB, Kelly AFB b. STAGE 3 c. STAGE 4								
14. LINE DIAGRAM See page(s) See attached sheet	15. SPACE SYSTEMS See page(s) N/A							
16. TYPE OF SERVICE(S) FOR STAGE 4 Fixed	17. STATION CLASS(ES) FOR STAGE 4 FX, FXD, FXE							
18. REMARKS (1) From item 4: More channels are expected to be used in the later stages. The tests for this stage are for evaluation of transmission channel quality and reliability. The emission designator for the later stages will be: 7M00F7D. The number of channels, channel spacing, and bandwidth will be determined by frequency availability and technological limitations. (2) From item 4: There is a possibility phase modulation may be used in the later stages as well as frequency modulation. (3) From item 8: The termination date is intended to apply to the test system used in Stage 2.								
DOWNGRADING INSTRUCTIONS N/A	CLASSIFICATION UNCLASSIFIED							

APPLICATION FOR FOREIGN SPECTRUM REVIEW	CLASSIFICATION UNCLASSIFIED	PAGE 6 of 6
FOREIGN COORDINATION GENERAL INFORMATION		
1. APPLICATION TITLE Millimeter Wave Non-rf Non-Hardwire Data Link		
2. SYSTEM NOMENCLATURE Long Range Non-rf Non Hardwire Data Link AN/TKC		
3. STAGE OF ALLOCATION (x one) <div style="display: flex; justify-content: space-around; align-items: flex-start;"> <div style="text-align: center;"> <input type="checkbox"/> a. STAGE 1 CONCEPTUAL </div> <div style="text-align: center;"> <input checked="" type="checkbox"/> b. STAGE 2 EXPERIMENTAL </div> <div style="text-align: center;"> <input type="checkbox"/> c. STAGE 3 DEVELOPMENTAL </div> <div style="text-align: center;"> <input type="checkbox"/> d. STAGE 4 OPERATIONAL </div> </div>		
4. FREQUENCY REQUIREMENTS a. FREQUENCY(IES) 27.3 GHz b. EMISSION DESIGNATOR(S) 7M00F2D (Experimental System) See Remarks (1) and (2)		
5. PROPOSED OPERATING LOCATIONS OUTSIDE US&P This system is intended to operate wherever an air base is deployed, e.g.: Saudi Arabia, Europe, Asia		
6. PURPOSE OF SYSTEM, OPERATIONAL AND SYSTEM CONCEPTS This system is a data transmission link intended for use in deployable automated security systems. This system will operate as a line of sight data transmission link within and around the perimeter of a forward deployed air base.		
7. INFORMATION TRANSFER REQUIREMENTS This system will transfer sensor data, sensor alarm data, and video data		
8. NUMBER OF UNITS OPERATING SIMULTANEOUSLY IN THE SAME ENVIRONMENT Stage 2: 2 Transmitter Receiver Pairs (ea pair at a different location), Stage 3: N/A, Stage 4: N/A		
9. REPLACEMENT INFORMATION This system in its final development will replace the current rf transmission system used in the Tactical Automated Security System (TASS).		
10. LINE DIAGRAM See page(s) See attached page	11. SPACE SYSTEMS See page(s) N/A	
12. PROJECTED OPERATIONAL DEPLOYMENT DATE January 1996 for Stage 4		
13. REMARKS (1) From item 4: More channels are expected to be used in the later stages. The tests for this stage are for evaluation of transmission channel quality and reliability. The emission designator for the later stages will be: 7M00F7D. The number of channels, channel spacing, and bandwidth will be determined by frequency availability and technological limitations. (2) From item 4: There is a possibility phase modulation may be used in the later stages as well as frequency modulation.		
DOWNGRADING INSTRUCTIONS N/A	CLASSIFICATION UNCLASSIFIED	

Long Range Non-RF Non-Hardware Data Link



This page intentionally left blank.

GLOSSARY OF TERMS

Antenna Aperture Efficiency. Aperture efficiency describes how efficiently the area of an antenna's aperture is used. Diffraction theory allows the calculation of simple theoretical limits on the maximum directivity that an aperture can achieve. The aperture efficiency is the ratio of an antenna's directivity and its theoretical maximum directivity as a result of the size of its aperture.

Antenna Directive Gain and Directivity. Directive gain in a given direction is the ratio of the received power in that direction to the received power of an isotropic antenna. Directivity is the maximum value of the directive gain; the direction of the directive gain maximum is usually along the antenna's main axis.

Antenna E-Plane and H-Plane. Many antennas radiate linearly polarized fields. The plane that bisects a linearly polarized antenna and is parallel to the radiated electric field vector is called the E-plane. The plane that bisects the antenna and is parallel to the magnetic field vector is called the H-plane.

Antenna Gain. Antenna gain is a measure of an antenna's directivity that takes into account the antenna's efficiency.

Cassegrain Reflector Antenna. A parabolic reflector configuration that allows the feed to be placed at or near the reflector's vertex. In a common front-fed configuration the feed is normally placed at the reflector's focal point in front of the antenna. Energy emitted from the feed at the focal point will be reflected by the parabolic surface into a collimated beam. In the Cassegrain configuration a hyperbolic subreflector is placed at the primary reflector's focal point to move the focal point of the entire system behind the primary reflector.

along the reflector's main axis. The Cassegrain configuration is used to reduce blockage caused by large feed systems.

Continuous Phase Frequency Shift Keying (CPFSK). A form of frequency shift keying (FSK) where the phase of the carrier is not disrupted when the frequency changes. An example of CPFSK is controlling the tuning pin of a voltage-controlled oscillator (VCO). A signal on the VCO's tuning pin does not cause discontinuities in the oscillator's phase; the signal alters the phase in a continuous manner.

Deviation Ratio. The ratio of the peak frequency deviation of the FM signal to the bandwidth of the modulating signal, W . If the deviation ratio is D , then it is calculated by the formula, $D = f_d / W$.

Dielectric Resonator Oscillator (DRO). A frequency source with a dielectric resonator as its frequency-determining element. Dielectric resonators are small pieces of ceramic material that are well-suited for integration into microwave integrated circuits. Its size, shape, electrical properties, and surroundings determine the resonant frequency of a dielectric resonator.

Direct Broadcast Satellite (DBS). The system for transmitting multiple channels of video and data directly to consumers from geostationary satellites. The system utilizes selected frequency bands in the range from 1.5 to 15 GHz. The system uses frequency-shift keying as its modulation scheme.

Electric Field Integral Equation (EFIE). The electric field integral equation relates unknown surface current densities to a known source electric field through electromagnetic boundary conditions.

Free Space Loss. Free space loss is the loss due to spherical spreading of the propagating wave, assuming a free-space path; i.e., there is no atmosphere

and no obstruction in the path, and the path is a straight line. Free space loss is defined as the ratio between the received power from an isotropic antenna and the transmitted power from an isotropic antenna. For isotropic antennas the received power is related to the transmitted power by

$$P_R = P_T \left(\frac{\lambda}{4\pi R} \right)^2 ,$$

where R is the distance between antennas. Thus, free space loss is defined in decibels as

$$L_{dB} = 10 \log_{10} \frac{P_T}{P_R} = 20 \log_{10} \left(\frac{\lambda}{4\pi R} \right) .$$

Frequency Shift Keying (FSK). A form of modulation where the information is encoded by changing the frequency of the RF carrier.

Fresnel Zones. Pick a path from the transmitter to the receiver that is a straight line from the transmitter to a point on an arbitrary cross section of the path, followed by a straight line from this point to the receiver. The phase of a ray following this path will be determined by the sum of the two path sections, transmitter to cross section and cross section to receiver. Fresnel zones are defined as concentric zones on the cross section that correspond to path lengths that are within a given multiple of half-wavelengths from the direct or center path.

Gunn Oscillator. A microwave or millimeter wave oscillator employing the negative resistance properties of a Gunn diode to produce oscillations. A Gunn diode is a bulk semiconductor device that has negative resistance characteristics under large dc biases.

Isotropic Antenna. An antenna that radiates power equally in all directions.

Link Margin. The ratio between the received signal power to the thermal noise level in the receiver, assuming only free space loss in the path.

Magnetic Field Integral Equation (MFIE). The magnetic field integral equation relates unknown current densities to a known source magnetic field through electromagnetic boundary conditions.

Manchester Encoding. A split-phase encoding scheme used to assure a zero-average value signal and to encode timing information. A non-return-to-zero (NRZ) bit stream is multiplied by a clock waveform with a period equal to the width of one bit of the NRZ data. The new encoded bit stream contains the original bit stream and a timing component for clock recovery, and it has a zero average mean. This technique is simple to implement in hardware, but uses more bandwidth than other encoding schemes.

Moment Method. The moment method is a technique used to numerically solve for an unknown variable within a linear operator. The unknown variable is first expanded into orthogonal basis functions with heights to be determined. The inner product of the new equation with the expanded unknown is then taken with a set of orthogonal weighting functions. The result is a set of independent linear equations that can be solved for the height of the basis functions.

Oxygen Absorption Band. Atmospheric oxygen absorbs electromagnetic energy in a narrow band of frequencies around 60 GHz. Oxygen causes the power of a signal in this band to attenuate exponentially with distance. The overall attenuation is the product of the losses due to oxygen absorption, free space loss, and other atmospheric and environmental losses. At 60 GHz, the oxygen absorption dominates the free space loss after a distance of approximately 1 km.

Polarization. An electromagnetic wave has a polarization associated with its electric field vector. The polarization of the field can be oriented in any direction transverse to the wave's direction of propagation. If the electromagnetic wave is propagating parallel to the horizon, its polarization can be either perpendicular to the horizon or parallel to the horizon, but still perpendicular to the direction of propagation. These two different orientations of the electric field are commonly referred to as vertical linear polarization and horizontal linear polarization, respectively. The electromagnetic wave can also be the superposition of two orthogonally polarized waves that are out of phase. The E-vector of this wave will appear to rotate in time when observed from a given point. Depending on the phase and the amplitude of the component waves, the polarization vector appears to rotate either clockwise or counterclockwise. As the vector rotates, its magnitude may also change, resulting in elliptical polarization. If the magnitude of the rotating vector does not change, the wave is called circularly polarized.

Return-To-Zero (RZ), Non-Return-To-Zero (NRZ). In a return-to-zero bit stream the signal returns to zero for a specific amount of time between bits. In a non-return-to-zero bit stream, the signal does not return to zero, but immediately transitions to the next bit at the end of each bit length.

This page intentionally left blank.

REFERENCES

1. K. Ohata et al., "Sixty-GHz-Band Ultra-Miniature Monolithic T/R Modules for Multimedia Wireless Communication Systems," *IEEE Transactions on Microwave Theory and Techniques* **44** (12), 2354-2360 (December 1996).
2. J. Goldhirsh et al., "Three Years of C-Band Signal Measurements for Overwater, Line-of-Sight Links in the Mid-Atlantic Coast: 1. Fade Statistics," *Radio Science* **29** (6), 1421-1431 (November-December 1994).
3. J. Goldhirsh et al., "Three Years of C-Band Signal Measurements for Overwater, Line-of-Sight Links in the Mid-Atlantic Coast: 2. Sustained Deep Fades," *Radio Science* **29** (6), 1433-1447 (November-December 1994).
4. A. R. Webster, "Extended Observations of Fading on a Terrestrial Microwave Link," *Radio Science* **32** (1), 231-238 (January-February 1997).
5. C. W. Tolbert and A. W. Straiton, "Radio Propagation Measurements Between Pikes Peak and Mount Evans at a Wavelength of 8.6 Millimeters," *Electrical Engineering Research Laboratory Report No. 77*, The University of Texas at Austin (September 1955).
6. R. L. Freeman, *Radio System Design for Telecommunications (1-100 GHz)* (Wiley & Sons, 1987), pp. 397-441.
7. P. B. Papazian et al., "Study of the Local Multipoint Distribution Service Radio Channel," *IEEE Transactions on Broadcasting* **43** (2), 1-10 (June 1997).
8. A. W. Love, *Electromagnetic Horn Antennas* (IEEE Press, 1976).
9. C. A. Balanis, *Antenna Theory Analysis and Design* (John Wiley and Sons, Inc., 1982), Chapter 12.
10. C. A. Balanis, *Antenna Theory Analysis and Design* (John Wiley and Sons, Inc., 1982), Chapter 11.
11. E. H. Braun, "Some Data for the Design of Electromagnetic Horns," *IEEE Trans. on Antennas and Propagation* **AP-4**, 29-31 (January 1956).

12. R. F. Harrington, *Field Computation by Moment Methods* (MacMillan, 1968), Chapter 3.
13. C. A. Balanis, *Advanced Engineering Electromagnetics* (John Wiley and Sons, Inc., 1982), Chapter 12.
14. M. A. Koerner, "Gain Enhancement of a Wide-Flare, X-band, Pyramidal Horn Using Metal Baffles," Master's Thesis, The University of Texas at Austin (August 1996).
15. C. A. Balanis, *Antenna Theory Analysis and Design* (John Wiley and Sons, Inc., 1982), Chapter 2.
16. C. A. Balanis, *Advanced Engineering Electromagnetics* (John Wiley and Sons, Inc., 1982), Chapter 2.
17. R. F. Harrington, *Time-Harmonic Electromagnetic Fields* (McGraw-Hill Book Co., Inc., 1982), Appendix D.
18. D. M. Pozar, *Microwave Engineering* (Addison-Wesley Publishing Co., Inc., 1990), pp. 76-101.

2 July 1998

**DISTRIBUTION LIST FOR
ARL-TR-98-2
Technical Report under Contract N00039-91-C-0082
TD No. 08A1011, Non RF/Non Hardwire Data Link**

Copy No.

1-3	Defense Threat Reduction Agency 6801 Telegraph Road Alexandria, VA 22310-3398 Attn: William J. Witter, NSCS
4	Defense Threat Reduction Agency 45045 Aviation Drive Dulles, VA 20166-7517 Attn: SWI
5	Defense Advanced Research Projects Agency 3701 North Fairfax Drive Arlington, VA 22203-1714 Attn: Library
6, 7	Defense Technical Information Center 8725 John J. Kingman Rd., Suite 0944 Fort Belvoir, VA 22060-6218 Attn: DTIC/OCP
8	OASD (C3I) Washington, DC 20301 Attn: ODASD (I&S) (CI & SP)
9	Under Secretary of Defense Acquisition & Technology 3140 Defense Program Washington, DC 20301-3140 Attn: ODDR&E/TS/LS
10 11	Commander in Chief U.S. Central Command 7115 South Boundary Blvd MacDill Air Force Base, FL 33621-5101 Attn: CCJ3 CCPM

**Distribution list for ARL-TR-98-2 under Contract N00039-91-C-0082,
TD No. 08A1011
(cont'd)**

Copy No.

12	Headquarters U.S. European Command Unit 30400 Box 1000 APO AE 09128 Attn: ECJ5D
13	U.S. Nuclear Command & Control System Support Staff Skyline #3, Suite 500 5201 Leesburg Pike Falls Church, VA 22041-3202 Attn: Document Control
14, 15	Headquarters Department of the Army 4401 Ford Avenue, Suite 225 Alexandria, VA 22302-1432 Attn: DAMO-ODL-S
16, 17	Director Night Vision & Electronic Sensors Directorate 10221 Burbeck Road Fort Belvoir, VA 22060-5806 Attn: Glenn B. Slagle
18	U.S. Army Corps of Engineers 215 N. 17th Street Omaha, NE 68102-4978 Attn: CEMP-ET
19	Commandant
20	U.S. Army Military Police School
21	Fort McClellan, AL 36205-5030
22	Attn: ATZN-MP-TS ATZN-MP-CD ATZN-MP-DE ATZN-MP-TB
23	Commander U.S. Army Nuclear & Chemical Agency 7150 Heller Loop, Suite 101 Springfield, VA 22150-3198 Attn: MONA-SU

**Distribution list for ARL-TR-98-2 under Contract N00039-91-C-0082,
TD No. 08A1011
(cont'd)**

Copy No.

24	Technical Director U.S. Army Research Institute 5001 Eisenhower Avenue Alexandria, VA 22333-5600 Attn: PERI-ZT
25	U.S. Army Research Laboratory AMSRL-SL-CS E3331 5101 Hoadley Road Aberdeen Proving Ground, MD 21010-5423 Attn: AMSRL-HR
26	AMSRL-HR-MM, David Harrah
27	Dr. D. Hodge
28	Commanding General U.S. Army Training & Doctrine Command Fort Monroe, VA 23651-5000 Attn: ATCD-SN
29	Commander USAS4A Aberdeen Proving Ground, MD 21005-5071 Attn: AMXSY-CA
30	Chief of Naval Operations 2000 Navy Pentagon Department of the Navy Washington, DC 20350-2000 Attn: N09N
31	Chief of Naval Operations 901 M. Street SE, Building 111 Washington Navy Yard Washington, DC 20388-5024 Attn: Code 24B
32	Commander David Taylor Research Center Bethesda, MD 20084-5000 Attn: Code 1203

**Distribution list for ARL-TR-98-2 under Contract N00039-91-C-0082,
TD No. 08A1011
(cont'd)**

Copy No.

	Commandant Marine Corps Department of the Navy Washington, DC 20380-0001
33	Attn: Code POC-30
34	POS-20
35	POS-16
36, 37	POS-30
	Naval Facilities Engineering Services Center 1100 23rd Avenue Port Hueneme, CA 93043-4370
38	Attn: ESC66
	Commander Naval Surface Warfare Center Building 300, Hwy 362 Crane, IN 47522
39	Attn: Code 2064/Larry D. Hembree
	Commander in Chief U.S. Atlantic Command 1562 Mitscher Avenue, Suite 250 Norfolk, VA 23551-2487
40	Attn: J324
	Headquarters Air Combat Command 220 Sweeney Blvd, Suite 112 Langley Air Force Base, VA 23665-2796
41	Attn: HQ ACC/SP
	Headquarters Air Force Material Command Wright Patterson Air Force Base Dayton, OH 45433
42	Attn: AFMC/SP
	Department of the Air Force Pentagon Washington, DC 20330
43	Attn: AF/RDST

**Distribution list for ARL-TR-98-2 under Contract N00039-91-C-0082,
TD No. 08A1011
(cont'd)**

Copy No.

- 44 Commander
Force Protection Battlelab
1631 Stewart Street, Building 5412
Lackland Air Force Base, TX 78236-5000
Attn: Physical Security Manager
- 45 Military Airlift Command
Scott Air Force Base, IL 62225
Attn: SP
- 46 Headquarters
Pacific Air Force
25 E Street, Suite 306
Hickam Air Force Base, HI 96853-5001
Attn: SP
- 47 Commander
Space & Naval Warfare Systems Command
Department of the Navy
Advanced Systems Division (D-37)
San Diego, CA 92152-7383
Attn: PME-121-3
- 48 Technical Director (NWI)
Nuclear Systems Integration
Division (AFMC)
1651 1st Street S. E.
Kirtland Air Force Base, NM 87117
Attn: NTSMS
- 49 United States Air Force
Electronic Systems Center
ESC/FDE
5 Elgin Street
Hanscom Air Force Base, MA 01731-2100
Attn: Morris H. Outwater
- 50 U.S. Air Force
Force Protection Battlelab
1631 Stewart Street, Bldg. 5412
Lackland Air Force Base, TX 78236-5000
Attn: SSMSGT Don Lowe

**Distribution list for ARL-TR-98-2 under Contract N00039-91-C-0082,
TD No. 08A1011
(cont'd)**

Copy No.

51 Commander in Chief
52 U.S. Air Forces in Europe
APO AE 09094-5001
Attn: USAFE/SPP
USAFE/SPO

53 Headquarters
54 USAF/SP
Pentagon, Room BF939B
Washington, DC 20330-5100
Attn: USAF/SPO
USAF/SP

55 Associated Universities, Inc.
Brookhaven National Laboratory
P.O. Box 155
Upton, NY 11973-5000
Attn: Document Custodian

56 Department of Energy
57 GTN
Washington, DC 20545
Attn: DASMA, DP-20
NN-513.4

58 Sandia National Laboratories
Attn: Mail Services
P.O. Box 5800
Albuquerque, NM 87185-0459
Attn: J. W. Kane/MS 0768

59 Central Intelligence Agency
Office of Facilities & Securities Services
Washington, DC 20505
Attn: Chief, Development Branch

60 National Institute of Standards and Technology
Physics Building, Room B157
Gaithersburg, MD 20899
Attn: Law Enforcement Standards Lab/
L. Elaison

**Distribution list for ARL-TR-98-2 under Contract N00039-91-C-0082,
TD No. 08A1011
(cont'd)**

Copy No.

61	Headquarters U.S. Secret Service 1800 G Street, NW Washington, DC 20332 Attn: Library
62	Computer Science Corporation 7405 Alban Station Court, Suite B200 Springfield, VA 22150-2318 Attn: Richard A. Swanson
63	ITT Industries
64	ITT Systems Corp Attn: AODTRA/DASIAC 1680 Texas St. S. E. Kirtland Air Force Base, NM 87117-5669 Attn: DASIAC DASIAC/DARE
65	JAYCOR 1410 Spring Hill Road, Suite 300 McLean, VA 22102 Attn: Dr. Cyrus P. Knowles
66	Vitro Corporation 15 Green Meadow Drive Langhorne, PA 19047 Attn: Thomas J. Whittle
67	J. M. Huckabay, ARL:UT
68	R. L. Rogers, ARL:UT
69	M. A. Koerner, ARL:UT
70	Library, ARL:UT
71	Advanced Technology Laboratory, ARL:UT
72-86	Reserve, Advanced Sonar Division, ARL:UT



APPLIED RESEARCH LABORATORIES

THE UNIVERSITY OF TEXAS AT AUSTIN

P. O. BOX 8029 • Austin, Texas 78713-8029 • (512) 835-3200 • FAX: (512) 835-3259

ERRATA

for

Report DSWA-TR-98-50 / Report ARL-TR-98-2

"Test and Development of High Data Rate Millimeter Wave Data Links
over Low Elevation Paths for Physical Security Systems"
by Robert L. Rogers and Matthew A. Koerner

Report DSWA-TR-98-50 / ARL-TR-98-2 was published with an incorrect DSWA report number on the Standard Form 298 (p. i). Block 10 of the SF 298, "Sponsoring/Monitoring Agency Report Number," should read DSWA-TR-98-50.

A self-adhesive label with the correct report number is attached. Please place the label over the incorrect information in Block 10 of the SF 298. Thank you.

Received
1/18/2000

A368850
19991004219